

# A gas phase approach for glycan analysis: Combining ultrahigh-resolution ion mobility spectrometry with cryogenic vibrational spectroscopy

Présentée le 9 avril 2021

Faculté des sciences de base  
Laboratoire de chimie physique moléculaire  
Programme doctoral en chimie et génie chimique

pour l'obtention du grade de Docteur ès Sciences

par

## Ahmed BEN FALEH

Acceptée sur proposition du jury

Prof. J. Vanicek, président du jury  
Prof. T. Rizzo, directeur de thèse  
Prof. G. Von Helden, rapporteur  
Prof. E. Garand, rapporteur  
Prof. U. Lorenz, rapporteur



# Abstract

Understanding the biological processes that mediate cellular interactions in living organisms is central to developing breakthroughs in diagnostics and therapeutics. The last decades have been punctuated by the development of revolutionary analytical technologies that have enabled the analysis of biomolecular structures and unraveled the roles they play in biological systems. However, certain classes of biomolecules remain less understood than others. In fact, despite being among the most abundant molecules on our planet, glycans remain among the least understood class of biological macromolecules due to their highly complex structure. The complexity of glycan molecules arises from their isomeric nature, which poses a significant challenge to classical analytical tools.

The advent of ionization methods such as ESI and MALDI has led to an unprecedented expansion of gas phase techniques for the analysis of biomolecules. Compared to condensed phase approaches, gas phase analysis allows for isolating specific molecules and collecting highly accurate and specific structural information.

In this work, we present an analytical approach for the analysis of glycan molecules based on the combination of different gas phase techniques. A central part of this thesis is the development, design, and characterization of two new instruments that have the capabilities to identify glycan isomers unambiguously. Our experimental approach is based on the combination of high-resolution ion mobility spectrometry with cryogenic IR spectroscopy. Ion mobility spectrometry allows to separate charged molecules in the gas phase according to their overall shape, serving as an isomer-selective prefilter to the IR spectroscopic interrogation process. While IMS provides a way to separate glycan isomers, vibrational

spectroscopy is used to identify the mobility-separated molecules. The IR absorptions characteristic of glycan molecules lead to distinct spectroscopic fingerprints, which are perfectly suited for the identification of glycan isomers.

In the first part of this work, we report the modification of an existing instrument that combined drift tube IMS with IR spectroscopy. We replaced the drift tube section by IMS device employing a relatively novel technique called SLIM, which provides the highest mobility resolution reported to date while ensuring a minimum loss of ions. The functioning principles, simulations, and characterization of the IMS SLIM device are presented in detail in this work. This prototype instrument was used in a series of proof-of-concept experiments where we successfully demonstrate that our approach provides highly accurate results, comparable to sophisticated double-resonance spectroscopic schemes. We also describe an analytical protocol that serves to identify the isomeric content of disaccharide and tetrasaccharide mixtures unambiguously using a database approach. Furthermore, we report a series of experiments in which we separate and identify the  $\alpha$  and  $\beta$  anomers of disaccharide molecules.

In the second part of the thesis, we describe a second-generation instrument based on the same approach. The design of this instrument was aimed at maximizing its sensitivity and throughput while adding more analytical functionalities. It includes a section designed to maximize the ion usage rate, a CID section enabling the performance of IMS<sup>n</sup> experiments, as well as a cryogenic multi-trap allowing for the multiplexed spectroscopic analysis of glycan isomers. We hereby report the characterization results highlighting the instrument capabilities in terms of ion transmission and IMS resolution. We also report the first rapid, multiplexed, IR spectral acquisition of two tetrasaccharide isomers, which emphasizes the unique capabilities of this home-built instrument.

# Résumé

La compréhension des processus biologiques qui servent de médiateurs aux interactions cellulaires dans les organismes vivants est essentielle au développement des domaines du diagnostic et de la thérapeutique. Les dernières décennies ont été ponctuées par le développement de technologies analytiques révolutionnaires qui ont permis d'analyser les structures biomoléculaires et de mettre en évidence le rôle qu'elles jouent dans les systèmes biologiques. Cependant, certaines classes de biomolécules restent moins comprises que d'autres. En effet, bien qu'ils soient parmi les molécules les plus abondantes de notre planète, les sucres, appelé aussi polysaccharides, ou encore glycanes, restent parmi les classes de macromolécules biologiques les moins étudiés en raison de leur structure très complexe. La complexité des molécules de glycanes découle de leur nature isomérique, ce qui pose un défi important aux outils d'analyse classiques.

L'avènement des méthodes d'ionisation telles que l'ionisation par électro-nébulisation a conduit à une expansion sans précédent des techniques en phase gazeuse pour l'analyse des biomolécules. Par rapport aux approches en phase condensée, l'analyse en phase gazeuse permet d'isoler des molécules spécifiques et de recueillir des informations structurales très précises et spécifiques.

Dans ce travail, nous présentons une approche analytique pour l'analyse des molécules de sucres basée sur la combinaison de différentes techniques en phase gazeuse. Une partie centrale de cette thèse concerne le développement, la conception et la caractérisation de deux nouveaux instruments qui ont la capacité d'identifier les isomères de glycanes sans ambiguïté. Notre approche expérimentale est basée sur la combinaison de la spectrométrie

de mobilité ionique (SMI) à haute résolution avec la spectroscopie infrarouge (IR) cryogénique. La spectrométrie de mobilité ionique permet de séparer les molécules chargées dans la phase gazeuse en fonction de leur forme globale, servant de préfiltre sélectif des isomères précédent le processus d'interrogation spectroscopique IR. Alors que la SMI permet de séparer les isomères de polysaccharide, la spectroscopie vibrationnelle est utilisée pour identifier les molécules séparées par mobilité. Les absorptions IR caractéristiques des molécules de glycanes conduisent à des empreintes spectroscopiques distinctes, qui sont parfaitement adaptées à l'identification des différents isomères.

Dans la première partie de ce travail, nous rapportons la modification d'un instrument existant qui combine un tube de dérive pour la SMI, avec la spectroscopie IR. Nous avons remplacé le tube de dérive par un dispositif SMI utilisant une technique relativement nouvelle appelée SLIM, qui fournit la plus haute résolution de mobilité signalée à ce jour tout en assurant une perte minimale d'ions. Les principes de fonctionnement, les simulations et la caractérisation du dispositif SLIM de la SMI sont présentés en détail dans ce travail. Ce prototype d'instrument a été utilisé dans une série d'expériences de démonstration de faisabilité au cours desquelles nous avons réussi à démontrer que notre approche donne des résultats très précis, comparables aux schémas spectroscopiques sophistiqués à double résonance. Nous décrivons également un protocole analytique qui sert à identifier sans ambiguïté le contenu isomérique des mélanges de disaccharides et de tétrasaccharides en utilisant une approche de base de données. En outre, nous présentons une série d'expériences dans lesquelles nous séparons et identifions les molécules de disaccharides et leurs anomères.

Dans la deuxième partie de la thèse, nous décrivons un instrument de deuxième génération basé sur la même approche. La conception de cet instrument vise à maximiser sa sensibilité et son rendement tout en ajoutant davantage de fonctionnalités analytiques. Il comprend une section conçue pour maximiser le taux d'utilisation des ions, une section de dissociation induite par collision (DIC) permettant la réalisation d'expériences SMI<sup>n</sup>, ainsi qu'un multi-

piège cryogénique permettant l'analyse spectroscopique simultanée de différents isomères de glycanes. Nous présentons ici les résultats de la caractérisation mettant en évidence les capacités de l'instrument en termes de transmission ionique et de résolution SMI. Nous rapportons également la première acquisition spectrale IR rapide et multiplexée de deux isomères de tétrasacharides, ce qui souligne les capacités uniques de cet instrument développé et fabriqué dans notre laboratoire.



# Content

<b>ABSTRACT</b> .....	<b>III</b>
<b>RÉSUMÉ</b> .....	<b>V</b>
<b>CONTENT</b> .....	<b>9</b>
<b>1. INTRODUCTION</b> .....	<b>13</b>
1.1.    THE IMPORTANCE OF GLYCAN ANALYSIS .....	13
1.2.    GLYCANS: MULTIDIMENSIONAL COMPLEXITY .....	16
1.3.    STANDARD METHODS FOR GLYCAN ANALYSIS .....	21
1.3.1    Separation techniques in glycan analysis.....	22
1.3.2    Multidimensional approaches.....	27
1.4.    OUTLINE OF THIS WORK.....	28
<b>REFERENCES</b> .....	<b>30</b>
<b>2. EXPERIMENTAL OVERVIEW</b> .....	<b>39</b>
2.1.    ION MOBILITY SPECTROMETRY.....	39
2.1.1    Drift tube ion mobility spectrometry (DTIMS).....	40
2.1.2    High-field asymmetric waveform ion mobility spectrometry (FAIMS) .....	44
2.1.3    Trapped ion mobility spectrometry (TIMS).....	46
2.1.4    Travelling wave ion mobility spectrometry (TWIMS).....	48
2.2.    STRUCTURES FOR LOSSLESS ION MANIPULATION (SLIM) .....	53
2.3.    SPECTROSCOPIC ANALYSIS OF BIOMOLECULES.....	55
2.3.1    Vibrational spectroscopy.....	55
2.4.    SUMMARY AND MOTIVATION .....	62
<b>REFERENCES</b> .....	<b>64</b>
<b>3. DESIGN AND CHARACTERIZATION OF THE PROTOTYPE</b> .....	<b>73</b>
3.1.    OVERVIEW .....	73
3.2.    VACUUM SYSTEM.....	77
3.3.    RADIO-FREQUENCY DEVICES FOR THE MANIPULATION OF ION MOTION .....	80
3.3.1    Ion funnel and ring electrode guides.....	82

3.3.2	Multipole guides .....	85
3.3.3	Planar RF devices .....	86
3.4.	TIME-OF-FLIGHT ANALYZER.....	96
3.5.	ELECTRONICS, TIME-SEQUENCE GENERATION, AND DATA ACQUISITION .....	98
3.6.	SLIM IMS PERFORMANCE CHARACTERIZATION .....	99
3.6.1	15 cm straight SLIM design .....	99
3.6.2	Serpentine SLIM device.....	104
<b>REFERENCES .....</b>		<b>114</b>
<b>4. IDENTIFICATION OF DISACCHARIDE ISOMERS: IR-IR VS. IMS-CIS...117</b>		
4.1.	INTRODUCTION .....	118
4.2.	EXPERIMENTAL METHODS.....	120
4.2.1	Sample preparation .....	120
4.2.2	IR-IR double-resonance messenger-tagging spectroscopy.....	121
4.2.3	Ion-mobility pre-selection for isomer-selective messenger-tagging spectroscopy.....	121
4.3.	RESULTS AND DISCUSSION.....	122
4.3.1	IR-IR double resonance spectroscopy.....	126
4.4.	CONCLUSIONS .....	129
<b>REFERENCES .....</b>		<b>131</b>
<b>5. IDENTIFYING THE COMPOSITION OF AN UNKNOWN GLYCAN MIXTURE.....139</b>		
5.1.	INTRODUCTION .....	139
5.2.	EXPERIMENTAL APPROACH .....	142
5.2.1	Samples .....	142
5.2.2	Instrument.....	143
5.3.	RESULTS AND DISCUSSION .....	144
5.3.1	Identification of glycans from mixtures .....	144
5.4.	CONCLUSIONS .....	150
<b>REFERENCES .....</b>		<b>152</b>
<b>6. IMS-CIS TO DISTINGUISH GLYCAN ANOMERS.....160</b>		
6.1.	INTRODUCTION .....	160
6.2.	MATERIALS AND METHODS .....	164
6.2.1	Samples .....	164
6.2.2	Ion-mobility-selective IR spectroscopy.....	165
6.3.	RESULTS AND DISCUSSION.....	166
6.3.1	IMS of glycans.....	166
6.3.2	Spectroscopic identification of anomers .....	168
6.3.3	Monitoring of glucose mutarotation .....	170
6.4.	CONCLUSIONS .....	172
<b>REFERENCES .....</b>		<b>173</b>

<b>7. DESIGN AND CHARACTERIZATION OF SECOND-GENERATION INSTRUMENT .....</b>	<b>180</b>
7.1. OVERVIEW .....	180
7.2. VACUUM SYSTEM.....	182
7.3. RADIO FREQUENCY DEVICES FOR ION MANIPULATION.....	184
7.3.1 Ring electrode ion guides.....	185
7.3.2 Multipole devices.....	187
7.3.3 Planar RF Devices.....	187
7.4. ELECTRONICS, TIME-SEQUENCE GENERATION, AND DATA ACQUISITION .....	197
7.5. CHARACTERIZATION RESULTS.....	199
7.5.1 SLIM IMS module.....	200
7.5.2 Cryogenic planar multi-trap.....	207
<b>REFERENCES .....</b>	<b>224</b>
<b>8. SUMMARY AND FUTURE PERSPECTIVES .....</b>	<b>225</b>
<b>REFERENCES .....</b>	<b>228</b>
<b>ANNEX A.....</b>	<b>229</b>
<b>ANNEX B.....</b>	<b>231</b>
<b>ACKNOWLEDGEMENTS.....</b>	<b>237</b>



# 1. Introduction

## 1.1. The Importance of glycan analysis

Our understanding of life has been highly impacted by recent advances in molecular biology. Over the last decades, technological breakthroughs and newly developed tools have allowed for a deeper comprehension of the biological information flowing from DNA to RNA, all the way to proteins.<sup>1</sup> Although major advances have been made in the study of proteins and nucleic acids, unraveling the secrets of living cells requires an understanding of their universal characteristics. These characteristics can be categorized into: (1) genetic coding, which is DNA-based and called the *genome*; (2) RNAs responsible for transcription (the *transcriptome*); (3) structural and functional proteins (the *proteome*); (4) energy flux and signaling (the *metabolome*); (5) the lipid membrane (the *lipidome*); and (6) the cell surface decorated with glycans (the *glycome*).<sup>2</sup> While the latter is crucially central to the understanding of life itself, its diversity makes it exceedingly complex to analyze.

The different domains in which glycans are involved are shown in the schematic of Figure 1.1. Glycans are the most abundant biological molecules on our planet and can be conjugated to proteins and lipids forming glycoproteins and glycolipids, respectively. They play a central role in biological systems as they decorate the surface of nearly all living cells. Glucose is perhaps the best known monosaccharide, as it serves as a source of energy in the metabolic system. Poor regulation of this key sugar in the body is at the origin of diabetes, a silent killer. A high glucose concentration can damage organs, while a low concentration can lead to the loss of consciousness and sudden death.

Glycans are literally involved in every aspect of life. At the molecular level, they bind covalently to proteins through a post-translational process called glycosylation. In glycoproteins, one finds two main types of glycans: (1) N-linked glycans, resulting from the glycan binding to the nitrogen of an asparagine or arginine amino acid; and (2) O-linked glycans, resulting from binding to the oxygen of either serine or threonine. Glycosylation affects critical properties of the proteins such as stability, folding, and immunogenicity.<sup>3</sup>

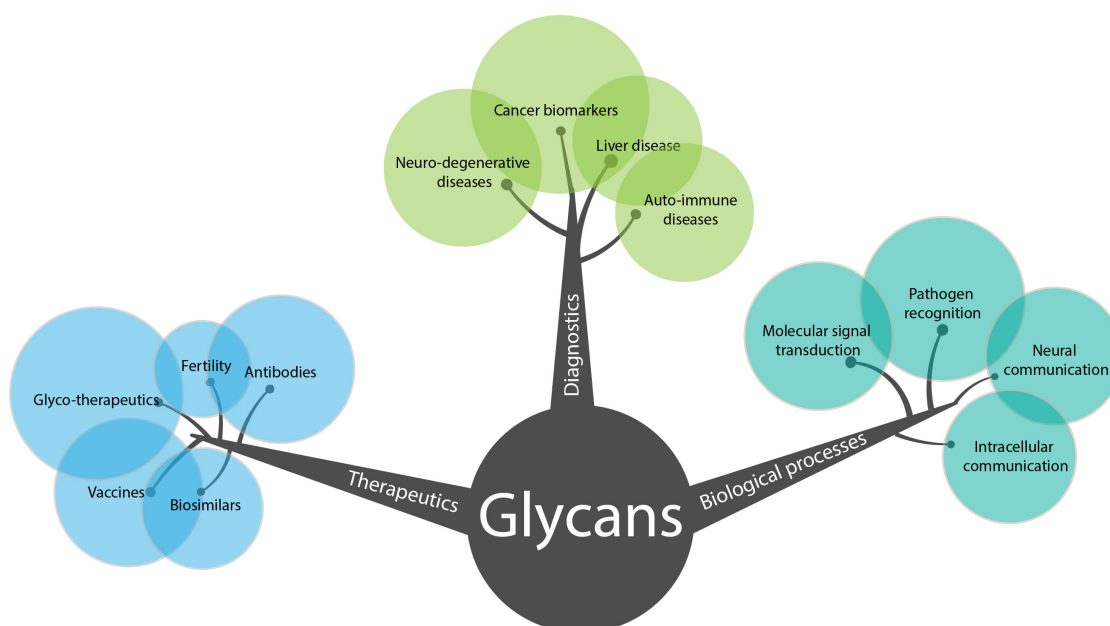


**Figure 1.1:** Glycans are involved in most biological processes, and are hence implicated one way or another in almost every human disease.

Located on the surface of cells, glycans and glycoconjugates are responsible for mediating cellular interactions with the surrounding environment. They are thus involved in molecular signal transduction, pathogen recognition, neural communication, and intracellular recognition. Glycans determine human blood type and mediate human fertilization.<sup>4</sup> They are also associated with immune response, viral and bacterial infections as well as different types of cancer, where differences in glycosylation are associated with tumor progression.<sup>5-6</sup> The fact that glycans are involved in viral pathogenesis led glycobiology to emerge as a key field in vaccine development.<sup>7</sup> Figure 1.2 shows the

glycosylation (in blue) of surface proteins of different viruses, among which is the so-called spike glycoprotein of the coronavirus family. These glycans play an important role in enabling the virus to enter targeted host cells and use them as a vector to multiply.<sup>8</sup>

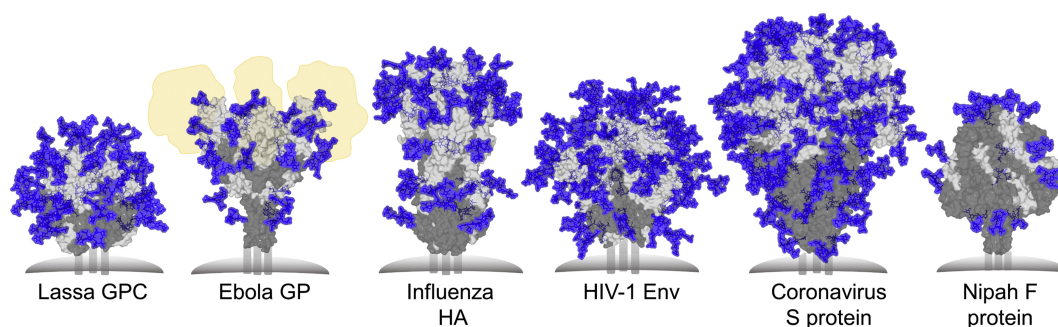


**Figure 1.2:** Each protein from these different viruses is covered with a glycan layer (in blue). This motivates the need for an in-depth characterization of the glycosylation pattern, in order to understand the role it plays in the interaction between a virus and its cellular targets.<sup>7</sup> This figure was reproduced with permission from the Elsevier journal.

The observation of disease-specific alteration of glycosylation of proteins on the surface of cells has led to the use of glycans as biomarkers in cancer and inflammation research<sup>9</sup> (middle branch in Figure 1.1). Anomalous glycosylation patterns have been associated with a wide range of diseases including ovarian<sup>10</sup>, colon<sup>11</sup>, and breast cancer<sup>12</sup>, rheumatoid arthritis, and liver disease.<sup>13-14</sup> Differences in glycosylation were also observed in neurodegenerative diseases such as Parkinson disease and Alzheimer's.<sup>15-16</sup>

In addition to their potential use in diagnostics, glycans are crucial to biological drug discovery and production (left branch in Figure 1.1). Indeed, biotherapeutics such as monoclonal antibodies are currently among the best-selling drugs and are well suited for the treatment of a wide range of pathologies including cancer and autoimmune diseases<sup>17</sup>. The glycosylation pattern of biotherapeutics is considered a critical quality attribute, as it directly affects their effectiveness, toxicity, and long term stability,<sup>18</sup> and thus plays an important role in the regulatory approval of biosimilars.<sup>19</sup>

To summarize, glycans play a key role in almost all biological processes. For this reason, the development of analytical tools appropriate for glycans is essential to advance our understanding of these processes as well as to facilitate the development of therapeutics to intervene in them.<sup>20</sup> However, the structural complexity of glycans make this an extremely challenging task.<sup>21</sup>

## 1.2. Glycans: Multidimensional complexity

Glycans give rise to one of the greatest analytical challenges in modern biology. The source of this challenge is two-fold: (1) the structural complexity due to multiple levels of isomerism; and (2) their non-template driven biosynthesis that is sensitive to multiple factors.

Glycans are oligomers of monosaccharides or sugars that are covalently attached by glycosidic linkages. As shown in Figure 1.3, monosaccharides present in mammals include *hexoses* (Hex) such as glucose (Glc), galactose (Gal) and mannose (Man); as well as *N-acetylhexosamines* (HexNac) such as N-acetylglucosamine (GlcNac); and *sialic acids* such as N-acetylneuraminic acid (Neu5Ac).<sup>22</sup>

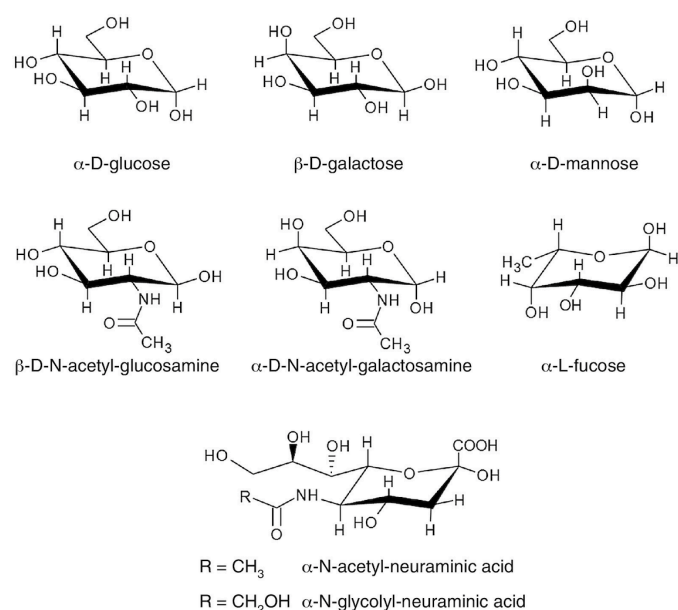


**Figure 1.3:** Different monosaccharides present in mammals.<sup>22</sup>

The various levels of isomeric complexity of glycans are represented in Figure 1.4. The different orientation of a single hydroxyl (OH) group gives rise to several isomeric forms of monosaccharide units (Figure 1.4a). For example, glucose differs from galactose only by the orientation of OH group bound to the asymmetric C4 carbon atom. In addition, each monosaccharide can exist in two different configurations specified by the orientation of the OH group attached to the C1 carbon (i.e., the so-called anomeric carbon) at the reducing-end, leading to isomeric  $\alpha$  and  $\beta$  anomers. The formation of glycosidic linkages at this anomeric carbon can thus result in two possible isomeric structures, shown in Figure 1.4b (green). Moreover, different carbon stereogenic centers can be involved in glycosidic linkages (Figure 1.4b red), resulting in regioisomers, and the formation of multiple glycosidic linkages to the same monosaccharide leads to branched structures (Figure 1.4c). Lastly, differences in the sequence of monosaccharides give rise to isomers composed by a different sequence of monosaccharides (Figure 1.4b black).

To summarize, different oligosaccharide isomeric forms can originate from the following configurations:

- i. A different monosaccharide content (glucose, galactose, mannose...)
- ii. A different sequence of the monosaccharide residues
- iii. A different glycosidic linkage site
- iv. A different stereogenic configuration of the glycosidic linkage ( $\alpha$  or  $\beta$ )
- v. Different branching possibilities

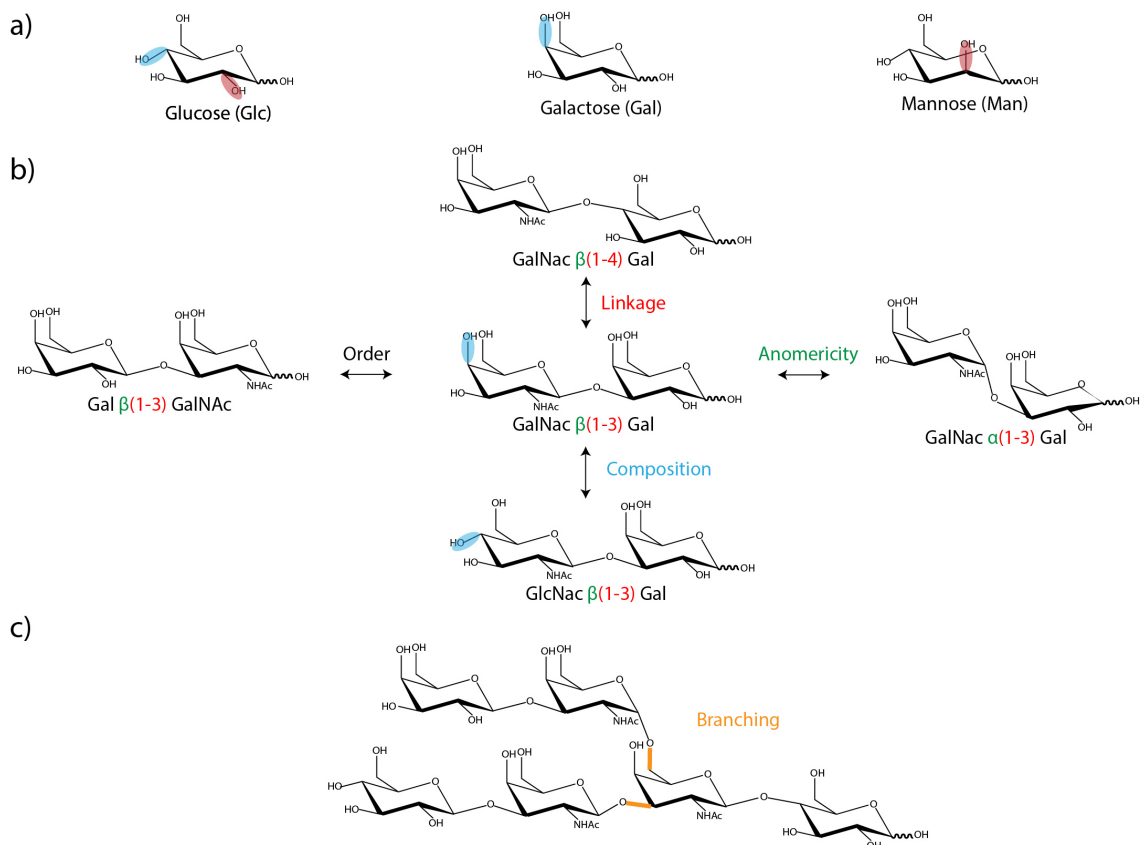


**Figure 1.4:** Different isomeric configurations present in glycans. a) The structure of three monosaccharide isomers different only in the orientation of a hydroxyl group b) Four different types of isomerism present in disaccharides: position of the monosaccharide in the sequence (black), different linkage positions (red), different anomerism of the glycosidic linkage (green), different monosaccharide content (blue) c) Different branching possibilities give rise to yet an additional

isomer configuration, as a single monosaccharide can be linked to more than one residue. Here the different branches are depicted (orange).

For the sake of simplicity, the SNFG symbol nomenclature is introduced in Figure 1.5.

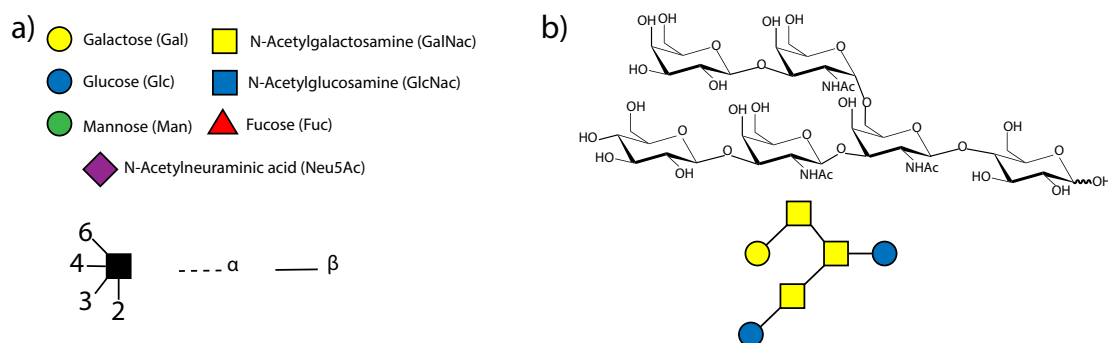


**Figure 1.5:** a) The SNFG<sup>23</sup> symbol nomenclature is used to simplify glycan structures. Different shapes and colors represent different monosaccharides. The linkage position is described by different angles and the anomericity by a dashed line in the case of an  $\alpha$  configuration and a solid line in the case of  $\beta$  configuration. b) The simplified structure of a glycan using the SNFG symbol nomenclature.

A second factor complicating the analysis of glycan structure lies in the nature of their biosynthesis. As opposed to DNA and proteins, the biosynthesis of glycans is not template driven and is highly influenced by numerous factors.<sup>22</sup> Glycosylation takes place in the Golgi apparatus and the endoplasmic reticulum of a given cell and is mainly driven by enzymes that shape the different oligosaccharides. A schematic overview of the different steps involved in this process are displayed in Figure 1.6. It begins with the transfer of an N-acetylglucosamine (GlcNAc) to a dolichol membrane anchor and the creation of a precursor glycan containing 14 monosaccharide units in the ER lumen. It is then transferred to the Asn residue of a protein before being processed by enzymes (MOGS, GANAB) that remove glucose monosaccharides, followed by MAN1, which removes mannose monosaccharides. The glycosylated protein is then transferred to the Golgi apparatus where it is further processed by MAN 1, cleaving further mannose residues and MGAT1, which adds GlcNAc

residues. Complex glycans are created through further cleavage of mannose residues by the MAN2 enzyme and the addition other monosaccharides by a series of transferases. Small molecules such as Kifunensine and Swainsonine act as enzymatic inhibitors, contributing to the variety of the produced N-glycans. Glycosylation is hence dependent on the internal properties of the cell such as its genetic profile,<sup>24</sup> as well as on the extracellular environment.<sup>25</sup> It has also been shown that bioreactor conditions such as dissolved oxygen tension (DOT), pH/[NH<sub>4</sub><sup>+</sup>], temperature, and nutrient supplements highly influence glycosylation.<sup>22</sup> For these reasons, the development of culture cells for glycan synthesis needs to be done in an iterative manner, and a thorough analysis of glycan products is necessary at each step to control the biosynthesis process.

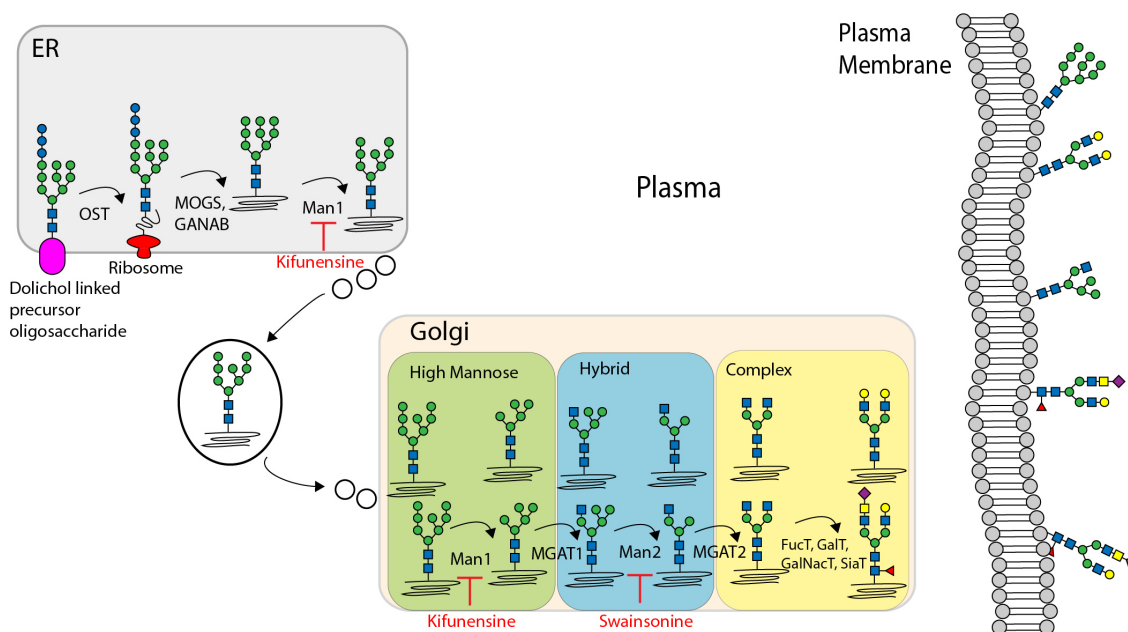


**Figure 1.6:** Schematic representation of N-Glycan biosynthesis in animals<sup>26-27</sup>.

To conclude, as opposed to the analysis of proteins and DNA, glycoscience deals with a tremendously higher degree of complexity and represents a significant challenge to conventional analytical approaches.

### 1.3. Standard methods for glycan analysis

Over the last decade, glycomics has evolved rapidly and shown great potential to benefit fields such as therapeutics and disease diagnostics. As stated in the previous section, an increasing number of drugs are based on glycoproteins. Although a clear standardized protocol to characterize the glycosylation of pharmaceuticals has not been defined yet, there are general guidelines of what needs to be analyzed. This includes, for example, the analysis of intact glycoforms of glycoproteins, glycan mapping, N-glycan macro- and micro-heterogeneity, and monosaccharide content.<sup>28-29</sup> While the analysis of glycoforms deals with intact glycoproteins and provide a rapid way to characterize oxidization and acetylation, glycan mapping is aimed to determine the primary structure of released glycans. Glycans are released from glycoproteins through enzymatic digestion, and the most common way to cleave glycans is the use of the peptide-N-glycosidase F (PNGase F) enzyme, which cleaves the linkage between the asparagine amino acid residue and the GlcNac monosaccharide attached to it. During the monitoring process, perhaps the most challenging task is to rapidly and accurately detect and identify different isomers among the released glycans.

Nuclear magnetic resonance (NMR) and X ray crystallography have been considered the go-to techniques for the characterization of glycan tertiary structures.<sup>30</sup> They allows to accurately determine glycans sequence, differentiate linkage positions and anomericity of the glycosidic bond<sup>31-32</sup>, and can be used to analyze glycoproteins. Besides, the non-destructive nature of NMR allows to analyze glycans in conditions that are closest to their physiological environment. Nevertheless, the large amounts of highly pure sample needed for NMR analysis, and the extensively long analysis times required, constitutes a major barrier for its use as an analytical tool for biological samples.

When considering the primary structure of glycans however, mass spectrometry (MS) based methods are more widely used. A glycan sample is ionized and brought into the gas phase using either matrix assisted laser desorption ionization (MALDI) or electrospray ionization

(ESI).<sup>33-34</sup> Analytes present in the sample are then identified according to their respective mass-to-charge ratios. However, conventional MS schemes are blind to the stereochemistry of glycans' primary structures. This renders the detection and identification of different isomers present in mixture, relying on their mass-to-charge ratio alone, a nearly impossible task. Although tandem MS (MS/MS) allows to collect more information on glycan structures, it is often not enough for an unambiguous elucidation of the stereochemistry of glycan isomers. To tackle this isomeric complexity, a multidimensional approach is needed. For this reason, most analytical tools used in glycomics rely on MS hyphenated with a separation technique.

### 1.3.1 Separation techniques in glycan analysis

The most commonly used separation techniques for glycan analysis are chromatographic techniques, and capillary electrophoresis. Lately, ion mobility spectrometry has emerged as a potential option to add to the palette of techniques commercially available for glycan analysis. These separation techniques are then combined with a detector, typically a mass spectrometer or a fluorescence detector in some cases.

## Chromatography

In liquid chromatography (LC), analytes dissolved in a mobile phase are separated following their different interactions with a stationary phase, and elute at different times referred to as retention times. Retention times are correlated to the size and shape of the molecules, as well as how they interact with the different component of the stationary phase column. A database of retention times is used to identify different glycan molecules. It is common to label glycans with fluorescence dye to enhance the sensitivity and resolution of the separation. The various LC techniques used for glycan analysis include hydrophilic-interaction chromatography (HILIC)<sup>35-36</sup>, reverse-phase chromatography (RP-LC)<sup>37</sup> and porous graphitized carbon (PGC)<sup>38-39</sup>.

In RP-LC, separation of glycans occurs through non-covalent interactions with the particles composing the column. The columns typically utilize C18 as a stationary phase and come in a variety of models with different diameters, lengths and particle sizes. All these parameters have an influence on the retention time of the analytes. As RP-LC operates on hydrophobic stationary phases, the derivatization of glycans is known to enhance retention as well as sensitivity, which is much needed for coupling with ESI-MS.

While RP-LC uses a non-polar stationary phase and a polar solvent, HILIC makes use of a stationary phase that is more polar than the mobile phase. The aqueous mobile phase is rich in acetonitrile, while a thin water layer is immobilized in the polar stationary phase. The retention of the fluorescently labelled glycans depends upon hydrogen bonding, ionic interactions and on the number and accessibility of polar groups.<sup>40</sup> To achieve glycan separation, a gradient shift from an organic aqueous phase rich in acetonitrile to a purely aqueous phase is employed.<sup>41</sup> HILIC provides a higher resolution and retention, a higher sensitivity and better defined peak shapes compared to other chromatographic techniques.<sup>36</sup>

PGC columns are also widely used in glycan analysis. As opposed to RP-LC, PGC is characterized by a high retention of native (non-derivatized) glycans. It makes use of a combination of a RP behavior with the high polar nature of the planar graphite material that composes the column. Hence, the separation is based on the hydrophobicity of the analytes as well as on their 3D structure.

Upon separation, glycans are ionized and brought to the gas phase typically through electrospray ionization ESI in positive or negative modes, meaning that the analyte will be positively or negatively charged, respectively. Positive mode is more widely used and the glycans are detected due to the charge of one or multiple adducts, which the analyte acquires during the ESI process. These can be protons, alkali metals or ammonium adducts. The presence of different adducts will depend upon the initial glycan solution as well as on the mobile phase used for the separation.<sup>42-43</sup>

It is important to note that the retention time is not an inherent property of the molecule and is highly dependent on the used column and on the experimental conditions. Furthermore, typical retention times range from minutes to tens of minutes, depending on the resolution that is required to separate certain isomeric forms. In addition, in certain cases, LC based methods lack the resolving power needed to separate certain isomeric forms. Moreover, and besides the time consuming labeling and derivatization steps that are often required, calibration using a so-called dextran ladder is needed periodically to calibrate retention times in glucose units (GU).<sup>44</sup>

## Capillary electrophoresis

Electrophoretic techniques have proven to be powerful tools for the analysis of biomolecules and have contributed to the development of life science research. They are well suited for large and small molecules alike, and can thus be used for the analysis of glycoproteins<sup>45-46</sup>, as well as for released glycans.<sup>47-49</sup> In glycan analysis, electrophoretic techniques such as capillary zone electrophoresis (CZE) and capillary gel electrophoresis (CGE) are often used. Molecules of different shapes interact differently with the capillary and elute at different migration times. By building a data base of migration times it is possible to identify the different components of a mixture.

In CZE, an electrical gradient is applied to a liquid sample. The separation is achieved due to the differences in electrophoretic migration of different species in an electric field and is directly related to the charge-to-size ratio of the analytes.<sup>50</sup> The mechanisms of CE separation are electroosmotic flow (EOF) and electrophoretic mobility.<sup>51</sup> While electrophoretic mobility depends upon the volume to charge ratio of the analytes, EOF is the flow of the background electrolyte and is directed from the anode towards the cathode. The separation is thus achieved due to the superposition of these two phenomena.<sup>47</sup>

CGE has mainly been used for protein separation and was introduced only recently as a high throughput analytical tool for glycans. The separation of biomolecules in CGE is

achieved in a sieving medium and is based on differences in the hydrodynamic radius. As opposed to CZE, in CGE, EOF needs to be suppressed for the separation to be exclusively based on the hydrodynamic radius.<sup>52</sup>

The combination of CE with laser induced fluorescence (LIF) have been widely used in glycan mapping since it offers a high-resolution separation and increased sensitivity due to the low detection limits offered by LIF. As glycans do not contain UV chromophores, a labeling step is required.<sup>53</sup>

Developments in liquid interfaces opened the door to the combination of CE with MS. The increased flow obtained by the use of sheath liquid interface ensures an effective electrospray and thus grants access to gas-phase techniques.<sup>54-55</sup> Other interfaces such as the sheathless interface<sup>56</sup> and the liquid junction interface were employed to perform CE-MS<sup>57</sup>.

As for LC, the migration time is not an inherent property of the molecule and depends on the used capillary as well as on operating conditions. Besides, a precise calibration of the device is needed at every measurement in order to identify the separated analytes. For glycan analysis, labelling is commonly used to enhance the sensitivity and resolution of the methods. Lastly, slight fluctuations in EOF, temperature or pH, highly influence the migration times, thus hindering the repeatability of the method.<sup>58</sup>

## Ion mobility spectrometry

Over the last decades, the combination of ion mobility spectrometry (IMS) with MS has developed into a tool of choice for the analysis of biomolecules in the gas phase. Owing to the fast isomer separation, IM-MS has found applications in numerous areas in bioanalysis, including glycan analysis.<sup>59-61</sup> The rapid separation of ionized glycans takes place in the gas phase and depends upon the ion's charge-to-size ratio as well as on different parameters related to the experimental conditions such as the composition and density of the drift gas, the applied voltages, the pressure, and the temperature. Nevertheless, it is possible to extract

a rotationally averaged collisional cross-section (CCS) of an ion in a specific drift gas, which is not the case when using LC.<sup>62</sup>

While drift tube (DT) technology has been the most commonly used in IMS instruments to date<sup>60, 63</sup>, various technologies exist including traveling wave (TW)<sup>64-65</sup>, field asymmetric waveform ion mobility spectrometry (FAIMS)<sup>66</sup>, and trapped ion mobility spectrometry (TIMS).<sup>67-68</sup>

The first successful separation of glycan isomers by IM-MS was achieved in the late 90's, using drift tube (DT) IMS technology. In these series of experiments, different glycan isomers were detected at different drift times proving the sensitivity of IMS to small structural differences.<sup>63, 69</sup>

Technological advancements during the last decade prompted the development of ultrahigh-resolution devices and opened the door to the incredible potential of IMS to revolutionize bioanalysis by providing a rapid way to separate isomeric species. However, despite the possibility to extract the CCS, the latter is not an exclusive property of the molecule and depends upon the drift gas used for separation. Moreover, experimentally determined CCSs often include a non-negligible error that can represent a serious barrier to the identification of isomers with the slightest differences in structure, typically when the difference in percentage exceed the error's interval.

Furthermore, using drift times for identification presents similar drawback as using retention times in LC, and imposes the use of a calibrant or the addition of a calibration step at each measurement adding steps to the analytical process.

Since IMS is central to this work, a thorough description of the different available IMS technologies including a scientific background for IMS separation, different principles as well as the latest developments will be described in the chapter to come.

### 1.3.2 Multidimensional approaches

The inability of one single analytical technique to elucidate the inherent isomeric complexity of glycans, despite the biological importance of the slightest differences in their structure, led to the use of multidimensional approaches for glycan characterization. To this end, the combination of orthogonal techniques such as IM-MS with spectroscopic schemes was proposed to tackle the analytical challenge at hand.

Gas-phase spectroscopy has been developed as a tool for characterizing biomolecules during the last decade, and IMS techniques such as FAIMS or DT-IMS were first combined to UV spectroscopy for the study of mobility selected isomers.<sup>70-72</sup> During the following years, the combination of IMS with infrared multi-photon dissociation (IRMPD) was proposed for the analysis of glycan isomers.<sup>73</sup> While IM-MS is sensitive to the overall size and shape of a molecule, IR spectroscopy allows to probe structure-sensitive intramolecular interactions. An IR spectrum can therefore be regarded as a molecular fingerprint. Although presenting promising results, the limited resolution of the obtained spectra for relatively small glycans using IRMPD suggests that the use of these spectra as fingerprints for identification may prove difficult for bigger and more complex glycans.<sup>74</sup> Recently, cryogenic-ion IR spectroscopy was applied in combination with IMS for glycan analysis. In contrast to IRMPD, cryogenic IR spectroscopy provides more structured and highly resolved spectra well suited for identification of complex molecules.<sup>75-77</sup>

Naturally, this IR fingerprinting approach to identify glycan isomers requires a database of highly resolved fingerprints for each isomer of interest. To obtain isomer specific fingerprints, an ultrahigh-resolution isomer-separation device, such as one using IMS, is required. Moreover, if this approach to stand the test against existing methods in glycan analysis it needs to fulfill the following requirements: (1) *Robustness*: provide reproducible results that can be used for universal identification (2) *Sensitivity*: sensitive enough detection suitable for the small sample amounts typical for biological samples (3) *Accuracy*: provide

an unmistakable way of identifying different biomolecules (4) *Rapidity*: A rapid identification allowing for high throughput analyses that are much needed in bioscience.

## 1.4. Outline of this work

The recent technological developments in ion mobility spectrometry resulted in outstanding capabilities when it comes to separating biomolecules in the gas phase. In conjunction with mass spectrometry, IMS represents a powerful tool that exhibits the potential to greatly benefit the analytical field. Furthermore, when coupled to a structural probe such as IR spectroscopy, it allows for the generation of unique fingerprints, thus offering a way to bridge the technological gap currently holding back advancements in glycoscience.

In this work, the application of ultrahigh-resolution IMS as a pre-filter to cryogenic IR spectroscopy fingerprinting for glycan identification by will be presented.

An experimental overview will be presented in Chapter 2 of this thesis, including a detailed description of different IMS technologies. This part will include an overview of the theory behind TW-IMS separation as well as simulation of the principals of SLIM technology. In the second part of this chapter an overview of different IR spectroscopic interrogation techniques is presented, with an emphasis on messenger tagging cryogenic vibrational spectroscopy as a probe for molecular structure.

The implementation of SLIM IMS technology as a pre-filter for cryogenic IR spectroscopy in a first prototype will be presented in Chapter 3. The technological aspects of the implementation of a coolable SLIM IMS add-on will be discussed followed by a description of the implementation of a cyclic serpentine path SLIM section. This chapter also includes the characterization results of the new IMS section as well as a comparison to a previously implemented DT-IMS apparatus.

In Chapter 4, results of the comparison between the isomeric sensitivity of IR-IR double resonance and SLIM IMS IR spectroscopy for the analysis of disaccharides are discussed as well as the benefits and limits of both techniques. This chapter is based on the paper '*Combining ultra-high resolution ion mobility spectrometry with cryogenic IR spectroscopy for the study of biomolecular ions*' published in the 'Faraday Discussions' journal.

The ability of the first prototype to detect and identify a set of disaccharides as well as two isomeric human milk tetrasaccharides, from an unknown mixture is presented in Chapter 5. This chapter is largely based on the paper '*Combining ultra-high resolution ion mobility spectrometry with cryogenic IR spectroscopy for the analysis of glycan mixtures*' published in the 'Analytical Chemistry' journal.

Chapter 6 addresses the separation and identification of disaccharide  $\alpha$  and  $\beta$  reducing end anomers using SLIM IMS and cryogenic IR spectroscopy. It also includes the monitoring of glucose mutarotation through ion mobility measurements. This chapter is largely based on the paper '*Separation and identification of glycan anomers using ultrahigh-resolution ion-mobility spectrometry and cryogenic ion spectroscopy*' published in the 'Journal of the American Society for Mass Spectrometry'.

Chapter 7 of this thesis focuses on the design and construction of a second-generation instrument based on SLIM technology, including capabilities to perform  $MS^n$  and  $IMS^n$  experiments as well as multiplexing of the IR spectroscopic interrogation step. This apparatus comes as our proposed solution to the current analytical challenges in glycan analysis. A detailed presentation of the different section of the apparatus including a 10 m cyclic serpentine SLIM IMS section with two subsections designed for collision induced dissociation (CID) of biomolecular ions. The device also comprises a cryogenic multi-trap for high-throughput fingerprinting of biomolecules. The characterization of the apparatus capabilities in terms of ion transmission and IMS resolution as well as the performance of the cryogenic multi-trap are also included in this chapter.

# References

1. Kornfeld., A. V. a. S., Essentials of Glycobiology . 3rd edition. *Cold Spring Harbor Laboratory Press* **2017**.
2. Varki, A., Biological roles of glycans. *Glycobiology* **2017**, *27* (1), 3-49.
3. Reily, C.; Stewart, T. J.; Renfrow, M. B.; Novak, J., Glycosylation in health and disease. *Nat Rev Nephrol* **2019**, *15* (6), 346-366.
4. Pang, P. C.; Chiu, P. C.; Lee, C. L.; Chang, L. Y.; Panico, M.; Morris, H. R.; Haslam, S. M.; Khoo, K. H.; Clark, G. F.; Yeung, W. S.; Dell, A., Human sperm binding is mediated by the sialyl-Lewis(x) oligosaccharide on the zona pellucida. *Science* **2011**, *333* (6050), 1761-4.
5. Wong, C.-H.; Taniguchi, N., Current Status and New Challenges in Glycoscience: Overview. In *Glycoscience: Biology and Medicine*, Taniguchi, N.; Endo, T.; Hart, G. W.; Seeberger, P. H.; Wong, C.-H., Eds. Springer Japan: Tokyo, 2015; pp 11-14.
6. Dube, D. H.; Bertozzi, C. R., Glycans in cancer and inflammation--potential for therapeutics and diagnostics. *Nat Rev Drug Discov* **2005**, *4* (6), 477-88.
7. Watanabe, Y.; Bowden, T. A.; Wilson, I. A.; Crispin, M., Exploitation of glycosylation in enveloped virus pathobiology. *Biochim Biophys Acta Gen Subj* **2019**, *1863* (10), 1480-1497.
8. Banerjee, N.; Mukhopadhyay, S., Viral glycoproteins: biological role and application in diagnosis. *Virusdisease* **2016**, *27* (1), 1-11.
9. Adamczyk, B.; Tharmalingam, T.; Rudd, P. M., Glycans as cancer biomarkers. *Biochimica et biophysica acta* **2012**, *1820* (9), 1347-53.
10. Leiserowitz, G. S.; Lebrilla, C.; Miyamoto, S.; An, H. J.; Duong, H.; Kirmiz, C.; Li, B.; Liu, H.; Lam, K. S., Glycomics analysis of serum: a potential new biomarker for ovarian cancer? *Int J Gynecol Cancer* **2008**, *18* (3), 470-5.
11. Sethi, M. K.; Thaysen-Andersen, M.; Smith, J. T.; Baker, M. S.; Packer, N. H.; Hancock, W. S.; Fanayan, S., Comparative N-glycan profiling of colorectal cancer cell lines reveals unique bisecting GlcNAc and alpha-2,3-linked sialic acid determinants are

associated with membrane proteins of the more metastatic/aggressive cell lines. *J Proteome Res* **2014**, *13* (1), 277-88.

12. Lee, L. Y.; Thaysen-Andersen, M.; Baker, M. S.; Packer, N. H.; Hancock, W. S.; Fanayan, S., Comprehensive N-glycome profiling of cultured human epithelial breast cells identifies unique secretome N-glycosylation signatures enabling tumorigenic subtype classification. *J Proteome Res* **2014**, *13* (11), 4783-95.

13. Post, M. A.; Lefeber, D. J., Clinical glycomics in the diagnostic laboratory. *Ann Transl Med* **2019**, *7* (Suppl 6), S220.

14. Vanderschaeghe, D.; Szekrenyes, A.; Wenz, C.; Gassmann, M.; Naik, N.; Bynum, M.; Yin, H.; Delanghe, J.; Guttman, A.; Callewaert, N., High-throughput profiling of the serum N-glycome on capillary electrophoresis microfluidics systems: toward clinical implementation of GlycoHepatoTest. *Anal Chem* **2010**, *82* (17), 7408-15.

15. Russell, A. C.; Simurina, M.; Garcia, M. T.; Novokmet, M.; Wang, Y.; Rudan, I.; Campbell, H.; Lauc, G.; Thomas, M. G.; Wang, W., The N-glycosylation of immunoglobulin G as a novel biomarker of Parkinson's disease. *Glycobiology* **2017**, *27* (5), 501-510.

16. Palmigiano, A.; Barone, R.; Sturiale, L.; Sanfilippo, C.; Bua, R. O.; Romeo, D. A.; Messina, A.; Capuana, M. L.; Maci, T.; Le Pira, F.; Zappia, M.; Garozzo, D., CSF N-glycoproteomics for early diagnosis in Alzheimer's disease. *J Proteomics* **2016**, *131*, 29-37.

17. Rajewsky, K., The advent and rise of monoclonal antibodies. *Nature* **2019**, *575* (7781), 47-49.

18. Valverde, P.; Arda, A.; Reichardt, N. C.; Jimenez-Barbero, J.; Gimeno, A., Glycans in drug discovery. *Medchemcomm* **2019**, *10* (10), 1678-1691.

19. Lemery, S. J.; Ricci, M. S.; Keegan, P.; McKee, A. E.; Pazdur, R., FDA's Approach to Regulating Biosimilars. *Clin Cancer Res* **2017**, *23* (8), 1882-1885.

20. A roadmap for glycoscience in Europe.

21. Sciences, N. A. o., Transforming Glycoscience: A Roadmap for the Future. *Washington (DC): National Academies Press (US)*.

22. Zhang, P.; Woen, S.; Wang, T.; Liau, B.; Zhao, S.; Chen, C.; Yang, Y.; Song, Z.; Wormald, M. R.; Yu, C.; Rudd, P. M., Challenges of glycosylation analysis and control: an integrated approach to producing optimal and consistent therapeutic drugs. *Drug Discov Today* **2016**, *21* (5), 740-65.
23. Varki, A.; Cummings, R. D.; Aebi, M.; Packer, N. H.; Seeberger, P. H.; Esko, J. D.; Stanley, P.; Hart, G.; Darvill, A.; Kinoshita, T.; Prestegard, J. J.; Schnaar, R. L.; Freeze, H. H.; Marth, J. D.; Bertozzi, C. R.; Etzler, M. E.; Frank, M.; Vliegthart, J. F.; Lutteke, T.; Perez, S.; Bolton, E.; Rudd, P.; Paulson, J.; Kanehisa, M.; Toukach, P.; Aoki-Kinoshita, K. F.; Dell, A.; Narimatsu, H.; York, W.; Taniguchi, N.; Kornfeld, S., Symbol Nomenclature for Graphical Representations of Glycans. *Glycobiology* **2015**, *25* (12), 1323-4.
24. Lauc, G.; Huffman, J. E.; Pucic, M.; Zgaga, L.; Adamczyk, B.; Muzinic, A.; Novokmet, M.; Polasek, O.; Gornik, O.; Kristic, J.; Keser, T.; Vitart, V.; Scheijen, B.; Uh, H. W.; Molokhia, M.; Patrick, A. L.; McKeigue, P.; Kolcic, I.; Lukic, I. K.; Swann, O.; van Leeuwen, F. N.; Ruhaak, L. R.; Houwing-Duistermaat, J. J.; Slagboom, P. E.; Beekman, M.; de Craen, A. J.; Deelder, A. M.; Zeng, Q.; Wang, W.; Hastie, N. D.; Gyllensten, U.; Wilson, J. F.; Wuhrer, M.; Wright, A. F.; Rudd, P. M.; Hayward, C.; Aulchenko, Y.; Campbell, H.; Rudan, I., Loci associated with N-glycosylation of human immunoglobulin G show pleiotropy with autoimmune diseases and haematological cancers. *PLoS Genet* **2013**, *9* (1), e1003225.
25. Hossler, P.; Khattak, S. F.; Li, Z. J., Optimal and consistent protein glycosylation in mammalian cell culture. *Glycobiology* **2009**, *19* (9), 936-49.
26. Tivey, T. R.; Parkinson, J. E.; Mandelare, P. E.; Adpressa, D. A.; Peng, W.; Dong, X.; Mechref, Y.; Weis, V. M.; Loesgen, S., N-Linked Surface Glycan Biosynthesis, Composition, Inhibition, and Function in Cnidarian-Dinoflagellate Symbiosis. *Microb Ecol* **2020**, *80* (1), 223-236.
27. Helenius, A.; Aebi, M., Intracellular functions of N-linked glycans. *Science* **2001**, *291* (5512), 2364-9.

28. Berkowitz, S. A.; Engen, J. R.; Mazzeo, J. R.; Jones, G. B., Analytical tools for characterizing biopharmaceuticals and the implications for biosimilars. *Nat Rev Drug Discov* **2012**, *11* (7), 527-40.
29. Planinc, A.; Bones, J.; Dejaegher, B.; Van Antwerpen, P.; Delporte, C., Glycan characterization of biopharmaceuticals: Updates and perspectives. *Anal Chim Acta* **2016**, *921*, 13-27.
30. Mulloy B, D. A., Stanley P, H. Prestegard J, Structural analysis of glycans. *Cold Spring Harbor Laboratory Press* **2017**.
31. M. F. Chaplin, J. F. K., Carbohydrate analysis, A practical approach. *IRL Press* **1994**.
32. Smith, G.; Leary, J. A., Differentiation of stereochemistry of glycosidic bond configuration: Tandem mass spectrometry of diastereomeric cobalt-glycosyl-glucose disaccharide complexes. *Journal of the American Society for Mass Spectrometry* **1996**, *7* (9), 953-957.
33. Yamashita, M.; Fenn, J. B., Electrospray ion source. Another variation on the free-jet theme. *The Journal of Physical Chemistry* **1984**, *88* (20), 4451-4459.
34. Fenn, J. B.; Mann, M.; Meng, C. K.; Wong, S. F.; Whitehouse, C. M., Electrospray ionization for mass spectrometry of large biomolecules. *Science* **1989**, *246* (4926), 64-71.
35. Hemstrom, P.; Irgum, K., Hydrophilic interaction chromatography. *J Sep Sci* **2006**, *29* (12), 1784-821.
36. Zauner, G.; Deelder, A. M.; Wuhler, M., Recent advances in hydrophilic interaction liquid chromatography (HILIC) for structural glycomics. *Electrophoresis* **2011**, *32* (24), 3456-66.
37. Vreeker, G. C.; Wuhler, M., Reversed-phase separation methods for glycan analysis. *Anal Bioanal Chem* **2017**, *409* (2), 359-378.
38. Ruhaak, L. R.; Deelder, A. M.; Wuhler, M., Oligosaccharide analysis by graphitized carbon liquid chromatography-mass spectrometry. *Anal Bioanal Chem* **2009**, *394* (1), 163-74.

39. Zhou, S.; Dong, X.; Veillon, L.; Huang, Y.; Mechref, Y., LC-MS/MS analysis of permethylated N-glycans facilitating isomeric characterization. *Anal Bioanal Chem* **2017**, *409* (2), 453-466.
40. Melmer, M.; Stangler, T.; Premstaller, A.; Lindner, W., Comparison of hydrophilic-interaction, reversed-phase and porous graphitic carbon chromatography for glycan analysis. *J Chromatogr A* **2011**, *1218* (1), 118-23.
41. Yoshida, T., Peptide separation by Hydrophilic-Interaction Chromatography: a review. *J Biochem Biophys Methods* **2004**, *60* (3), 265-80.
42. Wuhrer, M., Glycomics using mass spectrometry. *Glycoconj J* **2013**, *30* (1), 11-22.
43. Higel, F.; Demelbauer, U.; Seidl, A.; Friess, W.; Sorgel, F., Reversed-phase liquid-chromatographic mass spectrometric N-glycan analysis of biopharmaceuticals. *Anal Bioanal Chem* **2013**, *405* (8), 2481-93.
44. Veillon, L.; Huang, Y.; Peng, W.; Dong, X.; Cho, B. G.; Mechref, Y., Characterization of isomeric glycan structures by LC-MS/MS. *Electrophoresis* **2017**, *38* (17), 2100-2114.
45. Dotz, V.; Haselberg, R.; Shubhakar, A.; Kozak, R. P.; Falck, D.; Rombouts, Y.; Reusch, D.; Somsen, G. W.; Fernandes, D. L.; Wuhrer, M., Mass spectrometry for glycosylation analysis of biopharmaceuticals. *TrAC Trends in Analytical Chemistry* **2015**, *73*, 1-9.
46. Little, M. J.; Paquette, D. M.; Roos, P. K., Electrophoresis of pharmaceutical proteins: status quo. *Electrophoresis* **2006**, *27* (12), 2477-85.
47. Lu, G.; Carihfield, C. L.; Gattu, S.; Veltri, L. M.; Holland, L. A., Capillary Electrophoresis Separations of Glycans. *Chem Rev* **2018**, *118* (17), 7867-7885.
48. Szabo, Z.; Guttman, A.; Bones, J.; Karger, B. L., Rapid high-resolution characterization of functionally important monoclonal antibody N-glycans by capillary electrophoresis. *Anal Chem* **2011**, *83* (13), 5329-36.
49. Zhong, X.; Chen, Z.; Snovida, S.; Liu, Y.; Rogers, J. C.; Li, L., Capillary Electrophoresis-Electrospray Ionization-Mass Spectrometry for Quantitative Analysis of

- Glycans Labeled with Multiplex Carbonyl-Reactive Tandem Mass Tags. *Anal Chem* **2015**, *87* (13), 6527-34.
50. P.Landers, J., Handbook of Capillary Electrophoresis, Second Edition. **1996**.
51. S.F.Y. Li, Y. S. W., ELECTROPHORESIS: capillary electrophoresis. **2000**.
52. Sastre Torano, J.; Ramautar, R.; de Jong, G., Advances in capillary electrophoresis for the life sciences. *J Chromatogr B Analyt Technol Biomed Life Sci* **2019**, *1118-1119*, 116-136.
53. Szekrenyes, A.; Park, S. S.; Santos, M.; Lew, C.; Jones, A.; Haxo, T.; Kimzey, M.; Pourkaveh, S.; Szabo, Z.; Sosic, Z.; Feng, P.; Varadi, C.; de l'Escaille, F.; Falmagne, J. B.; Sejwal, P.; Niedringhaus, T.; Michels, D.; Freckleton, G.; Hamm, M.; Manuilov, A.; Schwartz, M.; Luo, J. K.; van Dyck, J.; Leung, P. K.; Olajos, M.; Gu, Y.; Gao, K.; Wang, W.; Wegstein, J.; Tep, S.; Guttman, A., Multi-Site N-glycan mapping study 1: Capillary electrophoresis - laser induced fluorescence. *MAbs* **2016**, *8* (1), 56-64.
54. Olivares, J. A.; Nguyen, N. T.; Yonker, C. R.; Smith, R. D., On-line mass spectrometric detection for capillary zone electrophoresis. *Analytical Chemistry* **2002**, *59* (8), 1230-1232.
55. Smith, R. D.; Barinaga, C. J.; Udseth, H. R., Improved electrospray ionization interface for capillary zone electrophoresis-mass spectrometry. *Analytical Chemistry* **2002**, *60* (18), 1948-1952.
56. Moini, M., Simplifying CE-MS operation. 2. Interfacing low-flow separation techniques to mass spectrometry using a porous tip. *Anal Chem* **2007**, *79* (11), 4241-6.
57. Lee, E. D.; Mück, W.; Henion, J. D.; Covey, T. R., Liquid junction coupling for capillary zone electrophoresis/ion spray mass spectrometry. *Biological Mass Spectrometry* **1989**, *18* (9), 844-850.
58. Nowak, P. M.; Wozniakiewicz, M.; Gladysz, M.; Janus, M.; Koscielniak, P., Improving repeatability of capillary electrophoresis-a critical comparison of ten different capillary inner surfaces and three criteria of peak identification. *Anal Bioanal Chem* **2017**, *409* (18), 4383-4393.

59. Mu, Y.; Schulz, B. L.; Ferro, V., Applications of Ion Mobility-Mass Spectrometry in Carbohydrate Chemistry and Glycobiology. *Molecules* **2018**, *23* (10).
60. Kanu, A. B.; Dwivedi, P.; Tam, M.; Matz, L.; Hill, H. H., Jr., Ion mobility-mass spectrometry. *J Mass Spectrom* **2008**, *43* (1), 1-22.
61. Both, P.; Green, A. P.; Gray, C. J.; Sardzik, R.; Voglmeir, J.; Fontana, C.; Austeri, M.; Rejzek, M.; Richardson, D.; Field, R. A.; Widmalm, G.; Flitsch, S. L.; Eyers, C. E., Discrimination of epimeric glycans and glycopeptides using IM-MS and its potential for carbohydrate sequencing. *Nat Chem* **2014**, *6* (1), 65-74.
62. Hofmann, J.; Pagel, K., Glycan Analysis by Ion Mobility-Mass Spectrometry. *Angew Chem Int Ed Engl* **2017**, *56* (29), 8342-8349.
63. Liu, Y.; Clemmer, D. E., Characterizing oligosaccharides using injected-ion mobility/mass spectrometry. *Anal Chem* **1997**, *69* (13), 2504-9.
64. Pringle, S. D.; Giles, K.; Wildgoose, J. L.; Williams, J. P.; Slade, S. E.; Thalassinou, K.; Bateman, R. H.; Bowers, M. T.; Scrivens, J. H., An investigation of the mobility separation of some peptide and protein ions using a new hybrid quadrupole/travelling wave IMS/oa-ToF instrument. *International journal of mass spectrometry* **2007**, *261* (1), 1-12.
65. Shvartsburg, A. A.; Smith, R. D., Fundamentals of traveling wave ion mobility spectrometry. *Anal Chem* **2008**, *80* (24), 9689-99.
66. Guevremont, R., High-field asymmetric waveform ion mobility spectrometry: A new tool for mass spectrometry. *Journal of Chromatography A* **2004**, *1058* (1-2), 3-19.
67. Michelmann, K.; Silveira, J. A.; Ridgeway, M. E.; Park, M. A., Fundamentals of trapped ion mobility spectrometry. *J Am Soc Mass Spectrom* **2015**, *26* (1), 14-24.
68. Fernandez-Lima, F.; Kaplan, D. A.; Suetering, J.; Park, M. A., Gas-phase separation using a trapped ion mobility spectrometer. *Int J Ion Mobil Spectrom* **2011**, *14* (2-3).
69. Lee, S.; Wyttenbach, T.; Bowers, M. T., Gas phase structures of sodiated oligosaccharides by ion mobility/ion chromatography methods. *International Journal of Mass Spectrometry and Ion Processes* **1997**, *167-168*, 605-614.

70. Papadopoulos, G.; Svendsen, A.; Boyarkin, O. V.; Rizzo, T. R., Spectroscopy of mobility-selected biomolecular ions. *Faraday Discuss* **2011**, *150*, 243-55; discussion 257-92.
71. Zucker, S. M.; Lee, S.; Webber, N.; Valentine, S. J.; Reilly, J. P.; Clemmer, D. E., An ion mobility/ion trap/photodissociation instrument for characterization of ion structure. *J Am Soc Mass Spectrom* **2011**, *22* (9), 1477-85.
72. Lee, S.; Valentine, S. J.; Reilly, J. P.; Clemmer, D. E., Analyzing a Mixture of Disaccharides by IMS-VUVPD-MS. *International journal of mass spectrometry* **2012**, *309*, 161-167.
73. Hernandez, O.; Isenberg, S.; Steinmetz, V.; Glish, G. L.; Maitre, P., Probing Mobility-Selected Saccharide Isomers: Selective Ion-Molecule Reactions and Wavelength-Specific IR Activation. *J Phys Chem A* **2015**, *119* (23), 6057-64.
74. Gray, C. J.; Migas, L. G.; Barran, P. E.; Pagel, K.; Seeberger, P. H.; Eyers, C. E.; Boons, G. J.; Pohl, N. L. B.; Compagnon, I.; Widmalm, G.; Flitsch, S. L., Advancing Solutions to the Carbohydrate Sequencing Challenge. *J Am Chem Soc* **2019**, *141* (37), 14463-14479.
75. Khanal, N.; Masellis, C.; Kamrath, M. Z.; Clemmer, D. E.; Rizzo, T. R., Cryogenic IR spectroscopy combined with ion mobility spectrometry for the analysis of human milk oligosaccharides. *Analyst* **2018**, *143* (8), 1846-1852.
76. Chiara Masellis, N. K., Michael Z. Kamrath, David E. Clemmer, and Thomas R. Rizzo, Cryogenic Vibrational Spectroscopy Provides Unique Fingerprints for Glycan Identification  
. *JASMS* **2017**, *28* (10), 2217-2222.
77. Mucha, E.; Gonzalez Florez, A. I.; Marianski, M.; Thomas, D. A.; Hoffmann, W.; Struwe, W. B.; Hahm, H. S.; Gewinner, S.; Schollkopf, W.; Seeberger, P. H.; von Helden, G.; Pagel, K., Glycan Fingerprinting via Cold-Ion Infrared Spectroscopy. *Angew Chem Int Ed Engl* **2017**, *56* (37), 11248-11251.



## 2. Experimental Overview

This chapter gives an overview of the methods central to the experimental approach employed in this work. Both instruments that were designed and constructed combine ion mobility spectrometry, mass spectrometry, and messenger-tagging cryogenic IR spectroscopy to probe the primary structure of glycans. To this end, IMS (Section 2.1) is used as an isomer-specific filter prior to spectroscopic interrogation. Messenger-tagging cryogenic IR spectroscopy (Section 2.3.2) is then used to generate unique fingerprints by which to identify glycans.

### 2.1. Ion Mobility Spectrometry

While ion mobility spectrometry (IMS) has emerged as a promising technique for molecular analysis over the past decades, its theoretical foundations goes back to the end of the 19<sup>th</sup> Century. In 1896, Thomson and Rutherford's work on the investigation of the relationship between electrical conductivity and gaseous media set the foundation for the study of ions in the gas phase.<sup>1</sup> Almost a decade later, Paul Langevin studied the motion of ions in an electric field, defining the basic principles of ion diffusion in gases and thus, IMS.<sup>2-3</sup> However, it took no less than 60 years to see the first ion mobility device known at the time as 'plasma chromatography'.<sup>4</sup> During the following years, IMS's early applications were in fields such as explosives and narcotics detection, chemical weapon monitoring,<sup>5-6</sup> air quality analysis,<sup>7</sup> airport security,<sup>8</sup> and space programs.<sup>9</sup> Recently, the use of IMS for the analysis of complex analytes such as biological samples from cells and bacteria has been enabled through hyphenated techniques. Perhaps the most successful of these is when IMS is combined with MS (i.e., IM-MS) for the detection of the mass-to-charge ( $m/z$ ) ratio of

mobility-separated analytes,<sup>10</sup> where the highly complementary nature of these two techniques has proven to be crucial for isomer analysis. The different timescales on which the two measurements are performed (tens to hundreds of milliseconds for IMS vs.  $\mu$ s for MS) enables their successful coupling.

The basic principle of an ion mobility measurement is the separation of different molecular ions in the gas phase according to their size-to-charge ratio. As described below, different ion mobility techniques exist and use different separation mechanisms.

### 2.1.1 Drift tube ion mobility spectrometry (DTIMS)

DTIMS is the oldest IMS technique and is based on the application of a weak electric field ( $E$ ) to an ion packet in a buffer gas medium. The drift velocity of the ions is expressed as

$$v_D = K \cdot E \quad \text{Eq 2.1}$$

and depends upon both the *mobility*  $K$ , which is a joint property of the ion and the buffer gas, and the applied weak electric field  $E$ .<sup>11</sup> The mobility of a given species is determined by ion-neutral interactions with gas molecules and is thus specific to the ions in a particular medium. As a result, the various ions composing an initial packet can be separated in space and time according to their different mobilities.

The electric field used for separation is considered a weak field when the ion motion that it causes is slower than ion diffusion in the buffer gas. In fact, if the gas density is high enough, ions are collisionally dampened and their internal temperature is that of the buffer gas.<sup>12-14</sup>

In this regime, the mobility  $K$  can be linked to the diffusion coefficient  $D$  following the Einstein relation,<sup>15</sup>

$$K = \frac{qD}{k_B T} \quad \text{Eq 2.2}$$

where  $q$  is the total charge,  $k_B$  the Boltzmann constant, and  $T$  the buffer gas temperature.

For the sake of comparison of mobilities measured under different conditions, it is common to determine the reduced mobility  $K_0$ , which normalizes the mobility to standard conditions:

$$K_0 = K \frac{P T_0}{P_0 T} \quad \text{Eq 2.3}$$

where  $P_0$  and  $T_0$  are the standard pressure and temperature, respectively.

The value  $K_0$  is determined by measuring the drift time  $t_D$  an ion spends to traverse the total drift distance following the relation below,<sup>11</sup>

$$K_0 = \frac{L^2 P T_0}{t_D V P_0 T} \quad \text{Eq 2.4}$$

where  $V$  corresponds to the voltage applied across the drift region and  $L$  its length. The Mason-Schamp equation relates the mobility to the ion's size through the determination of the average collisional cross-section (CCS) area  $\Omega$ ,<sup>3</sup>

$$\Omega = \frac{3q}{16N_0} \sqrt{\frac{2\pi}{\mu k_B T}} \frac{1}{K_0} \quad \text{Eq 2.5}$$

where the variables  $q$  and  $N_0$  correspond to the charge of the ion and the number density of the buffer gas respectively, and  $\mu = \frac{m_i m_g}{m_i + m_g}$  is the reduced mass with  $m_i$  the mass of the ion and  $m_g$  the mass of the neutral drift gas. The mobility of a specific ion is thus related to  $q/\sqrt{\mu}\Omega$  at constant  $T$  and  $P$ . Hence, for heavier ions that satisfy  $m_i \gg m_g$ , the mobility is largely determined by the charge  $q$  and size  $\Omega$  of the ion, leading to potentially different mobilities for ions of the same mass-to-charge ratio but different shapes. A schematic overview of DTIMS is shown in Figure 2.1. Ions of different CCS, depicted in different colors, drift through a ring-electrode device across which an electric field is applied. The analytes are injected into the drift region in pulses and the separated ions are detected at different arrival times. Ion detection events are recorded to generate an arrival time distribution (ATD) such as the one shown on the right panel of Figure 2.1.

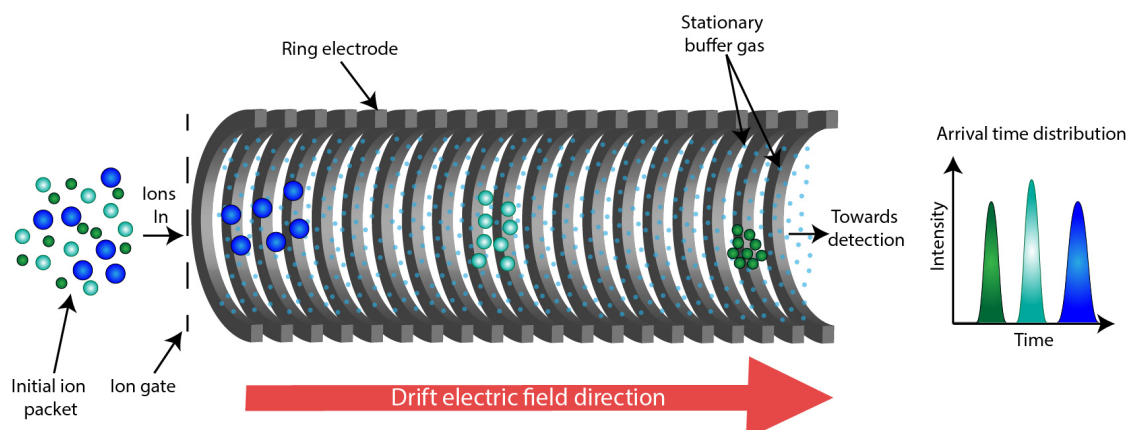


**Figure 2.1:** Schematic of a conventional drift tube device for ion mobility separation (DTIMS). The separation region is composed of a stack of ring electrodes to which an electric field gradient is applied. A pulsed ion packet composed of ions of different sizes drifts through the device. Ions are separated because of their different interactions with the electric field and the neutral buffer gas molecules.

The theoretical resolving power in DTIMS is a crucial property of the device as it defines its separation capabilities. It is defined as  $R=t/\Delta t$  where  $t$  corresponds to the drift time of a mobility peak, and  $\Delta t$  its full-width at half-maximum.<sup>12</sup> The resolving power is thus approximated by

$$R = \frac{t}{\Delta t} = \left( \frac{LEq}{16K_B T \ln 2} \right)^{\frac{1}{2}} \quad \text{Eq 2.6}$$

This relation shows that the resolving power increases with the square root of the drift length and the electric field, and decreases inversely proportional to the square root of the temperature.

To summarize, DTIMS enables the separation of ions in time and space through ion-neutral interactions in the gas phase due to the application of a weak electric field, yielding arrival

time distributions (ATDs). An ATD contains information on the ion's shape as drift times can be linked to the average CCS of a molecular ion in a specific buffer gas medium through Eqns. 2.4 and 2.5.

### 2.1.2 High-field asymmetric waveform ion mobility spectrometry (FAIMS)

The basic theory behind FAIMS was described by Buryakov et al.<sup>16</sup> during the early 90's and further developed by Guevermont et al. in the following years.<sup>17-19</sup> As in DTIMS, in FAIMS ions are separated by electric fields in a buffer gas medium. However, the separation process of ions in latter is based on a different mechanism. While in DTIMS, ions are introduced in discrete pulses and drift through the separation region, in FAIMS ions are separated as a continuous stream that is carried by a gas flow at atmospheric pressure.<sup>19</sup> Moreover, the separation is performed by applying a strong and weak field alternated at a high frequency, as opposed to the constant weak electric field used in DTIMS.

Figure 2.2 shows a schematic overview of a FAIMS device and the waveform applied to the electrodes perpendicular to the ion drift direction. A high field is applied during a time  $t_1$ , while a low field of opposite polarity is applied for a time  $t_2$ .<sup>16</sup> In this case, separation is due to the differences in mobility under strong and weak-field conditions.

While the weak field mobility is described by Eq. 2.2 mobility in strong fields  $K_s$  is given by:<sup>16</sup>

$$K_s = K \left[ 1 + \alpha \left( \frac{E}{N} \right)^2 + \beta \left( \frac{E}{N} \right)^4 + \dots \right] \quad \text{Eq 2.7}$$

where  $K$  is the mobility in a weak field;  $N$  the density of the buffer gas; and  $\alpha$  and  $\beta$  two experimentally derived coefficients related to the mobility of an ion under high-field conditions.

The strong field is the result of the peak voltage applied for a short time in the asymmetric waveform and is called dispersion voltage (DV), and the weak field of opposite polarity and is applied for a longer time. The fields are applied in a way that the integral of the voltage vs. time is equal for the strong and weak field regimes. When the mobilities of an ion in strong and in weak fields are different, the ion does not return to its original axial position and eventually collides with one of the electrodes of the device before the end of the separation region. To ensure that the ion is transported through the separation region, a compensation voltage (CV) is applied creating a weak field that compensates for the axial drift of the ions. Thus, a specific CV value contains information about the difference in high- and low-field mobility of a particular species. The transmitted ions can be detected as the CV value is scanned to obtain a mobiligram of all analytes present in a sample.

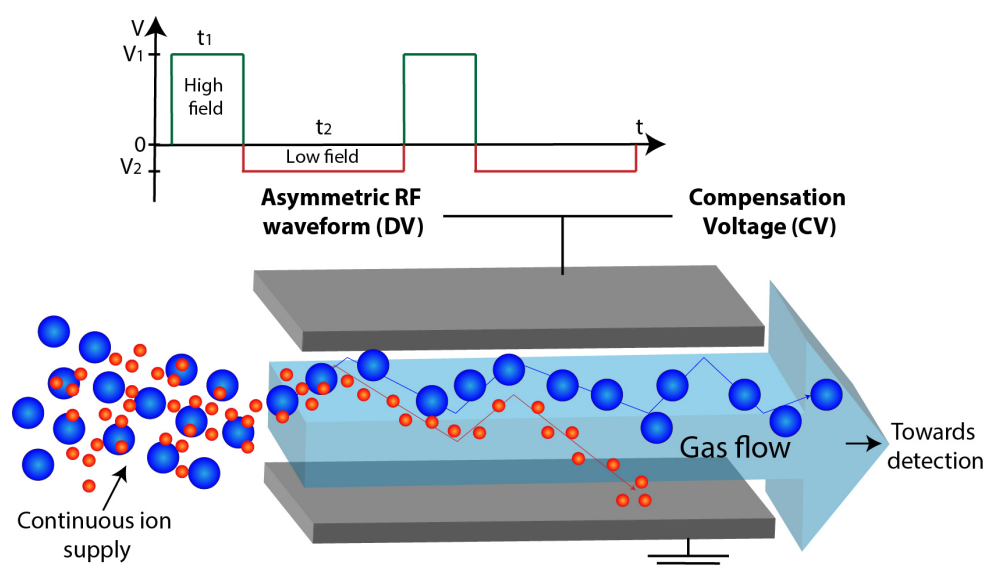


**Figure 2.2:** Schematic overview of a planar FAIMS device. Ions of different sizes are introduced continuously into the analyzer region following the gas flow. At a fixed RF asymmetric waveform (DV) and compensation voltage (CV) only ions that are in balanced conditions (blue) are transmitted through the separation region. The other ions (red) end up hitting one of the electrodes.

In this scheme, the shape of the asymmetric waveform is crucial and highly influences the experimentally measured CV value that is required for transmission, rendering any comparison of experimental results obtained using different devices and settings non trivial.<sup>20-21</sup> Thus, FAIMS can be used as an ion filter where a specific combination of DV and CV allows the transmission of a selection of ions according to their weak field and strong field mobilities, but it doesn't provide any direct geometric information on the shape of the molecule.

### 2.1.3 Trapped ion mobility spectrometry (TIMS)

Trapped IMS is a recently developed technique for ion mobility separation.<sup>22-25</sup> As opposed to DTIMS where the separation is based on a weak electric field pushing the ions through a stationary buffer gas, TIMS separation makes use of an electric field to trap the ions in fixed positions while the buffer gas is in motion. The ion packet is thus pushed forward by a controlled gas flow while a counter potential is applied to trap the charged molecules in the separation region. A schematic representation of a TIMS device is shown in Figure 2.3, where ions of different CCSs are depicted in different colors. Separation is achieved as ions with different shapes will interact differently with the buffer gas and as a result, will be trapped at different positions. Ions are then unloaded by gradually lowering the electric field, sequentially releasing the trapped ions. As for DTIMS, separation is based on ion-neutral interactions between the ions of interest and the buffer gas. In TIMS, however, the mobility of a specific ion in a neutral gas is defined by the drift velocity of the gas and the elution field applied across the mobility region for which the ion elutes, following the expression

$$K_i = \frac{v_g}{E_x(i)} = A(1/(V_{out} - V_{elut}(i))) \quad \text{Eq 2.8}$$

where  $K_i$  the mobility of a given ion;  $v_g$  the drift velocity of the gas, and  $E_x(i)$  the elution field at which the ion packet is released. By introducing the calibration constant  $A$ , which can be determined experimentally using known standards, it is possible to extract a direct relation between the mobility and the elution voltage.<sup>22</sup>

A TIMS device is composed of three main sections: (1) the entrance funnel, (2) the mobility analyzer (the so-called “TIMS tunnel”), and (3) the exit funnel. Like DTIMS, the funnels allow for efficiently loading and unloading ions into and out of the mobility region. The mobility analyzer is an assembly of ring electrodes composed by four segments each. A quadrupolar RF field is applied to radially confine the ions and prevent losses due to diffusion.

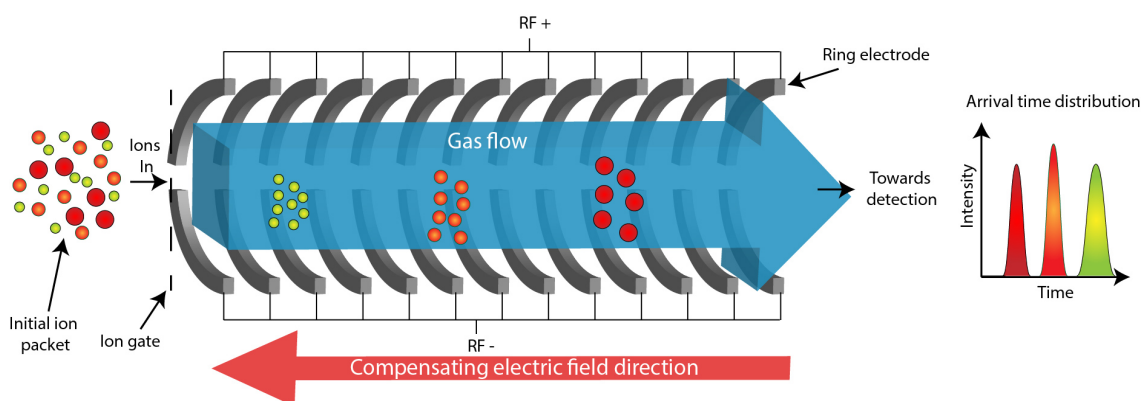


**Figure 2.3:** Schematic overview of a trapped ion mobility separation (TIMS) device. A pulse of ions of different size is introduced into the separation region carried by a buffer gas flow. As the electric field increases along the axis of the device, ions of different mobilities are trapped in different regions. By gradually lowering the electric field, ions begin to elute from the separation region from high to small size-to-charge ratios. Ions are confined radially by alternating RF phases of adjacent quadrants of each ring electrodes.

To achieve mobility separation, the DC potential initially applied to the exit of the mobility region must be higher than the potential applied to its entrance in a way that retards the ions. Then, the electric field across the analyzer section is slowly decreased and ions begin to elute from the mobility region. It is important to note that ions with a lower mobility will elute first, as they will be more easily carried by the gas flow.

To summarize, in a TIMS measurement, the elution voltage contains the information on the ion mobility. By using a known standard for calibration, it is possible to extract the CCS of a specific ion similarly to DTIMS. The fact that TIMS is achieved by using a gas flow rather than a long drift path in a bath of stationary gas presents a considerable advantage for the technique. This feature allows to perform a high-resolution separation using a relatively compact device as opposed to the long drift tubes needed to achieve similar results. As a result, coupled to a mass spectrometer, TIMS is considered, among other state-of-the-art IMS technologies, as a tool of choice for IMS analysis of biomolecules including glycans.<sup>26-29</sup>

#### 2.1.4 Travelling wave ion mobility spectrometry (TWIMS)

Travelling wave IMS is a separation method that was developed by Giles *et al.* in 2004.<sup>30</sup> Like DTIMS, ion packets are injected in pulses into the mobility separation region where they interact with a neutral buffer gas under the influence of an electric field. TWIMS is thus a dispersive method allowing multiple species to be separated and their mobility measured simultaneously. However, the separation mechanisms and parameters used in TWIMS differ from those employed in DTIMS technology, resulting in different ion dynamics to be considered.<sup>31</sup> TWIMS makes use of a periodic waveform to separate ions, although the separation is achieved under low-field mobility conditions as in DTIMS and TIMS.

The first implementation of TWIMS was achieved using stacked ring electrodes to which a sequence of voltages was applied and varied to form a travelling potential wave. To ensure radial confinement of the ions throughout the mobility region, an alternating RF field is also applied to adjacent electrodes, creating a pseudopotential that has a minimum on axis. The travelling wave is created by sequentially switching the voltages applied to the electrodes in such a way that different wave shapes of a defined pattern (such as triangular, rectangular and sinusoidal) can be made to propagate through a drift gas in the separation region. The switching frequency of the electrodes determines the propagation speed of the wave,  $s$ , and

constitutes a crucial parameter for separation. As shown in Figure 2.4, the wave pushes the ions into the stationary buffer gas, causing ions of different mobility to traverse the ring electrode stack at different velocities due to different collision rates.<sup>30, 32-33</sup> Upon collisions with the neutral gas molecules, ions with larger CCS roll over the wave, resulting in slower net drift velocity. The motion of the ions thus depends upon: their mobility in a specific buffer gas  $K$ ; the maximum electric field  $E_{max}$  defined by the pulse voltage; and the propagation speed of the travelling wave  $s$ . Different ion propagation regimes can be described by the maximum velocity of the ions relative to the wave speed and noted  $c$ .<sup>31</sup>

$$c = K \cdot E_{max} / s \quad \text{Eq 2.9}$$

This parameter is central to the mobility separation, as it defines the nature of ion propagation in the IMS region. It is possible to distinguish three different propagation regimes related to the parameter  $c$ : (1)  $c \ll 1$ , in which the wave passes underneath the ions which are ‘rolling over’ it; (2)  $c > 1$ , in which the ions are transported by the wave and are located at its front; and (3)  $c \approx 1$ , where the ions travel with a mean velocity that is close to the wave’s speed but occasionally roll over it.

As  $c$  depends upon the combination of the mobility of the analyte and the speed of the travelling wave, ions with different mobilities will interact differently with waves of the same speed, resulting in their separation. At the optimum wave speed, ions with compact structures and thus higher mobility are transported with the wave and evolve at the regime where  $c > 1$ , while more elongated structures with lower mobility have a higher probability of rolling over the wave and evolve in the regime where  $c < 1$  resulting in a slower net velocity.

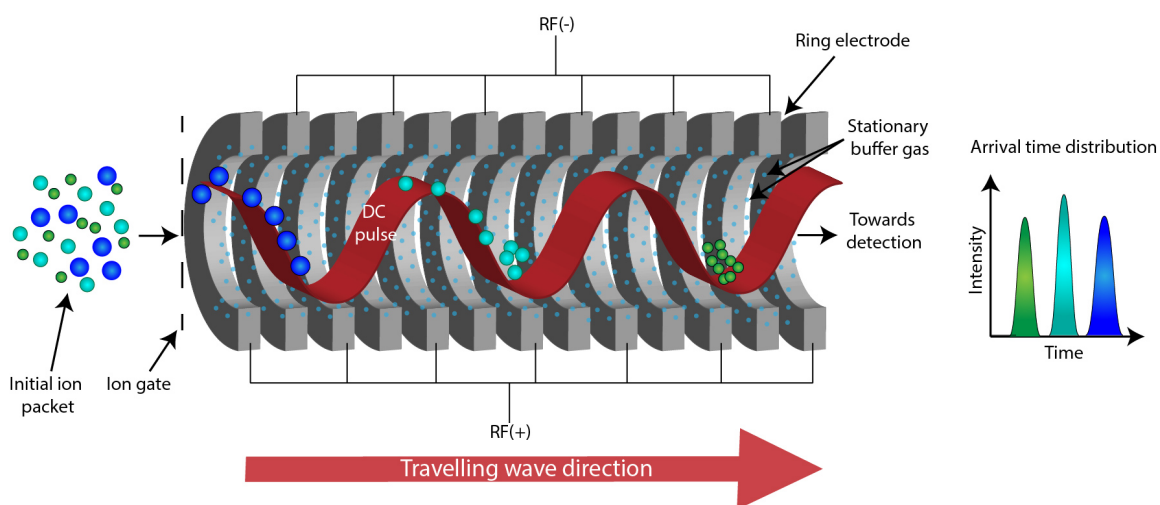


**Figure 2.4:** Schematic overview of a travelling wave IMS (TWIMS) ring electrode device. An initial ion packet is pulsed into the separation region. The travelling wave propagates along the axis of the device, transporting the analyte ions through the buffer gas. Due to interactions with the travelling wave and the neutral gas molecules, analytes experience different kinetics where larger ions (blue) roll over the wave more frequently than smaller ones, while the smallest ions (green) are carried with the wave. Ions are confined radially by alternating RF phases applied to adjacent ring electrodes.

To understand the kinetics driving the separation process and the influence of the waveform parameters on the drift time of a specific ion, we first consider a triangular wave profile with  $E = 2 U / b$  at both edges. Here  $b$  represents the width of a complete rise and fall of the potential  $U$  applied to an electrode as shown in Figure 2.5.

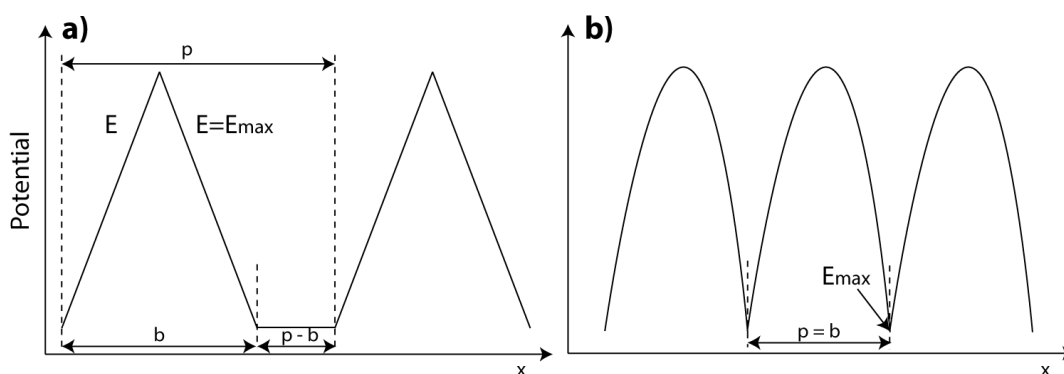


**Figure 2.5:** Travelling wave profiles: (a) triangular profile (b) Half-sinusoidal profile

In the case where  $c < 1$ , the ion climbs the front of the wave with a relative velocity equal to  $(s - K.E)$  which means that the ions reach the crest of the triangular wave at  $t_F = b/[2(s - K.E)]$ . Following that, ions slide back with relative velocity  $-(s + K.E)$  resulting in a sliding time of  $t_B = b/[2(s + K.E)]$ . The rest time of the ions between two consecutive waves is written  $t_0 = (p - b)/s$  where  $p$  represents the period of the wave. Knowing that the net displacement of the ions is given by the relation  $d = K.E(t_F - t_B)$ , and considering the case where there are no field-free segments between the waves ( $p = b$ ), the average velocity of the ions is written as

$$\bar{v} = \frac{d}{t_c} = (K \cdot E)^2 / s \quad \text{Eq 2.10}$$

where  $t_c$  represents the total cycle time. Thus, the drift velocity in TWIMS depends quadratically on the mobility as opposed to the linear relation in DTIMS. As a result, the total drift time  $t_D$  is given by the relation

$$t_D = \frac{L}{\bar{v}} = Ls / (K \cdot E)^2 \quad \text{Eq 2.11}$$

To obtain the mean velocity in the case of a smooth waveform such as a sinusoidal wave, the same calculation is performed and  $E^2$  is replaced by its average  $\bar{E}^2$ .<sup>31</sup>

Like DTIMS, the TWIMS resolving power is determined by the measured drift time of a mobility peak and its full width at half-maximum at specific separation parameters. However,  $R_{TW}$  depends upon the TW parameters in addition to the field, drift length, and temperature of the experiment. The resolving power can be expressed as<sup>31</sup>

$$R_{TW} = \left( \frac{LKE^2ze}{16sK_B T \ln 2} \right)^{\frac{1}{2}} \quad \text{Eq 2.12}$$

As the expression includes the mobility  $K$ , ions of different mobilities will be subject to different  $R_{TW}$  values. Moreover, the TW speed  $s$  needs to be slightly higher than  $K_{hi}E$ , where  $K_{hi}$  the highest mobility of the species of interest, to be in the separation regime for all the ions present in a sample. This means that the resolving power can be expressed as follows:

$$R_{TW} = \left( \frac{LKEze}{16K_{hi}K_B T \ln 2} \right)^{\frac{1}{2}} \quad \text{Eq 2.13}$$

Hence, the resolving power has a direct dependence on the mobility spread of the species being separated and can be written as  $R_{TW} = R_{max}(K/K_{hi})^{1/2}$  where  $R_{max}$  is the maximum resolving power and is written:

$$R_{max} = \left( \frac{LEze}{16K_B T \ln 2} \right)^{\frac{1}{2}} = \left( \frac{2zeUn}{16K_B T \ln 2} \right)^{\frac{1}{2}} \quad \text{Eq 2.14}$$

where  $n$  denotes the number of wave cycles and  $U$  the peak TW voltage used for separation.

While the resolving power scales with the drift voltage  $U$  in DTIMS, in TWIMS the resolving power at constant peak voltage  $U$  scales as  $n^{1/2}$ . Since  $n$  is essentially determined by the length of the separation path, the resolving power hence scales as  $L^{1/2}$ , meaning that longer drift paths result in an increased resolving power.

This is a crucial property of TWIMS, as it allows for building high resolution devices by extending the separation path length independent of the potential used for separation.

Commercial IMS devices that exploit TWIMS exist and combine IMS with a mass spectrometer for detection as is the case for the Waters Synapt HDMS.<sup>32</sup>

The development of cyclic IMS has allowed for a considerable increase of separation path length and as a result offers higher resolving power. Recently Waters released the new SELECT SERIES cyclic IMS device which offers an increased resolving power.<sup>34</sup>

## 2.2. Structures for lossless ion manipulation (SLIM)

A relatively recent breakthrough in IMS was developed in the group of Richard D. Smith and is called 'Structures for Lossless Ion Manipulation' (SLIM).<sup>35-36</sup> The basic principle behind SLIM is the use of an assembly of two printed circuit boards (PCBs) containing different types of electrodes to define DC and RF electric potentials. The PCBs are assembled in parallel to one another in what the authors refer to as a 'sandwich' configuration and are placed in a buffer gas such as Helium or Nitrogen at several mbar pressure.

The first implementation of SLIM was based on DTIMS and made use of two different electrode designs: (1) *rung* electrodes to which a combination of DC and an alternating RF voltage was applied (2) *guard* electrodes to which a DC voltage was applied. A schematic of the design is shown in Figure 2.6(a). The electrode design can be described as projection of a ring electrode guide onto the flat surface of PCBs, and the mobility separation is performed in a similar way to DTIMS. A DC gradient is applied to the rung electrodes across the length of the separation path and pushes an ion packet through the mobility region. Radial confinement of the ions is achieved by applying an RF voltage to the adjacent rung electrodes, while the DC voltage that is applied to the guard electrodes ensures ion confinement in the direction orthogonal to the ion drift motion. In comparison to classical

DTIMS, the superimposed RF and DC voltages ensure a more efficient (almost lossless) transmission of the ions throughout the mobility separation region.<sup>35, 37</sup>

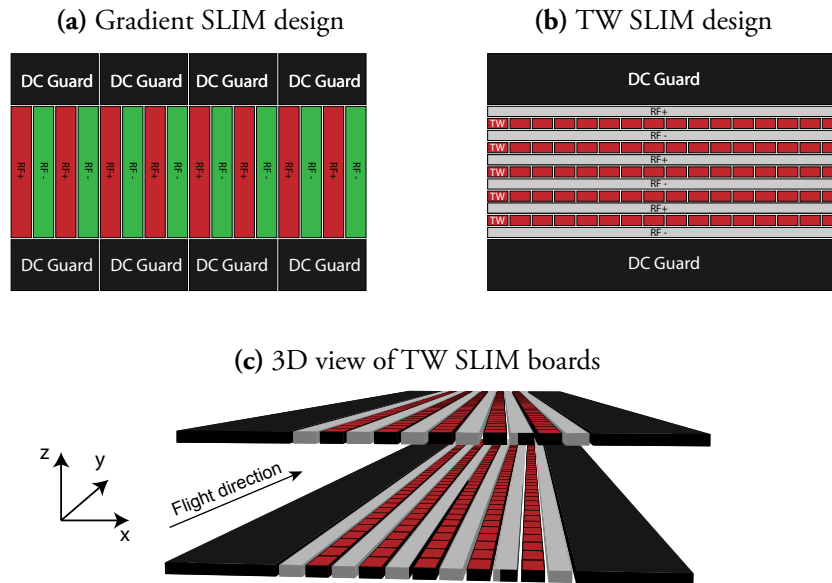


**Figure 2.6:** Illustration of the different SLIM designs: **(a)** The DC SLIM electrode design. The green and red electrodes represent the opposite phases of the RF voltages. A DC gradient is coupled to these electrodes and results in an electric field across the board. In black, the guard electrodes responsible for ion confinement orthogonally to the flight path. **(b)** TW SLIM electrode design. In grey, RF electrodes with alternate phases. The TW potentials are applied to the DC pads in red and propagates along the axis of the board. In black, the guard electrodes responsible for ion confinement orthogonally to the flight path. **(c)** A schematic of the ‘sandwich’ configuration. Ions propagate along the y-axis.

A second-generation SLIM design makes use of TWIMS technology.<sup>36, 38-41</sup> As in the first implementation, two PCBs are held parallel to each other in a buffer gas bath. However, the electrode design (depicted in Figure 2.6(b)) is different and includes three electrode types: (1) *travelling wave* electrodes, which are small DC pads forming a repeating pattern throughout the board and to which a sequence of voltages is applied to create the traveling wave potential; (2) *RF* electrodes in the form of long stripes and to which the RF voltage is applied; and (3) *guard* electrodes to which a DC voltage is applied in a similar manner to

the previous implementation of SLIM.<sup>39</sup> In the second variation however, the ions are transported through the IMS region by the travelling wave applied to the DC pads, while the radial confinement is achieved *via* the RF electrodes that are adjacent to the TW DC pads. Lastly, the guard electrodes play the same role as previously described and confine the ions orthogonally to the flight direction. A unique feature of the SLIM electrode design is that it allows for turning ions 90° which enables the introduction of serpentine like geometry thus increasing the total drift path and by that, the IMS resolving power.

In this thesis, the choice to implement SLIM TWIMS was made because of its unique capabilities with respect to IMS resolving power and accurate ion manipulation. A more detailed description of the SLIM TW characteristics will be presented in the next chapter.

## 2.3. Spectroscopic analysis of biomolecules

### 2.3.1 Vibrational spectroscopy

Vibrational spectroscopy is a powerful tool that is widely used in chemical analysis in a variety of fields such as geology, biomedicine, material, food, and environmental sciences.<sup>42</sup> IR absorption spectroscopy provides information about the structure of molecules by probing the vibrations of their functional groups.

In the gas phase, the advent of MALDI<sup>43</sup> and ESI<sup>44-45</sup> allowed for the spectroscopic analysis of intact biological molecules. In addition to structural elucidation, the unique features presented by a given spectrum of a biological molecule can be used for unambiguous identification the species present in a given sample *via* the use of a database approach. In this section we will focus on different vibrational spectroscopic techniques and their potential use in identifying biomolecules.

A classical method used in vibrational spectroscopy is *absorption spectroscopy*. Following this approach, a vibrational spectrum is obtained by measuring the attenuation of the beam of

light transmitted through a given sample. By comparing the intensity of the beam before and after the sample as a function of the wavelength, it is possible to obtain the absorption of a specific sample according to Beer-Lambert law:

$$I(\nu) = I_0 e^{-\sigma(\nu)Ln} \quad \text{Eq 2.15}$$

where intensities of the transmitted, and initial light beam are noted  $I(\nu)$  and  $I_0$  respectively.  $\sigma(\nu)$  represents the absorption cross section;  $L$  the path length of the sample, and  $n$  the number density of molecules in the sample.<sup>46</sup>

In the gas phase, however, the relatively low number density of the considered molecular ions at the space charge limit ( $n_{scl} \approx 10^6 \text{ cm}^{-3}$ ) impedes the applicability of this approach as light attenuation becomes almost undetectable.<sup>47</sup>

Efforts to overcome this limitation resulted in the development of *action spectroscopy*. As opposed to classical absorption spectroscopy, action spectroscopy is based on the effect of the absorbed light on the molecule itself *via* monitoring the changes that takes place due to resonant photon absorption. Different types of action spectroscopy exist and measure different effects such as fluorescence<sup>48</sup>, ionization<sup>49</sup>, and the fragmentation of the considered ion following photon absorption. By monitoring the fraction of the ionic molecules affected by the IR absorption, it is possible to obtain an IR vibrational spectrum. The fraction of affected molecules can be written in analogy to Beer-Lamberts law as

$$N(\nu) = N_0 e^{-\sigma(\nu)\Phi(\nu)} \quad \text{Eq 2.16}$$

where  $N(\nu)$  is the number of precursor ions after fragmentation and  $N_0$  their initial number before irradiation. Here,  $\Phi(\nu)$  denotes the photon fluence as a function of the wavenumber. In this case, the number of fragments  $N_f(\nu)$  is given by the relation

$$N_f(\nu) = N_0(1 - e^{-\sigma(\nu)\Phi(\nu)}) \quad \text{Eq 2.17}$$

Therefore, for the gas phase approach, a critical parameter is the flux of photons, in addition to the density of molecular ions.

## IR multiple photon dissociation (IRMPD)

IR multiple photon dissociation is a widely used technique in action spectroscopy. It is based on monitoring the fragment of precursor ions following the absorption of multiple resonant photons sequentially. For large biological molecules, photon absorption does not result from a sequential excitation of vibrational levels within a single mode, which ultimately results in the dissociation of the molecules.<sup>50</sup> Instead, when a resonant photon is absorbed, the incident energy is distributed to all vibrational degrees of freedom in a process called *intramolecular vibrational redistribution* (IVR).<sup>51-52</sup> This process happens in a fast time-scale (typically sub-ns) and enables the absorption of multiple photons of the same frequency, hence heating the molecule by increasing its overall internal energy and fragmenting it when the unimolecular dissociation threshold is exceeded (See Figure 2.7).

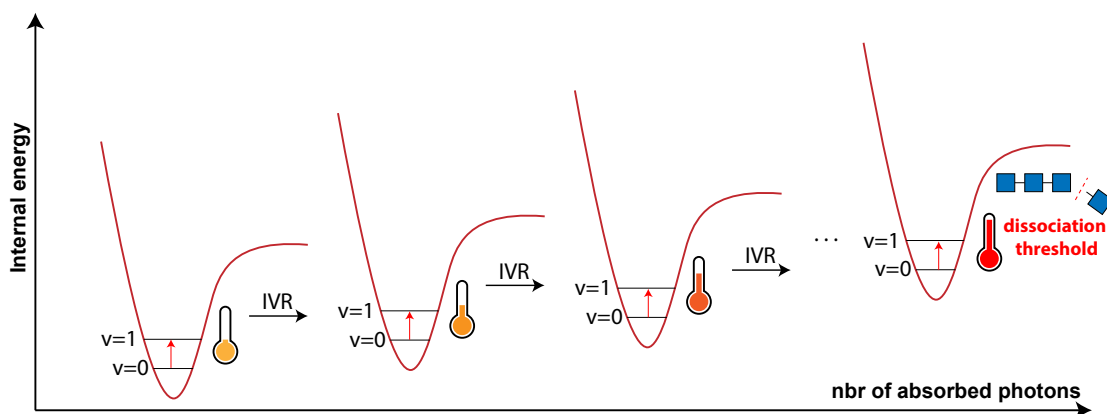


**Figure 2.7:** Schematic illustration of the IR multiple photon dissociation (IRMPD) pathway. The absorption of each resonant photon leads to an increase of the internal energy of the molecule *via* energy redistribution to the various vibrational degrees of freedom available (IVR). Once the internal energy exceeds the dissociation threshold, the molecule undergoes fragmentation. The IR spectrum is obtained by monitoring fragments as a function of the frequency of the absorbed IR photons.

While suited for molecules of relatively small size, using IRMPD to produce highly resolved vibrational spectra of biologically relevant molecules can prove to be challenging. The reason for this is spectral broadening inherent to the technique which limits the resolution of the produced spectra. The causes for spectral broadening are three-fold: (1) The relatively high initial temperature of the ions implies that multiple thermal conformations may coexist and result in different spectra being superimposed and averaged during the measurement. (2) A non-selective absorption of photons due to the quasi continuum nature of vibrational states at high internal energies.<sup>50</sup>

In addition, the multiphoton process means that the measured absorption intensity has a non-linear dependence on the photon flux leading to non-linear spectra that are highly influenced by the laser fluence.

Nevertheless, schemes involving IRMPD spectroscopy have been proposed for sequencing glycans.<sup>53</sup> A combination of tandem MS and IRMPD of glycan fragments produced by CID has been reported. By measuring spectra of fragment molecules no larger than mono- or

disaccharides, it was shown possible, to a certain degree, to rebuild the structure of the precursor polysaccharide.<sup>53</sup>

One way to overcome limitations inherent to the use of IRMPD, is by cooling the analyte ions to cryogenic temperatures. This allows to drastically reduce the number of populated vibrational states thus narrowing the observed absorption bands and yielding highly resolved spectra.

## Cryogenic ion spectroscopy

Several cryogenic spectroscopy techniques exist and make use of different experimental schemes to cool down the analyte ions. Spectroscopy of molecules inside helium nanodroplets is a technique that was developed in the early 90's and first used for small neutral molecules.<sup>54-55</sup> Recently, this technique was successfully applied to biological molecules such as peptides<sup>56</sup>, proteins<sup>57</sup>, and later glycans.<sup>58</sup> In helium-droplet spectroscopy, analytes of interest are embedded in helium nano-droplets which are optically transparent to IR radiation and retain a constant temperature of around 0.4 K. To achieve this, the ions of interest are held in an ion trap which is traversed by a beam of He nano-droplets that pick up the present analytes. The complexes are then irradiated by IR light, and the spectrum is obtained *via* the detection of the bare ions in a TOF mass spectrometer. The driving principle behind this technique lies within the fact that upon absorption of a resonant photon, the energy redistributed *via* IVR is transferred from the ion to the helium nanodroplet, and results in the evaporation of the latter. This process is repeated until a critical droplet size is reached and the analyte ion is ejected<sup>59-61</sup> prior to its detection by TOF-MS. However, the exact mechanism of this process is, to date, not fully understood. IR spectroscopy in nano-droplets produces highly resolved spectra compared to IRMPD, as it profits from the absence of thermal contribution at liquid-helium temperatures, thus eliminating line broadening and peak shifts. Nevertheless, it is still a multiphoton process which means that the measured absorption intensity has a non-linear dependence on the photon flux leading to non-linear spectra.

## Messenger tagging spectroscopy

Messenger tagging spectroscopy was first introduced in the 1980's by Y.T. Lee and coworkers<sup>62</sup> then further developed and optimized by Mark A. Johnson and coworkers<sup>63-64</sup>. Initially, molecular beams produced by the supersonic cooling of laser desorbed molecules were used. Weakly bound clusters composed of a small, ionized molecule and a co-expanded H<sub>2</sub> tag were formed because of the low temperature of the jet expansion. The clusters were gently injected into an RF ion trap, interrogated *via* IR photons by intersecting an IR beam with the ion cloud, then sent to a quadrupole mass analyzer and detected.<sup>46, 65</sup> The optimal messenger tag must fulfill two main requirements: (1) no intrinsic IR absorption; and (2) a detectable mass shift when forming complexes with the ion of interest. For these reasons, noble gas atoms are good candidates to serve as messengers and have been mainly used in research experiments.<sup>66-67</sup> As for previously described vibrational spectroscopic techniques, a resonant photon is absorbed and its energy is redistributed *via* IVR throughout the vibrational degrees of freedom of the molecule, resulting in the release of the weakly bound tag. Therefore, the IR spectrum of the analyte is obtained by monitoring the mass shift resulting from the detachment of the messenger as a function of the IR frequency of the light source. As the ions are at cryogenic temperatures, there are no thermal contributions during the measurement, hence resulting in highly resolved spectra. Furthermore, since the tag is weakly bound to the analyte, a single photon is sufficient to fragment the cluster, thus, simplifying the requirements for the light source needed in terms of photon intensity (OPO, fiber-pumped laser systems, etc.) and yielding linear absorption spectra. Different instruments have been employed to perform messenger tagging spectroscopy, such as multi-quadrupole devices<sup>68</sup> and time of flight mass spectrometers.<sup>69</sup>

To study biological molecules by this approach, different ionization techniques such as ESI or MALDI must be employed. While efficiently producing large molecular ions, these ion sources do not allow for the formation of weakly bound clusters and were thus not suitable to the early messenger tagging schemes.

The development of messenger tagging through cryogenic cooling of analytes using cold ion traps, provided a way to couple the technique with ESI and MALDI, widening its applicability to biological molecules.<sup>70-72</sup>

The early versions of cold ion traps were based on multipole geometry designs popularized by Gerlich *et al.*<sup>73</sup> Ions are trapped *via* RF confinement by applying alternate phases of an RF voltage to adjacent rods of a multipole structure. By connecting the ion trap to the cold head of a closed cycle He cryostat, it is possible to cool the structure to a range of a few Kelvin. A gas pulse mainly composed by He is introduced in the trap prior to the analytes, hence collisionally cooling them upon arrival (Figure 2.8(a)). Depending on the composition of the buffer gas, molecules from the latter are attached to the analytes *via* van der Waals interactions in a three-body collision process, forming weakly bound clusters (Figure 2.8(b)). The IR beam then traverses the trap overlapping with the tagged analytes, boiling off the weakly bound tags *via* IVR upon resonant absorption of a single photon (Figure 2.8(c)). The molecular ions are then unloaded from the cold trap and sent towards the detection region in order to monitor the depletion of the tags as a function of the IR photon frequency, resulting in a highly resolved vibrational spectrum (Figure 2.8(d)).

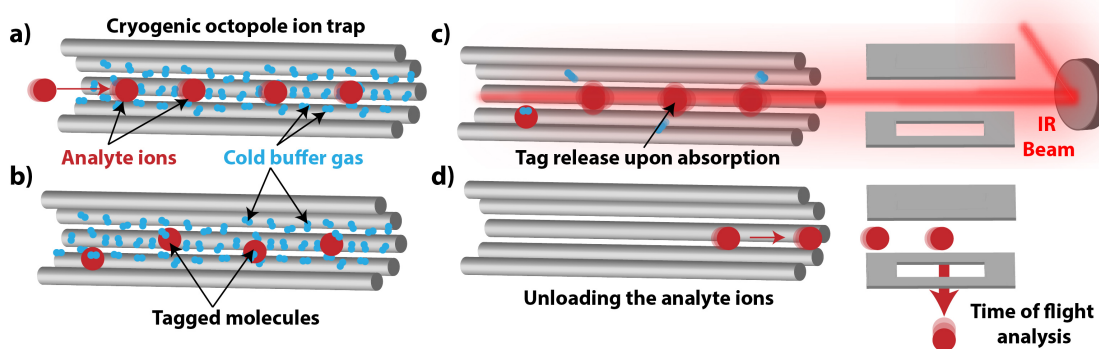


**Figure 2.8:** Schematic of cryogenic, messenger-tagging IR spectroscopy. (a) First, a gas pulse composed mainly of He is introduced into the cryogenic trap and cools down upon contact with the trap assembly surfaces. Analyte ions are then loaded into the cold trap. (b) The trapped molecules of interest are thermally cooled upon collision with the gas mixture. A three-body collision process between an ion and two gas molecules allows the formation of weakly bound clusters of

analytes + gas molecules. **(c)** The gas inside the trap is pumped out and an IR beam traverses the ion trap, overlapping with the tagged analytes. In the resonant case, an IR photon is absorbed by the analyte and its energy redistributed throughout the molecule *via* IVR, increasing its internal energy and boiling off the tag. **(d)** Lastly the analytes are unloaded from the trap towards detection. An IR spectrum is obtained by monitoring the depletion of the tags as a function of the IR photon frequency.

Different ion trap geometries have been successfully implemented for messenger-tagging spectroscopy, such as multipole, ring electrode<sup>72</sup> and planar traps.<sup>74</sup>

Recently, work in our laboratory has coupled messenger tagging cryogenic IR spectroscopy with IM-MS for glycan analysis.<sup>75-76</sup>

## 2.4. Summary and motivation

As described more fully in subsequent chapters, in this thesis we have chosen to combine SLIM TWIMS with messenger tagging cryogenic IR spectroscopy for the analysis of glycans. SLIM IMS was chosen for multiple reasons. (1) SLIM technology has the highest resolving power and ion transmission for IMS separation among all the available techniques to date. This is crucial, as we use it as a prefilter prior to spectroscopic interrogation, and thus it needs to be able to separate isomers with the slightest structural differences in order to build an isomer-specific glycan fingerprint database. High ion transmission is required when working with low-concentration biological samples and is crucial to the detection and identification of all present species. (2) SLIM is a relatively low-cost technology to implement, as it makes use of printed circuit boards. (3) It has unique capabilities in terms of ion manipulations (trapping, storing, enriching, compressing, fragmenting, etc.), which enable the development and implementation of complex schemes for the analysis of biomolecules.

The choice of cryogenic, messenger-tagging IR spectroscopy for glycan analysis is motivated by numerous reasons. (1) Gas-phase vibrational spectroscopy is well suited for glycan analysis because of the multiple IR absorption sites in glycans. (2) As opposed to room-

temperature IRMPD, cryogenic spectroscopy offers the possibility to obtain highly resolved spectra well suited for the identification of isomers of relatively large molecules. (3) Messenger-tagging spectroscopy is a linear technique and can be performed using commercially available light sources. It is also applicable at experimentally more easily accessible temperatures (40K – 70K for N<sub>2</sub> tagging), which simplifies the experimental apparatus.

The combination of these techniques offers an accurate, fast, and robust tool that has the potential to solve the current challenges in glycan analysis. The following chapters describe in detail our design and characterization of two instruments that employ these techniques.

# References

1. Thomson, J. J.; Rutherford, E., XL. On the passage of electricity through gases exposed to Röntgen rays. *The London, Edinburgh, and Dublin Philosophical Magazine and Journal of Science* **2009**, *42* (258), 392-407.
2. Langevin, M. P., *Annales de Chimie et de Physique* **1905**, *5*, 245-288.
3. McDaniel, E. A. M. E. W., *Transport Properties of Ions in Gases*. **1988**.
4. Cohen, M. J.; Karasek, F. W., Plasma Chromatography --A New Dimension for Gas Chromatography and Mass Spectrometry. *Journal of Chromatographic Science* **1970**, *8* (6), 330-337.
5. Makinen, M.; Nousiainen, M.; Sillanpaa, M., Ion spectrometric detection technologies for ultra-traces of explosives: a review. *Mass Spectrom Rev* **2011**, *30* (5), 940-73.
6. Makinen, M. A.; Anttalainen, O. A.; Sillanpaa, M. E., Ion mobility spectrometry and its applications in detection of chemical warfare agents. *Anal Chem* **2010**, *82* (23), 9594-600.
7. Eiceman, G. A.; Nazarov, E. G.; Tadjikov, B.; Miller, R. A., Monitoring volatile organic compounds in ambient air inside and outside buildings with the use of a radio-frequency-based ion-mobility analyzer with a micromachined drift tube. *Field Analytical Chemistry & Technology* **2000**, *4* (6), 297-308.
8. Ewing, R., A critical review of ion mobility spectrometry for the detection of explosives and explosive related compounds. *Talanta* **2001**, *54* (3), 515-529.
9. Limero, P. T. P. a. T. F., Mass spectrometry in the U.S. space program: Past, present, and future. *J Am Soc Mass Spectrom* **2001**.
10. Kanu, A. B.; Dwivedi, P.; Tam, M.; Matz, L.; Hill, H. H., Jr., Ion mobility-mass spectrometry. *J Mass Spectrom* **2008**, *43* (1), 1-22.

11. Bohrer, B. C.; Merenbloom, S. I.; Koeniger, S. L.; Hilderbrand, A. E.; Clemmer, D. E., Biomolecule analysis by ion mobility spectrometry. *Annu Rev Anal Chem (Palo Alto Calif)* **2008**, *1*, 293-327.
12. Revercomb HW, M. E., Theory of plasma chromatography/gaseous electrophoresis: a review. *Anal. Chem.* **1975**, *47*, 970-983.
13. Mason EA, M. E., Transport Properties of Ions in Gases. *New York: Wiley & Sons* **1988**, 560.
14. Clemmer DE, J. M., Ion mobility measurements and their applications to clusters and biomolecules. *Journal of mass spectrometry* **1997**, *32*, 577-592.
15. Einstein, A., *Annalen der Physik.* **1905**, *322*, 549-560.
16. Buryakov, I. A.; Krylov, E. V.; Nazarov, E. G.; Rasulev, U. K., A new method of separation of multi-atomic ions by mobility at atmospheric pressure using a high-frequency amplitude-asymmetric strong electric field. *International Journal of Mass Spectrometry and Ion Processes* **1993**, *128* (3), 143-148.
17. Purves, R. W.; Guevremont, R.; Day, S.; Pipich, C. W.; Matyjasczyk, M. S., Mass spectrometric characterization of a high-field asymmetric waveform ion mobility spectrometer. *Review of Scientific Instruments* **1998**, *69* (12), 4094-4105.
18. Purves, R. W.; Guevremont, R., Electrospray Ionization High-Field Asymmetric Waveform Ion Mobility Spectrometry–Mass Spectrometry. *Analytical Chemistry* **1999**, *71* (13), 2346-2357.
19. Guevremont, R., High-field asymmetric waveform ion mobility spectrometry: A new tool for mass spectrometry. *Journal of Chromatography A* **2004**, *1058* (1-2), 3-19.
20. Guevremont, R.; Barnett, D. A.; Purves, R. W.; Viehland, L. A., Calculation of ion mobilities from electrospray ionization high-field asymmetric waveform ion mobility spectrometry mass spectrometry. *The Journal of Chemical Physics* **2001**, *114* (23), 10270-10277.
21. Krylov, E.; Nazarov, E. G.; Miller, R. A.; Tadjikov, B.; Eiceman, G. A., Field Dependence of Mobilities for Gas-Phase-Protonated Monomers and Proton-Bound

Dimers of Ketones by Planar Field Asymmetric Waveform Ion Mobility Spectrometer (PFAIMS). *The Journal of Physical Chemistry A* **2002**, *106* (22), 5437-5444.

22. Hernandez, D. R.; Debord, J. D.; Ridgeway, M. E.; Kaplan, D. A.; Park, M. A.; Fernandez-Lima, F., Ion dynamics in a trapped ion mobility spectrometer. *Analyst* **2014**, *139* (8), 1913-21.

23. Fernandez-Lima, F. A.; Kaplan, D. A.; Park, M. A., Note: Integration of trapped ion mobility spectrometry with mass spectrometry. *Rev Sci Instrum* **2011**, *82* (12), 126106.

24. Fernandez-Lima, F.; Kaplan, D. A.; Suetering, J.; Park, M. A., Gas-phase separation using a trapped ion mobility spectrometer. *Int J Ion Mobil Spectrom* **2011**, *14* (2-3).

25. Michelmann, K.; Silveira, J. A.; Ridgeway, M. E.; Park, M. A., Fundamentals of trapped ion mobility spectrometry. *J Am Soc Mass Spectrom* **2015**, *26* (1), 14-24.

26. Zietek, B. M.; Mengerink, Y.; Jordens, J.; Somsen, G. W.; Kool, J.; Honing, M., Adduct-ion formation in trapped ion mobility spectrometry as a potential tool for studying molecular structures and conformations. *International Journal for Ion Mobility Spectrometry* **2017**, *21* (1-2), 19-32.

27. Pu, Y.; Ridgeway, M. E.; Glaskin, R. S.; Park, M. A.; Costello, C. E.; Lin, C., Separation and Identification of Isomeric Glycans by Selected Accumulation-Trapped Ion Mobility Spectrometry-Electron Activated Dissociation Tandem Mass Spectrometry. *Anal Chem* **2016**, *88* (7), 3440-3.

28. Dit Fouque, K. J.; Moreno, J.; Hegemann, J. D.; Zirah, S.; Rebuffat, S.; Fernandez-Lima, F., Identification of Lasso Peptide Topologies Using Native Nanoelectrospray Ionization-Trapped Ion Mobility Spectrometry-Mass Spectrometry. *Anal Chem* **2018**, *90* (8), 5139-5146.

29. Castellanos, A.; Benigni, P.; Hernandez, D. R.; DeBord, J. D.; Ridgeway, M. E.; Park, M. A.; Fernandez-Lima, F., Fast Screening of Polycyclic Aromatic Hydrocarbons using Trapped Ion Mobility Spectrometry - Mass Spectrometry. *Anal Methods* **2014**, *6* (23), 9328-9332.

30. Giles, K.; Pringle, S. D.; Worthington, K. R.; Little, D.; Wildgoose, J. L.; Bateman, R. H., Applications of a travelling wave-based radio-frequency-only stacked ring ion guide. *Rapid Commun Mass Spectrom* **2004**, *18* (20), 2401-14.
31. Shvartsburg, A. A.; Smith, R. D., Fundamentals of traveling wave ion mobility spectrometry. *Anal Chem* **2008**, *80* (24), 9689-99.
32. Pringle, S. D.; Giles, K.; Wildgoose, J. L.; Williams, J. P.; Slade, S. E.; Thalassinos, K.; Bateman, R. H.; Bowers, M. T.; Scrivens, J. H., An investigation of the mobility separation of some peptide and protein ions using a new hybrid quadrupole/travelling wave IMS/oa-ToF instrument. *International journal of mass spectrometry* **2007**, *261* (1), 1-12.
33. Giles, K.; Wildgoose, J. L.; Langridge, D. J.; Campuzano, I., A method for direct measurement of ion mobilities using a travelling wave ion guide. *International journal of mass spectrometry* **2010**, *298* (1-3), 10-16.
34. Waters, SELECT SERIE Cyclic IMS. **2019**.
35. Tolmachev, A. V.; Webb, I. K.; Ibrahim, Y. M.; Garimella, S. V.; Zhang, X.; Anderson, G. A.; Smith, R. D., Characterization of ion dynamics in structures for lossless ion manipulations. *Anal Chem* **2014**, *86* (18), 9162-8.
36. Ibrahim, Y. M.; Hamid, A. M.; Deng, L.; Garimella, S. V.; Webb, I. K.; Baker, E. S.; Smith, R. D., New frontiers for mass spectrometry based upon structures for lossless ion manipulations. *Analyst* **2017**, *142* (7), 1010-1021.
37. Webb, I. K.; Garimella, S. V.; Tolmachev, A. V.; Chen, T. C.; Zhang, X.; Norheim, R. V.; Prost, S. A.; LaMarche, B.; Anderson, G. A.; Ibrahim, Y. M.; Smith, R. D., Experimental evaluation and optimization of structures for lossless ion manipulations for ion mobility spectrometry with time-of-flight mass spectrometry. *Anal Chem* **2014**, *86* (18), 9169-76.
38. Webb, I. K.; Garimella, S. V.; Norheim, R. V.; Baker, E. S.; Ibrahim, Y. M.; Smith, R. D., A Structures for Lossless Ion Manipulations (SLIM) Module for Collision Induced Dissociation. *J Am Soc Mass Spectrom* **2016**, *27* (7), 1285-8.
39. Hamid, A. M.; Ibrahim, Y. M.; Garimella, S. V.; Webb, I. K.; Deng, L.; Chen, T. C.; Anderson, G. A.; Prost, S. A.; Norheim, R. V.; Tolmachev, A. V.; Smith, R. D.,

Characterization of Traveling Wave Ion Mobility Separations in Structures for Lossless Ion Manipulations. *Anal Chem* **2015**, *87* (22), 11301-8.

40. Hamid, A. M.; Garimella, S. V. B.; Ibrahim, Y. M.; Deng, L.; Zheng, X.; Webb, I. K.; Anderson, G. A.; Prost, S. A.; Norheim, R. V.; Tolmachev, A. V.; Baker, E. S.; Smith, R. D., Achieving High Resolution Ion Mobility Separations Using Traveling Waves in Compact Multiturn Structures for Lossless Ion Manipulations. *Anal Chem* **2016**, *88* (18), 8949-8956.

41. Deng, L.; Webb, I. K.; Garimella, S. V. B.; Hamid, A. M.; Zheng, X.; Norheim, R. V.; Prost, S. A.; Anderson, G. A.; Sandoval, J. A.; Baker, E. S.; Ibrahim, Y. M.; Smith, R. D., Serpentine Ultralong Path with Extended Routing (SUPER) High Resolution Traveling Wave Ion Mobility-MS using Structures for Lossless Ion Manipulations. *Anal Chem* **2017**, *89* (8), 4628-4634.

42. Hashimoto, K.; Badarla, V. R.; Kawai, A.; Ideguchi, T., Complementary vibrational spectroscopy. *Nat Commun* **2019**, *10* (1), 4411.

43. Karas, M.; Bachmann, D.; Bahr, U.; Hillenkamp, F., Matrix-assisted ultraviolet laser desorption of non-volatile compounds. *International Journal of Mass Spectrometry and Ion Processes* **1987**, *78*, 53-68.

44. Yamashita, M.; Fenn, J. B., Electrospray ion source. Another variation on the free-jet theme. *The Journal of Physical Chemistry* **1984**, *88* (20), 4451-4459.

45. Fenn, J. B.; Mann, M.; Meng, C. K.; Wong, S. F.; Whitehouse, C. M., Electrospray ionization for mass spectrometry of large biomolecules. *Science* **1989**, *246* (4926), 64-71.

46. Anouk M. Rijs, J. O., Gas-Phase IR Spectroscopy and Structure of Biological Molecules. *Springer* **2015**.

47. Oomens, J.; Sartakov, B. G.; Meijer, G.; von Helden, G., Gas-phase infrared multiple photon dissociation spectroscopy of mass-selected molecular ions. *International journal of mass spectrometry* **2006**, *254* (1-2), 1-19.

48. Yao, H.; Jockusch, R. A., Fluorescence and electronic action spectroscopy of mass-selected gas-phase fluorescein, 2',7'-dichlorofluorescein, and 2',7'-difluorofluorescein ions. *J Phys Chem A* **2013**, *117* (6), 1351-9.

49. von Helden, G.; van Heijnsbergen, D.; Meijer, G., Resonant Ionization Using IR Light: A New Tool To Study the Spectroscopy and Dynamics of Gas-Phase Molecules and Clusters. *The Journal of Physical Chemistry A* **2003**, *107* (11), 1671-1688.
50. Polfer, N. C., Infrared multiple photon dissociation spectroscopy of trapped ions. *Chem Soc Rev* **2011**, *40* (5), 2211-21.
51. Lehmann, K. K.; Scoles, G.; Pate, B. H., Intramolecular Dynamics from Eigenstate-Resolved Infrared Spectra. *Annual Review of Physical Chemistry* **1994**, *45* (1), 241-274.
52. Nesbitt, D. J.; Field, R. W., Vibrational Energy Flow in Highly Excited Molecules: Role of Intramolecular Vibrational Redistribution. *The Journal of Physical Chemistry* **1996**, *100* (31), 12735-12756.
53. Schindler, B.; Barnes, L.; Renois, G.; Gray, C.; Chambert, S.; Fort, S.; Flitsch, S.; Loison, C.; Allouche, A. R.; Compagnon, I., Anomeric memory of the glycosidic bond upon fragmentation and its consequences for carbohydrate sequencing. *Nat Commun* **2017**, *8* (1), 973.
54. Goyal, S.; Schutt, D. L.; Scoles, G., Vibrational spectroscopy of sulfur hexafluoride attached to helium clusters. *Phys Rev Lett* **1992**, *69* (6), 933-936.
55. Grebenev, S.; Hartmann, M.; Havenith, M.; Sartakov, B.; Toennies, J. P.; Vilesov, A. F., The rotational spectrum of single OCS molecules in liquid <sup>4</sup>He droplets. *The Journal of Chemical Physics* **2000**, *112* (10), 4485-4495.
56. Gonzalez Florez, A. I.; Ahn, D. S.; Gewinner, S.; Schollkopf, W.; von Helden, G., IR spectroscopy of protonated leu-enkephalin and its 18-crown-6 complex embedded in helium droplets. *Phys Chem Chem Phys* **2015**, *17* (34), 21902-11.
57. Gonzalez Florez, A. I.; Mucha, E.; Ahn, D. S.; Gewinner, S.; Schollkopf, W.; Pagel, K.; von Helden, G., Charge-Induced Unzipping of Isolated Proteins to a Defined Secondary Structure. *Angew Chem Int Ed Engl* **2016**, *55* (10), 3295-9.
58. Mucha, E.; Gonzalez Florez, A. I.; Marianski, M.; Thomas, D. A.; Hoffmann, W.; Struwe, W. B.; Hahm, H. S.; Gewinner, S.; Schollkopf, W.; Seeberger, P. H.; von Helden, G.; Pagel, K., Glycan Fingerprinting via Cold-Ion Infrared Spectroscopy. *Angew Chem Int Ed Engl* **2017**, *56* (37), 11248-11251.

59. Filsinger, F.; Ahn, D. S.; Meijer, G.; von Helden, G., Photoexcitation of mass/charge selected hemin<sup>+</sup>, caught in helium nanodroplets. *Phys Chem Chem Phys* **2012**, *14* (38), 13370-7.
60. Zhang, X.; Brauer, N. B.; Berden, G.; Rijs, A. M.; Drabbels, M., Mid-infrared spectroscopy of molecular ions in helium nanodroplets. *J Chem Phys* **2012**, *136* (4), 044305.
61. Smolarek, S.; Brauer, N. B.; Buma, W. J.; Drabbels, M., IR spectroscopy of molecular ions by nonthermal ion ejection from helium nanodroplets. *J Am Chem Soc* **2010**, *132* (40), 14086-91.
62. Lisy, J. M., Infrared studies of ionic clusters: the influence of Yuan T. Lee. *J Chem Phys* **2006**, *125* (13), 132302.
63. Wolk, A. B.; Leavitt, C. M.; Garand, E.; Johnson, M. A., Cryogenic ion chemistry and spectroscopy. *Acc Chem Res* **2014**, *47* (1), 202-10.
64. Kamrath, M. Z.; Garand, E.; Jordan, P. A.; Leavitt, C. M.; Wolk, A. B.; Van Stipdonk, M. J.; Miller, S. J.; Johnson, M. A., Vibrational characterization of simple peptides using cryogenic infrared photodissociation of H<sub>2</sub>-tagged, mass-selected ions. *J Am Chem Soc* **2011**, *133* (16), 6440-8.
65. Okumura, M.; Yeh, L. I.; Myers, J. D.; Lee, Y. T., Infrared spectra of the cluster ions H<sub>7</sub>O<sup>+</sup>·3·H<sub>2</sub> and H<sub>9</sub>O<sup>+</sup>·4·H<sub>2</sub>. *The Journal of Chemical Physics* **1986**, *85* (4), 2328-2329.
66. Dopfer, O., Spectroscopic and theoretical studies of CH<sub>3</sub>-R<sub>g</sub>n clusters (R<sub>g</sub>=He, Ne, Ar): From weak intermolecular forces to chemical reaction mechanisms. *International Reviews in Physical Chemistry* **2003**, *22* (3), 437-495.
67. Bieske, E. J.; Dopfer, O., High-resolution spectroscopy of cluster ions. *Chem Rev* **2000**, *100* (11), 3963-98.
68. Kamariotis, A.; Boyarkin, O. V.; Mercier, S. R.; Beck, R. D.; Bush, M. F.; Williams, E. R.; Rizzo, T. R., Infrared spectroscopy of hydrated amino acids in the gas phase: protonated and lithiated valine. *J Am Chem Soc* **2006**, *128* (3), 905-16.

69. Piest, H.; von Helden, G.; Meijer, G., Infrared spectroscopy of jet-cooled neutral and ionized aniline–Ar. *The Journal of Chemical Physics* **1999**, *110* (4), 2010-2015.
70. Leavitt, C. M.; Wolk, A. B.; Kamrath, M. Z.; Garand, E.; Van Stipdonk, M. J.; Johnson, M. A., Characterizing the intramolecular H-bond and secondary structure in methylated GlyGlyH<sup>+</sup> with H<sub>2</sub> predissociation spectroscopy. *J Am Soc Mass Spectrom* **2011**, *22* (11), 1941-52.
71. Kamrath, M. Z.; Relph, R. A.; Guasco, T. L.; Leavitt, C. M.; Johnson, M. A., Vibrational predissociation spectroscopy of the H<sub>2</sub>-tagged mono- and dicarboxylate anions of dodecanedioic acid. *International journal of mass spectrometry* **2011**, *300* (2-3), 91-98.
72. Asmis, K. R.; Neumark, D. M., Vibrational spectroscopy of microhydrated conjugate base anions. *Acc Chem Res* **2012**, *45* (1), 43-52.
73. D, G., Inhomogeneous RF fields: a versatile tool for the study of processes with slow ions. In: Ng C-Y, Baer M (eds) State-selected and state-to-state ion-molecule reaction dynamics. Part 1: experiment. *Wiley, New York* **1992**, *LXXXII*.
74. Lorenz, U. J.; Rizzo, T. R., Planar multipole ion trap/time-of-flight mass spectrometer. *Anal Chem* **2011**, *83* (20), 7895-901.
75. Khanal, N.; Masellis, C.; Kamrath, M. Z.; Clemmer, D. E.; Rizzo, T. R., Cryogenic IR spectroscopy combined with ion mobility spectrometry for the analysis of human milk oligosaccharides. *Analyst* **2018**, *143* (8), 1846-1852.
76. Chiara Masellis, N. K., Michael Z. Kamrath, David E. Clemmer, and Thomas R. Rizzo, Cryogenic Vibrational Spectroscopy Provides Unique Fingerprints for Glycan Identification. *JASMS* **2017**, *28* (10), 2217-2222.



## 3. Design and characterization of the prototype

In this chapter we present an overview of the prototype instrument that we designed and constructed combining ion mobility spectrometry with messenger tagging cryogenic spectroscopy. During the course of this work, a SLIM travelling wave mobility separation device was constructed and appended to an existing drift tube instrument.<sup>1</sup> The background of the techniques employed as well as design details are addressed in the following sections.

### 3.1. Overview

A schematic overview of the instrument layout is shown in Figure 3.1. It is composed of an ESI ion source, a coolable SLIM IMS device, a quadrupole mass filter, a cryogenic planar ion trap and a time-of-flight mass spectrometer.

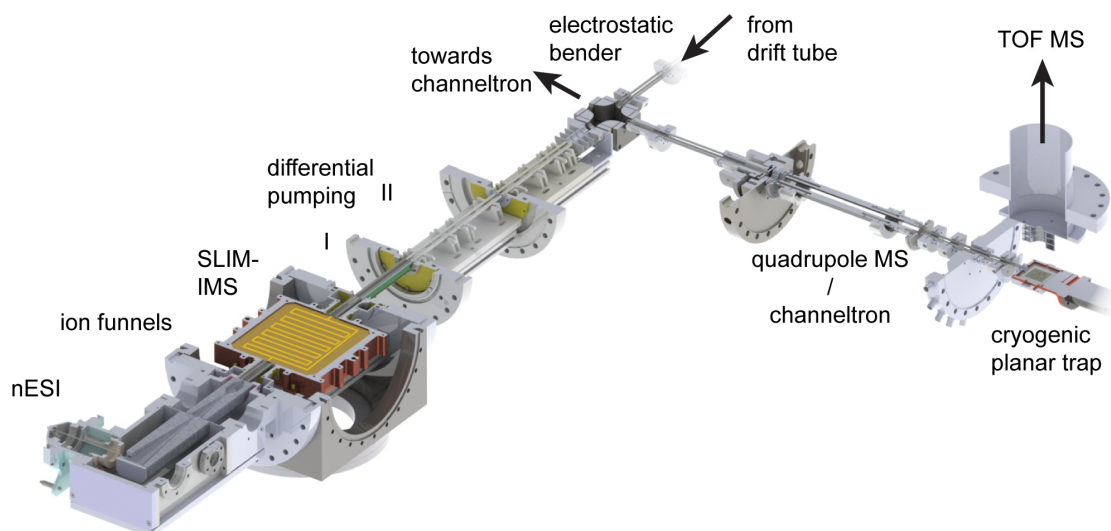


**Figure 3.1:** Schematic overview of the instrument combining ultrahigh resolution SLIM IMS with messenger-tagging cryogenic IR spectroscopy

Ions are generated by nano-electrospray ionization (nESI) at atmospheric pressure. They are then transferred into vacuum (mbar range) using a flared capillary inlet.<sup>2</sup> The capillary is connected to a commercial dual ion funnel source (MassTech, United States)<sup>3</sup> where ions are collimated radially, transported and trapped in an hourglass section for tens of milliseconds. Next, packets of the ionized analytes are released in pulses of varying width ( $100\mu\text{s} - 250\mu\text{s}$ ), transmitted through a conductance limiting electrode and towards an initial ring electrode RF guide (*entrance guide*) prior to the SLIM IMS region. The ring electrode guide was designed to have an inner aperture geometry that is gradually morphed from circular at the entrance to rectangular at the exit, ensuring a smooth transition between the electric field at the end of the ion funnel and the rectangular geometry at the entrance of the SLIM device, thus optimizing ion transmission. The SLIM TW-IMS device is composed of two parallel PCBs with a specific electrode design, similar to the one described in chapter 2 (see Figure 2.6).

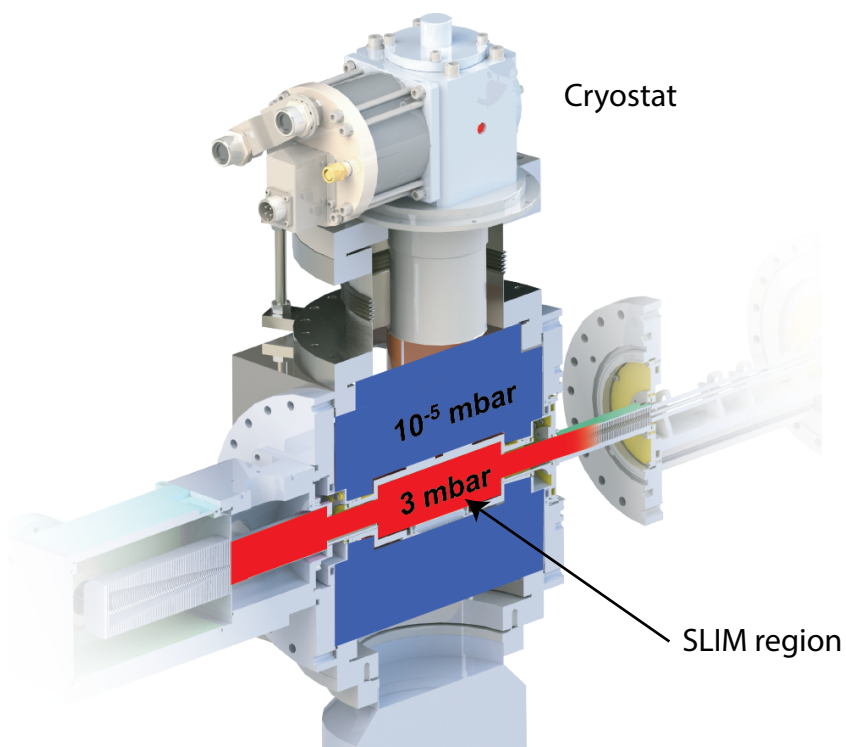


**Figure 3.2:** Schematic of the dual chamber design needed for coolable SLIM IMS. The SLIM device as well as the entrance and exit funnels are operated at 3 mbar (red) for IMS, loading and unloading ions. The cold head of the cryostat installed in the outer chamber is operated at  $10^{-5}$  mbar (blue). Both regions are decoupled to allow for different pressures.

A closed-cycle, single-stage He cryostat is mounted on the top flange of the cubic vacuum chamber and its cold head connected to the copper SLIM housing *via* thermal straps composed of braided copper. This assembly allows for cooling the SLIM IMS region to temperatures as low as 30 K, and gives the possibility to perform cold IMS experiments, which allows for increasing the resolving power and accessing conformers that might otherwise interconvert.

A second morphed-interior ring electrode RF guide (*exit guide*) is mounted at the exit of the SLIM region and ensures the efficient unloading of the mobility separated analytes. The entire assembly composed of the entrance guide, the SLIM IMS region and the exit guide is decoupled from the cubic chamber to enable maintaining different pressure regimes: mbar

range for ion transfer and IMS; high vacuum ( $10^{-5}$  mbar) for the good functioning of the cryostat cold head.

Ions are then transferred into differentially pumped stages (shown in Figure 3.1), separated by conductance-limiting electrodes, using a third ring electrode guide (differential pumping stage I) followed by a hexapole guide (differential pumping stage II). A lens assembly including a set of four steering plates is mounted after the hexapole and to focus and direct the ion cloud efficiently through a conductance limit. The steering electrodes are also used to electrostatically deflect unwanted ions, giving the possibility to selectively send single mobility peaks towards the cryogenic trap and mass analyzer for further investigation.

Subsequently, a quadrupole bender offers the possibility to direct ions either the left towards a channeltron detector, or toward the right, where it passes through an octupole guide and a quadrupole mass filter. Following the mass filter, a set of lenses are placed prior to a planar cold trap, which has been described in detail previously.<sup>4</sup> The cold trap is composed of two PCBs mounted in parallel onto a copper structure, which is itself connected to the cold head of a dual stage cryostat, which allows cooling the trap assembly to temperatures as low as 13 K. The temperature is controlled using a Lakeshore 350 PI controller and a cartridge heater. Before the ions are loaded into the cryogenic trap, a gas pulse, typically composed of 90% He and 10% N<sub>2</sub>, is introduced *via* a pulsed valve (Parker 9 series) and ensures the cooling and tagging of the trapped analytes. The ions are trapped *via* RF confinement for tens of milliseconds thus allowing for: (1) collisional cooling and complexing of the analytes, forming clusters with the N<sub>2</sub> molecules present in the pulsed gas mixture; (2) irradiating the tagged analyte ions using an IR light source (in this case an OPO system or a commercial fiber-pumped laser); and (3) pumping the excess gas molecules of the trap to prepare for ion extraction into the TOF mass analyzer. An infrared spectrum is recorded by monitoring the ratio between the tagged and untagged analytes as a function of the IR wavelength through the measurement of the mass-to-charge ratio of the contents of the trap upon each extraction.

It should be noted that an alternative mobility selection device, a 2 m drift tube (DT), is attached to the electrostatic bender, opposite to the SLIM-arm of the device (see Figure 3.1). The DT instrument was previously described and characterized,<sup>1</sup> and its performance will later be compared to the new part of the instrument.

## 3.2. Vacuum system

Different sections of the apparatus were designed to implement different experimental techniques, each of which requires a different operating pressure, ranging from 1 bar for ion generation, to ultrahigh vacuum ( $<10^{-6}$  mbar) for spectroscopic and mass spectrometric measurements. The design of the differential pumping stages needed to maintain these different pressure regimes is shown in Figure 3.3. The combination of the apertures size of the conductance limits, the available pumping speeds, and the pressure of the prior stage define the ultimate pressure at a given section. This experimental setup comprises eight different pressure regions ( $P_0 - P_7$ ), which can be categorized into four regimes: (1) atmospheric pressure (ESI); (2) mbar range (ion funnels, IMS); (3)  $10^{-2}$ - $10^{-6}$ mbar range (ion guides, bender, channeltron detector) (4)  $<10^{-6}$ mbar (quadrupole mass filter, ion trap, TOF-MS).

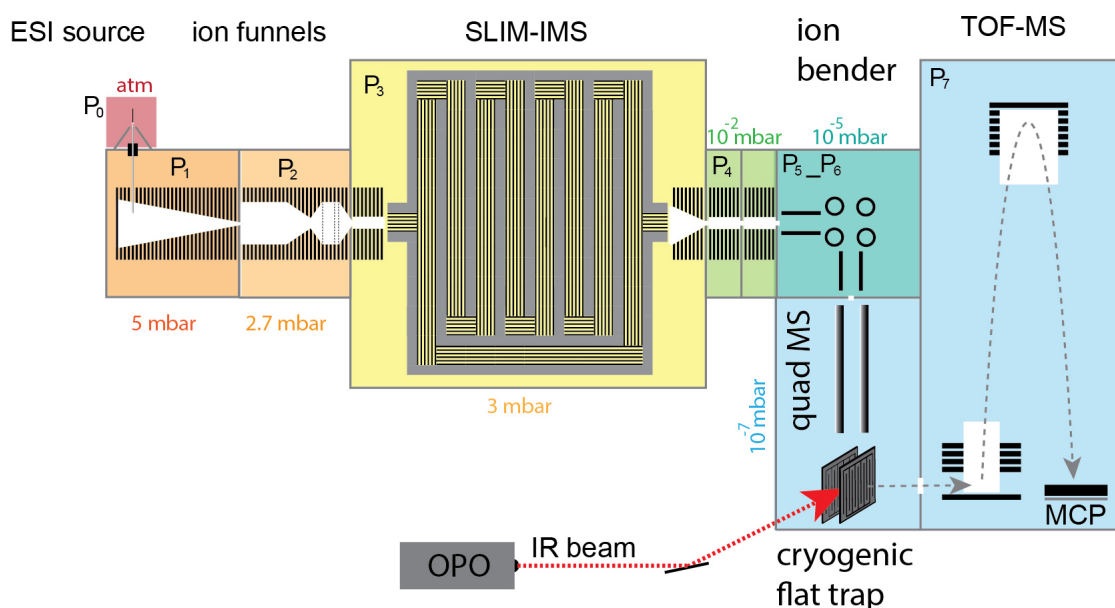


**Figure 3.3:** Schematic of the instrument displaying the operating pressure regimes for different sections: ESI at atmospheric pressure (red); dual ion funnel and SLIM IMS device at mbar pressure (orange, yellow); differential pumping stages including a ring electrode guide and several multipole guides at  $10^{-2}$ - $10^{-5}$  mbar (green, turquoise); and quadrupole mass filter, cryogenic planar trap, and TOF analyzer  $<10^{-7}$  mbar (blue)

As described previously, ions are produced using nESI at ambient pressure  $P_0$  and transferred into the first section of the ion funnel assembly through a stainless-steel capillary. The ion funnel is composed of two sections separated by a conductance limit in a way that  $P_1$  in the first section is different from  $P_2$  in the second. It is important to note that the inner diameter of the inlet capillary defines the minimal pressure in the first stage, hence impacting the minimal pressure in the second. The typical operating range for the ion funnel trap (IFT) sections is 4-8 mbar for the first section and 1-3 mbar for the second section, depending on the conditions needed in the IMS region. Each section is separately pumped using scroll pumps (Edwards XDS 35i). A second conductance limit separates the ion funnel from the SLIM IMS section, which runs at a different pressure,  $P_3$ . The pressures  $P_2$  and  $P_3$  are adjusted with two manual leak valves by introducing a controlled gas flow of  $N_2$  into these chambers. To ensure the purity of the buffer gas used for IMS, it is crucial that the gas flows is permanently directed from the SLIM region into the IFT ( $\Delta P = P_3 - P_2$

> 0). Experiments were run at a positive differential pressure of 0.3 mbar between the SLIM module and the IFT.

One of the main design challenges of the instrument was the implementation of the cold IMS section. While IMS is performed at mbar pressure regime, the cold head of the cryostat requires pressures lower than  $10^{-5}$  mbar to operate most efficiently. For this reason, a dual chamber design, depicted in Figure 3.2, was required to separate the coolable IMS region from the cryostat region.

The SLIM boards are enclosed in a copper housing, which is mounted on the lower face of the cubic vacuum chamber (see Figure 3.4). The entrance and exit ring electrode guides are mounted on flanges and slid into PEEK tubes that are fixed onto the copper housing of the SLIM.

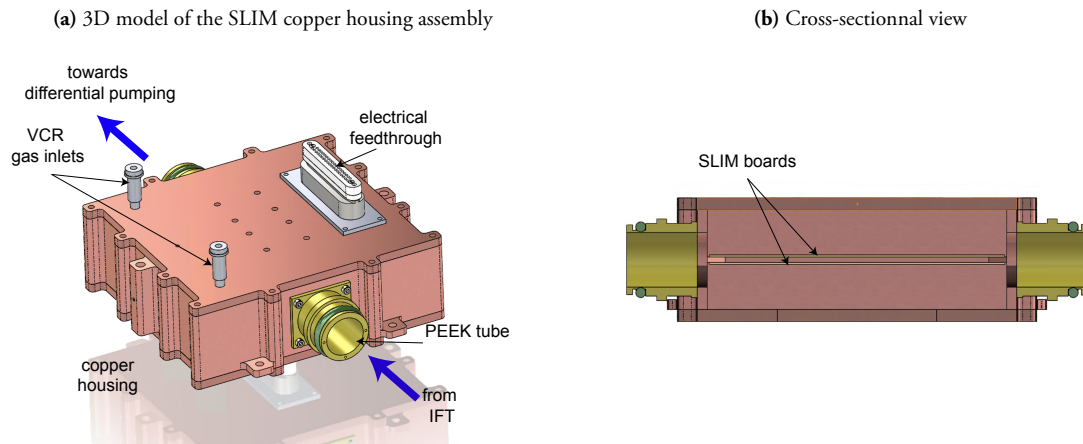


**Figure 3.4:** (a) 3D model of the SLIM copper housing assembly including the PEEK structure separating the ring entrance and exit guides from the outer cubic chamber, electrical feedthroughs, gas and inlets. (b) A cross sectional view of the assembly showing the position of the SLIM boards within the copper housing

The complete SLIM housing assembly is shown in Figure 3.4. An O-ring is placed on the peak structures to ensure that the guides and IMS region are completely decoupled from the cubic chamber. Thus, by separately pumping the cubic chamber, it is possible to reach

pressures low enough to operate the cold head, while maintaining a mbar pressure regime inside the copper chamber that encloses the SLIM device.

The following section (depicted in green in Figure 3.3) of the apparatus is composed of a cylindrical chamber separated from the exit guide by a conductance limit. It includes a ring electrode guide with a constant circular aperture that is operated at  $P_4 \approx 10^{-2} - 10^{-3}$  mbar. The following hexapole guides are held by a structure mounted on a cubic vacuum chamber which also includes the lenses and steering plates assembly. This section is connected to a second turbo-pump and is operated at high vacuum ( $P_5 \approx 10^{-5}$  mbar).

The next part of the instrument was kept unmodified from the apparatus initially described by Masson *et. al*<sup>1</sup>. The octupole guides and the bender are operated at  $P_6 \approx 10^{-5} - 10^{-6}$  mbar while the quadrupole and TOF analyzer are operated at  $P_7 < 10^{-7}$ .

To operate the ion trap, however, a gas pulse is introduced prior to the arrival of the ion packet and is pumped out before ion extraction towards the TOF. While the exact instantaneous pressure cannot be easily determined, when operating the trap, an average pressure of  $\approx 10^{-6}$  mbar is required for optimal trapping and tagging of the analytes. The trap region is connected to a 200 l/s turbo pump, which ensures fast pumping of the gas prior to extraction. This is crucial to the spectroscopic experiments, because if the pressure remains too high inside the trap, the weakly bound tag molecules may get dissociated from the analyte ions upon collisions with the residual gas during extraction, rendering the detection of photon absorption difficult if not impossible.

### 3.3. Radio-frequency devices for the manipulation of ion motion

The manipulation of gas-phase ions in different pressure regimes is a crucial aspect to carefully consider in designing an IM-MS instrument. A multitude of tasks such as loading

and unloading, storing, and guiding ions through relatively small size conductance limits need to be performed with precise control to limit ion loss. The use of multipole devices based on alternating electric fields generated by radio-frequency (RF) waveform generators is common for efficient ion control, transmission and focusing. The need to use RF potentials results from the fact that, as stated in Earnshaw's theorem<sup>5</sup>, a charged particle cannot be held in a stable equilibrium by electrostatic forces alone. Mathematically, this results from the fact that the divergence of an electrical force  $F(\mathbf{r})$  that derives from a potential  $U(\mathbf{r})$  needs to be null, to satisfy the Laplace's equation.<sup>6</sup>

$$\nabla \cdot \mathbf{F} = -\nabla^2 U = 0 \quad \text{Eq 3.1}$$

However, while electric potentials cannot have any minima or maxima in free space, they do have a saddle point in a three-dimensional space. Inverting the saddle point at the appropriate frequency, creates a net force that drive the charged particle towards the center of the potentials. Hence, depending on the mass-to-charge ratio of a specific ion, at a certain oscillation frequency and amplitude of the electric field, it is possible to efficiently confine a charged analyte close to the central axis of an RF device.

A mixture of the RF sinusoidal waveform of amplitude  $A$  oscillating at a frequency  $f$ , and a DC component  $U$  generates an electric potential  $\Phi_0$  which can be expressed as:

$$\Phi_0(t) = U + A \sin(2\pi ft + \phi) \quad \text{Eq 3.2}$$

Where  $\phi$  represents the phase angle and is shifted by  $180^\circ$  between adjacent electrodes (electrodes in different colors in Figure 3.5). While the DC component  $U$  is equal to  $0V$  when an RF device is used as an ion guide, it defines, together with the frequency  $f$ , the mass window that is transferred when operating a quadrupole as a mass filter device. Typical

$f$  values range from hundreds of kHz to few MHz while the amplitude of the peak-to-peak voltage can go up to hundreds of volts.

The instrument described in this chapter includes three main types of RF devices; (1) multipole guides; (2) ring-electrode guides; (3) planar electrode devices.

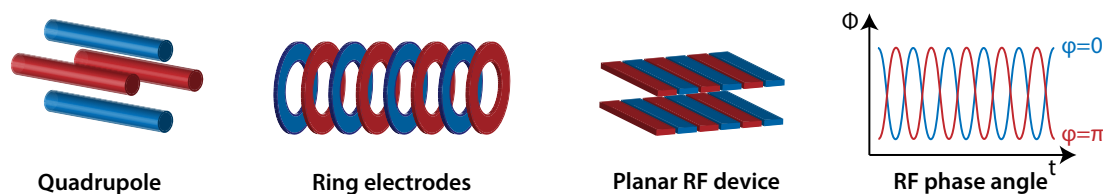


**Figure 3.5:** Schematic representation of the different types of RF devices used in this instrument. The stacked ring electrode design is used in the dual funnel, entrance and exit morphed-geometry guides as well as the third guide in the first differential pumping stage. Three different multipole designs are used: a hexapole and two octupole guides in differential pumping stages. A quadrupole that plays the role of mass filter. The SLIM IMS device and the cryogenic trap have both a planar geometry. The electrodes are divided into two groups (red and blue) each carrying a shifted phase (by  $\pi$  in rad) of a sinusoidal RF waveform.

### 3.3.1 Ion funnel and ring electrode guides

In a relatively high-pressure regime (mbar range), a large number of collisions (in the range of  $10^5$  to  $10^6$  per second depending upon the size of the considered analytes) occur between ions and neutral gas molecules, and in this case the main component contributing to the ions kinetic energy is the thermal energy of the buffer gas. Thus, to focus and guide ions in a specific direction, electric fields need to be applied. A ring-electrode structure has the advantage of allowing the application of both an RF potential and a DC bias potential to each electrode. While the former confines the ions to the axis of the assembly, a DC gradient along the electrodes drives them in the desired direction.

A ring-electrode guide, illustrated in Figure 3.5, is built by stacking multiple ring electrodes along their circular axis. The instrument described in this chapter includes a dual ion-funnel assembly, which represents the first vacuum stage of the instrument.<sup>7</sup> Operating at pressures in the mbar range, it is composed by a stack of plated PCBs with a circular geometry in the center, and with apertures of varying diameters. The PCBs are interleaved by an insulating material to decouple adjacent electrodes. A cross-sectional view of the ion funnel assembly is shown in Figure 3.6.

The first funnel of the assembly has a conical geometry, where the diameter of the apertures is constantly decreasing, enabling the radial focusing of the initially diffuse ion cloud. This is crucial as it allows for an efficient transmission of the ions through the first conductance limit toward the second funnel of the assembly.<sup>8-10</sup> The funnel in the second section is of so-called 'hour-glass' shape. In addition to focusing and efficiently transmitting the ion cloud through the next conductance limit, it is used to store ions and release them in pulses into the IMS region, hence the need for a geometry that maximizes the trapping volume as shown in Figure 3.6. The hour-glass funnel includes grids on three of the ring electrodes that are mainly used for trapping and releasing purposes, but can as well be used to fragment the analytes *via* CID.

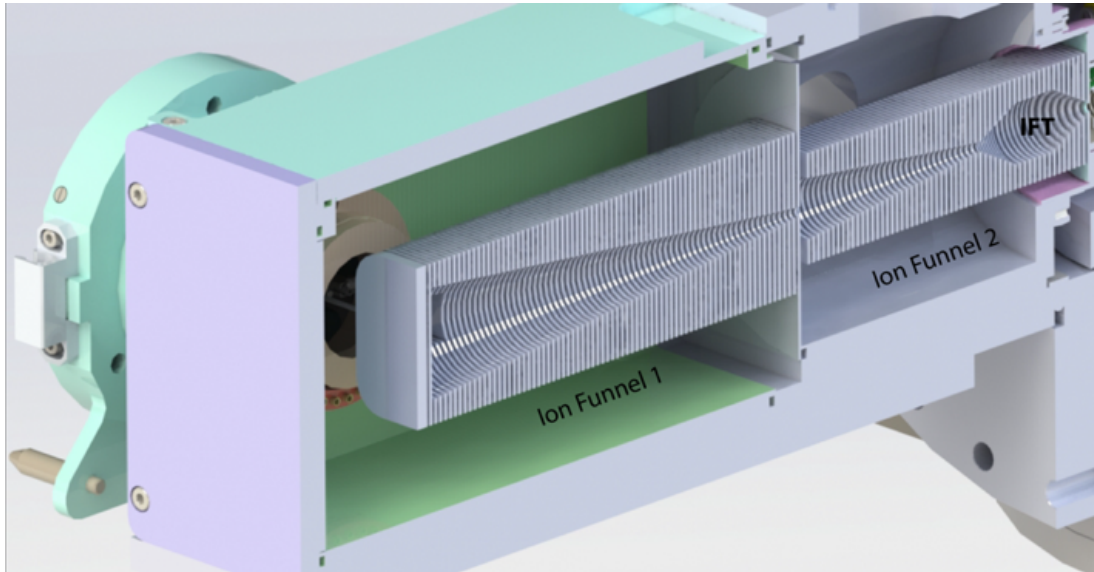


**Figure 3.6:** Cross-sectional view of the commercial dual funnel assembly constituted by a first region including a simple conical funnel followed by a conductance limit. The second region includes a conical section at the entrance followed by an hour-glass section for trapping and releasing ion pulses into the following region.

Ring-electrode guides are installed both at the entrance and the exit of the SLIM IMS sub-chamber. The apertures of the electrodes follow a morphed geometry, evolving from a circular shape to a rectangular shape one to ensure a smooth transition into and out of the SLIM device. The geometry of these guides is shown in Figure 3.7.

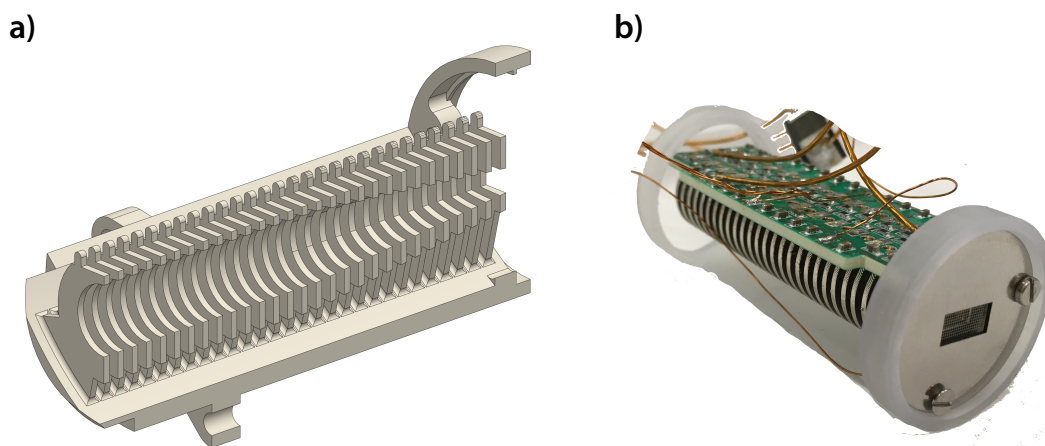


**Figure 3.7:** (a) Cross-sectional view of the 3D printed ion guide displaying the morphed inner geometry of the ring electrodes. (b) Picture of the plated guide displaying the PCBs that includes all the needed connection to operate it.

Lastly, a third ring-electrode guide, which has a circular aperture of constant diameter, is installed in the next section of the instrument and ensures the transition from the IMS pressure regime (mbar) to the lower pressure ( $10^{-2}$  mbar) pumping stage.

Notably, the three guides consist of 3D-printed material (Formlabs, United states) that was coated with a layer of gold and then nickel, to ensure a conductive surface of the rings.<sup>11</sup>

### 3.3.2 Multipole guides

A multipole guide is a device composed by  $2n$  metallic cylindrical rods to which RF potentials are applied. The instrument described here includes hexapole and octupole guides for ion transmission as well as a quadrupole that can be operated as a mass filter. By appropriately setting the frequency and amplitude of the RF potential, it is possible to focus the ions at the center of the device, preventing them from colliding with the rods. It is important to note that the ions' motion depends not only on the electric field, but also on their mass-to-charge ( $m/z$ ) ratio. In fact, this behavior is central to quadrupole mass filters that are widely used in mass spectrometry.<sup>12-13</sup> For specific combinations of the RF voltage

and the DC differential voltage between the two pairs of rods forming a quadrupole, it is possible to define a stability window for ions of specific  $m/z$ . This window can be accurately controlled to either enable a stable trajectory for a large range of  $m/z$  ratios (transmission mode), or to specifically let ions of the same  $m/z$  ratio experience a stable trajectory (mass filter mode). In the latter case, all other ions will end up colliding with one of the rods and thus not being further transmitted for detection.

In general, the rods need to be precisely machined and positioned to create a homogeneous electric field across the length of the guide. The modified section of the instrument contains a hexapole guide composed by two 3D-printed and nickel-coated pieces, manufactured in a similar manner to the previously described ring electrode guides.

### 3.3.3 Planar RF devices

Ion manipulation devices of planar geometry have been developed only recently, and their use has expanded from simply trapping ions in an RF field towards IMS applications.

## SLIM components: Structures & Simulations

SLIM offers a unique way to implement TWIMS using a PCB-based device. Not only is manufacturing cost for such a device greatly reduced (compared to traditional TW techniques), but the relatively simple setup offers a multitude of possibilities to design customized components.

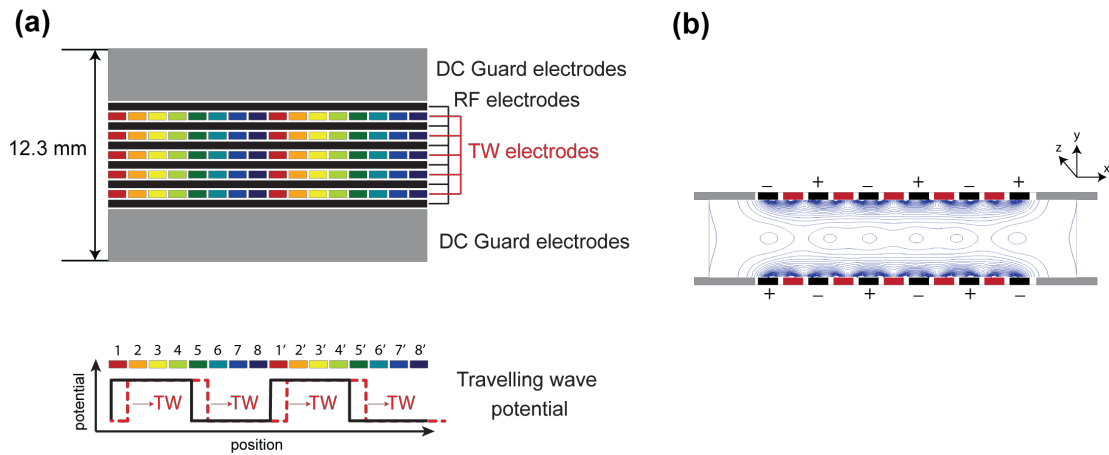


**Figure 3.8:** TW SLIM electrode design and electric potentials **(a)** The building block of a SLIM device is composed of 8 DC (TW) pads (different colors). A sequence of voltages is periodically applied to the DC electrodes numbered from 1 to 8, creating the TW. This sequence is repeated throughout the entire path. **(b)** A view of the plane the direction of ion transport. The contour lines of the RF potential are displayed in blue. The circular shapes of the potential between the boards represent the ion channels through which ions are transported.

The basic structure of a SLIM device is composed of the three types of electrodes shown in Figure 3.8(a). Although different electrode designs are possible, we describe here the structures first reported by Smith and coworkers when referring to SLIM TW IMS. The bottom panel of Figure 3.8(a) illustrates the electric field between the boards and how the TW propagates through SLIM structures. A SLIM separation device is thus composed of several building blocks along which the applied TW potential pushes ions through the buffer gas, resulting in mobility-specific drift times and hence ion separation. Ions are confined in the center of the SLIM device by the RF field restricted to travel in RF defined ion pipes, shown in Figure 3.8(b).

One of the major advantages of the SLIM electrode design is that it enables the implementation of  $90^\circ$  turns in the ion path, as shown in Figure 3.9(a). This is a crucial property of SLIM, as it removes a considerable design constraint that has been a limiting factor for DT and TW-IMS. By introducing  $90^\circ$  turns, it is possible to implement extended,

serpentine pathlengths on the PCB, as indicated in Figure 3.9(c). Using such paths, it is possible to reach a 10 m drift path on a board smaller than 1 m<sup>2</sup>. This results in a substantial increase in IMS resolving power  $R$  without increasing in instrument size, since  $R$  scales with  $L^{1/2}$  in TWIMS, where  $L$  is the total path length.

Furthermore, SLIM technology allows for the design of ion switches using DC electric potentials to block or open alternative drift paths, as shown in Figure 3.9(b). By switching a set of electrodes at the exit of the SLIM separation region, it is possible to either turn ions by 90° towards the next section of the instrument or to push them towards a return path that goes back to the beginning of the separation region. By cycling the ions in this way, it is possible to extend the path length and hence increase the resolving power even further.

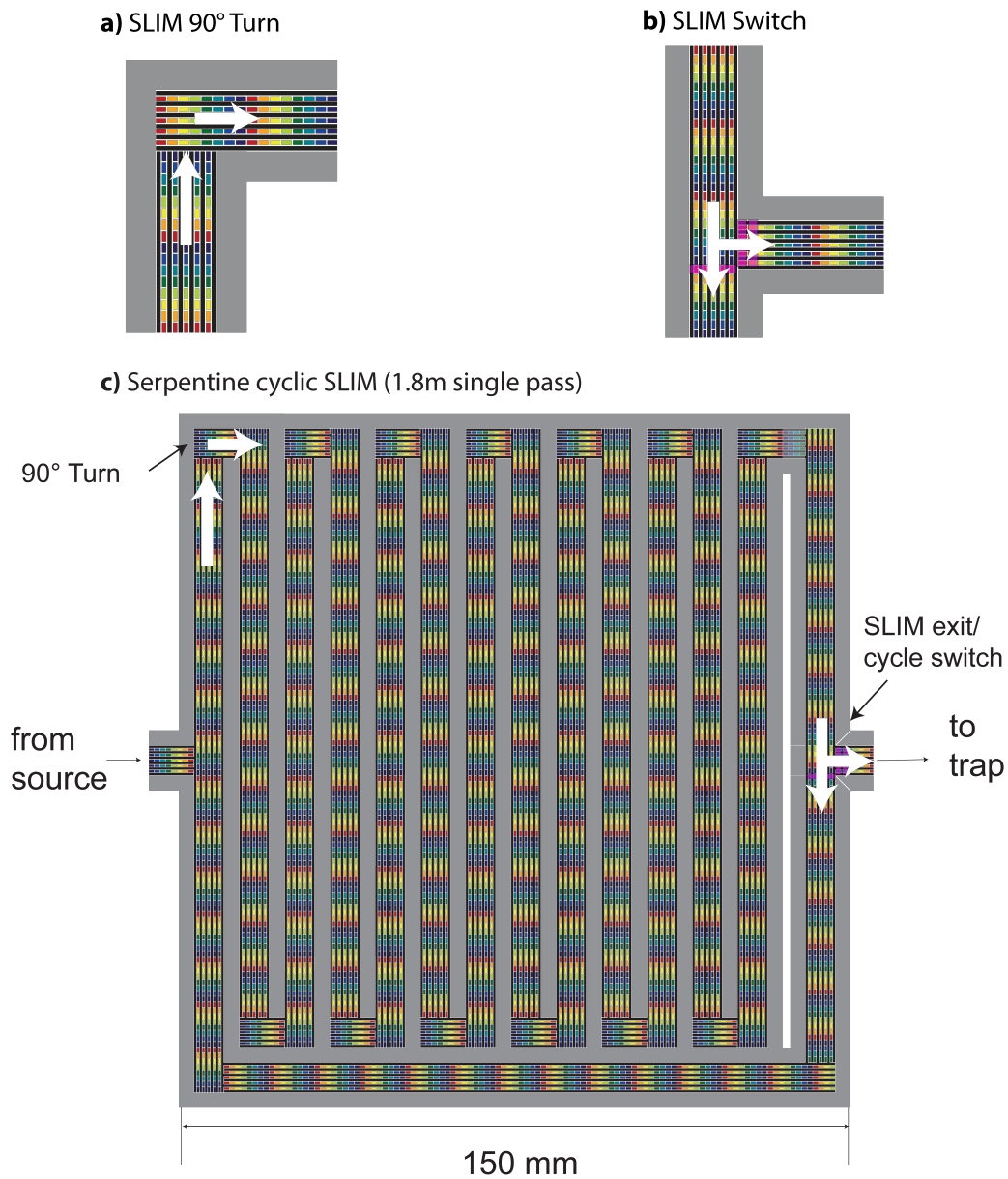


**Figure 3.9:** An illustration of different SLIM components used to build board with a 1.8m path. **(a)** SLIM 90° turn using a specific DC pad arrangement to turn ions perpendicular to their initial direction of motion. This feature enables the design of a serpentine path. **(b)** SLIM switch that is implemented by controlling specific rows of DC pads (pink) to either direct the ions in a perpendicular direction towards the exit of the SLIM region, or to continue straight for another loop. This feature enables the implementation of cyclic IMS in SLIM. **(d)** A 1.8m serpentine cyclic SLIM board of size 15 x 15 cm.

## SLIM Simulations

To obtain a better understanding of ion motion inside a SLIM device and estimate of the voltage range needed for operation, ion trajectories were simulated. The SLIM structures used in the simulations were designed using the SolidWorks software package and the geometry CAD files were then imported as potential arrays (PA) into SIMION. The travelling wave (TW) as well as RF potentials were generated and applied to predefined sets of electrodes using a custom algorithm defined in the *Lua* programming language. The algorithm defines a loop-like use of the ‘fast adjust’ function in SIMION, which allows for rapid field variations during ion motion. To simulate collisions with the neutral buffer gas, a SIMION user program based on statistical diffusion simulations (SDS) was used.<sup>14</sup> The SDS model takes into consideration both the drift of the ions defined by Stoke’s law and random diffusion, which is implemented as randomized ion jumps. Simulations were performed for a pressure range of 1-3 mbar and collision cross sections corresponding to N<sub>2</sub> buffer gas molecules at a temperature of 300 K.

First, the ion motion in a straight TW SLIM section was simulated. Figure 3.10(b) shows the behavior of an ion that is created within the SLIM section while applying an RF field combined with a travelling wave across the section. It also shows the electric potential created by the TW profile Figure 3.10(c).

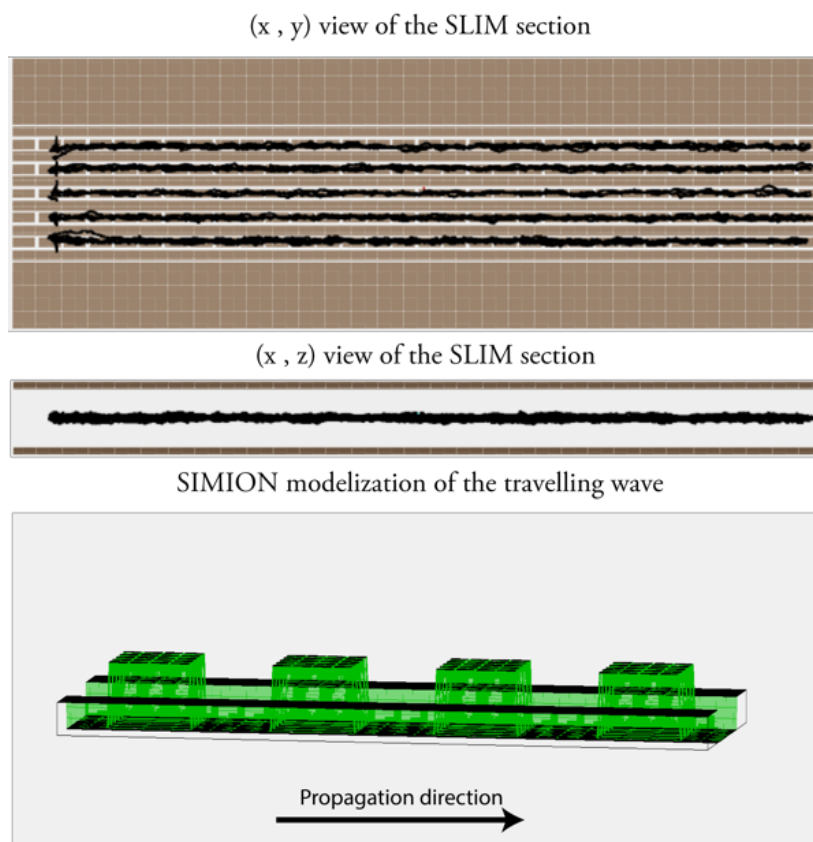


**Figure 3.10:** SIMION simulation of a 50 charged molecules trajectory (black traces) transmitted through a SLIM IMS section from left to along the y axis. (x,y) view (top panel), (y,z) view (middle panel). SIMION model of the travelling wave (bottom panel).

As shown in the figure above, ions travel in low-field regions, referred to as ‘ion pipes’. The positions of the ion pipes are defined by the RF phase applied to opposing parallel electrodes. Figure 3.11 shows the effect of different RF configurations on the positions of the low field regions. In the case when opposite RF phases are applied to parallel electrodes, the ion pipes are aligned with the RF electrodes (Figure 3.11b top panel). In the case when the same RF phase is applied to parallel electrodes (Figure 3.11b bottom panel), the ion pipes are shifted to be aligned with the TW electrodes.

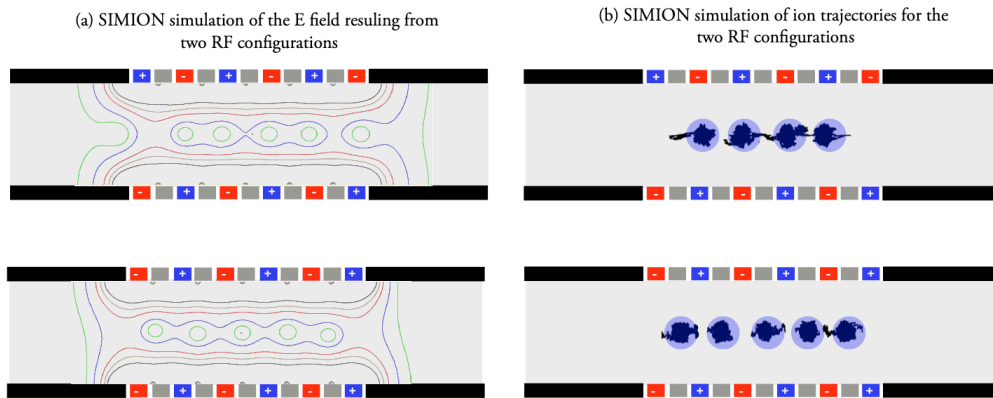


**Figure 3.11:** SIMION simulation of the effect of the RF voltages on ion propagation (a) Electric field lines showing the field free region when applying opposite RF phases to parallel electrodes (top panel) and the same RF phases to parallel electrodes. (b) Ion trajectories (in black) for each RF configuration. The blue circles depict the ion pipes created in the case of opposite RF phase (top panel) and same RF phase (bottom panel)

The effect of the DC potential on the guard electrodes is shown in Figure 3.12. While in the first case (left panel) the ions propagate following their initial positions in the SLIM section from top to bottom, the second case (right panel) shows that, by increasing the Guard voltage from 15 V to 25 V during ion propagation, it is possible to drive the ions into the center of the SLIM path.

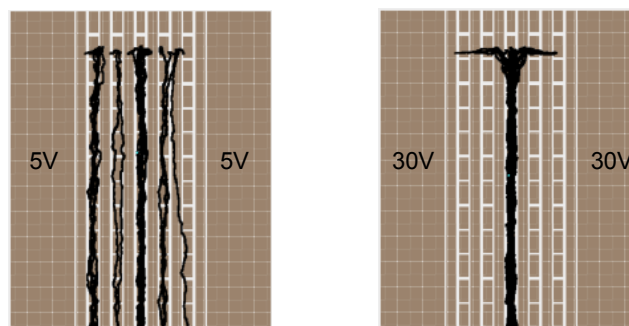


**Figure 3.12:** Effect of the guard voltage on the propagation of ions in a SLIM device, with the trajectories shown in black. (a) Low guard voltage (5V): ions propagate in different channels depending on their initial position, within the SLIM straight section. (b) High guard voltage (30V): Ions are focused to the center of the SLIM straight section and travel in a single channel.

The ability to implement 90° turns in a SLIM device is crucial for high-resolution IMS devices and results in the implementation of U-turn structures that can be used as building blocks for the construction of extended, serpentine-path SLIM devices. In Figure 3.13, the simulation results of a U-turn structure are displayed as along with the fields created by the traveling wave at the 90° corner that enable the turning process.

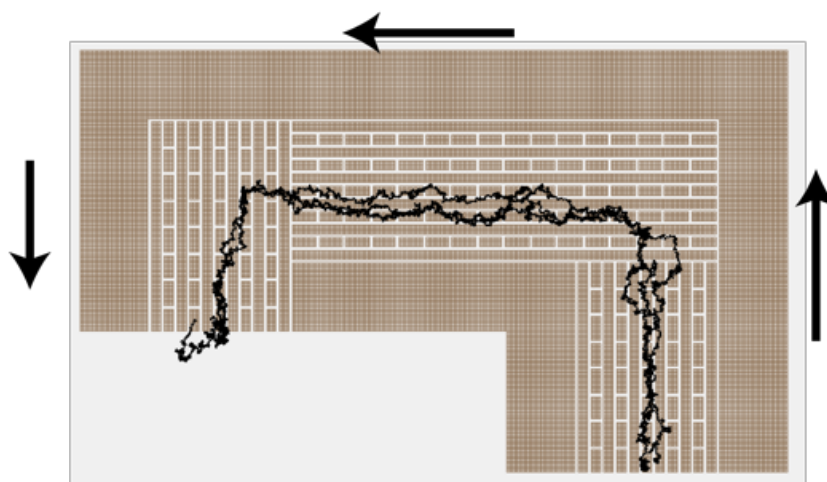


**Figure 3.13:** SLIM U-turn. Top panel: SIMION simulation of 3 charged-molecule trajectories (black traces) following the propagation direction shown by the arrows.

As described in the previous chapter, TW-SLIM can be operated in two different regimes depending upon the operating parameters: ion transport regime and mobility separation regime. During ion transport, ions are mainly located at the valley of the wave and are thus transported at the same speed as the latter. When operating in a separation regime, the wave propagates at a high enough speed that causes the ions to roll-over the wave's crest with a certain probability upon collision with the neutral gas molecule present in the separation region. Ions with lower mobility will have a higher probability of rolling over due to their larger CCS, leading to a lower net velocity. As a result, analytes with different CCS are separated with respect to their respective shapes. Figure 3.14 shows the different ion trajectories while in transmission (blue, right panel) or separation mode (red, left panel).

The backward motion of the ion, as it rolls over the wave (red trajectory), results in a lower net velocity, hence affecting the total flight-time through the SLIM section.

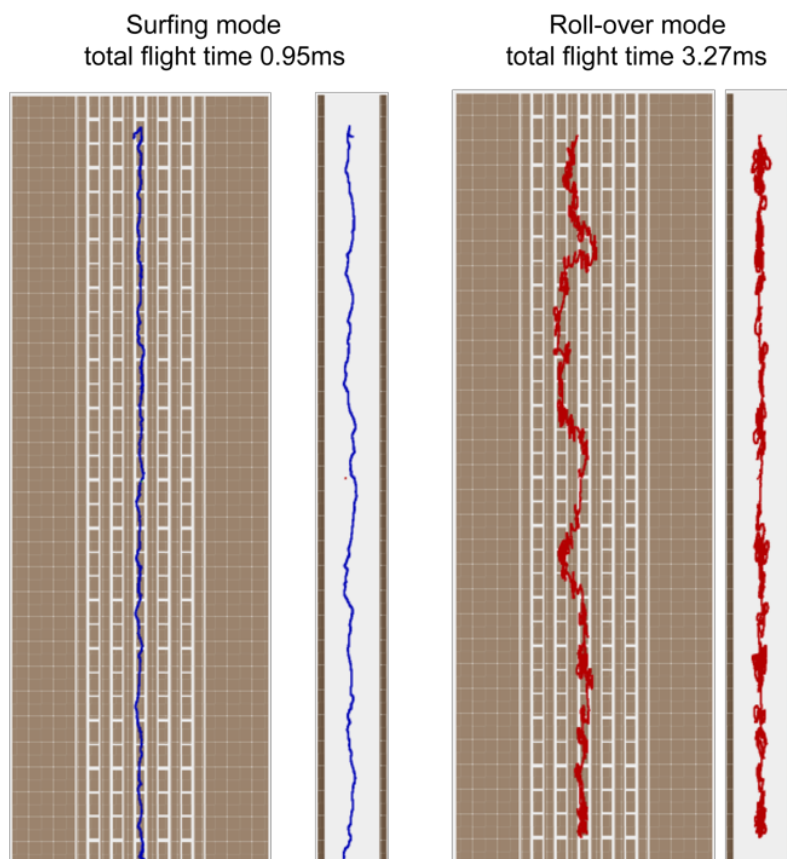


**Figure 3.14:** SIMION simulation of transmission mode vs. separation mode: (a) Simulated trajectory of a charged molecule in transmission mode (blue trace) shown in two view planes. The ion travels at the wave's propagation speed and follows a straight trajectory. (b) Simulated trajectory of a charged molecule in separation mode (red trace). At higher wave propagation speeds, ions experience a rolling over motion due to collisions with the buffer gas (simulated using SDS collision mode in SIMION) and are thus slowed down. Ions of different mobilities with roll over with different probabilities, resulting in separation.

## Planar cryogenic ion trap

The implementation of a planar ion trap was first reported by Wester *et al.*, where they describe a microchip-based trap with a multipole arrangement of RF electrodes.<sup>15</sup> The planar geometry presents several advantages compared to the classical cylindrical geometry.

While the latter requires a precise machining of the multipole rods and their accurate placement, the former can be easily made by lithography and only requires minimal manual alignment. In addition, the planar RF device geometry ensures a finite depth of the effective potential and hence a large field-free region. This is a crucial property especially when considering cryogenic cooling of trapped analytes. The application of this technology for cryogenic spectroscopy was developed and optimized by U. Lorenz and T. Rizzo.<sup>4</sup> The cryogenic ion trap used in our prototype instrument was designed by M. Kamrath, and is composed of two PCBs containing a set of RF electrodes as well as four DC electrodes for ion trajectory control and focusing of the ion cloud (as displayed in the top left panel of Figure 3.15). The PCB's are mounted on a copper spacer which includes a gas inlet. As the trap assembly is mounted at the entrance of a TOF analyzer, the PCB assembly acts as the extraction plates of the TOF and for this reason, the material between two adjacent RF electrodes was removed. This allows ions to be extracted through the RF electrodes into the flight tube.

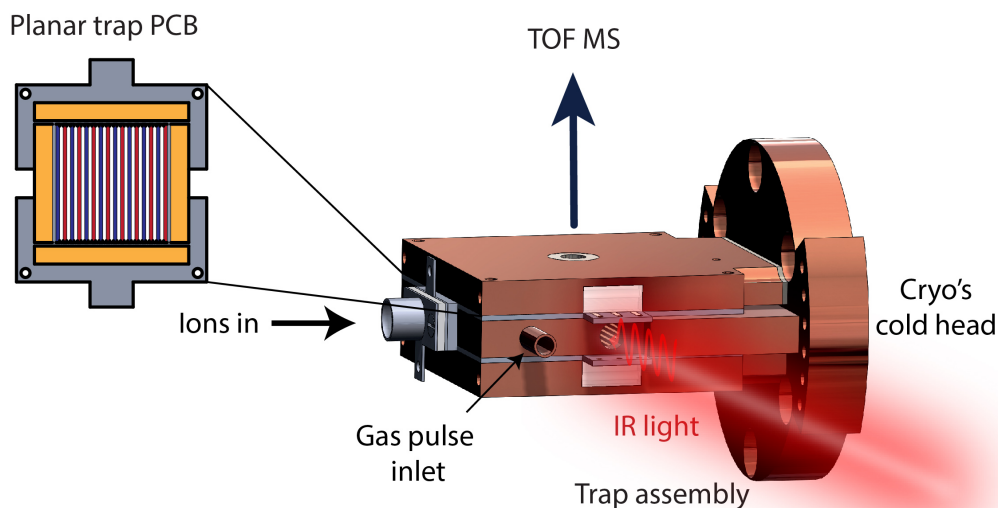


**Figure 3.15:** Schematic overview of the planar cryogenic ion trap. The trap assembly is composed of copper plates mounted directly on the cold head of the cryostat *via* an adapter plate. The assembly includes top and bottom plates as well as a spacer separating a set of two PCBs. The electrode design of the PCB is displayed on the top left. It includes RF electrodes (red and blue) for radial RF confinement and trapping of the analytes as well as DC electrodes (yellow) that are used to define

the position of the ion cloud. Ions are stored between the electrode arrays, acquire tags from a previously pulsed cold gas, and are interrogated by a beam of IR light. Lastly, ions are extracted through a hole in the top plate towards the TOF analyzer.

The trap operates as follows. (1) Mobility-separated and mass-filtered ions arrive to the planar trap after being spatially focused using a lens assembly mounted on the copper spacer and placed at the entrance of the trap. (2) Ions are confined by RF fields (red and blue electrodes in Figure 3.15) and stopped by the DC voltages applied to the front and back DC electrodes (yellow electrodes in Figure 3.15) of the trap. (3) After cooling, tagging, and IR interrogation of the ions, DC voltages on the side electrodes are ramped to concentrate the ions in the middle of the assembly, facing the extraction region. (4) RF voltages are quenched and the repeller/extractor plates are switched to their respective high voltages to extract the ions toward the TOF analyzer.

### 3.4. Time-of-flight analyzer

The analytes are detected using a time-of-flight (TOF) mass analyzer. A schematic representation of the TOF analyzer is shown in Figure 3.16. In TOF analysis, ions are accelerated in ultra-high vacuum by applying high voltage pulses to a set of electrodes in the ion path. The ion time-of-flight is obtained by measuring the time needed for them to travel from the acceleration region to the detector. Since the ion velocity is dependent upon their mass and charge, analytes with different mass-to-charge ratios ( $m/z$ ) will reach the detector at different times.

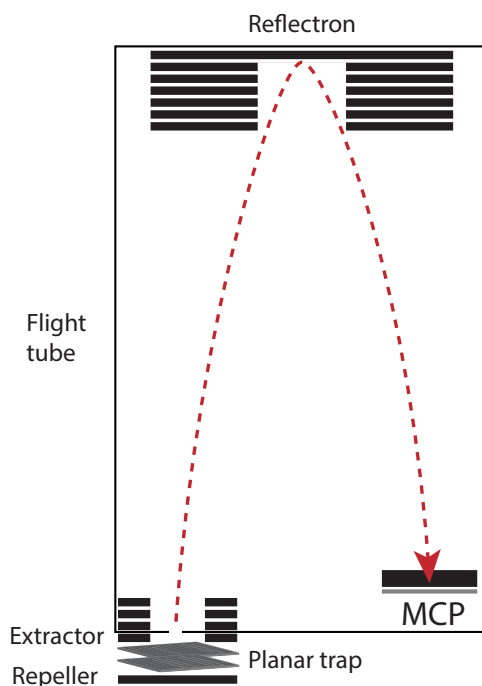


**Figure 3.16:** Schematic representation of the TOF mass spectrometer used to analyze the ions produced by the electrospray. Pulsed high voltages are used to accelerate the ions from the planar trap toward the flight tube. Ions are then directed by a reflectron towards a micro-channel plate (MCP) detector connected to a preamplifier and an analog-to-digital converter that processes the signal.

It is hence possible to extract the  $m/z$  of a specific ion from its flight time  $t$ , from the following relation,

$$t = k \sqrt{\frac{m}{z}} \quad \text{Eq 3.3}$$

where  $k$  is an instrument-dependent constant that represents the voltage settings, the flight tube geometry, as well as other instrument characteristics.<sup>16</sup> The device is mounted on top of the planar trap assembly and provides a  $M/\Delta M$  mass resolution up to approximately 1500 when operated at 10Hz. The average pressure in the TOF region is in the range of  $10^6$ - $10^8$  mbar, depending on the operation regime. After extraction from the planar ion trap,

the ions are detected using a microchannel plate (MCP) detector connected to a current-to-voltage converter. The analogue signal generated by the ion detection events is then converted using the analogue-to-digital converter (ADC) of an oscilloscope (LeCroy).

### 3.5. Electronics, time-sequence generation, and data acquisition

To operate the newly developed part of the instrument, a multitude of DC voltages, RF voltages, and triggers are required. DC voltages are generated using different commercial and custom-built power supplies. The nano-electrospray source is operated using a standalone high-voltage power supply generating up to 3 kV. The IFT source is operated using its commercial MassTech power supply which generates the DC voltages as well as the RF voltage and frequency required to run the different funnels. A pulser device allows to switch the voltage applied to the grids of the IFT assembly between the voltage generated by the MassTech power supply (low) and the voltage provided by a home-built generator (high), accumulating and releasing ions in pulses of defined width. The delay and width that trigger the ion packet release are defined by a pulse and delay generator (Berkley Nucleonics Corporation BNC). A commercial power supply (MIPS modular system, GAA Custom Electronics) generates the DC and RF voltages needed for the SLIM IMS device, the 3D printed ring electrode guides, and the 3D printed hexapole guide. It also generates the TW potentials used for separation and allows for the control of its speed and sequence. The SLIM ion switches are controlled by custom built TW-to-DC switches. The switches have three inputs: (1) DC block, (2) TW voltage, (3) time trigger; and a single output, which provides the needed sequence of different voltages at the desired timings to enable IMS cycling. The MassTech and MIPS systems are controlled *via* a local ethernet switch using their respective commercial software systems. The voltages used to control the different guides in the differential pumping stages, the quadrupole (Ardara Technologies, US), the ion trap, and the Jordan TOF are generated using commercial power supplies and controlled by LabView.

Arrival-time distributions and mass spectra are acquired using an oscilloscope (LeCroy) that includes an analogue-to-digital converter. A LabView program is used to visualize mass spectra as well as to generate and visualize IR spectra. An IR fragment yield spectrum is obtained by: (1) selecting the signal corresponding to the bare molecules as well as the tagged molecules (*ie.* regions of interest (ROIs)) from the mass spectrum; (2) plotting the ratio between the sum of the integrated areas of the mass peaks of the tagged species divided by the sum of the integrated areas of the mass peaks of the bare ions and tagged ions as a function of the infrared wavenumber. Spectra obtained in this way are used as fingerprints of a particular analyte molecule.

## 3.6. SLIM IMS performance characterization

### 3.6.1 15 cm straight SLIM design

Initial experiments using the newly designed IMS device were performed with a straight SLIM board of 15 cm length, depicted in Figure 3.17. As this was a newly developed technology at the time, the purpose of this step was to get a better understanding of the functioning principles of SLIM IMS.

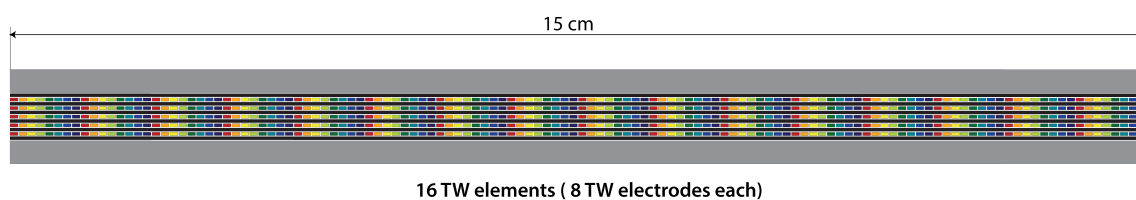


**Figure 3.17:** Display of a straight 15 cm SLIM device composed by 16 TW elements containing 8 TW electrodes each.

### IMS of the protonated Bradykinin

Bradykinin (BK) is a 9-amino acid peptide that is a physiologically and pharmacologically active and known to promote inflammation. It is also often used for ion mobility characterization as it has a high ionization efficiency in positive ion mode and presents

different charge states, each including conformers with slightly different CCSs. Ions were produced by nano-ESI from a solution containing 100  $\mu\text{M}$  BK (Sigma Aldrich) in a 50/50 water methanol mixture. A 3% volume of formic acid was added to favor the formation of protonated species. Ions were accumulated in the hour-glass section of the IFT and released in 100  $\mu\text{s}$  pulses into the IMS region at a frequency of 10Hz. The experiment was conducted at an RF frequency of 880 kHz, and peak-to-peak amplitude of 100V applied to SLIM RF electrodes. A 25V square wave at a speed of 450 m/s was used to propel ions across the mobility separation region, as well as a guard voltage of 30 V to confine the ions to the SLIM track. Ions were detected using a channeltron detector.

The ATD of triply protonated bradykinin obtained using SLIM (Figure 3.18 top panel, blue) contains three features that are distinctive of the  $\text{BK}^{3+}$  ions. Similar features were observed when performing the experiment in our previous drift tube device (Figure 3.18 bottom panel, red). A resolving power of approximately 10 was calculated for the third conformer of  $\text{BK}^{3+}$  of CCS  $\Omega=305\text{\AA}$ ,<sup>17</sup> upon separation in the 15 cm SLIM.

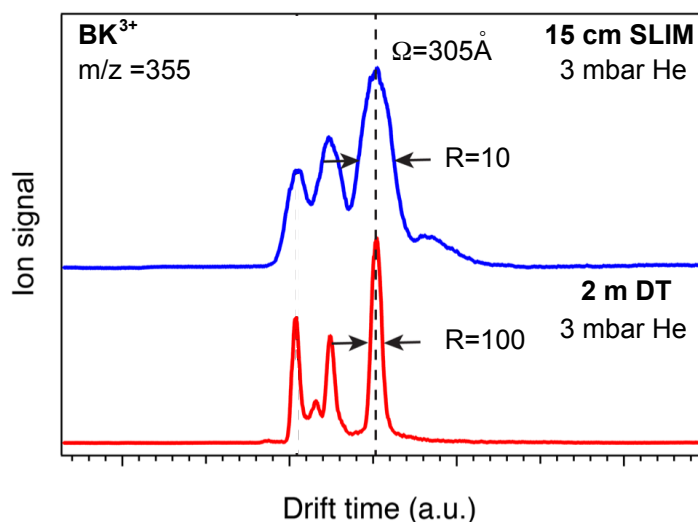
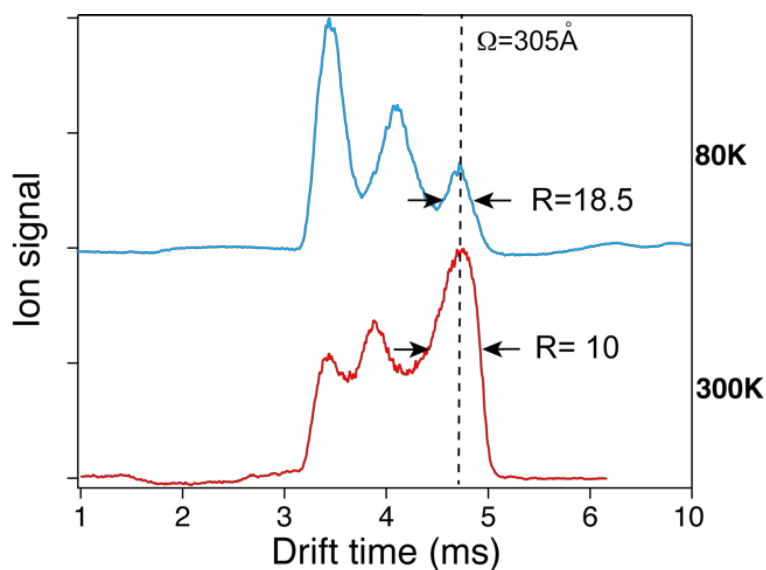


**Figure 3.18:** Arrival time distributions (ATDs) of the triply protonated Bradykinin ions obtained using the 15 cm SLIM device (top panel blue) and obtained using the 2m DT device (bottom panel, red).

## Cryogenic SLIM IMS

Low-temperature ion mobility was first developed to study atomic clusters and transition metals.<sup>18-19</sup> Cold IMS was exclusively implemented using drift tube IMS cooled by either liquid nitrogen or helium. Later developments of the instrumentation enabled the study of biological ions and provided a deeper understanding of the conformational thermodynamics of anhydrous peptides and proteins.<sup>20</sup> Cryogenic temperature ion mobility presents several advantages including an increased resolving power through reduction in diffusional broadening of the ion cloud, as well as the ability to kinetically trap interconverting conformers during the IM measurement.<sup>21-23</sup>

Our cryogenic IMS experiments were performed on  $BK^{3+}$  ions produced by nano-ESI from a solution similar to the one described in the previous section. The SLIM IMS region was maintained at a 1.5 mbar pressure of nitrogen gas and cooled to a temperature of 80 K using the cold head of a single-stage He closed-cycle cryostat, connected to the SLIM copper housing *via* thermal straps. The temperature was controlled by a Lakeshore 350 PI controller and a set of two cartridge heaters placed on each side of the SLIM copper housing. The experiment was conducted at an RF frequency of 880 kHz, and peak-to-peak amplitude of 100 V applied to SLIM RF electrodes. An 18 V square-wave pulse at a speed of 100 m/s was used to propel ions across the low temperature mobility separation region, as well as a guard voltage of 30 V to confine the ions to the SLIM track. While the room-temperature measurement was performed using the same traveling wave voltage and RF amplitude and frequency to ensure similar activation conditions, the speed of the travelling wave was set to lower values. As the buffer gas density is lower at higher temperatures, the TW conditions needed to be adapted to ensure an optimal separation of the different conformers and allow for a realistic comparison of the resolving power at different temperatures. Ions were mass selected by the quadrupole mass filter then detected using a channeltron detector.



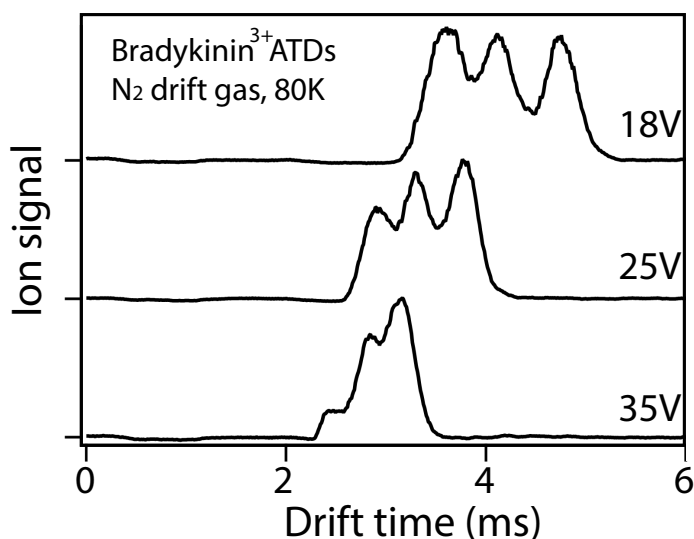
**Figure 3.19:** Comparison between the ATDs of the  $\text{BK}^{3+}$  ions at 80K and at 300K.

Figure 3.19 shows a comparison between the ATDs of the triply protonated Bradykinin ions obtained at 300K and 80K. We observe an increase of the resolving power from the initially calculated 10 at room temperature, to a value of 18.5 at 80K. This corresponds to an increase of the resolving power by a factor of  $\sim 1.85$ , which confirms the previously described relation of  $R_{TW}$  with the temperature  $T$ .<sup>24</sup>

$$R_{TW} \propto \sqrt{\frac{1}{T}} \quad \text{Eq 3.4}$$

Here, the square root of a factor of 3.75 between 80 K and 300 K yields roughly the same value for the improved resolving power at lower temperature as determined experimentally. In addition, we observe a shift in the relative intensities at low temperatures towards the most compact structure, which suggests a change in the population of the different conformers. This indicates that at room temperature, ions in the most compact conformation easily convert to the most elongated one as the average energy of the

molecules becomes comparable to the isomerization barrier. At lower temperatures (80K) the average energy of the system decreases, slowing conformer interconversion. As a result, low-temperature IMS offers a more accurate indication on the actual abundance of the three conformations of the  $\text{BK}^{3+}$  ions produced in the nano-ESI source.



**Figure 3.20:** The TW parameters effect on the population of conformers was assessed by increasing the TW pulse voltage from 18 V (top panel) to 35 V (bottom panel).

The reverse effect can be achieved by increasing the TW pulse voltage, thus activating the  $\text{BK}^{3+}$  ions, which leads to a change in the relative distribution of the conformers as shown in Figure 3.20. While an 18 V TW pulse voltage allows transmission of the most compact form of  $\text{BK}^{3+}$  (top), most of these ions are annealed into the more extended conformations at a TW voltage of 35 V (bottom). It is important to note that, in this case, the shift of the overall ATD towards shorter drift times when going from 18V to 35V reflects the mode in which the TW IMS is operated and not the actual conformation of the ions. At a higher pulse voltage and constant speed, the probability of ions rolling over the wave decreases, as they are transported at the valley of wave, thus the shorter overall drift times and the lower IMS resolution.

### 3.6.2 Serpentine SLIM device

Our second implementation of SLIM TW IMS uses a 15 cm x 15 cm PCB design, depicted in Figure 3.9, featuring a 1.8 m serpentine path and a T-switch at the exit of the SLIM path to enable cycling, thus further increasing the effective drift path.

#### Ion transmission

An important feature of SLIM technology is that it allows for nearly lossless ion transmission. This is crucial, as it has a significant impact on the sensitivity of the instrument, which is an important characteristic when working with biological samples.

To characterize the transmission through this SLIM module as a function of the number of cycles, we used a solution of the peptide GRGDS, which is a standard in ion mobility characterization. The solution was prepared by diluting GRGDS (Sigma Aldrich) in a 50/50 water/methanol mixture to a concentration of 100  $\mu\text{M}$ . A 3% volume of formic acid was added to favor the formation of protonated species. The SLIM module was operated at 3 mbar He pressure at room temperature, an RF frequency of 880 kHz, and an RF amplitude of 100 V. The travelling wave height was set to 30 V and the speed such that the ions were in transmission (surfing) mode. The ions were detected without mass selection using a channeltron detector.

The result, depicted in Figure 3.21, shows a loss of  $\sim 3\%$  per cycle of the ions produced by the nESI. This value was obtained by integrating the area of the mobility peaks after each cycle and was consistent for the 16 cycles of the measurement.

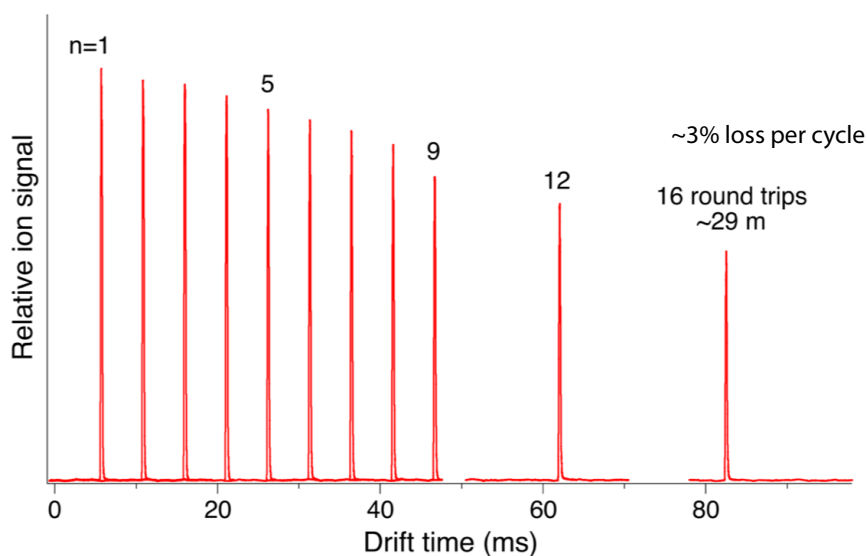


**Figure 3.21:** The ATDs of the GRGDS<sup>2+</sup> ions after different number of cycles (up to 16 round trips) are shown in red.

Although this per-cycle loss is relatively small, the transmission cannot be considered completely lossless, as the SLIM acronym suggests. A possible cause of the loss can be the fact that the ion cloud is composed of ions of various species having a wide range of  $m/z$  values. The SLIM module, being an RF device, has optimal RF parameters for transmission of a specific  $m/z$  window. Thus, the heterogeneity of the species produced by the ESI source may cause the loss in transmission. This does not exclude ion loss due to imperfections and field anomalies in our SLIM module.

## Characterization of the resolving

The single-pass drift length on the serpentine SLIM module is equal to 1.8 m. The T-switch at the exit of the modules allows for either unloading the ions from the IMS region towards the cryogenic trap or routing the ions back to the entrance of the SLIM device to complete another separation cycle. This operation can be repeated until the desired resolving power is achieved. To test the separation performance of the TW serpentine SLIM module, we

used a mixture of two reverse-sequence peptides, GRGDS and SDGRD. These peptides are often used as standards in ion mobility characterization and differ in CCS by  $\sim 2.8\%$  in their doubly protonated form.<sup>25</sup>

The peptide samples were prepared following the protocol described in the previous section. As the SLIM module is based on TW IMS, CCS values cannot be directly extracted from the measured drift times. Instead, we use previously published CCS values of GRGDS<sup>2+</sup> and SDGRG<sup>2+</sup> in He,  $145.6 \text{ \AA}^2$  and  $149.7 \text{ \AA}^2$  respectively.<sup>25</sup> Figure 3.22 (a) shows the ATDs of the peptide mixture after different number of separation cycles on the SLIM module.

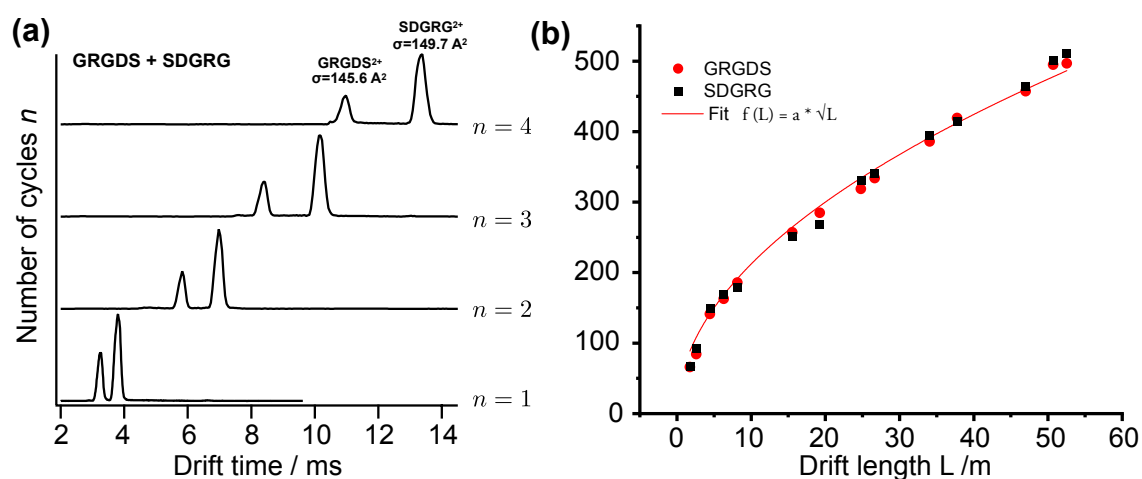


**Figure 3.22:** (a) Arrival time distribution from the mixture of the isomeric peptides GRGDS and SDGRG (doubly protonated form) displayed for different number of separation cycles  $n$ . (b) IMS resolution of the SLIM device as a function of the drift length. The fit function is shown in red where  $a=67$

The lowest panel displays the ATD after a single separation cycle. The peptide pair is already baseline separated, and the result is approximatively equivalent to that achieved by Bowers and coworkers using a 2 m drift tube device (with a resolving power of  $100$ )<sup>25</sup>, as shown in Figure 3.23.

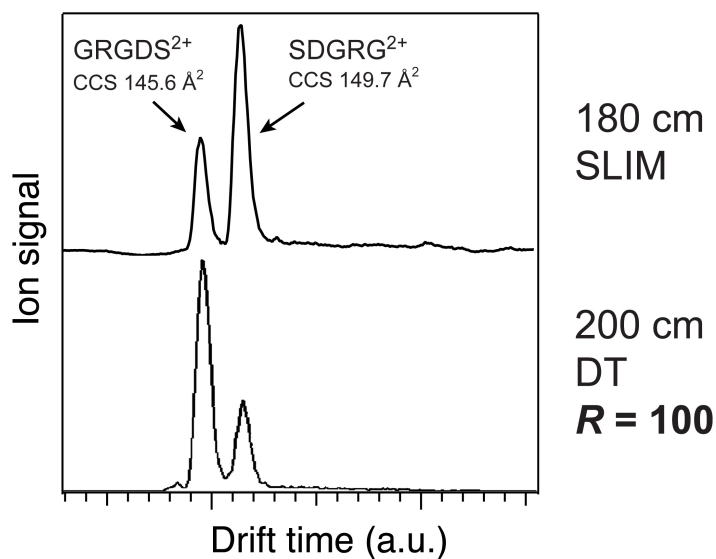


**Figure 3.23:** Arrival time distribution from the mixture of the isomeric peptides GRGDS and SDGRG (doubly protonated form) obtained after a single cycle using the 1.8 m SLIM device (top ATD) and a 2 m drift tube IMS device (bottom ATD) from Reference 29.

By routing the peptide mixture for a higher number of passes, we clearly observe an increased separation of the mobility peaks. Using the previously published CCS values for the two peptides, we calibrate the drift time and quantify the resolution of the device, assuming a linear relation over the small range of CCS considered. Therefore, we use the peak-width definition of the resolution:

$$R = \Omega / \Delta\Omega \quad \text{Eq 3.5}$$

where  $\Omega$  and  $\Delta\Omega$  are the CCS and peak width on the CCS axis, respectively.

Figure 3.22 (b) shows the evolution of the resulting resolution as a function of the drift length. The fit function (red line) is of the form  $f(L) = 67\sqrt{L}$  and confirms the  $\sqrt{L}$

dependence of  $R$ . The instrument reaches a resolution of  $\sim 500$  for the considered pair of peptides after 28 cycles, which corresponds to  $\sim 50$  m drift length. The number of cycles can further be increased but comes at the cost of the duty cycle of the experiment, as drift times would exceed the 100 ms period defined by the 10 Hz repetition rate. Two practical limitations to the maximum number of separation cycles are the previously mentioned 3% loss per cycle, as well as the peak capacity of the 15x15 cm board size. For more complex samples containing species with a wider range of mobilities, different analytes begin to overlap when being separated in the IMS region, as they spatially extend over the entire board, thus limiting the number of possible separation cycles. These two limitations have been addressed in the development of our second-generation instrument (see Chapter 7).

## The 1.8 m serpentine SLIM vs the 2 m drift tube

The aim of this work is to further develop the combination of IMS with cryogenic IR spectroscopy for the analysis of biomolecules. While the combination of these methods has proven to be successful for the identification of glycan molecules, its limitation lies within the achievable resolution of the IMS separation prior to spectroscopic interrogation of the charged biomolecules.

The implementation of a SLIM-based IMS module has proven to be ideal for separating isomeric species, thus providing isomer-specific glycan spectroscopic fingerprints well suited for identification. In this section, we compare results from the analysis of a set of disaccharides, obtained previously in our laboratory using a 2 m drift tube, with those from our 1.8 m cyclic serpentine SLIM module. The study includes arrival time distributions as well as IR spectra of the considered analytes.

All disaccharides used in this experiment were purchased from Carbosynth Limited (UK) or Dextra Laboratories (UK) and were processed using the same protocol. The disaccharide powder was diluted in a 50/50 water methanol mixture to a concentration of  $\sim 100$   $\mu\text{M}$ . The measurements were made on sodiated species, and we thus added a 1.5 equivalent of

NaCl to favor their formation. Ions were produced by nESI then accumulated in the hourglass region of the IFT prior to being injected as 120  $\mu$ s long pulses into the SLIM module.

Figure 3.24 shows the disaccharides, using the SNFG symbol nomenclature, as well as their ATDs recorded using the 2 m drift tube (first column) and using the SLIM module (second column). Both IMS experiments were performed at 3 mbar He pressure and at voltages set for optimal separation.

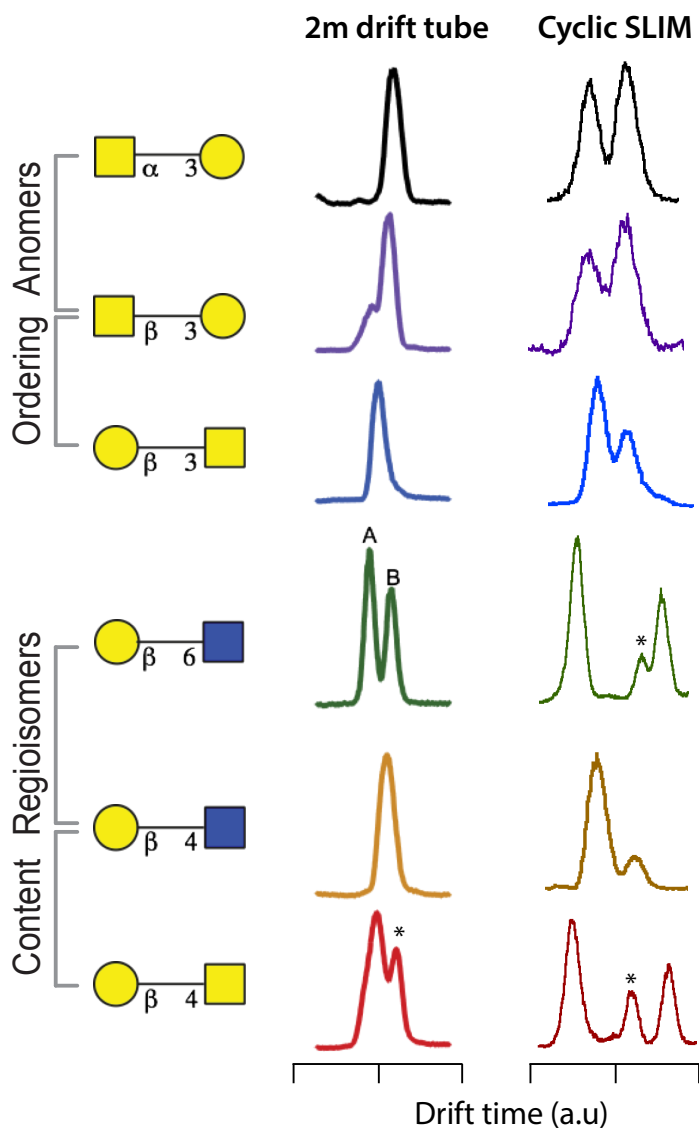


**Figure 3.24:** Comparison of the 2 m drift tube and the cyclic SLIM resolution. The signals marked with an asterisk are due to impurities with slightly different but unresolved  $m/z$ .

While using the 2 m DT we only observe a single peak in the ATDs (except for glycan (d)), we can clearly distinguish two mobility peaks for each disaccharide when separating with SLIM. This points towards the existence of multiple conformers per disaccharide, which

could be attributed to the fact that all reducing glycans exist naturally in two anomeric forms defined by the orientation of the hydroxyl group at the reducing end (*i.e.*  $\alpha$  or  $\beta$ ). This assumption was further investigated and will be addressed in more detail in Chapter 6 of this thesis.

Figure 3.25 shows the ATDs and IR spectra of the singly sodiated  $\text{Gal}\beta(1-4)\text{GlcNac}$  disaccharide. The mobility signals separated using SLIM were isolated to record their respective IR spectra (red and blue).

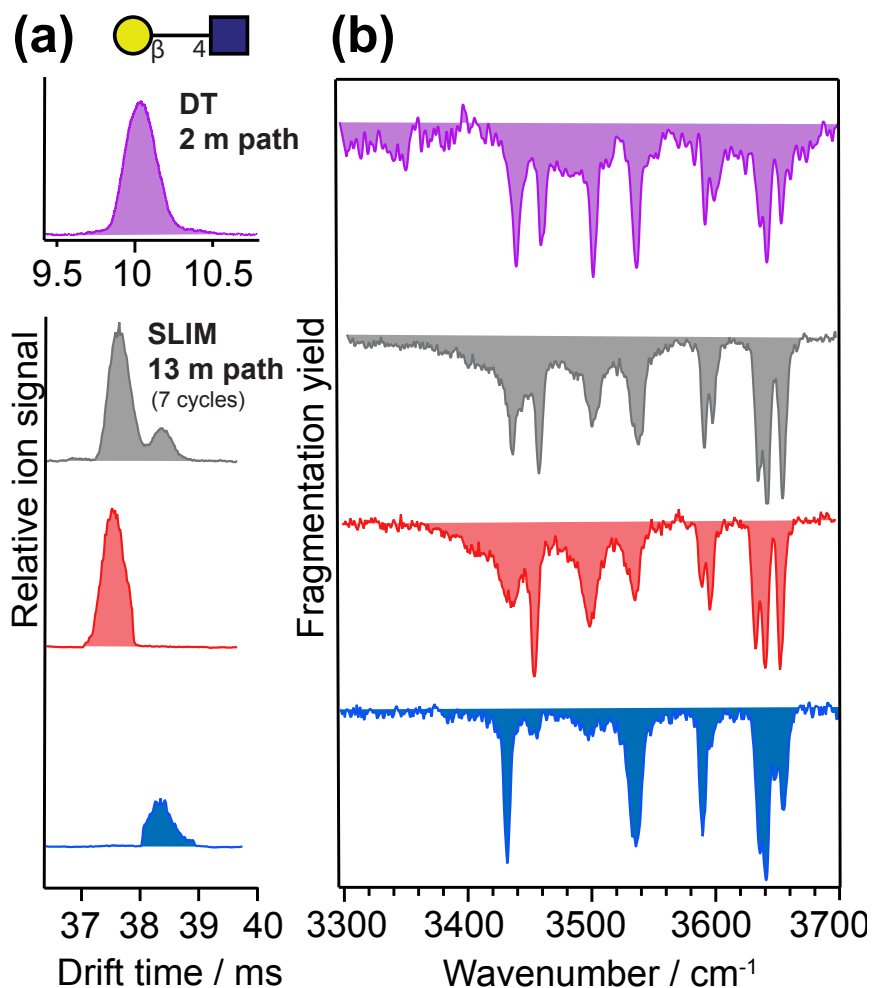


**Figure 3.25:** Comparison of data from the 2 m drift tube and the cyclic SLIM instrument. (a) ATD of the sodiated disaccharide  $\text{Gal}\beta(1-4)\text{GlcNac}$  obtained using the 2 m DT (top, purple) and that obtained using the cyclic SLIM device (second from top, grey). The two different signals separated

by SLIM were selected for spectroscopic interrogation. (b) IR spectra of the non-separated species using the 2 m DT (top purple), and the cyclic SLIM device (grey). Spectra obtained after mobility selection of the first mobility peak (red) and the second mobility peak (blue).

The IR spectra are recorded in the wavenumber range between  $3200\text{ cm}^{-1}$  to  $3800\text{ cm}^{-1}$ , which corresponds to OH and NH stretching vibrations. While absorption bands above  $\sim 3580\text{ cm}^{-1}$  can be assigned to weakly hydrogen-bonded or free-OH oscillators, strongly hydrogen-bonded OH and NH oscillators are expected to appear at lower wavenumbers.

The spectrum previously measured using the DT instrument<sup>26</sup> was acquired using  $\text{D}_2$  as messenger tag and at a trap temperature of  $\sim 13\text{ K}$ , whereas the acquisition of the spectrum using the newly designed SLIM apparatus was performed using  $\text{N}_2$  as messenger tag at a trap temperature of  $40\text{ K}$ .

Except for slight differences in observed band widths, the spectra appear to be virtually identical. This suggests that the  $\text{D}_2$  or  $\text{N}_2$  tag molecules bind to the sodium cation rather than the molecule, and thus the vibrational bands of the disaccharide are unaffected. The narrower bandwidths in the spectra from the  $\text{D}_2$  tagging experiment can be attributed to the lower trap temperature. In addition, the weaker interaction of the  $\text{D}_2$  molecule with the analytes due to its different polarizability, might be responsible for other small differences when compared to the  $\text{N}_2$  tag, such as minor shifts in band positions and intensities. To ensure the robustness of the method, the IR spectra were acquired months apart on the same instrument as well as on different instruments, with identical results. Since IR spectra are sensitive to the slightest structural differences, we performed these experiments under conditions where different molecular conformers should be annealed to avoid the presence of kinetically trapped structures. Hence, experiments are always performed on the most stable set of gas-phase structures, guaranteeing the reproducibility of the results. Since the spectra obtained at  $14\text{ K}$  and at  $40\text{ K}$  are almost identical,  $\text{N}_2$  tagging appears to be the preferable method for the spectroscopic interrogation, as it is less demanding from an experimental point of view.

Using the SLIM IMS device for separation, we observe two mobility peaks (red and blue) after 7 separation cycles. At this number of cycles, the resolution of the IMS module is of  $\sim 230$  which indicates that the two separated species differ by only 0.5% in their CCS. The similarity in the species CCSs further strengthens the hypothesis that they represent the  $\alpha$  and  $\beta$  anomers. By recording the IR fingerprint of each mobility feature separately we were able to decompose the initially obtained IR spectrum of Gal  $\beta(1-4)$  GlcNac into two separate spectra. Although generally similar, the spectra exhibit slightly different band positions and intensities, which reflect the differences in the intramolecular hydrogen-bonding network of the two isomeric forms. In Chapter 5, we demonstrate that these spectra can be used to identify different disaccharides from a mixture of unknowns.

# References

1. Antoine Masson, M. Z. K., Marta A. S. Perez, Matthew S. Glover, U. Rothlisberger, David E. Clemmer, and Thomas R. Rizzo, Infrared Spectroscopy of Mobility-Selected H<sup>+</sup>-Gly-Pro-Gly-Gly (GPGG). *J. Am. Soc. Mass Spectrom.* **2015**, *26* (9), 1444–1454.
2. Pauly, M.; Sroka, M.; Reiss, J.; Rinke, G.; Albarghash, A.; Vogelgesang, R.; Hahne, H.; Kuster, B.; Sesterhenn, J.; Kern, K.; Rauschenbach, S., A hydrodynamically optimized nano-electrospray ionization source and vacuum interface. *Analyst* **2014**, *139* (8), 1856-67.
3. Ibrahim, Y. M.; Shvartsburg, A. A.; Smith, R. D.; Belov, M. E., Ultrasensitive identification of localization variants of modified peptides using ion mobility spectrometry. *Anal Chem* **2011**, *83* (14), 5617-23.
4. Lorenz, U. J.; Rizzo, T. R., Planar multipole ion trap/time-of-flight mass spectrometer. *Anal Chem* **2011**, *83* (20), 7895-901.
5. Earnshaw, S., Transactions of the Cambridge Philosophical Society. **1842**, *7*, 97.
6. Jackson, J. D., Classical Electrodynamics 3rd ed. *John Wiley & Sons* **1998**.
7. Chen, T. C.; Fillmore, T. L.; Prost, S. A.; Moore, R. J.; Ibrahim, Y. M.; Smith, R. D., Orthogonal Injection Ion Funnel Interface Providing Enhanced Performance for Selected Reaction Monitoring-Triple Quadrupole Mass Spectrometry. *Analytical Chemistry* **2015**, *87* (14), 7326-31.
8. Schaffer, S. A.; Tang, K.; Anderson, G. A.; Prior, D. C.; Udseth, H. R.; Smith, R. D., A novel ion funnel for focusing ions at elevated pressure using electrospray ionization mass spectrometry. *Rapid Communications in Mass Spectrometry* **1997**, *11* (16), 1813-1817.
9. Kim, T.; Tolmachev, A. V.; Harkewicz, R.; Prior, D. C.; Anderson, G.; Udseth, H. R.; Smith, R. D., Design and implementation of a new electrodynamic ion funnel. *Anal Chem* **2000**, *72* (10), 2247-55.
10. Kelly, R. T.; Tolmachev, A. V.; Page, J. S.; Tang, K.; Smith, R. D., The ion funnel: theory, implementations, and applications. *Mass Spectrom Rev* **2010**, *29* (2), 294-312.
11. Gordon, S. D. S.; Osterwalder, A., 3D-Printed Beam Splitter for Polar Neutral Molecules. *Physical Review Applied* **2017**, *7* (4).

12. Paul, W.; Reinhard, H. P.; von Zahn, U., Das elektrische Massenfilter als Massenspektrometer und Isotopentrenner. *Zeitschrift für Physik* **1958**, *152* (2), 143-182.
13. Miller, P. E.; Denton, M. B., The quadrupole mass filter: Basic operating concepts. *Journal of Chemical Education* **1986**, *63* (7).
14. Appelhans, A. D.; Dahl, D. A., SIMION ion optics simulations at atmospheric pressure. *International journal of mass spectrometry* **2005**, *244* (1), 1-14.
15. Debatin, M.; Kröner, M.; Mikosch, J.; Trippel, S.; Morrison, N.; Reetz-Lamour, M.; Woias, P.; Wester, R.; Weidemüller, M., Planar multipole ion trap. *Physical Review A* **2008**, *77* (3).
16. C. G. Herbert, R. A. W. J., Mass Spectrometry Basics. *CRC Press, Boca Raton* **2003**.
17. Pierson, N. A.; Chen, L.; Valentine, S. J.; Russell, D. H.; Clemmer, D. E., Number of solution states of bradykinin from ion mobility and mass spectrometry measurements. *J Am Chem Soc* **2011**, *133* (35), 13810-3.
18. Jarrold, M. F.; Bower, J. E.; Creegan, K., Chemistry of semiconductor clusters: A study of the reactions of size selected Si<sub>n</sub> (n=3–24) with C<sub>2</sub>H<sub>4</sub> using selected ion drift tube techniques. *The Journal of Chemical Physics* **1989**, *90* (7), 3615-3628.
19. Bowers, P. R. K. M. T., A hybrid double-focusing mass spectrometer—High-pressure drift reaction cell to study thermal energy reactions of mass-selected ions. *J Am Soc Mass Spectrom* **1990**, *1* (3), 197–207.
20. von Helden, G.; Wyttenbach, T.; Bowers, M. T., Inclusion of a MALDI ion source in the ion chromatography technique: conformational information on polymer and biomolecular ions. *International Journal of Mass Spectrometry and Ion Processes* **1995**, *146-147*, 349-364.
21. Gidden, J.; Bushnell, J. E.; Bowers, M. T., Gas-phase conformations and folding energetics of oligonucleotides: dTG- and dGT. *J Am Chem Soc* **2001**, *123* (23), 5610-1.
22. Silveira, J. A.; Servage, K. A.; Gamage, C. M.; Russell, D. H., Cryogenic ion mobility-mass spectrometry captures hydrated ions produced during electrospray ionization. *J Phys Chem A* **2013**, *117* (5), 953-61.

23. J. C. May, D. H. R., A Mass-Selective Variable-Temperature Drift Tube Ion Mobility-Mass Spectrometer for Temperature Dependent Ion Mobility Studies. *J. Am. Soc. Mass Spectrom.* **2011**, *22* (7).
24. Shvartsburg, A. A.; Smith, R. D., Fundamentals of traveling wave ion mobility spectrometry. *Anal Chem* **2008**, *80* (24), 9689-99.
25. Kemper, P. R.; Dupuis, N. F.; Bowers, M. T., A new, higher resolution, ion mobility mass spectrometer. *International journal of mass spectrometry* **2009**, *287* (1-3), 46-57.
26. Masellis, C.; Khanal, N.; Kamrath, M. Z.; Clemmer, D. E.; Rizzo, T. R., Cryogenic Vibrational Spectroscopy Provides Unique Fingerprints for Glycan Identification. *J Am Soc Mass Spectrom* **2017**, *28* (10), 2217-2222.

## 4. Identification of disaccharide isomers: IR-IR vs. IMS-CIS\*

Isomer-specific analysis of biomolecules poses a challenge to conventional mass-spectrometry-based techniques. Double-resonance spectroscopic schemes, in combination with cryogenic ion traps, offer a powerful tool to address these analytical challenges. However, the implementation of such schemes for isomer identification are complicated and the measurements are time-consuming, inhibiting the adoption of this technique for analytical purposes. In this chapter we present an alternative approach for the analysis of isomeric biomolecules based on the combination of ion mobility spectrometry (IMS) with messenger tagging cryogenic IR spectroscopy. Isomeric species are separated by IMS prior to selective IR interrogation, thus producing isomer-specific IR fingerprints. The main limiting factor to this approach has been the relatively low IMS resolution of the available separation technologies. Nevertheless, recently developed SLIM technology offers the possibility to perform IM separation over extended path lengths in a relatively compact device. This gives access to ultrahigh-resolution separation, which when combined with cryogenic spectroscopic schemes, produces mobility-resolved spectra. In this chapter we demonstrate the power of this approach by comparing the mobility-resolved IR spectra of a disaccharide molecule, to those acquired using IR-IR double resonance.

---

\* This chapter is largely based on reference 1. Warnke, S.; Ben Faleh, A.; Pellegrinelli, R. P.; Yalovenko, N.; Rizzo, T. R., Combining ultra-high resolution ion mobility spectrometry with cryogenic IR spectroscopy for the study of biomolecular ions. *Faraday Discuss* **2019**, *217* (0), 114-125. The content and figures were adapted with permission from the Royal Society of Chemistry.

## 4.1. Introduction

The development of atmospheric pressure ionization (API) sources such as electrospray or MALDI over the last three decades has opened exciting new directions in molecular ion spectroscopy.<sup>2-9</sup> Molecules of virtually any size can be transferred into the gas phase, where action-spectroscopic schemes in the IR or UV can reveal details about their structure and intramolecular interactions, aided by quantum-chemical calculations. While vibrational spectra of relatively small molecular ions can be well resolved even at room temperature<sup>10-11</sup>, spectral congestion from thermal inhomogeneous broadening and conformational heterogeneity complicates interpretation of spectra for larger molecules. Both effects gain in importance as the size of the molecule, and hence the number of vibrational degrees of freedom, increases. The former can be largely eliminated by cooling molecular ions to their vibrational ground state, which is most commonly achieved using collisions with a buffer gas in cryogenic multipole traps.<sup>5-6, 9, 12-14</sup> When used in combination with either IR-UV photofragment spectroscopy<sup>9, 13-14</sup> or messenger-tagging spectroscopy<sup>6, 15-17</sup>, one can generate greatly simplified, linear IR spectra, which facilitates the determination of molecular structure by comparison to calculations. Spectral congestion arising from conformational heterogeneity is more difficult to eliminate, however. Two approaches are commonly employed. By simultaneously requiring molecules to satisfy two or more resonance conditions, one can often separate overlapping spectra. As an example, by fixing a UV probe laser on a conformer-specific electronic transition and then scanning an IR pump laser that arrives prior to the probe, one can induce a "dip" in the UV-induced fragment signal when its wavelength is in resonance with a vibrational transition in the probed conformer.<sup>9, 18-19</sup> In this case a UV chromophore and a conformer-resolved electronic spectrum are required, which limits the general applicability of this approach. Alternatively, IR-IR hole-burning on messenger-tagged molecules can achieve similar results while being more general<sup>15</sup>, however this still requires the presence of resolved conformer-specific transitions. One could envision higher-order multi-color schemes in the IR or the UV, but the necessity to identify

conformer-specific transitions persists. This can be extremely time consuming and, in many cases, simply impossible.

Another approach is to physically separate molecules of different conformations or isomeric forms prior to spectroscopic investigation using, for example, ion mobility spectrometry (IMS).<sup>20</sup> The technique makes use of the difference in the mobility of isomers or conformers when they drift through an inert buffer gas under the influence of an electric field. In addition to reducing the conformational complexity of an ensemble of ions, IMS can determine an orientationally-averaged collision cross section (CCS), which can then serve as a filter for calculated structures, greatly simplifying the conformational search.<sup>21-24</sup> Ion mobility spectrometry has gained popularity in analytical applications since IMS-MS instruments became commercially available about a decade ago.<sup>25</sup> In different IMS variants, ions of a particular mobility can either be continuously filtered using, for example, differential IMS or FAIMS<sup>26-30</sup>, or they can be selected in a pulsed fashion after separation in time as occurs, for example, in drift tube (DT) IMS<sup>31-33</sup>, where a constant electric field propels the ions through the drift region. Recent reports using IMS-MS as a conformational pre-filter for spectroscopic investigation have applied this approach to study small drug molecules<sup>11</sup>, carbohydrates<sup>34-36</sup>, peptides and proteins<sup>16, 37-40</sup>, and even weakly bound peptide aggregates or clusters<sup>41-42</sup>.

How does the combination of IMS-MS with spectroscopic methods compare to double-resonance spectroscopic schemes in terms of isomer selectivity? While spectroscopic approaches can have extremely high sensitivity to the slightest structural differences, they rely on one's ability to find and resolve transitions that are characteristic of a particular conformer. For an IMS technique to be similarly sensitive to different isomers of the same molecule, its resolving power would need to be sufficiently high to distinguish minute differences in CCS. While the resolving power of linear IMS instruments is limited by constraints in the use of high voltages and instrument size, new technological developments in travelling wave (TW) IMS using so-called structures for lossless ion manipulation (SLIM)

have emerged as a promising alternative.<sup>43-44</sup> In its most recent implementation, ions can drift in a nearly lossless manner inside travelling-wave electric potentials produced by mirrored pairs of electrodes on planar printed circuit boards (PCBs), separated by a gap of a few millimeters. Using SLIM, ions can be directed around corners, enabling the entire two-dimensional space of the SLIM device to be used for IM separation. This poses a tremendous advantage over previous IM techniques in terms of resolving power, since it is approximately proportional to the square root of the drift-path length.<sup>45</sup> Moreover, the drift length can be further extended to almost arbitrary length by cycling ions repeatedly through the same SLIM structure until the desired resolving power is reached.<sup>46</sup>

Here we explore the capability of SLIM-based IMS for isomer selectivity in combination with cryogenic, messenger-tagging IR spectroscopy. To demonstrate the promise of this approach, we directly compare it with IR-IR double resonance spectroscopy on the same disaccharide molecules. We expect the rapidly evolving techniques of ultra-high resolution IMS to soon be able to separate molecules with the most miniscule differences in molecular structure, which can then be probed by cryogenic messenger-tagging spectroscopy to provide their fingerprints for identification and structural analysis.

## 4.2. Experimental Methods

### 4.2.1 Sample preparation

The disaccharide Gal $\beta$ (1-4)GlcNAc was purchased from Dextra UK and used without further purification. Solvents were purchased from Sigma-Aldrich. For (nano) electrospray ionization, samples were diluted with water/methanol v/v 50/50 to yield a concentration of 100  $\mu$ M. To enhance the formation of singly sodiated disaccharides, 1.5 equivalents of NaCl were added.

### 4.2.2 IR-IR double-resonance messenger-tagging spectroscopy

Experiments were performed on home-built tandem quadrupole instrument equipped with a cryogenically cooled octupole ion trap to allow for messenger-tagging spectroscopy.<sup>47</sup> A detailed description of the instrument can be found elsewhere.<sup>48</sup> Briefly, ions are electrosprayed into the instrument using commercially available nano-electrospray emitters (Thermo Fisher) and transferred into high vacuum. Here, they are  $m/z$  selected by a quadrupole mass filter before being trapped and cooled by collisions with helium buffer gas inside an octupole ion trap, which is maintained at a temperature below 5 K using a closed-cycle helium cryostat. Helium atoms condense onto the molecular ions due to their low internal temperature. The contents of the ion trap can be analyzed using a second quadrupole mass filter and a channeltron ion detector. To acquire an IR vibrational spectrum, the helium-tagged ions are irradiated with light from a pulsed OPO laser system. When the light is resonant with a vibrational transition, the absorption of a single photon by the molecule provides enough energy to dissociate the helium-ion complex, which results in a change in mass. We then generate the IR spectrum by monitoring the wavelength-dependent ion signal of the singly helium-tagged ions. To achieve conformer selectivity, we first use an IR pulse from a second OPO at a fixed wavelength corresponding to a conformer-specific IR transition in the molecule to deplete the helium-tagged ions corresponding to this particular conformation from the ensemble. Scanning the wavelength of the second laser pulse then results in an IR spectrum of the remaining conformations. This so-called IR-IR hole-burning spectroscopic scheme<sup>15</sup> is applied to various absorption bands to sample all the isomers present.

### 4.2.3 Ion-mobility pre-selection for isomer-selective messenger-tagging spectroscopy

Mobility-selective IR spectroscopic experiments were performed on the instrument described in Chapter 3. Briefly, ions are electrosprayed and transferred into the instrument where they are accumulated inside the hour-glass section of a dual ion funnel trap.<sup>49</sup> From

there, packets of ions are injected into the IMS region, where they are separated based on their size and shape. Subsequently,  $m/z$  selection occurs in a quadrupole mass filter. So-called arrival time distributions (ATDs) can be acquired by monitoring the drift time of  $m/z$  selected ions on a channeltron detector. Alternatively, size- and  $m/z$ -selected species can be investigated spectroscopically using a messenger-tagging spectroscopic scheme.<sup>47</sup> For this, ions are injected into a planar ion trap<sup>16</sup> held at a temperature of 40 K using a helium cryostat, where they are trapped and cooled by collisions with a He/N<sub>2</sub> (90/10) buffer gas mixture. Nitrogen molecules condense on the internally cold ions, which can be observed as a shift in mass of +28 u in a subsequent time-of-flight (TOF) analysis. In the case of the here-investigated disaccharide ions, mainly singly tagged ions are observed. To obtain IR spectra, we irradiate the nitrogen-tagged ions with an OPO laser pulse (5 mJ - 10 mJ) and monitor the wavelength dependent loss of N<sub>2</sub> tag molecules as a shift in the TOF mass spectrum.

High-resolution ion mobility separation is achieved using so-called structures for lossless ion manipulation (SLIM)<sup>43</sup>, which employs electrodes on printed circuit boards (PCBs) to generate travelling wave (TW) electric potentials that propel the ions forward. We implemented this technique using a 15 cm x 15 cm SLIM IMS device, featuring a single-pass pathlength  $L$  of 1.8 m, following a previously published electrode design.<sup>43</sup> To increase IM resolution, ions can be cycled through the same SLIM structure multiple times. Typical IMS parameters were: RF frequency 800 kHz; TW amplitude 27 V; TW speed 600 m/s; He buffer gas pressure 3 mbar.

## 4.3. Results and Discussion

### Ion-mobility selective IR spectroscopy

To date, ion mobility spectrometry (IMS) has been considered a low-resolution technique, and with commercial instruments featuring IMS resolutions typically well below 100, isomers need to differ in their size by a few percent for them to be distinguishable. Cyclic

IMS instruments in which ions pass the same drift region multiple times are a promising approach to increase the resolving power while maintaining a reasonable size of the instrument. The recently developed structures for lossless ion manipulation (SLIM) allows for the straightforward implementation of cyclic IMS.<sup>46</sup> As demonstrated in Figure 3.22 of Chapter 3, ions that complete a cycle on the serpentine drift path of length  $L$  of the SLIM ion mobility region of our new instrument can be either sent further downstream towards the cryogenic ion trap or they can be routed back to the beginning of the drift section to complete another IM separation cycle until the desired resolving power is reached.

Our focus here lies on the preparation of conformer-pure ion ensembles for spectroscopic investigation. We test this multi-dimensional IMS-MS-IR spectroscopic approach on carbohydrates - a class of biomolecules that poses a particular challenge to established analytical methods because of their immense structural complexity resulting from various types of isomerism.<sup>50</sup> An IMS arrival time distribution (ATD) of the singly sodiated disaccharide Gal $\beta$ (1-4)GlcNAc is depicted in Figure 4.1(top). After a 13 m drift path (i.e., seven SLIM cycles), we separate two distinct conformations of this molecule. Since we start with an isomerically pure sample, these two species cannot result from different linkage positions or isomerization of the glycosidic bond. However, different drift times can be a result of multiple stable conformations of the monosaccharide ring structures, different positions of the sodium ion on the molecule, or the difference that results from the C1-OH of the reducing end being in axial or equatorial configuration with respect to the cyclic structure of the first monosaccharide subunit. These so-called  $\alpha$  and  $\beta$  anomers at the reducing end interconvert in solution through mutarotation of the C1-OH in a ring-opening event and have recently been suggested to be responsible for multiple IMS features of a range of glycans studied with an ultra-high resolution SLIM IMS instrument.<sup>51</sup> The separation of the two observed species in our disaccharide sample required seven IMS cycles, at which our instrument features a resolving power of approximately 230 (see Figure 3.22 of Chapter 3). This translates into a difference in collisional cross section (CCS) of  $\sim 0.5\%$  between the almost baseline-separated ions. The difference in orientation of a single OH

group that distinguishes two anomers would result in a change in CCS consistent with what we measure. After IM separation, ions of a particular mobility can be selected by electrostatically deflecting the unwanted ions as shown in the middle and bottom traces of Figure 4.1. We then transfer either ion packet into the cryogenic ion trap, where their vibrational spectrum is measured.

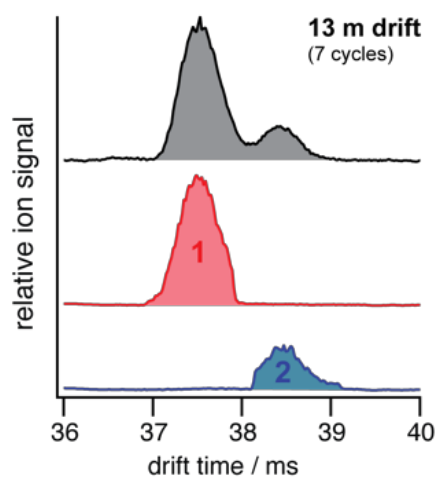


**Figure 4.1:** (Top) Ion mobility arrival time distribution (ATD) of the sodiated disaccharide Gal $\beta$ (1-4)GlcNAc after seven cycles of mobility separation. The portions selected for further spectroscopic analysis are displayed in red (species 1) and blue (species 2), respectively.

The large number of OH and NH oscillators in carbohydrate molecules provide excellent structural probes. We thus focus on the wavenumber range between 3300  $\text{cm}^{-1}$  and 3700  $\text{cm}^{-1}$ , where the corresponding stretching bands are expected, as shown in Figure 4.2. For both species 1 and 2 (red and blue, respectively), we find five of the eight expected absorption bands in the region of 3580  $\text{cm}^{-1}$  and above, in which free or weakly hydrogen-bonded OH groups are expected.<sup>52</sup> Vibrational bands in the lower wavenumber range are considered to originate from strongly hydrogen-bonded OH and NH oscillators.<sup>52</sup> It is noteworthy that both 1 and 2 feature unique bands that cannot be found in the spectrum of the other, and hence are characteristic for their respective isomeric structures. This observation alone illustrates the power of ion-mobility isomer pre-selection for spectroscopic studies. When no ion-mobility separation is applied prior spectroscopic

analysis of the disaccharide, the spectrum in the upper panel (grey) is obtained. From this spectrum alone, it is not evident that two distinct species are present. To emphasize this, a linear combination at a ratio 4/1 of spectra 1 and 2 is displayed (purple) below the spectrum of the non-IMS selected species in Figure 4.2. This synthetic mixture is virtually identical with the experimentally obtained spectrum, which is evident by visual comparison as well as by the almost featureless difference spectrum in Figure 4.2 (in grey) obtained by subtracting the synthetic spectrum from the isomer-unresolved spectrum.

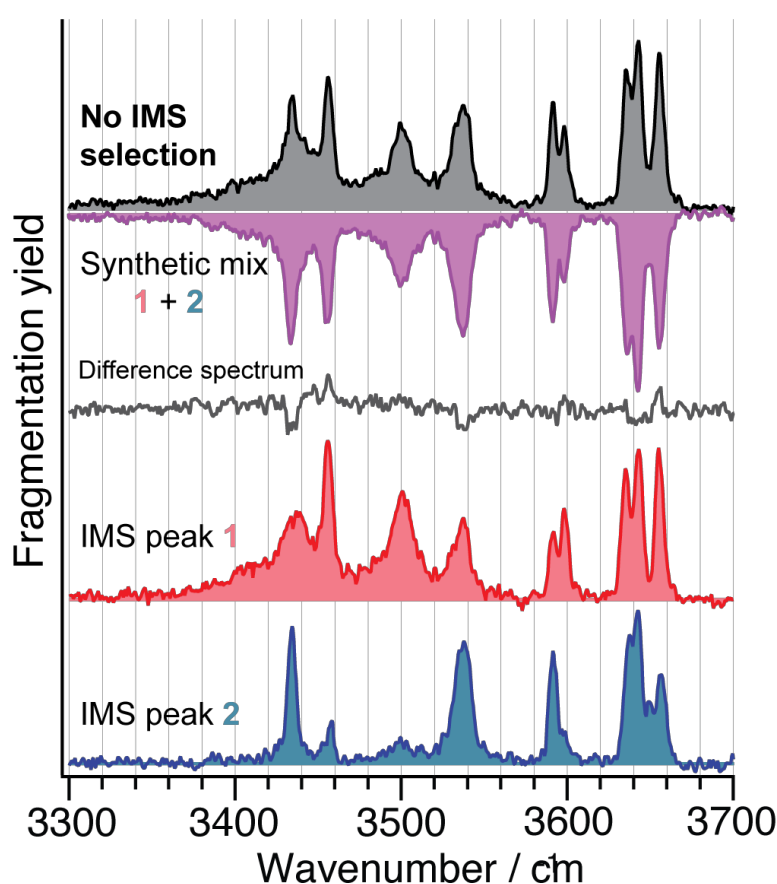


**Figure 4.2:** IR spectra of the nitrogen-tagged disaccharide Gal $\beta$ (1-4)GlcNAc at 40 K when no ion-mobility separation is applied (top, grey) and after ion-mobility separation and selection of the first (red) and second (blue) drift peak (compare Figure 4.1). Adding the spectra of species 1 and 2 in a 4 : 1 ratio yields the synthetic mixture displayed in pink (2nd from top), and subtraction from the conformer unresolved spectrum yields the difference spectrum displayed in grey for comparison.

### 4.3.1 IR-IR double resonance spectroscopy

The conformer-selective messenger-tagging IR-IR double-resonance technique was first developed for cold neutral molecules in supersonic jet experiments<sup>53</sup> but quickly found application for ionized species.<sup>15</sup> It presents a more generally applicable alternative to IR-UV spectroscopic schemes, which require a UV chromophore to be present in the molecule. Here we apply an IR-IR hole burning double resonance spectroscopic scheme<sup>15</sup>, using a previously described instrument that allows to perform helium-tagging spectroscopic experiments on  $m/z$ -selected ions at temperatures just below 5 K.

The resulting IR spectra of two different conformers of the sodiated disaccharide Gal $\beta$ (1-4)GlcNAc are depicted in Figure 4.3 as downward-pointing depletion signals of the singly tagged ions. The pump laser was fixed at 3536  $\text{cm}^{-1}$  to acquire the upper spectrum (red) and at 3498  $\text{cm}^{-1}$  for the lower spectrum (blue). Also here, the spectra exhibit distinct features that are characteristic for the probed isomers, and the number of observed absorption bands is

consistent with the total of eight OH and NH oscillators present in the molecule. Despite having fixed the pump wavenumber on every resolved absorption signal (data not shown), we only find the two presented spectra that differ from one another. These are likely a result of the two anomeric forms of the disaccharide that are expected to coexist in solution and in the gas phase.

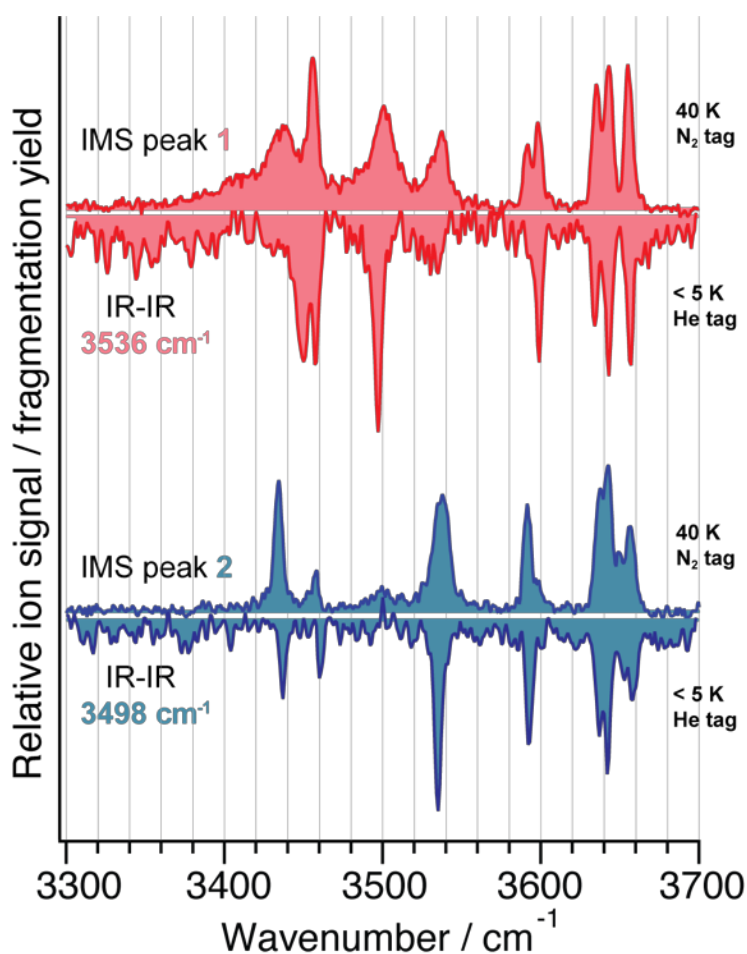


**Figure 4.3:** IR spectra of two conformers of Gal $\beta$ (1-4)GlcNAc acquired with the IR-IR double resonance method (downward pointing) with the pump laser fixed at 3536  $\text{cm}^{-1}$  (red) and at 3498  $\text{cm}^{-1}$  (blue), respectively. The spectra of the ion-mobility separated species 1 and 2 (upward pointing) are displayed for comparison in red and blue, respectively.

In Figure 4.3 the spectra obtained from the double resonance experiments are directly compared to those obtained after ion-mobility separation. Upon visual inspection one finds many similarities between the spectra obtained through the two different methods. Most strikingly, the bands observed above 3600  $\text{cm}^{-1}$ , corresponding to reasonably free OH oscillators<sup>52</sup>, are conserved in their peak positions and intensities. For lower wavenumbers, where hydrogen-bonded oscillators are probed, absorption bands of the mobility-selected ions can be slightly shifted or broadened with respect to those measured using IR-IR double resonance. This is attributed to the higher trap temperature of 40 K in the IMS method

versus a temperature of  $\sim 5\text{K}$  in the double-resonance experiments and the different tag molecules used in the experiments. Nitrogen, which used as a tag for the mobility-separated species, has a polarizability that exceeds that of helium by a factor of about nine<sup>54</sup> and will therefore have stronger charge-induced dipole interaction with the molecule than the helium tag. As a consequence, nitrogen tags will have a more prominent structure-disturbing effect than helium tags as previously observed for small molecules and clusters.<sup>55-</sup>  
<sup>56</sup> As the molecules under investigation get larger, the effect of a single tag molecule on the analyte structure will be less pronounced, and the overall good agreement of the spectra acquired with the two different methods justifies the use of nitrogen tagging at higher temperature.

The key difference between ion-mobility isomer pre-selection and double-resonance spectroscopic simplification is in the generality and ease of implementation of the former. For the latter to be effective, an IR spectrum with well-resolved isomer-specific transitions is required. For larger molecules this can be challenging, since the vibrational degrees of freedom quickly increase with the molecular size. On the other hand, mobility pre-selection can only help to simplify an ensemble of conformers if the potentially miniscule size difference between two species can be resolved in the experiment. With the advent of cyclic travelling-wave ion-mobility methods such as SLIM, the resolution-defining drift length can be extended into the kilometer range.<sup>46</sup> Considering the experimental parameters used here, a one-kilometer drift path would result in a resolving power of about 2000, enough to separate two ions that differ in their collision cross section by only 0.05 %. We are in the process of constructing an instrument with such capabilities. Finally, one must consider the time that is needed for analysis of all components in the ion ensemble; the IR-IR method requires probing each absorption line for potential isomer specificity, which is extremely time consuming. In contrast, ions can be readily separated with IMS after typically tens to hundreds of milliseconds, thereby facilitating single-laser, isomer-pure IR spectroscopic experiments.

## 4.4. Conclusions

The combination of ultra-high resolution ion mobility spectrometry with high-resolution (cryogenic) IR spectroscopy presents an alternative to IR-IR double-resonance techniques for isomer- or conformer-selective vibrational spectroscopic experiments. We use structures for lossless ion manipulation (SLIM) to achieve high IMS resolution on a cyclic IMS device in which ions cycle the same serpentine drift path multiple times. Species with small structural differences can thereby readily be separated in time followed by spectroscopic analysis. The approach is particularly promising for larger molecules that possess inherently congested vibrational spectra due to conformational heterogeneity. In this case, sampling of the entire conformational ion ensemble can be cumbersome using double resonance techniques, since the required knowledge about conformer specificity of vibrational bands is not *a priori* given. A direct comparison between the two techniques using data of a sodiated disaccharide acquired on two different platforms shows an excellent agreement in both the conformer selectivity of the techniques and quality of the spectra. The latter is particularly interesting as it shows that the experimentally more accessible nitrogen-tagging method represents a good alternative to helium tagging to probe molecular structures the size of disaccharides and larger. The fact that we can separate the same isomeric species of the analyte ions in both experiments represents a success for the SLIM IMS method that we employ with moderately sized PCBs (15 cm x 15 cm). The two separated disaccharide species differ in their size by less than 1 % and can possibly be attributed to the  $\alpha$  and  $\beta$  anomers of the reducing-end C<sub>1</sub>-OH group. Anticipated increases in the resolving power of TW IMS will make this approach even more attractive.

This study opens potential applications in the field of glycan analysis, where one's ability to separate and identify different isomeric species in a timely manner is of utmost importance. The combination short isomer-separation times with isomer-characteristic fingerprint IR spectra could result in new analytical workflows that are orders of magnitude faster and more accurate than established methods.



## References

1. Warnke, S.; Ben Faleh, A.; Pellegrinelli, R. P.; Yalovenko, N.; Rizzo, T. R., Combining ultra-high resolution ion mobility spectrometry with cryogenic IR spectroscopy for the study of biomolecular ions. *Faraday Discuss* **2019**, *217* (0), 114-125.
2. Rijs, A. M.; Oomens, J., *Gas-Phase IR Spectroscopy and Structure of Biological Molecules*. Springer International Publishing: 2015.
3. Oomens, J.; Sartakov, B. G.; Meijer, G.; von Helden, G., Gas-phase infrared multiple photon dissociation spectroscopy of mass-selected molecular ions. *International journal of mass spectrometry* **2006**, *254* (1-2), 1-19.
4. Polfer, N. C.; Oomens, J., Vibrational spectroscopy of bare and solvated ionic complexes of biological relevance. *Mass Spectrometry Reviews* **2009**, *28* (3), 468-494.
5. Heine, N.; Asmis, K. R., Cryogenic ion trap vibrational spectroscopy of hydrogen-bonded clusters relevant to atmospheric chemistry. *International Reviews in Physical Chemistry* **2014**, *34* (1), 1-34.
6. Wolk, A. B.; Leavitt, C. M.; Garand, E.; Johnson, M. A., Cryogenic ion chemistry and spectroscopy. *Acc Chem Res* **2014**, *47* (1), 202-10.
7. Zabuga, A. V.; Kamrath, M. Z.; Boyarkin, O. V.; Rizzo, T. R., Fragmentation mechanism of UV-excited peptides in the gas phase. *J Chem Phys* **2014**, *141* (15), 154309.
8. Manz, C.; Pagel, K., Glycan analysis by ion mobility-mass spectrometry and gas-phase spectroscopy. *Curr Opin Chem Biol* **2018**, *42*, 16-24.
9. Redwine, J. G.; Davis, Z. A.; Burke, N. L.; Oglesbee, R. A.; McLuckey, S. A.; Zwier, T. S., A novel ion trap based tandem mass spectrometer for the spectroscopic study of cold gas phase polyatomic ions. *International journal of mass spectrometry* **2013**, *348*, 9-14.
10. Kamariotis, A.; Boyarkin, O. V.; Mercier, S. R.; Beck, R. D.; Bush, M. F.; Williams, E. R.; Rizzo, T. R., Infrared spectroscopy of hydrated amino acids in the gas phase: protonated and lithiated valine. *J Am Chem Soc* **2006**, *128* (3), 905-16.
11. Warnke, S.; Seo, J.; Boschmans, J.; Sobott, F.; Scrivens, J. H.; Bleiholder, C.; Bowers, M. T.; Gewinner, S.; Schollkopf, W.; Pagel, K.; von Helden, G., Protomers of

- benzocaine: solvent and permittivity dependence. *J Am Chem Soc* **2015**, *137* (12), 4236-42.
12. Jašík, J.; Žabka, J.; Roithová, J.; Gerlich, D., Infrared spectroscopy of trapped molecular dications below 4K. *International journal of mass spectrometry* **2013**, *354-355*, 204-210.
13. Rizzo, T. R.; Stearns, J. A.; Boyarkin, O. V., Spectroscopic studies of cold, gas-phase biomolecular ions. *International Reviews in Physical Chemistry* **2009**, *28* (3), 481-515.
14. Stearns, J. A.; Mercier, S.; Seaiby, C.; Guidi, M.; Boyarkin, O. V.; Rizzo, T. R., Conformation-specific spectroscopy and photodissociation of cold, protonated tyrosine and phenylalanine. *J Am Chem Soc* **2007**, *129* (38), 11814-20.
15. Leavitt, C. M.; Wolk, A. B.; Fournier, J. A.; Kamrath, M. Z.; Garand, E.; Van Stipdonk, M. J.; Johnson, M. A., Isomer-Specific IR-IR Double Resonance Spectroscopy of D2-Tagged Protonated Dipeptides Prepared in a Cryogenic Ion Trap. *J Phys Chem Lett* **2012**, *3* (9), 1099-105.
16. Masson, A.; Kamrath, M. Z.; Perez, M. A.; Glover, M. S.; Rothlisberger, U.; Clemmer, D. E.; Rizzo, T. R., Infrared Spectroscopy of Mobility-Selected H<sup>+</sup>-Gly-Pro-Gly-Gly (GPGG). *J Am Soc Mass Spectrom* **2015**, *26* (9), 1444-54.
17. Goebbert, D. J.; Wende, T.; Bergmann, R.; Meijer, G.; Asmis, K. R., Messenger-tagging electrosprayed ions: vibrational spectroscopy of suberate dianions. *J Phys Chem A* **2009**, *113* (20), 5874-80.
18. Wassermann, T. N.; Boyarkin, O. V.; Paizs, B.; Rizzo, T. R., Conformation-specific spectroscopy of peptide fragment ions in a low-temperature ion trap. *J Am Soc Mass Spectrom* **2012**, *23* (6), 1029-45.
19. Stearns, J. A.; Seaiby, C.; Boyarkin, O. V.; Rizzo, T. R., Spectroscopy and conformational preferences of gas-phase helices. *Phys Chem Chem Phys* **2009**, *11* (1), 125-32.
20. Wyttenbach, T.; Pierson, N. A.; Clemmer, D. E.; Bowers, M. T., Ion mobility analysis of molecular dynamics. *Annu Rev Phys Chem* **2014**, *65*, 175-96.

21. Laphorn, C.; Pullen, F. S.; Chowdhry, B. Z.; Wright, P.; Perkins, G. L.; Heredia, Y., How useful is molecular modelling in combination with ion mobility mass spectrometry for 'small molecule' ion mobility collision cross-sections? *Analyst* **2015**, *140* (20), 6814-23.
22. Schubert, F.; Rossi, M.; Baldauf, C.; Pagel, K.; Warnke, S.; von Helden, G.; Filsinger, F.; Kupser, P.; Meijer, G.; Salwiczek, M.; Koksich, B.; Scheffler, M.; Blum, V., Exploring the conformational preferences of 20-residue peptides in isolation: Ac-Ala19-Lys + H(+) vs. Ac-Lys-Ala19 + H(+) and the current reach of DFT. *Phys Chem Chem Phys* **2015**, *17* (11), 7373-85.
23. Schubert, F.; Pagel, K.; Rossi, M.; Warnke, S.; Salwiczek, M.; Koksich, B.; von Helden, G.; Blum, V.; Baldauf, C.; Scheffler, M., Native like helices in a specially designed beta peptide in the gas phase. *Phys Chem Chem Phys* **2015**, *17* (7), 5376-85.
24. Voronina, L.; Masson, A.; Kamrath, M.; Schubert, F.; Clemmer, D.; Baldauf, C.; Rizzo, T., Conformations of Prolyl-Peptide Bonds in the Bradykinin 1-5 Fragment in Solution and in the Gas Phase. *J Am Chem Soc* **2016**, *138* (29), 9224-33.
25. Pringle, S. D.; Giles, K.; Wildgoose, J. L.; Williams, J. P.; Slade, S. E.; Thalassinos, K.; Bateman, R. H.; Bowers, M. T.; Scrivens, J. H., An investigation of the mobility separation of some peptide and protein ions using a new hybrid quadrupole/travelling wave IMS/oa-ToF instrument. *Int J Mass Spectrom* **2007**, *261* (1), 1-12.
26. Buryakov, I. A.; Krylov, E. V.; Nazarov, E. G.; Rasulev, U. K., A new method of separation of multi-atomic ions by mobility at atmospheric pressure using a high-frequency amplitude-asymmetric strong electric field. *International Journal of Mass Spectrometry and Ion Processes* **1993**, *128* (3), 143-148.
27. de la Mora, J. F.; Ude, S.; Thomson, B. A., The potential of differential mobility analysis coupled to MS for the study of very large singly and multiply charged proteins and protein complexes in the gas phase. *Biotechnol J* **2006**, *1* (9), 988-97.
28. Guevremont, R., High-field asymmetric waveform ion mobility spectrometry: A new tool for mass spectrometry. *Journal of Chromatography A* **2004**, *1058* (1-2), 3-19.

29. Hogan, C. J., Jr.; Ruotolo, B. T.; Robinson, C. V.; Fernandez de la Mora, J., Tandem differential mobility analysis-mass spectrometry reveals partial gas-phase collapse of the GroEL complex. *J Phys Chem B* **2011**, *115* (13), 3614-21.
30. Kolakowski, B. M.; Mester, Z., Review of applications of high-field asymmetric waveform ion mobility spectrometry (FAIMS) and differential mobility spectrometry (DMS). *Analyst* **2007**, *132* (9), 842-64.
31. Kemper, P. R.; Dupuis, N. F.; Bowers, M. T., A new, higher resolution, ion mobility mass spectrometer. *International journal of mass spectrometry* **2009**, *287* (1-3), 46-57.
32. Tang, K.; Shvartsburg, A. A.; Lee, H. N.; Prior, D. C.; Buschbach, M. A.; Li, F.; Tolmachev, A. V.; Anderson, G. A.; Smith, R. D., High-sensitivity ion mobility spectrometry/mass spectrometry using electrodynamic ion funnel interfaces. *Anal Chem* **2005**, *77* (10), 3330-9.
33. Bohrer, B. C.; Merenbloom, S. I.; Koeniger, S. L.; Hilderbrand, A. E.; Clemmer, D. E., Biomolecule analysis by ion mobility spectrometry. *Annu Rev Anal Chem* **2008**, *1*, 293-327.
34. Khanal, N.; Masellis, C.; Kamrath, M. Z.; Clemmer, D. E.; Rizzo, T. R., Cryogenic IR spectroscopy combined with ion mobility spectrometry for the analysis of human milk oligosaccharides. *Analyst* **2018**, *143* (8), 1846-1852.
35. Masellis, C.; Khanal, N.; Kamrath, M. Z.; Clemmer, D. E.; Rizzo, T. R., Cryogenic Vibrational Spectroscopy Provides Unique Fingerprints for Glycan Identification. *J Am Soc Mass Spectrom* **2017**, *28* (10), 2217-2222.
36. Hernandez, O.; Isenberg, S.; Steinmetz, V.; Glish, G. L.; Maitre, P., Probing Mobility-Selected Saccharide Isomers: Selective Ion-Molecule Reactions and Wavelength-Specific IR Activation. *J Phys Chem A* **2015**, *119* (23), 6057-64.
37. Papadopoulos, G.; Svendsen, A.; Boyarkin, O. V.; Rizzo, T. R., Conformational distribution of bradykinin [bk + 2 H]<sub>2</sub><sup>+</sup> revealed by cold ion spectroscopy coupled with FAIMS. *J Am Soc Mass Spectrom* **2012**, *23* (7), 1173-81.

38. Seo, J.; Hoffmann, W.; Warnke, S.; Bowers, M. T.; Pagel, K.; von Helden, G., Retention of Native Protein Structures in the Absence of Solvent: A Coupled Ion Mobility and Spectroscopic Study. *Angew Chem Int Ed Engl* **2016**, *55* (45), 14173-14176.
39. Hoffmann, W.; Marianski, M.; Warnke, S.; Seo, J.; Baldauf, C.; von Helden, G.; Pagel, K., Assessing the stability of alanine-based helices by conformer-selective IR spectroscopy. *Phys Chem Chem Phys* **2016**, *18* (29), 19950-4.
40. Papadopoulos, G.; Svendsen, A.; Boyarkin, O. V.; Rizzo, T. R., Spectroscopy of mobility-selected biomolecular ions. *Faraday Discussions* **2011**, *150*, 243.
41. Seo, J.; Warnke, S.; Pagel, K.; Bowers, M. T.; von Helden, G., Infrared spectrum and structure of the homochiral serine octamer-dichloride complex. *Nat Chem* **2017**, *9* (12), 1263-1268.
42. Seo, J.; Hoffmann, W.; Warnke, S.; Huang, X.; Gewinner, S.; Schollkopf, W.; Bowers, M. T.; von Helden, G.; Pagel, K., An infrared spectroscopy approach to follow beta-sheet formation in peptide amyloid assemblies. *Nat Chem* **2017**, *9* (1), 39-44.
43. Hamid, A. M.; Ibrahim, Y. M.; Garimella, S. V.; Webb, I. K.; Deng, L.; Chen, T. C.; Anderson, G. A.; Prost, S. A.; Norheim, R. V.; Tolmachev, A. V.; Smith, R. D., Characterization of Traveling Wave Ion Mobility Separations in Structures for Lossless Ion Manipulations. *Anal Chem* **2015**, *87* (22), 11301-8.
44. Deng, L.; Ibrahim, Y. M.; Hamid, A. M.; Garimella, S. V.; Webb, I. K.; Zheng, X.; Prost, S. A.; Sandoval, J. A.; Norheim, R. V.; Anderson, G. A.; Tolmachev, A. V.; Baker, E. S.; Smith, R. D., Ultra-High Resolution Ion Mobility Separations Utilizing Traveling Waves in a 13 m Serpentine Path Length Structures for Lossless Ion Manipulations Module. *Anal Chem* **2016**, *88* (18), 8957-64.
45. Shvartsburg, A. A.; Smith, R. D., Fundamentals of traveling wave ion mobility spectrometry. *Anal Chem* **2008**, *80* (24), 9689-99.
46. Deng, L.; Webb, I. K.; Garimella, S. V. B.; Hamid, A. M.; Zheng, X.; Norheim, R. V.; Prost, S. A.; Anderson, G. A.; Sandoval, J. A.; Baker, E. S.; Ibrahim, Y. M.; Smith, R. D., Serpentine Ultralong Path with Extended Routing (SUPER) High Resolution Traveling

Wave Ion Mobility-MS using Structures for Lossless Ion Manipulations. *Anal Chem* **2017**, *89* (8), 4628-4634.

47. Kamrath, M. Z.; Garand, E.; Jordan, P. A.; Leavitt, C. M.; Wolk, A. B.; Van Stipdonk, M. J.; Miller, S. J.; Johnson, M. A., Vibrational characterization of simple peptides using cryogenic infrared photodissociation of H<sub>2</sub>-tagged, mass-selected ions. *J Am Chem Soc* **2011**, *133* (16), 6440-8.

48. Svendsen, A.; Lorenz, U. J.; Boyarkin, O. V.; Rizzo, T. R., A new tandem mass spectrometer for photofragment spectroscopy of cold, gas-phase molecular ions. *Review of Scientific Instruments* **2010**, *81* (7), 073107.

49. Chen, T. C.; Fillmore, T. L.; Prost, S. A.; Moore, R. J.; Ibrahim, Y. M.; Smith, R. D., Orthogonal Injection Ion Funnel Interface Providing Enhanced Performance for Selected Reaction Monitoring-Triple Quadrupole Mass Spectrometry. *Analytical Chemistry* **2015**, *87* (14), 7326-31.

50. Varki, A.; Cummings, R. D.; Esko, J. D.; Stanley, P.; Hart, G. W.; Aebi, M.; Darvill, A. G.; Kinoshita, T.; Packer, N. H.; Prestegard, J. H.; Schnaar, R. L.; Seeberger, P. H., *Essentials of Glycobiology, 3rd edition*. Cold Spring Harbor Laboratory Press: 2017.

51. Nagy, G.; Attah, I. K.; Garimella, S. V. B.; Tang, K.; Ibrahim, Y. M.; Baker, E. S.; Smith, R. D., Unraveling the isomeric heterogeneity of glycans: ion mobility separations in structures for lossless ion manipulations. *Chem Commun (Camb)* **2018**, *54* (83), 11701-11704.

52. Voss, J. M.; Kregel, S. J.; Fischer, K. C.; Garand, E., IR-IR Conformation Specific Spectroscopy of Na<sup>(+)</sup>(Glucose) Adducts. *J Am Soc Mass Spectrom* **2018**, *29* (1), 42-50.

53. Elliott, B. M.; Relph, R. A.; Roscioli, J. R.; Bopp, J. C.; Gardenier, G. H.; Guasco, T. L.; Johnson, M. A., Isolating the spectra of cluster ion isomers using Ar-"tag" -mediated IR-IR double resonance within the vibrational manifolds: Application to NO<sub>2</sub><sup>-</sup> \*H<sub>2</sub>O. *J Chem Phys* **2008**, *129* (9), 094303.

54. Haynes, W. M.; Lide, D. R., *CRC handbook of chemistry and physics, 92nd ed.* Boca Raton, Fla. : CRC Press: 2011.

55. Johnson, C. J.; Wolk, A. B.; Fournier, J. A.; Sullivan, E. N.; Weddle, G. H.; Johnson, M. A., Communication: He-tagged vibrational spectra of the SarGlyH(+) and H(+)(H<sub>2</sub>O)<sub>(2,3)</sub> ions: quantifying tag effects in cryogenic ion vibrational predissociation (CIVP) spectroscopy. *J Chem Phys* **2014**, *140* (22), 221101.
56. Masson, A.; Williams, E. R.; Rizzo, T. R., Molecular hydrogen messengers can lead to structural infidelity: A cautionary tale of protonated glycine. *J Chem Phys* **2015**, *143* (10), 104313.



## 5. Identifying the composition of an unknown glycan mixture<sup>\*</sup>

The isomeric complexity of glycans makes their analysis by traditional techniques particularly challenging. While the recent combination of ion mobility spectrometry (IMS) with cryogenic IR spectroscopy has demonstrated promise as a new technique for glycan analysis, this approach has been limited by the modest resolution of the ion mobility stage. In this work we report results from a newly developed instrument that combines ultrahigh-resolution IMS with cryogenic IR spectroscopy for glycan analysis. This apparatus makes use of the recent development in traveling-wave IMS called structures for lossless ion manipulation (SLIM). The IMS stage allows the selection of glycan isomers that differ in collisional cross section by as little as 0.2% before injecting them into a cryogenic ion trap for IR spectral analysis. We compare our results to those using drift-tube IMS and highlight the advantages of the substantial increase in resolution. Application of this approach to glycan mixtures demonstrates our ability to isolate individual components, measure a cryogenic IR spectrum, and identify them using a spectroscopic database.

### 5.1. Introduction

It is difficult to overstate the importance of glycans in biological systems.<sup>2-4</sup> Nearly every cell of every organism is coated with a layer of glycans that plays a key role in cell-to-cell

---

<sup>\*</sup> This chapter is largely based on reference 1. Ben Faleh, A.; Warnke, S.; Rizzo, T. R., Combining Ultrahigh-Resolution Ion-Mobility Spectrometry with Cryogenic Infrared Spectroscopy for the Analysis of Glycan Mixtures. *Anal Chem* **2019**, *91* (7), 4876-4882.- S. The content and figures were adapted with permission from the American Chemical Society.

recognition and signaling. Glycans govern the interaction of cells with bacteria and viruses and are central to molecular recognition, immune response, and inflammation.<sup>5</sup> Despite their importance, glycans are extremely difficult to analyze because of their isomeric complexity. Unlike linear sequences of monomers with distinct mass as found in proteins, many of the monosaccharide building blocks of glycans are isomeric, differing only in the stereochemistry of the asymmetric carbon atoms. In addition, the glycosidic bond linking these monosaccharides involves a stereogenic carbon, leading to isomeric  $\alpha$  and  $\beta$  anomers. Moreover, glycosidic bonds can have different attachment points, leading to different regioisomers. Finally, the ability of a monosaccharide unit to support multiple glycosidic bonds can result in the formation of branched structures that are isomeric with the corresponding linear chains of the same monosaccharide content. Because these various types of isomerism are present simultaneously, there is a vast number of possible glycan isomers,<sup>6</sup> and many of the powerful tools used to sequence proteins are not able to distinguish them.

The speed and sensitivity of mass spectrometry (MS) make it particularly attractive as a tool for glycan analysis. The most detailed structural information comes from the use of tandem MS techniques,<sup>7-8</sup> and these have employed a variety of different dissociation methods to generate the cross-ring fragments needed to determine linkage positions and stereochemistry.<sup>9-15</sup> While permethylation of the free hydroxyl groups prior to fragmentation<sup>13, 16</sup> helps to reveal the locations of the glycosidic bonds, even MS-MS cannot distinguish all of the various glycan isomers. Several studies have shown that the combination of ion mobility and mass spectrometry (IMS-MS) can often resolve glycan isomers that are indistinguishable by MS alone.<sup>17-24</sup> A particularly promising approach is to combine tandem MS with ion mobility, using both the mass of the fragments and their collision cross section to help reconstruct the primary structure of the parent glycan.<sup>25-27</sup> Nevertheless, IMS is blind to many of the subtle structural details that distinguish isomeric glycans.<sup>19</sup>

One other possibility is to add a spectroscopic dimension to MS to achieve further isomer discrimination, since spectroscopic fingerprints can be extremely sensitive to the slightest differences in structure. Several groups have successfully combined MS with infrared multiple-photon dissociation (IRMPD) spectroscopy for identification of small glycans,<sup>28-33</sup> but the absorption bands in the room temperature IRMPD spectra are often too broad to uniquely identify isomeric disaccharides in a mixture. In recent work, Mucha et al.<sup>34</sup> used a free-electron laser to obtain spectroscopic fingerprints of oligosaccharides cooled in liquid helium droplets and demonstrated that sufficiently resolved spectra could indeed distinguish the various types of isomerism, albeit with an extremely complex instrument that would be impractical as a broadly used tool.

Recently, IRMPD spectroscopy has been combined with tandem MS and ion mobility to determine the structure of small glycans.<sup>31</sup> In this case, information from separately performed IR-MS/MS and IMS-MS/MS experiments on the same systems are used together.<sup>31</sup> Results from this work are particularly significant in that they suggest that stereochemistry of the glycosidic bond is retained in the C-fragments of cationized disaccharides.<sup>35</sup> More recently, the group of Compagnon has combined HPLC and IRMPD spectroscopy to measure spectra of the two anomeric forms of glucosamine separately.<sup>36</sup>

In a series of proof-of-principle experiments,<sup>37-39</sup> we have recently combined ion mobility spectrometry in a 2 m drift tube with messenger-tagging infrared spectroscopy in a cryogenic ion trap coupled to a TOF-MS to identify and characterize glycans. Our application of this approach to a set of isomeric disaccharides<sup>38-39</sup> as well as series of human milk oligosaccharides<sup>37</sup> clearly demonstrate that a low-temperature vibrational spectrum can easily distinguish the subtlest differences between glycan isomers. Although we succeeded in characterizing different isomers, the IMS arrival-time distributions (ATDs) for the isomeric species were very similar, making it difficult to separate them. While a spectral deconvolution could in principle determine the composition of a complex mixture, an increase in the resolving power of the IMS stage that would allow us to separate isomers

with extremely small differences in CCS would greatly simplify the deconvolution procedure. A promising direction in the field of ultrahigh-resolution IMS has been the development by Smith and co-workers of what they call Structures for Lossless Ion Manipulations (SLIM),<sup>40-41</sup> which is a type of travelling wave ion mobility using a “sandwich” of printed circuit boards that combine RF and DC potentials. Recent work from Nagy et al.<sup>42</sup> has demonstrated the possibility of using SLIM to separate different conformers of a single disaccharide, speculated to be its  $\alpha$  and  $\beta$  anomers.

In this work, we describe and characterize our newly developed approach combining ultrahigh-resolution, SLIM-based, IMS-MS with messenger-tagging, cryogenic IR spectroscopy for the characterization of glycans. We compare our results to our previously published drift-tube IMS results and demonstrate the simplification that arises from increasing the IMS resolution by more than a factor of 6. As a proof of principle, we use this method to identify disaccharide isomers from mixtures. Finally, we apply our method to a pair of human milk oligosaccharides, demonstrating that it can identify the composition of mixtures of biologically relevant components.

## 5.2. Experimental Approach

### 5.2.1 Samples

Oligosaccharide samples were purchased from Dextra (UK) and Carbosynth (UK) and used without further purification. For nano-electrospray ionization (nESI), the samples were diluted in 50/50 water/methanol or water/acetonitrile at a concentration of 100  $\mu$ M. All our measurements were made on the sodiated species, and thus we add 1.5 equivalents of NaCl to enhance their formation. Because our goal is to identify the isomeric form of glycans and not their 3-dimensional structure, the fact that we study the sodiated species has no consequence, as long as the database to which we compare is constructed for sodiated glycans.

## 5.2.2 Instrument

We perform our experiments on the instrument described in Chapter 3 (Figure 3.1). Briefly, ions produced by nano-electrospray were transferred into the instrument through a flared stainless-steel capillary<sup>43</sup> and stored in the hourglass section of a commercial dual ion-funnel trap assembly (MassTech, USA).<sup>44</sup> From there, ion pulses 120  $\mu$ s in duration are released into the ion-mobility section, where they are separated based on their respective collision cross sections (CCS). They are then directed through differential pumping stages using ring-electrode ion guides and hexapoles. Ions of a particular drift time can be selected by electrostatically deflecting unwanted ions using a steering-lens assembly prior to the electrostatic ion bender. After  $m/z$  selection in a quadrupole mass filter, the ions enter the cryogenic ion trap (40 K) where they are stored and cooled through collisions with a cold buffer gas composed of helium and nitrogen in a 90:10 mixture. Nitrogen molecules condense on the internally cold ions, which can be observed as a shift in mass in subsequent TOF analysis. To record an IR spectrum, the content of the ion trap is irradiated by a single pulse ( $\sim 10$  mJ) from an IR OPO system. When the light is resonant with a molecular vibration, the absorption of a single photon and subsequent redistribution of vibrational energy causes the weakly bound  $N_2$  molecule to boil off. An IR spectrum of the  $m/z$ - and size-selected ions is generated by monitoring the wavelength-dependent ion signal of the  $N_2$  tagged species in the TOF mass spectrum. Spectral data points are acquired in  $1\text{ cm}^{-1}$  increments by averaging signal from 10 filling events at a repetition rate of 10 Hz, which is determined by our OPO. For the wavenumber range presented here, a single scan requires six to eight minutes to complete, and our final data represents the average of two such scans. An ion-mobility arrival time distribution (ATD) can be recorded by inserting a channeltron electron multiplier to monitor the time-dependent ion current of  $m/z$ -selected ions after they pass through the quadrupole MS.

To achieve ultrahigh-resolution ion-mobility separation, we use SLIM-based travelling-wave ion mobility spectrometry (TW-IMS) developed by Smith and coworkers.<sup>40-41</sup> A pair

of mirrored printed circuit boards (PCBs) produce confining RF and DC fields as well as a travelling square-well potential (Figure 3.8 of Chapter 3)<sup>40, 45</sup> that propels the ions through a drift gas. The potential is defined by a repeating sequence of eight electrodes to which we apply a DC voltage in a binary fashion: four pads receive a positive DC voltage while the following four are kept at 0 V. This situation can be represented by a binary sequence of the type 11110000. The potential wave then propagates by shifting this sequence one bit at a time to 01111000 and so on. Smith and coworkers have demonstrated that these fields can be used to propel ions around corners, and thus one can lead them along a serpentine path<sup>45</sup> that covers a large fraction of the surface area of the printed circuit board.

In our implementation of this technique, illustrated in Figure 3.9, we use PCBs 15 x 15 cm on edge placed 2.75 mm apart to achieve a single-pass ion path of approximately 1.8 m. Moreover, we incorporate an electrostatic switch<sup>46</sup> at the end of the drift path either to send ions towards the cryogenic ion trap or to cycle them multiple times through the same track, thereby increasing the effective path length and hence the resolving power, which should scale with  $\sqrt{n}$ .<sup>47</sup> The resolution of the instrument as a function of the number of separation cycles is displayed in Figure 3.22.

For each type of molecule, the optimum TW amplitude and speed for ion mobility separation are determined empirically. Typical IMS parameters for the here-reported experiments were: RF frequency 880 kHz; RF amplitude 100 V<sub>pp</sub>; TW amplitude 27 V; TW speed 600 m/s; He buffer gas pressure 3 mbar.

## 5.3. Results and discussion

### 5.3.1 Identification of glycans from mixtures

We tested the capability of our new multidimensional ultrahigh-resolution IMS-cryogenic IR spectroscopy approach to distinguish and identify carbohydrate molecules in mixtures using a set of isomeric disaccharides as well as biologically relevant human milk

oligosaccharides. For the former, we used the particularly challenging case of identification of epimers. We do this by comparing disaccharides with glucose versus galactose at the non-reducing end, yielding molecules that differ only in the orientation of the C-4 carbon (Figure 5.1(a)).

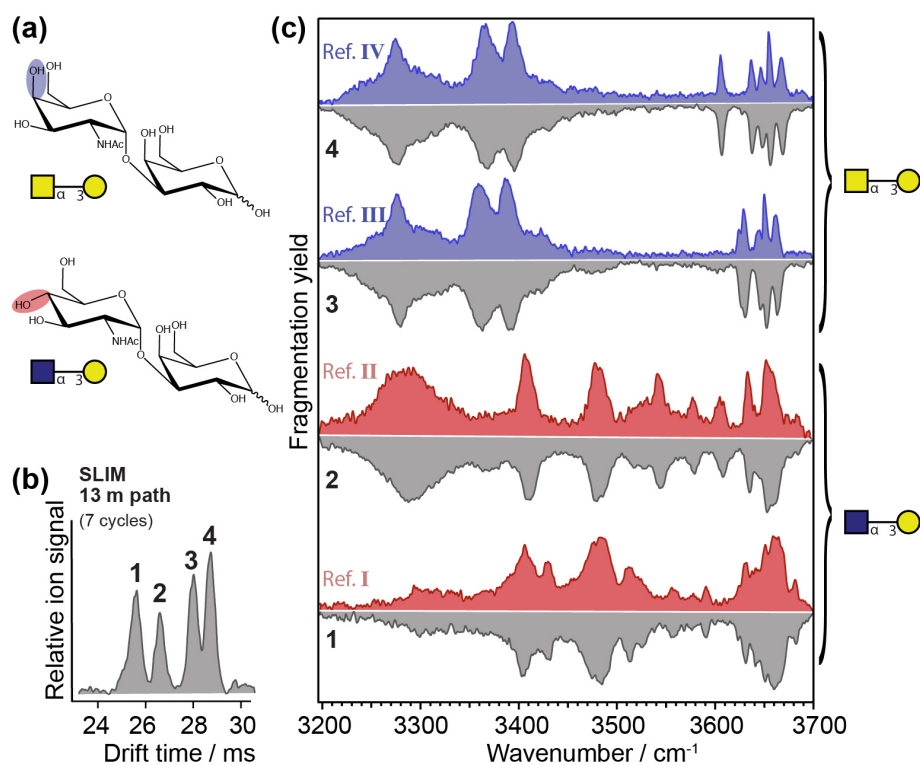


**Figure 5.1:** (a) Structures of GalNAc $\alpha$ (1-3)Gal and GlcNAc $\alpha$ (1-3)Gal highlighting the subtle difference in structure between them. (b) Arrival time distribution of the mixture of the two sodiated disaccharides (c) IR spectra of the different nitrogen tagged, mobility-selected species from the mixture (gray) and obtained from individually investigated substances as references (red and blue).

Solutions of disaccharide epimers GalNAc $\alpha$ (1-3)Gal and GlcNAc $\alpha$ (1-3)Gal were first electrosprayed separately to record their IR spectra for reference. In both cases, two distinct drift peaks were observed for each molecule after several separation cycles, leading to two fingerprint IR spectra per glycan. These are displayed in Figure 5.1(c) in red and blue for GlcNAc $\alpha$ (1-3)Gal (labeled I and II) and GalNAc $\alpha$ (1-3)Gal (labeled III and IV),

respectively. These spectra can then be used for the identification of components in a mixture. Subsequently, a 1:1 mixture of the disaccharides was prepared and analyzed using our multidimensional approach. Figure 5.1(b) shows the ATD obtained from the mixture after eight cycles in the SLIM IMS region to reach a drift length of 15 m, which corresponds to a resolving power of approximately 250. Four distinct species (labeled 1 through 4) can be completely separated under these conditions and selected for spectroscopic analysis, and we show the resulting IR spectra in Figure 5.1(c) (in grey).

Comparison of the spectra with reference spectra from the individually investigated compounds is required to test if the signals from the mixture can be assigned. Indeed, for each of the spectra 1 through 4, a virtually identical reference spectrum can be found, which leads us to conclude that the first two drift peaks from the mixture (1 and 2) correspond to signals from GlcNAc $\alpha$ (1-3)Gal and the last two peaks (3 and 4) correspond to GalNAc $\alpha$ (1-3)Gal.

As a second demonstration of our approach, we use the human milk oligosaccharides lacto-N-tetraose (LNT) and lacto-N-neo-tetraose (LNnT). These tetrasaccharides are regioisomers that differ in the glycosidic linkage ( $\beta$ 1-3 vs.  $\beta$ 1-4) at the non-reducing end. As in the case of the disaccharides, ATDs of the individually electrosprayed, singly sodiated reference compounds each exhibit two distinct features (Figure 5.2).

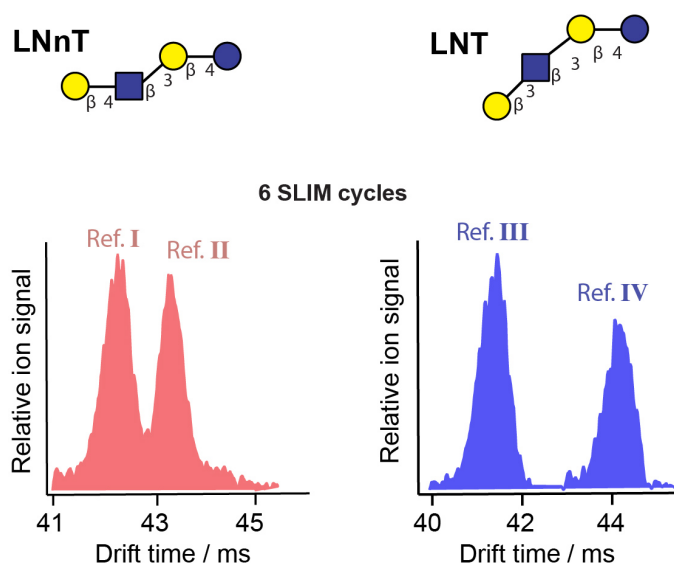


**Figure 5.2:** Arrival time distributions of the two sodiated human milk tetrasaccharides LNnT (left) and LNT (right) electrosprayed individually.

The reference IR spectra for these species are displayed in Figure 5.3(c) in red and blue for the two drift peaks of LNnT (labeled I and II) and LNT (labeled III and IV), respectively. Each spectrum shows several sharp transitions in the free-OH region above  $3580\text{ cm}^{-1}$  and considerably broader absorption bands in the hydrogen-bonded region at lower wavenumber. Even though the spectra are generally more congested than those of the smaller disaccharides, they are still distinct and highly characteristic for a given structure of the molecule.

We then electrosprayed a 1:1 mixture of LNT and LNnT and observed three mobility-resolved species in the ATD after five cycles in the SLIM IMS section (labeled 1 through 3 in Figure 5.3 (b)). It is likely that the expected fourth component is simply not resolved under these experimental conditions. While the ion-mobility resolving power can be further increased using more separation cycles, this comes at the cost of the total number of ions transmitted to the ion trap. Nevertheless, IR spectra were recorded for the three individual ion mobility peaks from the mixture, displayed in Figure 5.3(c) (grey) and labeled accordingly. As in the case of the disaccharide, it is straightforward to find a matching

reference spectrum for each of the spectra 1, 2, and 3 by visual comparison and therefore to unambiguously determine the presence of both LNnT (peaks 1 and 2) and LNT (peak 3) in the mixture. The fact that the second component of LNT is not resolved here does not represent an obstacle for identification of the compound, because either one of the two reference IR spectra contain enough information to serve as a unique fingerprint.

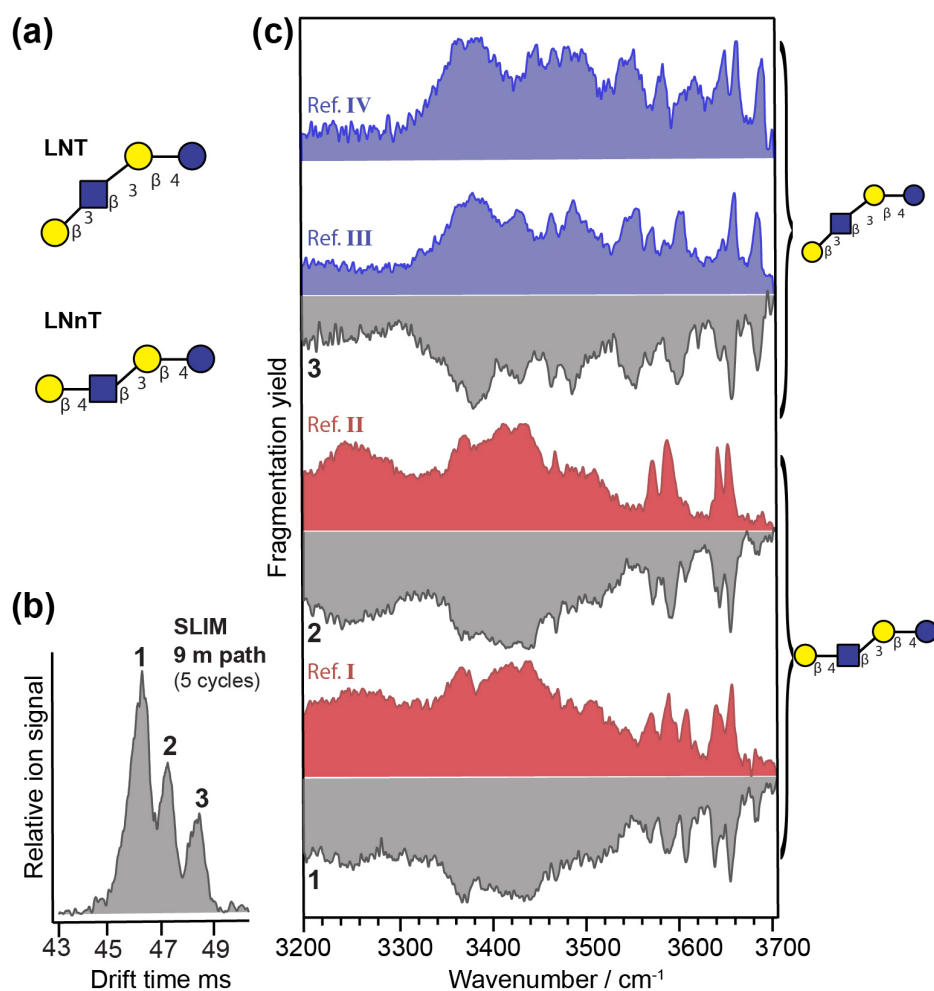


**Figure 5.3:** (a) Human milk tetrasaccharides LNT and LNnT in Oxford notation. (b) Arrival-time distribution of the mixture of sodiated LNT and LNnT. (c) IR spectra of the different nitrogen-tagged, mobility-selected species from the mixture (gray) and obtained from in-dividually investigated substances as references (red and blue).

These results represent the first demonstration of using a database approach to unambiguously identify ion-mobility separated carbohydrates from a mixture on basis of their IR vibrational spectra. Two other examples where isomeric disaccharides are separated and identified from a mixture can be found in Figure A.1 and Figure A.2 in Annex A. While in the results reported here, spectra obtained from mixtures were compared and matched to reference spectra by simple visual inspection, in the future this process will be rapidly done by computer.

As demonstrated in the case of LNT and LNnT, the method is still easily applicable even when all gas-phase structures of one compound cannot be fully separated in the preparative IMS step. However, in a case where the ion-mobility resolving power will not be sufficient to separate different species, the resulting IR spectrum will simply be the sum of those from overlapping structures and can be deconvoluted using the reference database. Given the rapid development of ultrahigh-resolution ion-mobility instrumentation, we anticipate that such a deconvolution step will only be necessary in rare cases. The same technological development will also be beneficial for the analysis of larger glycan structures.

Lastly, it should be noted that the same methods that are routinely being employed in MS-MS or MS-IMS-MS<sup>48</sup> applications, where the fragments of MS or IMS selected analyte ions are used to obtain additional information about the internal structure of the parent, can also be incorporated into the IR fingerprint method. An adapted workflow would include a fragmentation step of an unknown ion-mobility and  $m/z$ -selected glycan, subsequent IMS-MS analysis of its fragments, and finally an IR spectroscopic interrogation step to obtain fingerprint spectra of the fragment ions for their unambiguous identification by comparison with previously recorded reference spectra. This approach could solve three possible problems: inconclusive ion-mobility and IR spectroscopic data of a parent compound could be backed by analyzing its fragments;<sup>49</sup> glycans that exceed the size limit for a conclusive spectroscopic analysis could be identified by reconstructing the sequence from a fragment analysis; and the monosaccharide sequence of a compound for which a database entry does

not yet exist could be reconstructed by successively breaking the molecule into fragments for which database entries do exist.

## 5.4. Conclusions

The combination of ultrahigh-resolution SLIM-based IMS-MS with messenger-tagging cryogenic IR spectroscopy was proven to be a powerful technique for analyzing and distinguishing between isomeric glycan structures. The strength of this technique arises from the high degree of orthogonality between data from IMS-MS and cryogenic IR spectroscopy and its exquisite sensitivity to the finest details of glycan structures. Our newly fashioned instrument combines these techniques, making use of the recently developed SLIM travelling-wave IMS technique for ultrahigh-resolution mobility separation as a preparative step for high-resolution IR spectroscopy of size- and  $m/z$ -selected species. The ability of our approach to separate and distinguish different glycan isomers emphasizes its feasibility.

This method has the potential to profoundly impact in the field of glycomics and can in principle be incorporated in easy-to-use workflows. The required setup is a relatively straightforward extension of well-established IMS-MS instrument designs. Moreover, the required laser systems are no longer restricted to experts and can be viewed as turn-key instruments. For our approach to meet the conditions for use as an analytical tool, these measurements will have to operate at high throughput. Ongoing developments in our laboratory are aimed at multiplexing this approach to reduce measurement time to less than one minute per species in a mixture, which is a necessary requirement for the technique to be combined with an online LC-based separation step prior gas-phase analysis.



## References

1. Ben Faleh, A.; Warnke, S.; Rizzo, T. R., Combining Ultrahigh-Resolution Ion-Mobility Spectrometry with Cryogenic Infrared Spectroscopy for the Analysis of Glycan Mixtures. *Anal Chem* **2019**, *91* (7), 4876-4882.
2. Varki, A., Biological roles of glycans. *Glycobiology* **2017**, *27* (1), 3-49.
3. Varki, A.; Cummings, R. D.; Esko, J. D.; Freeze, H. H.; Stanley, P.; Bertozzi, C. R.; Hart, G. W.; Etzler, M. E., *Essentials of Glycobiology*. 2nd ed.; Cold Spring Harbor Laboratory Press; 2009. : Cold Spring Harbor (NY), 2009.
4. *Transforming Glycoscience: A Roadmap for the Future*. The National Academies Press: Washington, D.C., 2012.
5. Rudd, P. M.; Elliott, T.; Cresswell, P.; Wilson, I. A.; Dwek, R. A., Glycosylation and the immune system. *Science* **2001**, *291* (5512), 2370-2376.
6. Laine, R. A., A calculation of all possible oligosaccharide isomers both branched and linear yields  $1.05 \times 10^{12}$  structures for a reducing hexasaccharide - The isomer-barrier to development of single-method saccharide sequencing or synthesis systems. *Glycobiology* **1994**, *4* (6), 759-767.
7. Hofmann, J.; Stuckmann, A.; Crispin, M.; Harvey, D. J.; Pagel, K.; Struwe, W. B., Identification of Lewis and Blood Group Carbohydrate Epitopes by Ion Mobility-Tandem-Mass Spectrometry Fingerprinting. *Analytical Chemistry* **2017**, *89* (4), 2318-2325.
8. Harvey, D. J.; Struwe, W. B., Structural Studies of Fucosylated N-Glycans by Ion Mobility Mass Spectrometry and Collision-Induced Fragmentation of Negative Ions. *Journal of the American Society for Mass Spectrometry* **2018**, *29* (6), 1179-1193.
9. Domon, B.; Costello, C. E., A systematic nomenclature for carbohydrate fragmentations in FAB-MS spectra of glycoconjugates *Glycoconjugate Journal* **1988**, *5* (4), 397-409.
10. Khatri, K.; Pu, Y.; Klein, J. A.; Wei, J.; Costello, C. E.; Lin, C.; Zaia, J., Comparison of Collisional and Electron-Based Dissociation Modes for Middle-Down Analysis of

Multiply Glycosylated Peptides. *Journal of the American Society for Mass Spectrometry* **2018**, *29* (6), 1075-1085.

11. Adamson, J. T.; Håkansson, K., Electron Capture Dissociation of Oligosaccharides Ionized with Alkali, Alkaline Earth, and Transition Metals. *Analytical Chemistry* **2007**, *79* (7), 2901-2910.

12. Wolff, J. J.; Amster, I. J.; Chi, L.; Linhardt, R. J., Electron detachment dissociation of glycosaminoglycan tetrasaccharides. *Journal of the American Society for Mass Spectrometry* **2007**, *18* (2), 234-244.

13. Zhao, C.; Xie, B.; Chan, S.-Y.; Costello, C. E.; O'Connor, P. B., Collisionally activated dissociation and electron capture dissociation provide complementary structural information for branched permethylated oligosaccharides. *Journal of the American Society for Mass Spectrometry* **2008**, *19* (1), 138-150.

14. Yu, X.; Jiang, Y.; Chen, Y. J.; Huang, Y. Q.; Costello, C. E.; Lin, C., Detailed Glycan Structural Characterization by Electronic Excitation Dissociation. *Analytical Chemistry* **2013**, *85* (21), 10017-10021.

15. Tang, Y.; Pu, Y.; Gao, J. S.; Hong, P. Y.; Costello, C. E.; Lin, C., De Novo Glycan Sequencing by Electronic Excitation Dissociation and Fixed-Charge Derivatization. *Analytical Chemistry* **2018**, *90* (6), 3793-3801.

16. Lin, Z.; Lubman, D. M., Permethylated N-Glycan Analysis with Mass Spectrometry. In *Mass Spectrometry Data Analysis in Proteomics*, Matthiesen, R., Ed. Humana Press: Totowa, NJ, 2013; pp 289-300.

17. Gray, C. J.; Thomas, B.; Upton, R.; Migas, L. G.; Eyers, C. E.; Barran, P. E.; Flitsch, S. L., Applications of ion mobility mass spectrometry for high throughput, high resolution glycan analysis. *Biochimica et biophysica acta* **2016**, *1860* (8), 1688-709.

18. Gaye, M. M.; Nagy, G.; Clemmer, D. E.; Pohl, N. L. B., Multidimensional Analysis of 16 Glucose Isomers by Ion Mobility Spectrometry. *Analytical Chemistry* **2016**, *88* (4), 2335-2344.

19. Hofmann, J.; Hahm, H. S.; Seeberger, P. H.; Pagel, K., Identification of carbohydrate anomers using ion mobility-mass spectrometry. *Nature* **2015**, *526* (7572), 214-244.
20. Gaye, M. M.; Kurulugama, R.; Clemmer, D. E., Investigating carbohydrate isomers by IMS-CID-IMS-MS: precursor and fragment ion cross-sections. *Analyst* **2015**, *140* (20), 6922-6932.
21. Pagel, K.; Harvey, D. J., Ion Mobility-Mass Spectrometry of Complex Carbohydrates: Collision Cross Sections of Sodiated N-linked Glycans. *Analytical Chemistry* **2013**, *85* (10), 5138-5145.
22. Guttman, M.; Lee, K. K., Site-Specific Mapping of Sialic Acid Linkage Isomers by Ion Mobility Spectrometry. *Analytical Chemistry* **2016**, *88* (10), 5212-5217.
23. Both, P.; Green, A. P.; Gray, C. J.; ŠardžikR; VoglmeirJ; FontanaC; AusteriM; RejzekM; RichardsonD; Field, R. A.; WidmalmG; Flitsch, S. L.; Evers, C. E., Discrimination of epimeric glycans and glycopeptides using IM-MS and its potential for carbohydrate sequencing. *Nat Chem* **2014**, *6* (1), 65-74.
24. Chen, Z.; Glover, M. S.; Li, L., Recent advances in ion mobility–mass spectrometry for improved structural characterization of glycans and glycoconjugates. *Current Opinion in Chemical Biology* **2018**, *42*, 1-8.
25. Pu, Y.; Ridgeway, M. E.; Glaskin, R. S.; Park, M. A.; Costello, C. E.; Lin, C., Separation and Identification of Isomeric Glycans by Selected Accumulation-Trapped Ion Mobility Spectrometry-Electron Activated Dissociation Tandem Mass Spectrometry. *Anal. Chem.* **2016**, *88* (7), 3440-3443.
26. Harvey, D. J.; Watanabe, Y.; Allen, J. D.; Rudd, P.; Pagel, K.; Crispin, M.; Struwe, W. B., Collision Cross Sections and Ion Mobility Separation of Fragment Ions from Complex N-Glycans. *Journal of the American Society for Mass Spectrometry* **2018**, *29* (6), 1250-1261.
27. Struwe, W. B.; Pagel, K.; Benesch, J. L. P.; Harvey, D. J.; Campbell, M. P., GlycoMob: an ion mobility-mass spectrometry collision cross section database for glycomics. *Glycoconjugate Journal* **2016**, *33* (3), 399-404.

28. Polfer, N. C.; Valle, J. J.; Moore, D. T.; Oomens, J.; Eyler, J. R.; Bendiak, B., Differentiation of isomers by wavelength-tunable infrared multiple-photon dissociation-mass spectrometry: Application to glucose-containing disaccharides. *Analytical Chemistry* **2006**, *78* (3), 670-679.
29. Hernandez, O.; Isenberg, S.; Steinmetz, V.; Glish, G. L.; Maitre, P., Probing Mobility-Selected Saccharide Isomers: Selective Ion-Molecule Reactions and Wavelength-Specific IR Activation. *J. Phys. Chem. A* **2015**, *119* (23), 6057-6064.
30. Tan, Y. L.; Polfer, N. C., Linkage and Anomeric Differentiation in Trisaccharides by Sequential Fragmentation and Variable-Wavelength Infrared Photodissociation. *Journal of the American Society for Mass Spectrometry* **2015**, *26* (2), 359-368.
31. Gray, C. J.; Schindler, B.; Migas, L. G.; Pičmanová, M.; Allouche, A. R.; Green, A. P.; Mandal, S.; Motawia, M. S.; Sánchez-Pérez, R.; Bjarnholt, N.; Møller, B. L.; Rijs, A. M.; Barran, P. E.; Compagnon, I.; Eyers, C. E.; Flitsch, S. L., Bottom-Up Elucidation of Glycosidic Bond Stereochemistry. *Analytical Chemistry* **2017**, *89* (8), 4540-4549.
32. Schindler, B.; Barnes, L.; Gray, C. J.; Chambert, S.; Flitsch, S. L.; Oomens, J.; Daniel, R.; Allouche, A. R.; Compagnon, I., IRMPD Spectroscopy Sheds New (Infrared) Light on the Sulfate Pattern of Carbohydrates. *Journal of Physical Chemistry A* **2017**, *121* (10), 2114-2120.
33. Schindler, B.; Renois-Predelus, G.; Bagdadi, N.; Melizi, S.; Barnes, L.; Chambert, S.; Allouche, A.-R.; Compagnon, I., MS/IR, a new MS-based hyphenated method for analysis of hexuronic acid epimers in glycosaminoglycans. *Glycoconjugate Journal* **2017**, *34* (3), 421-425.
34. Mucha, E.; González Flórez, A. I.; Marianski, M.; Thomas, D. A.; Hoffmann, W.; Struwe, W. B.; Hahm, H. S.; Gewinner, S.; Schöllkopf, W.; Seeberger, P. H.; von Helden, G.; Pagel, K., Glycan Fingerprinting using Cold-Ion Infrared Spectroscopy. *Angewandte Chemie International Edition* **2017**, n/a-n/a.
35. Schindler, B.; Barnes, L.; Renois, G.; Gray, C.; Chambert, S.; Fort, S.; Flitsch, S.; Loison, C.; Allouche, A.-R.; Compagnon, I., Anomeric memory of the glycosidic bond

- upon fragmentation and its consequences for carbohydrate sequencing. *Nature Communications* **2017**, *8*.
36. Schindler, B.; Laloy-Borgna, G.; Barnes, L.; Allouche, A.-R.; Bouju, E.; Dugas, V.; Demesmay, C.; Compagnon, I., Online separation and identification of isomers using IRMPD ion spectroscopy coupled to liquid chromatography: application to the analysis of disaccharides regio-isomers and monosaccharide anomers. *Analytical chemistry* **2018**.
37. Khanal, N.; Masellis, C.; Kamrath, M. Z.; Clemmer, D. E.; Rizzo, T. R., Cryogenic IR spectroscopy combined with ion mobility spectrometry for the analysis of human milk oligosaccharides. *Analyst* **2018**, *143* (8), 1846-1852.
38. Masellis, C.; Khanal, N.; Kamrath, M. Z.; Clemmer, D. E.; Rizzo, T. R., Cryogenic Vibrational Spectroscopy Provides Unique Fingerprints for Glycan Identification. *J. Am. Soc. Mass Spectrom.* **2017**, *28*, 2217-2222.
39. Khanal, N.; Masellis, C.; Kamrath, M. Z.; Clemmer, D. E.; Rizzo, T. R., Glycosaminoglycan analysis by cryogenic messenger-tagging IR spectroscopy combined with IMS-MS. *Analytical Chemistry* **2017**, *89*, 7601–7606.
40. Deng, L.; Ibrahim, Y. M.; Hamid, A. M.; Garimella, S. V.; Webb, I. K.; Zheng, X.; Prost, S. A.; Sandoval, J. A.; Norheim, R. V.; Anderson, G. A.; Tolmachev, A. V.; Baker, E. S.; Smith, R. D., Ultra-High Resolution Ion Mobility Separations Utilizing Traveling Waves in a 13 m Serpentine Path Length Structures for Lossless Ion Manipulations Module. *Anal Chem* **2016**, *88* (18), 8957-64.
41. Hamid, A. M.; Garimella, S. V. B.; Ibrahim, Y. M.; Deng, L.; Zheng, X.; Webb, I. K.; Anderson, G. A.; Prost, S. A.; Norheim, R. V.; Tolmachev, A. V.; Baker, E. S.; Smith, R. D., Achieving High Resolution Ion Mobility Separations Using Traveling Waves in Compact Multiturn Structures for Lossless Ion Manipulations. *Anal. Chem.* **2016**, *88* (18), 8949-8956.
42. Nagy, G.; Attah, I. K.; Garimella, S. V. B.; Tang, K.; Ibrahim, Y. M.; Baker, E. S.; Smith, R. D., Unraveling the isomeric heterogeneity of glycans: ion mobility separations in structures for lossless ion manipulations. *Chem Commun (Camb)* **2018**, *54* (83), 11701-11704.

43. Pauly, M.; Sroka, M.; Reiss, J.; Rinke, G.; Albarghash, A.; Vogelgesang, R.; Hahne, H.; Kuster, B.; Sesterhenn, J.; Kern, K.; Rauschenbach, S., A hydrodynamically optimized nano-electrospray ionization source and vacuum interface. *Analyst* **2014**, *139* (8), 1856-67.
44. Ibrahim, Y.; Belov, M. E.; Tolmachev, A. V.; Prior, D. C.; Smith, R. D., Ion funnel trap interface for orthogonal time-of-flight mass spectrometry. *Anal Chem* **2007**, *79* (20), 7845-52.
45. Ibrahim, Y. M.; Hamid, A. M.; Deng, L.; Garimella, S. V.; Webb, I. K.; Baker, E. S.; Smith, R. D., New frontiers for mass spectrometry based upon structures for lossless ion manipulations. *Analyst* **2017**, *142* (7), 1010-1021.
46. Garimella, S. V.; Ibrahim, Y. M.; Webb, I. K.; Ipsen, A. B.; Chen, T. C.; Tolmachev, A. V.; Baker, E. S.; Anderson, G. A.; Smith, R. D., Ion manipulations in structures for lossless ion manipulations (SLIM): computational evaluation of a 90 degrees turn and a switch. *Analyst* **2015**, *140* (20), 6845-52.
47. Shvartsburg, A. A.; Smith, R. D., Fundamentals of Traveling Wave Ion Mobility Spectrometry. *Anal. Chem.* **2008**, *80* (24), 9689-9699.
48. Hoffmann, W.; Hofmann, J.; Pagel, K., Energy-resolved ion mobility-mass spectrometry--a concept to improve the separation of isomeric carbohydrates. *J Am Soc Mass Spectrom* **2014**, *25* (3), 471-9.
49. Mucha, E.; Stuckmann, A.; Marianski, M.; Struwe, W. B.; Meijer, G.; Pagel, K., In-depth structural analysis of glycans in the gas phase. *Chemical Science* **2019**.





## 6. IMS-CIS to distinguish glycan anomers<sup>\*</sup>

The analysis of carbohydrates, or glycans, is challenging for established structure-sensitive gas-phase methods. The multitude of possible stereo-, regio-, and structural isomers makes them substantially more complex to analyze than DNA or proteins, and no one method is currently able to fully resolve them. While the combination of tandem mass spectrometry (MS) and ion-mobility spectrometry (IMS) have made important inroads in glycan analysis, in many cases, this approach is still not able to identify the precise isomeric form. To advance the techniques available for glycan analysis, we employ two important innovations. First, we perform ultrahigh-resolution mobility separation using structures for lossless ion manipulations (SLIM) for isomer separation and pre-selection. We then complement this IMS-MS stage with a cryogenic IR spectroscopic dimension, since a glycan's vibrational spectrum provides a fingerprint that is extremely sensitive to the precise isomeric form. Using this unique approach in conjunction with oxygen-18 isotopic labeling, we show on a range of disaccharides how the  $\alpha$  and  $\beta$  anomers that every reducing glycan adopts in solution can be readily separated by mobility and identified based on their IR spectra. In addition to highlighting the power of our technique to detect minute differences in the structure of isomeric carbohydrates, these results provide the means to determine if and when anomericity is retained during collision-induced dissociation (CID) of larger glycans.

### 6.1. Introduction

The diversity in both the structure and function of glycans is perhaps unparalleled in biological systems. As individual molecules or as decoration on proteins and lipids, they play

---

<sup>\*</sup> This chapter is largely based on reference 1. Warnke S., B. F. A., Scutelnic V, Rizzo T. R., Separation and Identification of Glycan Anomers Using Ultrahigh-Resolution Ion-Mobility Spectrometry and Cryogenic Ion Spectroscopy. *J. Am. Soc. Mass Spectrom.* **2019**, *30* (11), 2204–2211. The content and figures were adapted with the permission of the Journal of American Society of Mass Spectrometry.

a vital role in a myriad of physiological processes and take active part in the molecular choreography that represents life.<sup>2-5</sup> The paramount importance of glycans is not, however, reflected in the current state of the analytical tools available for their analysis. Techniques combining liquid chromatography (LC) and mass spectrometry (MS),<sup>6-7</sup> which allow for routine sequencing of proteins, have difficulties to provide rapid structural analysis of carbohydrates.<sup>8-10</sup> These difficulties arise from the many levels of isomerism that glycans possess:<sup>3</sup> (1) their monosaccharide constituents are often isomeric, differing only in the stereochemistry of a single carbon atom; (2) multiple OH groups of a single monosaccharide provide a variety of potential attachment points for the next subunit, resulting in isomers that differ in their linkage position as well as allowing the formation of branched structures; (3) the anomeric (C<sub>1</sub>) carbon where the glycosidic linkage is realized represents another stereocenter, which results in each glycosidic bond being in either  $\alpha$  or  $\beta$  configuration. In addition, each glycan with a free reducing-end OH will be present in solution in both its  $\alpha$  and  $\beta$  anomeric form at ratios determined by the equilibrium of the mutarotation reaction that leads to their interconversion (Figure 6.1(a)).<sup>11</sup> It is this immense isomeric heterogeneity throughout the glycome that represents a major bottleneck for the development of robust, structure-sensitive, high-throughput analytical techniques and workflows.

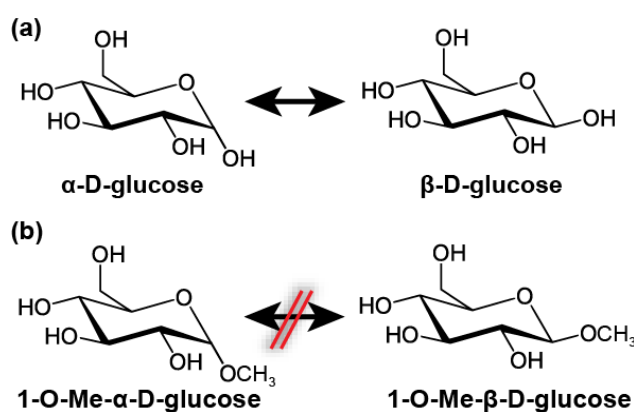


**Figure 6.1:** (a) Mutarotation of the C1 carbon leads to an equilibrium between the  $\alpha$  and  $\beta$  anomers of reducing carbohydrates in solution. (b) The carbohydrates' reducing end is locked in  $\alpha$  or  $\beta$  configuration when the respective hydroxy group is methylated.

Ion mobility spectrometry<sup>12-13</sup> (IMS), which is based on the difference in size and shape of a molecular ion when it is subjected to collisions with an inert buffer gas, is potentially sensitive to all kinds of different isomers. First studies using IMS-MS methods to separate glycan isomers were promising,<sup>14-15</sup> and these have been followed by more systematic investigations<sup>16</sup> of the feasibility of this approach for routine glycan analysis. This included the use of IMS-MS/MS methods,<sup>17-18</sup> where structural information can be obtained by fragment analysis of mobility-separated precursor ions in analogy to established LC-MS/MS workflows. Despite its promise, IMS alone cannot identify the subtlest forms of glycan isomerism, such as the difference in stereochemistry of a single carbon atom in an oligosaccharide.

Infrared (IR) spectroscopy of gas-phase molecular ions, on the other hand, can be exquisitely sensitive to the smallest of structural details.<sup>19-20</sup> Carbohydrates possess hydroxyls, amines, and other substituents that can serve as structural probes because their frequencies will be highly characteristic for their local environment. A vibrational spectrum will therefore contain information about the structure-defining hydrogen-bonding network within each molecule. Aided by quantum-mechanical calculations, IR spectroscopy becomes the ideal method for precise structural analysis of smaller sugar molecules,<sup>21-25</sup> with the size-limiting factor being the computational methods available on the one hand and increasingly congested experimental spectra as the molecules become larger on the other. Nevertheless, a vibrational spectrum will always represent a characteristic fingerprint for a given carbohydrate structure. This realization initiated a series of studies that explored the sensitivity of different spectroscopic schemes to the various forms of carbohydrate isomerism,<sup>26-31</sup> with the idea that an unknown carbohydrate compound could be identified by comparing its fingerprint spectrum to those from a database, bringing spectroscopy closer to becoming a routine-analysis tool.

Spectral congestion needs to be minimized for IR fingerprinting to be applicable as generically as possible. Considerably narrower bandwidths can be achieved when the

number of vibrationally excited states within the molecules are reduced by cooling them to low temperatures and applying, for example, messenger-tagging spectroscopic schemes,<sup>32-35</sup> which yield linear absorption spectra. The applicability of cryogenic ion spectroscopy to carbohydrates has recently been demonstrated using both low-temperature ion traps<sup>27-28</sup> and liquid helium droplets<sup>26</sup> to cool the ions. While decreasing the thermal internal energy distribution before spectral analysis is a prerequisite for resolved absorption bands, the isomeric heterogeneity of glycans will invariably result in the superposition of unique fingerprint spectra. In this case, the physical separation of isomers prior to spectroscopic investigation will greatly simplify the measured IR spectra and their analysis. Liquid chromatography is one of the most commonly applied techniques for carbohydrate isomer separation, but a mismatch in experimental timescales renders a combination of LC with gas-phase spectroscopic methods a challenging task. Nevertheless, this approach has been recently employed in a study of isomeric disaccharides using the stop-flow technique to extend the elution time of an LC-separated compound to that needed to acquire a room-temperature IR multiple photon dissociation spectrum.<sup>36</sup>

The timescale of IMS-MS, on the other hand, is ideally suited for combination with spectroscopy, and the potential of IMS to resolve small differences in size of isomeric molecules prior to their spectral analysis makes this approach particularly appealing.<sup>37-38</sup> We have previously demonstrated how orthogonal MS, IMS, and IR spectroscopic data of carbohydrates could serve as reference for identification of glycans from unknown samples and even from mixtures.<sup>28, 39</sup> We first used a drift-tube IMS instrument coupled to a cryogenic ion trap to measure the collision cross sections (CCS) of isomeric disaccharides prior to their spectroscopic analysis,<sup>27-28</sup> however it became evident that the IMS resolution provided by our 2 m drift tube would not be sufficient to resolve most of these species from a mixture. In addition, most of the carbohydrates we investigated showed either single or only partially resolved ion-mobility features, which does not reflect the situation in solution where all glycans with a free reducing-end OH are known to coexist in both their  $\alpha$  and  $\beta$  anomeric forms with distinct structures. Consequently, to separate glycan isomers as

completely as possible before spectroscopic interrogation, we constructed a new instrument where we combine ultrahigh-resolution IMS, using structures for lossless ion manipulation (SLIM),<sup>40-41</sup> with a cryogenic ion trap and a time-of-flight (TOF) MS to allow messenger-tagging IR spectroscopy of CCS- and *m/z*-selected glycans.<sup>39,42</sup> Using SLIM travelling-wave ion-mobility, we achieved a resolution of over 500 by cycling ions multiple times through a serpentine path, providing an extended drift length not feasible with conventional IMS methods.<sup>43</sup> We and others have shown that a resolving power between 100 and 300 is necessary to separate multiple species of disaccharides or larger milk oligosaccharides.<sup>39,42,44-</sup>

45

In this paper we demonstrate the ability to resolve  $\alpha$  and  $\beta$  anomers of reducing glycans by high-resolution SLIM IMS and measure a cryogenic IR spectrum of the separated species. We use selective oxygen-18 isotopic substitution to identify the anomeric OH band in the IR spectrum and assign each anomer by comparison with the spectra of the corresponding anomerically pure methylated species. The ability to separate and identify such species on a millisecond timescale is particularly significant in view of the recent evidence for retention of anomericity of a glycosidic bond upon collision-induced dissociation (CID).<sup>29</sup> Application of an IMS-MS-MS-IR spectroscopic workflow to the  $C_n$ -fragments of glycans should be able to verify under which conditions such anomeric retention occurs. This could then be incorporated into a CID-based sequencing scheme to determine the stereochemistry of glycosidic linkages. Rapid identification of anomers would also open new possibilities for online monitoring of the mutarotation process.

## 6.2. Materials and Methods

### 6.2.1 Samples

Samples were purchased from Dextra (UK) or Carbosynth (UK) and used without further purification. Solvents were purchased from Sigma-Aldrich. For electrospray ionization, samples were dissolved in water/methanol (*v/v* 50/50) to yield a final concentration of 50 -

100  $\mu\text{M}$ . To enhance the abundance of the here-investigated sodiated species, we added 1.5 equivalents of NaCl to the solution. Oxygen-18 isotope labeling of disaccharides was achieved by dissolving samples in  $\text{H}_2^{18}\text{O}$  and incubating them at room temperature for three days. It is known that only the anomeric OH at the reducing end exchanges under these conditions.<sup>46</sup>

## 6.2.2 Ion-mobility-selective IR spectroscopy

We use travelling-wave (TW) ion mobility implemented with structures for lossless ion manipulation (SLIM), developed by Smith and coworkers,<sup>40-41</sup> where the TW potentials created between a mirrored pair of printed circuit boards (15 x 15 cm in size) propel ions through a cyclic serpentine path (1.8 m single pass) to achieve high mobility resolution. The number of cycles  $n$  can be varied using an electrostatic switch.<sup>43</sup> A detailed description of the instrument can be found in Chapter 3. Briefly, ions are electrosprayed using commercial nano-emitters (Thermo Fisher) and transferred into the instrument through a capillary. A dual-stage ion funnel assembly<sup>47</sup> collimates and stores ions in the hour-glass section of the second funnel before pulses of ions, 120  $\mu\text{s}$  in duration, are released into the ion-mobility region where different species are separated based on their CCS.

After separation by their drift time, ions are ejected from the SLIM board, pass through a mass-resolving quadrupole, and sent to the cryogenic ion trap, which is held at a temperature of 40 K. Collisions with the cold buffer gas (10%  $\text{N}_2$  in He) leads to cooling and formation of nitrogen-tagged ions, allowing the application of messenger-tagging spectroscopy.<sup>32-35</sup> A single laser pulse (10 mJ) from an infrared optical parametric oscillator (OPO) irradiates the trapped ions before they are pulsed into the TOF region for  $m/z$  analysis. An IR spectrum is obtained by monitoring the wavelength-dependent dissociation yield of the nitrogen-tagged molecular ions. A single laser scan in the wavelength range reported here requires 6-8 minutes, and the spectra represent the average of two such scans.

## 6.3. Results and Discussion

### 6.3.1 IMS of glycans

In analogy to bimodal distributions in LC chromatograms that are often reported for glycans, ion mobility arrival time distributions (ATDs) can also exhibit multiple features that were speculated to originate from the respective  $\alpha$  and  $\beta$  anomers<sup>31, 42, 44</sup>, however, identification of the two anomeric forms has remained elusive. In the present study we investigated a set of roughly 20 different sodiated glycans ranging from small mono- and disaccharides to larger oligosaccharides using our ultrahigh-resolution IMS instrument, a subset of which is displayed in Figure 6.2(a). Most interestingly, all investigated glycans with a free reducing-end OH exhibit two features in their ATD. For the three disaccharides displayed here, seven separation cycles were necessary to resolve these different species, whereas nine cycles were required to resolve two different features of glucose (top panel). Other disaccharides and larger oligosaccharides require different number of separation cycles in the SLIM section (i.e., different IMS resolution) to separate two features (see Figure B.1 in Annex B).

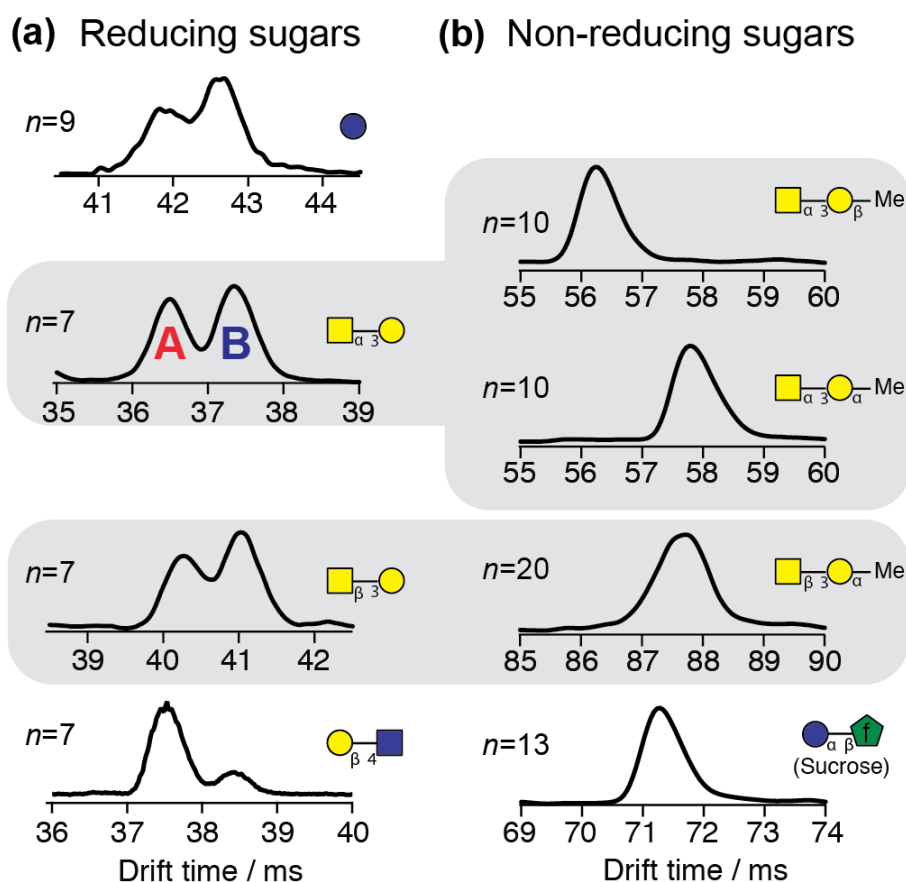


**Figure 6.2:** IMS arrival time distributions of reducing (a) and non-reducing glycans (b) at high IMS resolving power settings. The label  $n$  indicates the number of IMS cycles employed for separation.

Conversely, when the hydroxyl at the reducing end of a glycan is methylated, we observe only one peak in the ATDs, even at the higher resolving power reached after 20 separation cycles (Figure 6.2(b)). The absence of a second species can be interpreted by the locking of the reducing-end  $C_1$  atom upon methylation, blocking the mutarotation process that is responsible for coexisting  $\alpha$  and  $\beta$  anomers in solution (Figure 6.1(b)). Table sugar (sucrose) is also unable to form anomers, since the disaccharide is formed by  $C_1$ - $C_1$   $\alpha$ - $\beta$  glycosidic linkage of fucose and glucose and has no hydroxyl group at the reducing end. Its ATD in the bottom panel of Figure 6.2(b) shows only a single feature after 13 cycles, corresponding to an IMS resolution of approximately 300. In light of the observation that glycans with a

free OH at the reducing end always seem to exhibit two peaks in their ATD, we used cryogenic ion spectroscopy to identify these species.

### 6.3.2 Spectroscopic identification of anomers

The two mobility-separated species of sodiated GalNAc- $\alpha$ -(1-3)-Gal (labeled A and B in the ATD in Figure 6.2(a)) were selected by electrostatic deflection and loaded separately into the cryogenic trap where their infrared (IR) spectrum is measured. The results are displayed in Figure 6.3(b) and e for species A and B, respectively. Bands in the wavenumber range below 3550  $\text{cm}^{-1}$  can be attributed to strongly hydrogen-bonded OH and NH oscillators, while relatively free OH vibrational bands are expected to occur from 3600  $\text{cm}^{-1}$  and above.<sup>21</sup> The high sensitivity of IR spectroscopy to smallest structural details are reflected in these spectra. While most absorption bands appear at the same wavenumber with almost identical relative intensities between the spectra of the two drift peaks, other signals, such as the band around 3600  $\text{cm}^{-1}$  for species A and the broader absorption at 3630  $\text{cm}^{-1}$  for species B, are clearly characteristic of each structure. We expect a total of eight OH and NH oscillators for these molecules, which coincides with the number of resolved absorption bands in the spectrum of A. In the spectrum of B there appear to be only 7 bands, but the broad absorption signal around 3630  $\text{cm}^{-1}$  appears to be unresolved.

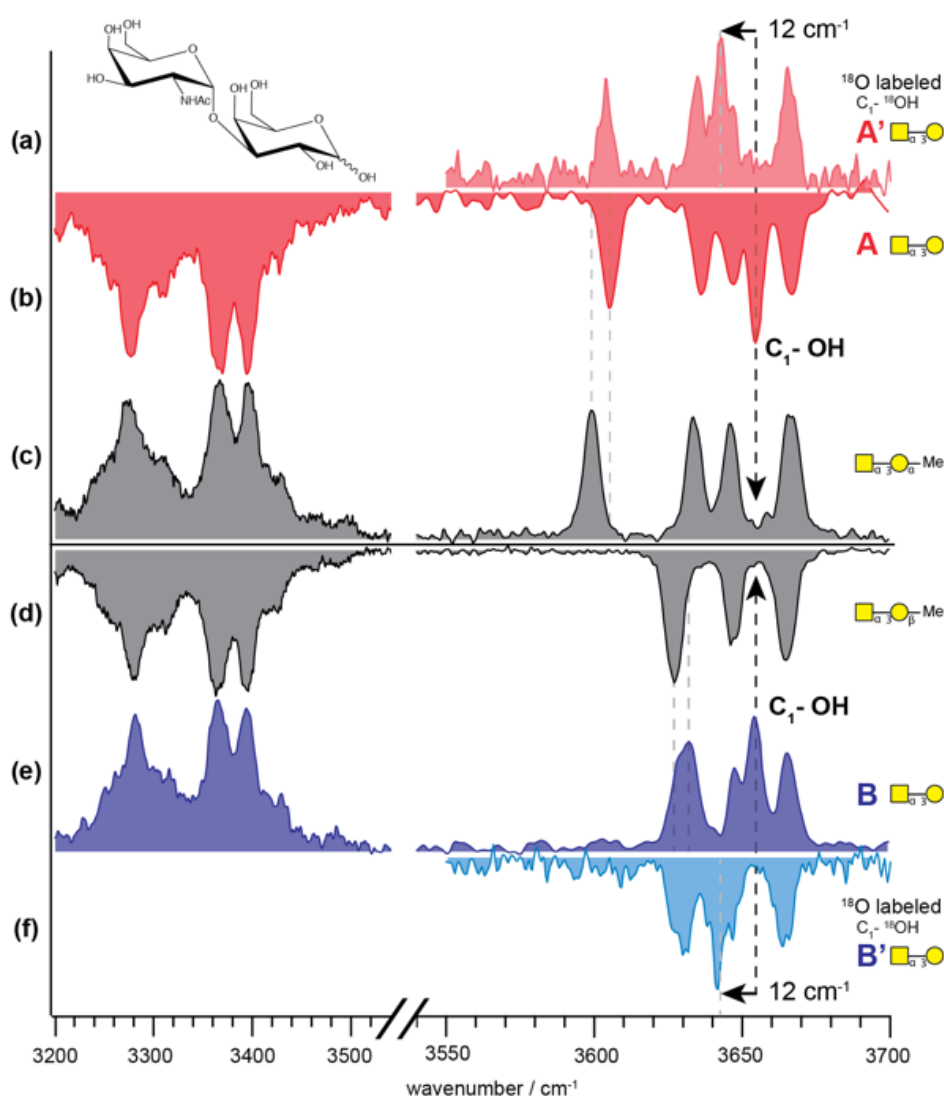


**Figure 6.3:** IR spectra of mobility-selected species A and B of sodiated GalNAc- $\alpha$ (1-3)-Gal ((b) and (e)) and their C<sub>1</sub>- $^{18}\text{OH}$  labelled equivalents ((a) and (f)) and the corresponding C<sub>1</sub>-O-methylated species with the C<sub>1</sub> locked in  $\alpha$  (c) or in  $\beta$  (d) configuration.

Proving the hypothesis that the two mobility-separated glycan species represent the  $\alpha$  and  $\beta$  anomers requires a deeper analysis of the IR spectra. The band corresponding to the anomeric C<sub>1</sub>-OH oscillator can be identified using oxygen-18 isotopic labelling, which should induce a spectral redshift. Indeed, a redshift of  $12\text{ cm}^{-1}$  corresponding to the change in reduced mass of the respective O-H oscillator can be observed for the absorption band at  $3655\text{ cm}^{-1}$  as the only noticeable change when comparing spectra A and B with those of

their C<sub>1</sub>-<sup>18</sup>O labelled analogs **A'** and **B'** in Figure 6.3(a) and (f), respectively. We thus identify the band at 3655 cm<sup>-1</sup> in the spectrum of both mobility-separated species as that from the anomeric OH.

Infrared spectra of the C<sub>1</sub>-methylated species of the same glycan with the C<sub>1</sub>-configuration locked in its  $\alpha$  and  $\beta$  positions are shown in Figure 6.3(c) and (d), respectively. Most noticeably, the absorption band at 3655 cm<sup>-1</sup> attributed to the C<sub>1</sub>-OH oscillator of the unsubstituted species is absent in these spectra, which is a direct result of the C<sub>1</sub>-O-CH<sub>3</sub> substitution. Moreover, the spectra of the methylated species resemble those of the corresponding unsubstituted species in the position and relative intensities of the remaining absorption bands. It is particularly striking that for each one of the two mobility-separated, unsubstituted species, its spectrum matches that of one of the methylated molecules to within a few cm<sup>-1</sup>. This leads to the conclusion that species **A** represents the  $\alpha$  anomer and species **B** represents the  $\beta$  anomer of GalNAc- $\alpha$ (1-3)-Gal. The same strategy to identify mobility-separated glycan anomers was applied to two additional disaccharides with similar results (see Figures B.2 and B.3 in Annex B).

### 6.3.3 Monitoring of glucose mutarotation

The ability to separate glycan anomers on a sub-second timescale can now be used to investigate the mutarotation process. When a sample of freshly prepared, anomerically pure  $\alpha$ -D-glucose is injected into our instrument, we observe a single IMS feature for singly sodiated ions after nine separation cycles (Figure 6.4(a)).

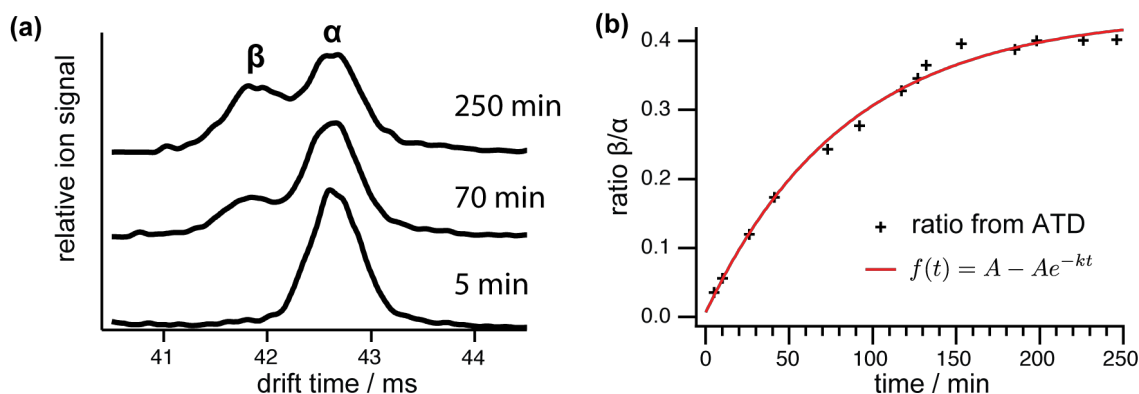


**Figure 6.4:** (a) ATDs of a sample of  $\alpha$ -D-Glucose at different times after sample preparation after  $n=9$  separation cycles. (b) Relative ratios of the drift signals corresponding to the  $\alpha$  and  $\beta$  anomers as a function of time after sample preparation.

After several minutes, a second feature at earlier drift times continues to increase in intensity until an equilibrium in relative signal intensities is reached after several hours (Figure 6.4(a), other traces). Given that  $\alpha$ -D-glucose will form its  $\beta$  anomer in an equilibrium reaction on the observed timescales, it is likely that the two observed mobility-separated species represent these  $\alpha$  and  $\beta$  anomers and an IR spectroscopic analysis of the two species separately and comparison of the resulting spectra to published reference spectra<sup>21</sup> confirms this assumption (Figure B.4, Annex B).

The IMS separation technique can thus be used to determine rate constants for the dynamic conversion reaction  $\alpha$ -D-glucose  $\rightleftharpoons_{k_{\beta}}^{k_{\alpha}}$   $\beta$ -D-glucose by simply monitoring the formation of the  $\beta$  species in real time. The ratio ( $\beta/\alpha$ ) of the relative intensities of the two signals in the ATD are plotted in Figure 6.4(b) as a function of time after sample preparation. The conversion can be treated as a first order reaction<sup>48-49</sup> and the resulting differential rate equation describing the concentration of the  $\beta$  species can be solved analytically by a function of the form  $f(t) = A - Ae^{-kt}$ , with the observable reaction rate  $k = k_{\alpha} + k_{\beta}$ . This function is represented by the solid red curve in Figure 6.4(b) using  $A$  and  $k$  as fit parameters, which can then be used to obtain the rate constants  $k_{\alpha}$  and  $k_{\beta}$  (for details see Annex B).<sup>48</sup> At the temperature and solvent conditions used here (25°C, MeOH/H<sub>2</sub>O

50/50) we determined  $k_{\alpha} = 0.88 \times 10^{-4} \text{ s}^{-1}$  and  $k_{\beta} = 1.13 \times 10^{-4} \text{ s}^{-1}$ , in accordance with previously published values.<sup>48, 50</sup>

## 6.4. Conclusions

We demonstrate the power of the combined ultrahigh-resolution IMS and cryogenic IR spectroscopic approach to separate and identify multiple species of different glycan structures. Cyclic IMS, which can be realized using structures for lossless ion manipulation (SLIM), provides remarkable resolving power and has previously been applied to separate multiple species of oligosaccharides.<sup>39, 42, 44-45</sup> The addition of an IR spectroscopic dimension allows us to probe the intramolecular hydrogen bonding network of the  $m/z$  and mobility-selected glycan species and is used here to identify the mobility-separated  $\alpha$  and  $\beta$  anomers of the reducing end of different disaccharides, in conjunction with oxygen-18 labelling techniques. We find evidence for the presence of multiple conformations with miniscule differences within each of the IMS separated  $\alpha$  and  $\beta$  anomer ensembles. The extraction of rate constants for the mutarotation reaction of glucose from IMS data follows as a direct application of the anomer separation capabilities and opens new doors for real-time kinetic studies, which could be used, for example, to investigate glycan anomericity and mutarotation after enzymatic release or cleavage of an oligosaccharide.<sup>51</sup>

Our results further highlight the benefit of ultrahigh-resolution IMS as a tool for rapid separation of different glycan structures on one hand, and illustrates the exquisite sensitivity of high-resolution vibrational spectroscopy to smallest structural differences on the other. Ongoing research in our and other laboratories is focused on the development of this IMS and IR fingerprinting technique into an analytical tool for routine glycan analysis.

## References

1. Warnke S., B. F. A., Scutelnic V, Rizzo T. R., Separation and Identification of Glycan Anomers Using Ultrahigh-Resolution Ion-Mobility Spectrometry and Cryogenic Ion Spectroscopy. *J. Am. Soc. Mass Spectrom.* **2019**, *30* (11), 2204–2211.
2. Varki, A., Biological roles of glycans. *Glycobiology* **2017**, *27* (1), 3-49.
3. Varki, A.; Cummings, R. D.; Esko, J. D.; Stanley, P.; Hart, G. W.; Aebi, M.; Darvill, A. G.; Kinoshita, T.; Packer, N. H.; Prestegard, J. H.; Schnaar, R. L.; Seeberger, P. H., *Essentials of Glycobiology*. 3rd ed.; Cold Spring Harbor Laboratory Press: 2017.
4. Varki, A., Biological roles of oligosaccharides: all of the theories are correct. *Glycobiology* **1993**, *3* (2), 97-130.
5. Dwek, R. A., Glycobiology: Toward Understanding the Function of Sugars. *Chemical Reviews* **1996**, *96* (2), 683-720.
6. Aebersold, R.; Mann, M., Mass spectrometry-based proteomics. *Nature* **2003**, *422* (6928), 198-207.
7. Shi, Y.; Xiang, R.; Horváth, C.; Wilkins, J. A., The role of liquid chromatography in proteomics. *Journal of Chromatography A* **2004**, *1053* (1-2), 27-36.
8. Zaia, J., Mass spectrometry of oligosaccharides. *Mass Spectrom Rev* **2004**, *23* (3), 161-227.
9. Veillon, L.; Huang, Y.; Peng, W.; Dong, X.; Cho, B. G.; Mechref, Y., Characterization of isomeric glycan structures by LC-MS/MS. *Electrophoresis* **2017**, *38* (17), 2100-2114.
10. Marino, K.; Bones, J.; Kattla, J. J.; Rudd, P. M., A systematic approach to protein glycosylation analysis: a path through the maze. *Nat Chem Biol* **2010**, *6* (10), 713-23.
11. Pigman, W.; Isbell, H. S., Mutarotation of Sugars in Solution\*: Part I: History, Basic Kinetics, and Composition of Sugar Solutions. *Advances in Carbohydrate Chemistry* **1968**, *23*, 11-57.
12. Bowers, M. T., Ion mobility spectrometry: A personal view of its development at UCSB. *International journal of mass spectrometry* **2014**, *370*, 75-95.

13. Lanucara, F.; Holman, S. W.; Gray, C. J.; Evers, C. E., The power of ion mobility-mass spectrometry for structural characterization and the study of conformational dynamics. *Nat Chem* **2014**, *6* (4), 281-94.
14. Liu, Y.; Clemmer, D. E., Characterizing oligosaccharides using injected-ion mobility/mass spectrometry. *Anal Chem* **1997**, *69* (13), 2504-9.
15. Lee, S.; Wyttenbach, T.; Bowers, M. T., Gas phase structures of sodiated oligosaccharides by ion mobility/ion chromatography methods. *International Journal of Mass Spectrometry and Ion Processes* **1997**, *167-168*, 605-614.
16. Hofmann, J.; Pagel, K., Glycan Analysis by Ion Mobility-Mass Spectrometry. *Angew Chem Int Ed* **2017**, *56* (29), 8342-8349.
17. Hofmann, J.; Stuckmann, A.; Crispin, M.; Harvey, D. J.; Pagel, K.; Struwe, W. B., Identification of Lewis and Blood Group Carbohydrate Epitopes by Ion Mobility-Tandem-Mass Spectrometry Fingerprinting. *Anal Chem* **2017**, *89* (4), 2318-2325.
18. Li, H.; Bendiak, B.; Siems, W. F.; Gang, D. R.; Hill, H. H., Jr., Carbohydrate structure characterization by tandem ion mobility mass spectrometry (IMMS)<sup>2</sup>. *Anal Chem* **2013**, *85* (5), 2760-9.
19. Manz, C.; Pagel, K., Glycan analysis by ion mobility-mass spectrometry and gas-phase spectroscopy. *Curr Opin Chem Biol* **2018**, *42*, 16-24.
20. Boyarkin, O. V., Cold ion spectroscopy for structural identifications of biomolecules. *International Reviews in Physical Chemistry* **2018**, *37* (3-4), 559-606.
21. Voss, J. M.; Kregel, S. J.; Fischer, K. C.; Garand, E., IR-IR Conformation Specific Spectroscopy of Na<sup>(+)</sup>(Glucose) Adducts. *J Am Soc Mass Spectrom* **2018**, *29* (1), 42-50.
22. Scutelnic, V.; Rizzo, T. R., Cryogenic Ion Spectroscopy for Identification of Monosaccharide Anomers. *J Phys Chem A* **2019**, *123* (13), 2815-2819.
23. Barnes, L.; Schindler, B.; Chambert, S.; Allouche, A.-R.; Compagnon, I., Conformational preferences of protonated N-acetylated hexosamines probed by InfraRed Multiple Photon Dissociation (IRMPD) spectroscopy and ab initio calculations. *International journal of mass spectrometry* **2017**, *421*, 116-123.

24. Contreras, C. S.; Polfer, N. C.; Oomens, J.; Steill, J. D.; Bendiak, B.; Eyler, J. R., On the path to glycan conformer identification: Gas-phase study of the anomers of methyl glycosides of N-acetyl-d-glucosamine and N-acetyl-d-galactosamine. *International journal of mass spectrometry* **2012**, *330-332*, 285-294.
25. Tan, Y.; Zhao, N.; Liu, J.; Li, P.; Stedwell, C. N.; Yu, L.; Polfer, N. C., Vibrational Signatures of Isomeric Lithiated N-acetyl-D-hexosamines by Gas-Phase Infrared Multiple-Photon Dissociation (IRMPD) Spectroscopy. *J Am Soc Mass Spectrom* **2017**, *28* (3), 539-550.
26. Mucha, E.; Gonzalez Florez, A. I.; Marianski, M.; Thomas, D. A.; Hoffmann, W.; Struwe, W. B.; Hahm, H. S.; Gewinner, S.; Schollkopf, W.; Seeberger, P. H.; von Helden, G.; Pagel, K., Glycan Fingerprinting via Cold-Ion Infrared Spectroscopy. *Angew Chem Int Ed* **2017**, *56* (37), 11248-11251.
27. Khanal, N.; Masellis, C.; Kamrath, M. Z.; Clemmer, D. E.; Rizzo, T. R., Cryogenic IR spectroscopy combined with ion mobility spectrometry for the analysis of human milk oligosaccharides. *Analyst* **2018**, *143* (8), 1846-1852.
28. Masellis, C.; Khanal, N.; Kamrath, M. Z.; Clemmer, D. E.; Rizzo, T. R., Cryogenic Vibrational Spectroscopy Provides Unique Fingerprints for Glycan Identification. *J Am Soc Mass Spectrom* **2017**, *28* (10), 2217-2222.
29. Schindler, B.; Barnes, L.; Renois, G.; Gray, C.; Chambert, S.; Fort, S.; Flitsch, S.; Loison, C.; Allouche, A. R.; Compagnon, I., Anomeric memory of the glycosidic bond upon fragmentation and its consequences for carbohydrate sequencing. *Nat Commun* **2017**, *8* (1), 973.
30. Saparbaev, E.; Kopysov, V.; Yamaletdinov, R.; Pereverzev, A.; Boyarkin, O. V., Interplay of H-bonds with Aromatics in Isolated Complexes Identifies Isomeric Carbohydrates. *Angewandte Chemie International Edition* **2019**, doi:10.1002/ange.201902377.
31. Hernandez, O.; Isenberg, S.; Steinmetz, V.; Glish, G. L.; Maitre, P., Probing Mobility-Selected Saccharide Isomers: Selective Ion-Molecule Reactions and Wavelength-Specific IR Activation. *J Phys Chem A* **2015**, *119* (23), 6057-64.

32. Wolk, A. B.; Leavitt, C. M.; Garand, E.; Johnson, M. A., Cryogenic ion chemistry and spectroscopy. *Acc Chem Res* **2014**, *47* (1), 202-10.
33. Leavitt, C. M.; Wolk, A. B.; Fournier, J. A.; Kamrath, M. Z.; Garand, E.; Van Stipdonk, M. J.; Johnson, M. A., Isomer-Specific IR-IR Double Resonance Spectroscopy of D2-Tagged Protonated Dipeptides Prepared in a Cryogenic Ion Trap. *J Phys Chem Lett* **2012**, *3* (9), 1099-105.
34. Masson, A.; Kamrath, M. Z.; Perez, M. A.; Glover, M. S.; Rothlisberger, U.; Clemmer, D. E.; Rizzo, T. R., Infrared Spectroscopy of Mobility-Selected H<sup>+</sup>-Gly-Pro-Gly-Gly (GPGG). *J Am Soc Mass Spectrom* **2015**, *26* (9), 1444-54.
35. Goebbert, D. J.; Wende, T.; Bergmann, R.; Meijer, G.; Asmis, K. R., Messenger-tagging electrosprayed ions: vibrational spectroscopy of suberate dianions. *J Phys Chem A* **2009**, *113* (20), 5874-80.
36. Schindler, B.; Laloy-Borgna, G.; Barnes, L.; Allouche, A. R.; Bouju, E.; Dugas, V.; Demesmay, C.; Compagnon, I., Online Separation and Identification of Isomers Using Infrared Multiple Photon Dissociation Ion Spectroscopy Coupled to Liquid Chromatography: Application to the Analysis of Disaccharides Regio-Isomers and Monosaccharide Anomers. *Anal Chem* **2018**, *90* (20), 11741-11745.
37. Warnke, S.; Seo, J.; Boschmans, J.; Sobott, F.; Scrivens, J. H.; Bleiholder, C.; Bowers, M. T.; Gewinner, S.; Schollkopf, W.; Pagel, K.; von Helden, G., Protomers of benzocaine: solvent and permittivity dependence. *J Am Chem Soc* **2015**, *137* (12), 4236-42.
38. Kamrath, M. Z.; Rizzo, T. R., Combining Ion Mobility and Cryogenic Spectroscopy for Structural and Analytical Studies of Biomolecular Ions. *Acc Chem Res* **2018**, *51* (6), 1487-1495.
39. Ben Faleh, A.; Warnke, S.; Rizzo, T. R., Combining Ultrahigh-Resolution Ion-Mobility Spectrometry with Cryogenic Infrared Spectroscopy for the Analysis of Glycan Mixtures. *Anal Chem* **2019**, *91* (7), 4876-4882.
40. Hamid, A. M.; Ibrahim, Y. M.; Garimella, S. V.; Webb, I. K.; Deng, L.; Chen, T. C.; Anderson, G. A.; Prost, S. A.; Norheim, R. V.; Tolmachev, A. V.; Smith, R. D.,

Characterization of Traveling Wave Ion Mobility Separations in Structures for Lossless Ion Manipulations. *Anal Chem* **2015**, *87* (22), 11301-8.

41. Deng, L.; Ibrahim, Y. M.; Hamid, A. M.; Garimella, S. V.; Webb, I. K.; Zheng, X.; Prost, S. A.; Sandoval, J. A.; Norheim, R. V.; Anderson, G. A.; Tolmachev, A. V.; Baker, E. S.; Smith, R. D., Ultra-High Resolution Ion Mobility Separations Utilizing Traveling Waves in a 13 m Serpentine Path Length Structures for Lossless Ion Manipulations Module. *Anal Chem* **2016**, *88* (18), 8957-64.

42. Warnke, S.; Ben Faleh, A.; Pellegrinelli, R. P.; Yalovenko, N.; Rizzo, T. R., Combining ultra-high resolution ion mobility spectrometry with cryogenic IR spectroscopy for the study of biomolecular ions. *Faraday Discuss* **2019**, doi:10.1039/c8fd00180d.

43. Deng, L.; Webb, I. K.; Garimella, S. V. B.; Hamid, A. M.; Zheng, X.; Norheim, R. V.; Prost, S. A.; Anderson, G. A.; Sandoval, J. A.; Baker, E. S.; Ibrahim, Y. M.; Smith, R. D., Serpentine Ultralong Path with Extended Routing (SUPER) High Resolution Traveling Wave Ion Mobility-MS using Structures for Lossless Ion Manipulations. *Anal Chem* **2017**, *89* (8), 4628-4634.

44. Nagy, G.; Attah, I. K.; Garimella, S. V. B.; Tang, K.; Ibrahim, Y. M.; Baker, E. S.; Smith, R. D., Unraveling the isomeric heterogeneity of glycans: ion mobility separations in structures for lossless ion manipulations. *Chem Commun* **2018**, *54* (83), 11701-11704.

45. Ujma, J.; Ropartz, D.; Giles, K.; Richardson, K.; Langridge, D.; Wildgoose, J.; Green, M.; Pringle, S., Cyclic Ion Mobility Mass Spectrometry Distinguishes Anomers and Open-Ring Forms of Pentasaccharides. *Journal of the American Society for Mass Spectrometry* **2019**.

46. Risley, J. M.; Van Etten, R. L., Kinetics of oxygen exchange at the anomeric carbon atom of D-glucose and D-erythrose using the oxygen-18 isotope effect in carbon-13 nuclear magnetic resonance spectroscopy. *Biochemistry* **2002**, *21* (25), 6360-6365.

47. Chen, T. C.; Fillmore, T. L.; Prost, S. A.; Moore, R. J.; Ibrahim, Y. M.; Smith, R. D., Orthogonal Injection Ion Funnel Interface Providing Enhanced Performance for Selected Reaction Monitoring-Triple Quadrupole Mass Spectrometry. *Analytical Chemistry* **2015**, *87* (14), 7326-31.

48. Lin, C. E.; Yu, C. J.; Chen, C. L.; Chou, L. D.; Chou, C., Kinetics of glucose mutarotation assessed by an equal-amplitude paired polarized heterodyne polarimeter. *J Phys Chem A* **2010**, *114* (4), 1665-9.
49. Ballash, N. M.; Robertson, E. B., The Mutarotation of Glucose in Dimethylsulfoxide and Water Mixtures. *Can. J. Chem.* **1972**, *51*, 556-564.
50. Kendrew, J. C.; Moelwyn-Hughes, E. A., The Kinetics of Mutarotation in Solution. *Proceedings of the Royal Society of London. Series A, Mathematical and Physical Sciences* **1940**, *176* (966), 352-367.
51. Shen, Y. H.; Tsai, S. T.; Liew, C. Y.; Ni, C. K., Mass spectrometry-based identification of carbohydrate anomeric configuration to determine the mechanism of glycoside hydrolases. *Carbohydr Res* **2019**, *476*, 53-59.



## 7. Design and characterization of second-generation instrument

In this chapter, we present an overview of a second-generation instrument combining SLIM IMS with messenger-tagging cryogenic IR spectroscopy. This machine was designed as an upgrade to the prototype described in Chapter 3 to overcome limitations in IMS resolution, IR spectral acquisition speed, and overall data quality. The design details of the home-built apparatus, as well as the newly implemented features, are presented in the following sections.

### 7.1. Overview

An overview of the instrument layout is shown in Figure 7.1, with detailed information about specific elements of the machine to follow in subsequent sections. The machine consists of an ESI dual-funnel ion source, a TW SLIM IMS device, ion optics designed to guide the charged analytes through differential pumping stages, a cryogenic multi-trap assembly, and a time-of-flight mass analyzer. Ions are produced by nano-ESI and transferred through a heated stainless-steel capillary into vacuum and towards the dual-funnel ion source assembly (MassTech, US), similar to the one used in our prototype instrument. The continuous ion current then passes a conductance limit separating the ion funnel assembly from the IMS region and travels towards a ring electrode ion guide with a morphed inner geometry placed at the entrance of the SLIM module (entrance guide). Ions are accumulated in a 2 m section of the SLIM module and released in pulses ranging from hundreds of  $\mu\text{s}$  to 10 ms in duration, which then undergo one or more cycles along the serpentine path for mobility separation. After separation, ions are diverted off the SLIM module and sent through a second ring-electrode guide (exit guide), which has a morphed inner geometry reversed compared to the entrance guide.

Ions are then guided through differential pumping stages into high vacuum. The differential pumping is achieved using a segmented chamber mounted on a multi-stage pump. The first pumping stage includes a third ring-electrode guide with a uniform inner radius, followed by a quadrupole and an octupole in the second stage. A lens assembly is embedded between the second and third pumping stages. A second octupole guide and planar ion guide assembly are placed in the third stage of the segmented chamber. The planar RF guide consists of a pair of PCBs placed in parallel, similar to a SLIM module. Slits between RF electrodes on both PCBs represent an extraction region that offers the possibility to record ATDs by extracting ions orthogonally to their flight direction into two channeltron detectors.

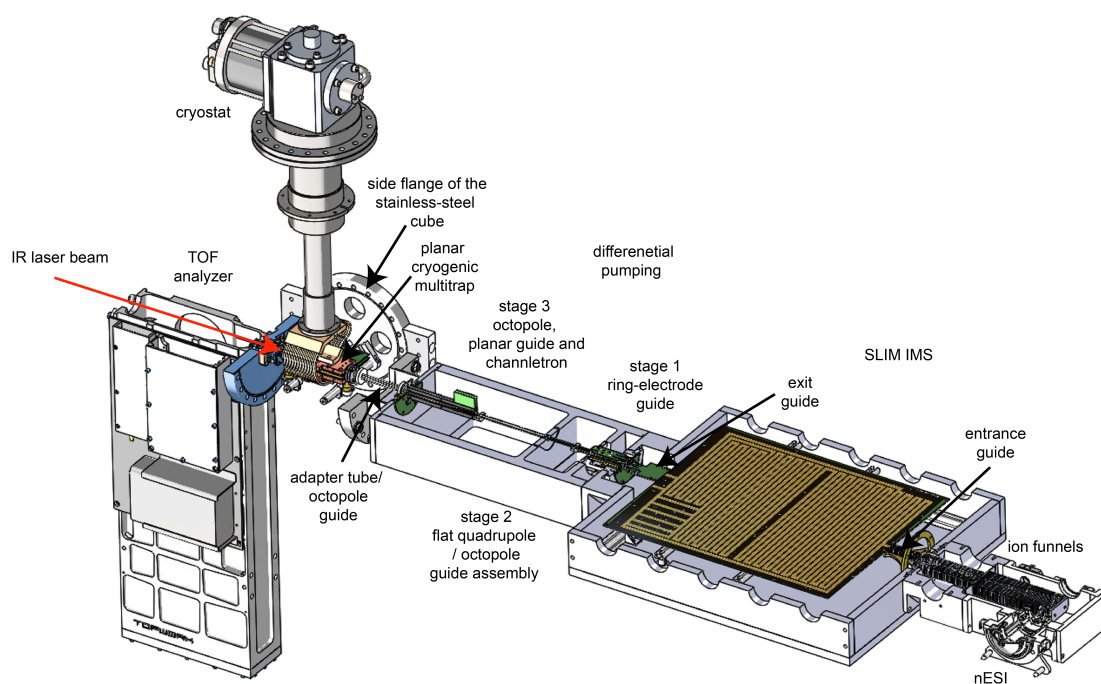


**Figure 7.1:** Schematic overview of the instrument combining ultrahigh resolution SLIM IMS with messenger-tagging cryogenic IR spectroscopy in a multiplexed approach. The cryogenic multi-trap is enclosed within a stainless-steel chamber which does not appear in the schematic.

The differential pumping chamber is connected to a stainless-steel cube through an adapter tube. An octupole ion guide is mounted at the entrance of the adapter tube and is used to

bridge the gap between the conductance limit separating the cube from the segmented chamber and the planar cryogenic multi-trap assembly. The multi-trap assembly includes Einzel lens assemblies at the entrance and at the exit, which focus the ion beam coming into and going out of the trap.

The electrode design of the trap follows the same principle used in the planar PCB trap described in Chapter 3, with the important distinction that additional DC electrodes allow the elongated trap to be segmented into multiple sub-traps. This allows multiple mobility-separated species to be trapped, N<sub>2</sub> tagged, and interrogated with the same laser pulse and within the same measurement cycle. This technical innovation represents an important step towards high-throughput analysis of biomolecular isomers. Details of the new trap assembly and operations will be presented below. Ions exiting the trap pass through different ion optics including electrostatic lenses and steering plates, which enable manipulating the focal point of the ion beam as well as its vertical and horizontal direction of flight. After exiting the multi-trap, ions are pulsed perpendicular to their direction of motion towards a commercial TOF mass analyzer (TOFWERK AG, Switzerland). The TOF chamber design includes a window that provides optical access to the multi-trap region, enabling the overlap between an IR beam and the trapped ion cloud.

## 7.2. Vacuum system

Accurate control over the pressure at different stages of the setup is required for the operation of the different experimental techniques that are combined in the IMS-CIS instrument. While the vacuum system is similar to the one described in Chapter 3, an optimized pumping scheme was designed for this second-generation instrument. It comprises eight different pressure regions ranging from atmospheric pressure for ion generation to 10<sup>-8</sup> mbar at the TOF mass analyzer.

The operating pressure regimes of the different sections of the instrument are shown in Figure 7.2, depicted by different colors.

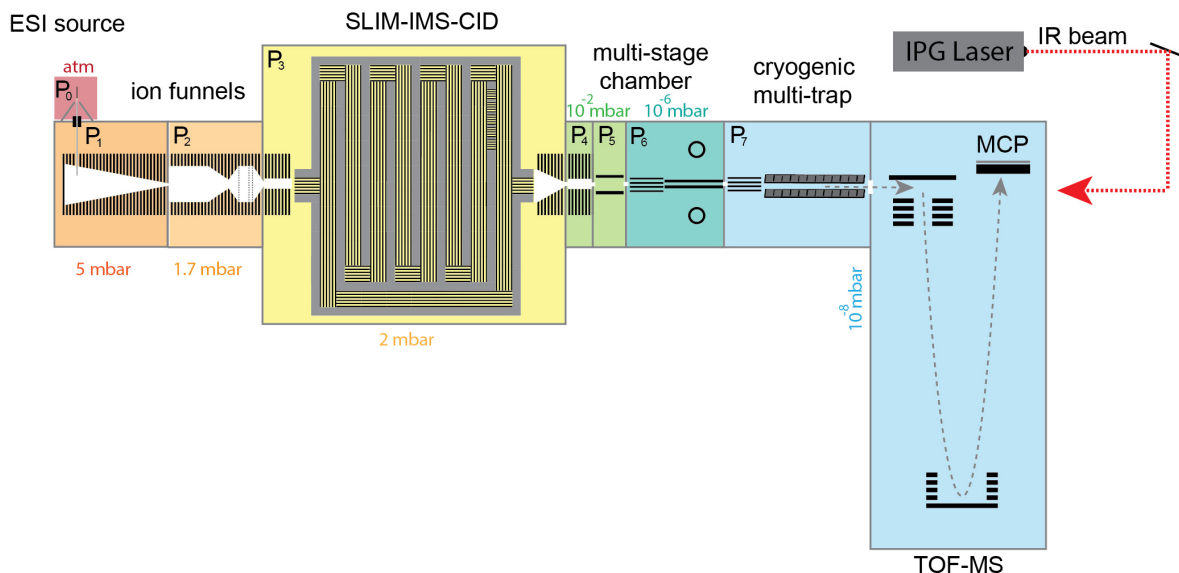


**Figure 7.2:** Schematic of the instrument displaying the operating pressure regimes for different section: ESI at atmospheric pressure (red); dual ion funnel and SLIM IMS device at mbar pressure (orange, yellow); differential pumping stages including a ring-electrode guide, several multipole guides, a planar RF guide, and two channeltron detector at  $10^{-2}$ - $10^{-6}$  mbar (green, turquoise); a cryogenic, planar multi-trap and TOF analyzer  $<10^{-7}$  mbar (blue).

The ion funnel source and the SLIM IMS region are operated in the mbar regime (orange – yellow in Figure 7.2). The regions are separated by conductance limiting electrodes, and the pressures are controlled by two scroll pumps (XDS 35i, Edwards) as well as two flow controllers (MKS). The gas flow is directed from the SLIM region towards the ion funnel source to ensure the purity of the buffer gas used for IMS operations. Typical operating pressures when using  $N_2$  gas are between 4 - 6 mbar for the first stage of the ion funnel  $P_1$ , 1.2 - 2.5 mbar for  $P_2$  at the second stage of the ion funnel, and 1.5 to 3 mbar for  $P_3$  at the SLIM IMS chamber. Both  $P_2$  and  $P_3$  are monitored using high precision MKS pressure gauges, as they are crucial for IMS measurements.

The differential pumping chamber following the IMS module is pumped using a multi-stage turbo pump (Leybold, GmbH) backed by a scroll pump (Edwards). The first sub-

chamber is held at  $P_4 \sim 10^{-2}$  mbar (depicted in green in Figure 7.2), and the last sub-chamber including the planar RF guide and channeltron detector is operated at high vacuum with  $P_6 \sim 10^{-7}$  mbar (depicted in turquoise in Figure 7.2). The different pressures are monitored *via* Pirani and Penning-type pressure gauges (Pfeiffer).

The cubic chamber containing the multi-trap assembly and the TOF region are pumped using separate turbo pumps (Pfeiffer) and are operated at  $P_7 \sim 10^{-8}$  mbar (depicted in blue in Figure 7.2).

During operation, we distinguish between two modes: (1) IMS-MS mode, where the cryogenic trap is operated as an RF guide, and (2) spectroscopy mode, where ions are trapped, tagged, irradiated with IR light, and gently unloaded toward the TOF mass analyzer. During operation in the IMS-MS mode, the trap region is operated a constant pressure of  $\sim 10^{-6}$  mbar, which enhances the ion transmission by reducing the energy spread of the ions *via* collisional damping for a more efficient extraction in the time-of-flight tube.

In spectroscopy mode, a solenoid-actuated valve (Parker 9 series) is used to introduce a short gas pulse (typically a 9:1 mixture of He:N<sub>2</sub>) into the multi-trap prior to the ions arrival. The gas molecules are cooled upon collisions with the cold trap surfaces and ensure the cooling and tagging of the ions prior to spectroscopic interrogation. The gas is pumped out prior to unloading the trapped ions toward the TOF mass analyzer, to avoid dissociation of the tags from the analyte molecules.

### 7.3. Radio frequency devices for ion manipulation

The instrument includes several RF devices having different geometries and operated in different pressure regimes. In this section we will describe the design and operation modes of the custom-designed ring electrode guides, as well as the planar RF devices, which include

the TW SLIM IMS module, the planar RF guide in the differential pumping region, and the segmented, cryogenic multi-trap.

### 7.3.1 Ring electrode ion guides

All ring-electrode ion guides are operated using a combination of RF and DC voltages as described in section 3.3. The first vacuum stage of the instrument consists of the same commercial dual ion funnel assembly (MassTech, US) used in the first prototype (see Figure 3.6 of Chapter 3). Here, the funnel is exclusively used as an ion guide that focuses and transmits the ion cloud through the mbar pressure region, as opposed to its use for ion accumulation as was the case for the prototype.

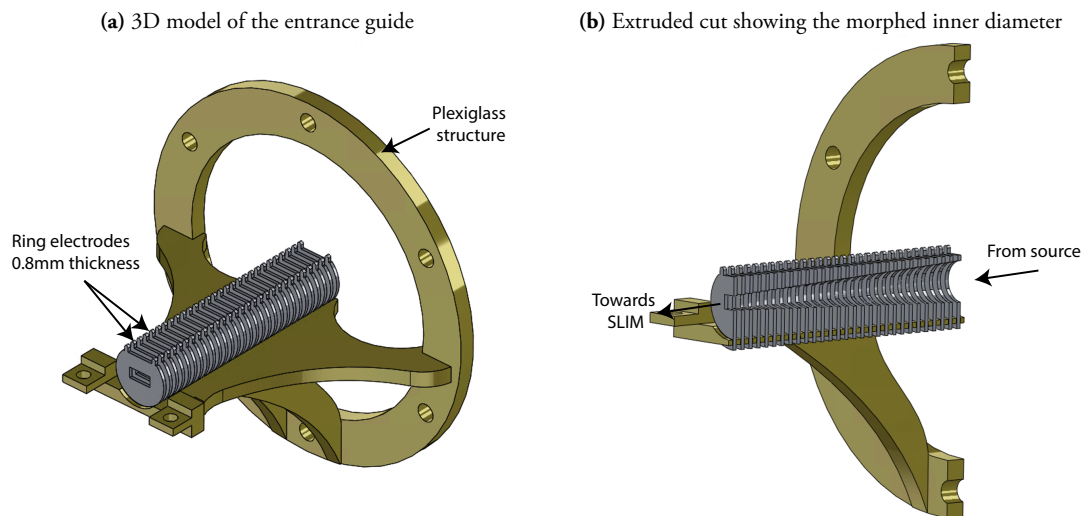


**Figure 7.3:** (a) 3D model of the entrance guide displaying ring electrodes and the plexiglass structure used for mounting. (b) Cross-sectional view of the entrance guide displaying the morphed inner geometry of the ring electrodes).

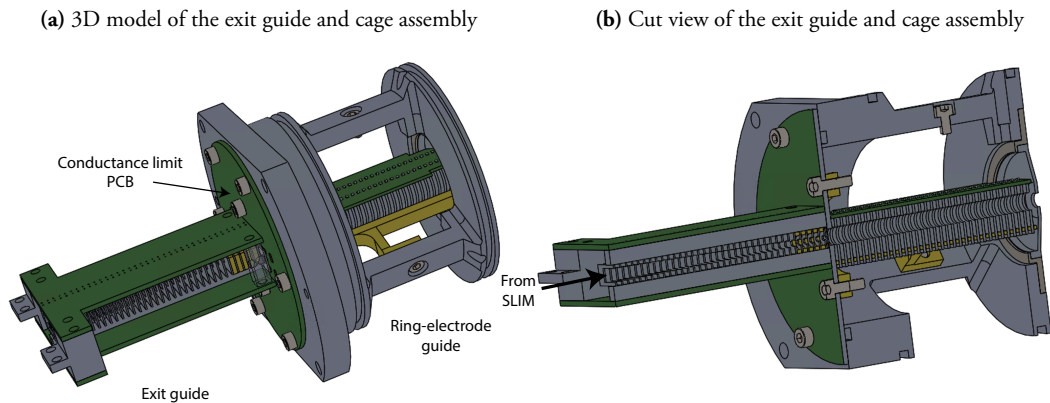


**Figure 7.4:** (a) 3D model of the assembly displaying the exit guide (left) and the third ring-electrode guide (right). Both guides are mounted on a circular PCB that serves as a conductance limit separating the SLIM region and the first differential pumping stage. Cross-sectional view of the assembly displaying the morphed inner geometry of the exit guide and the constant inner diameter of guide 3.

Ring-electrode guides (Figure 7.3 and Figure 7.4) are installed at the entrance and at the exit of the SLIM IMS module and have a morphed inner geometry to ensure a smooth transition of the ions into and out of the SLIM. A third ring-electrode guide (Figure 7.4) is placed in the first differential pumping region following the SLIM chamber. All ring-electrode guides are composed of stainless-steel electrodes assembled on custom mounting structures. The electrodes have a thickness of 0.8 mm and are separated by 0.5 mm from each other. All electrical connections of the ring guides are realized by PCBs which are soldered directly to the electrodes.

The ring electrodes of the entrance guide are placed in equidistant slits milled into a plexiglass structure, which defines the distance between adjacent electrodes. The assembly is glued using an epoxy glue and mounted on the SLIM chamber. The exit-guide electrodes, however, were designed differently. Electrodes include connector pins on both sides (top and bottom) and are held together in a ‘sandwich’ between two PCBs, which are directly soldered onto the electrodes. The third ring-electrode guide has a circular inner geometry with a constant radius and is mounted on a cage-like aluminum structure. Figure 7.4 shows the assembly formed by the third guide and the exit guide. Both are mounted on either side

of a circular PCB, which serves as a conductance limit separating the SLIM region and the first differential pumping stage, as well as containing a feedthrough for the electrical connections needed for the third guide.

### 7.3.2 Multipole devices

The instrument includes a flat quadrupole ion guide as well as two octupole guides. These are composed of stainless-steel and molybdenum rods, respectively, held together by structures made from PEEK. The flat quadrupole and the first octupole are mounted onto the lid of the differential pumping chamber. The second octupole is mounted using a clamp structure on a conductance limiting PCB separating the differential pumping chamber and the adapter tube preceding the stainless-steel cube housing the cryogenic multi-trap.

### 7.3.3 Planar RF Devices

The instrument includes three planar RF devices used for different purposes: a TW SLIM device for IMS, a planar RF ion guide, and a planar cryogenic multi-trap.

#### TW SLIM IMS device

Ultrahigh-resolution IMS is performed using a TW SLIM device. While the electrode design is the same as the prototype described in Chapter 3, the device includes several new features. The larger size of the boards (50 cm x 40 cm) enables a single-pass drift path of 10 m, which allows for a much higher peak capacity. The higher peak capacity prevents ions of different mobilities from overlapping in the separation region, thus allowing for the analysis of complex samples including several species with a wide range of mobilities. It also allows to perform an increased number of separation cycles before compact ions start catching up to more elongated ones within the separation path.

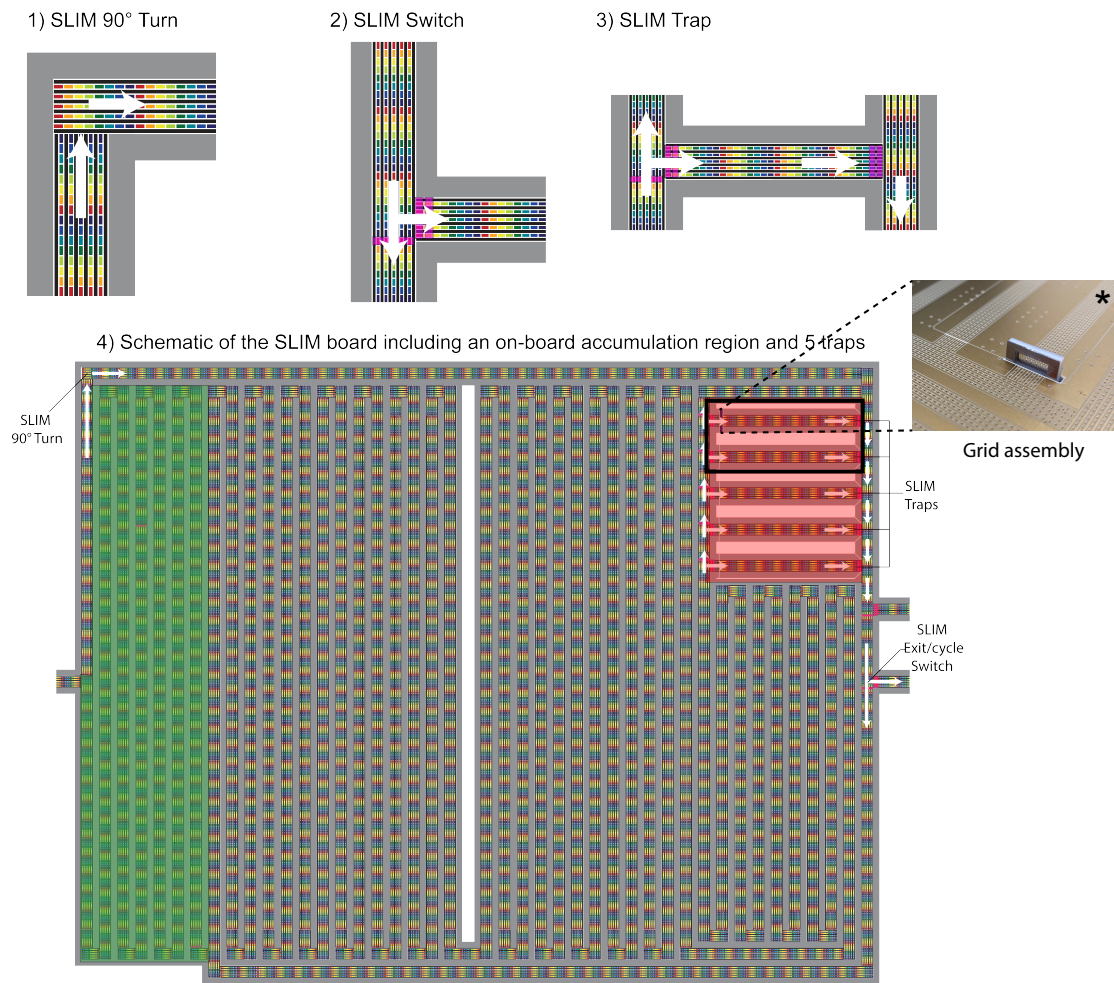


**Figure 7.5:** An illustration of different SLIM components used to build a 10 m SLIM board. (1) 90° turns, (2) switches, (3) traps, and (4) a 10 m serpentine separation path and picture of the CID grid assembly (\*).

The SLIM module includes multiple regions shown in different colors in Figure 7.5. The first section of the board (depicted in green) is used for ion accumulation prior to releasing ion pulses into the rest of the board for separation. The large size (2 m) of this region enables a high ion utilization efficiency compared to the use of the hour-glass region in the ion-funnel trap, as was the case for the prototype. The TW parameters in this section are controlled separately from the rest of the board, and a row of DC pads at the end of the section is used as a switch to block ions during accumulation and release them in pulses to

start the separation cycle. The voltage applied to these pads is switched between the blocking DC voltage of  $\sim 50$  V relative to the bias of the SLIM boards, and the TW potential during the 'open' state of the switch.

Furthermore, the new design includes 5 SLIM traps based on the design of the SLIM T-switches, which are placed towards the end of the path, as shown in Figure 7.5 (region depicted in red). By routing the ions in a controlled manner, it is possible to trap them and release them in defined time sequences. The SLIM traps offer a multitude of possibilities and can be used to simplify ATDs by unloading previously mobility-separated ions in predefined sequences, compressing empty space between ion packets, and enriching specific species from a low concentration sample. Two of the five SLIM traps (top black square in the red region in Figure 7.5) have separate electric connections, decoupling the bias, RF, TW, and guard electrodes from the rest of the board. Controlling the voltage applied to these electrodes offers the possibility to perform fragmentation *via* collision induced dissociation (CID).<sup>1</sup> Fragmentation is achieved by loading the ions into the trap region while creating a voltage step (typical values  $\sim 100$  V) at the entrance of this region. The acceleration of the analyte ions upon entry to the trap leads to collisions with the  $N_2$  buffer gas, leading to the dissociation of the parent ions. One of the CID traps also includes a grid assembly (\* panel in Figure 7.5) that is composed of two grids separated by a Teflon spacer of 0.8 mm thickness. By applying a voltage gradient across the grid assembly, it is possible to create a well-defined electric field that accelerates the ions leading to fragmentation.

## Planar RF guide

The third section of the differential pumping chamber includes a planar RF guide composed of a pair of PCBs. A schematic of this guide is shown in Figure 7.6(a). The assembly is supported by a pair of solid guard electrodes (stainless steel) inserted between the PCBs, which also define the distance between the boards (5 mm). The structure is mounted onto a round conductance limit PCB that separates the differential pumping chamber from the

cryogenic multi-trap region. The boards include 4 RF electrodes, 3 DC stripes, a pair of solid guard electrodes, as well as slits between RF electrodes for ion extraction. The guide was designed such that the slits are facing channeltron detectors on each side of the assembly. This way, ions can either be guided through the RF device towards the conductance limit or be extracted perpendicular to their flight direction towards the channeltron detectors. The overall assembly is shown in Figure 7.6(b).

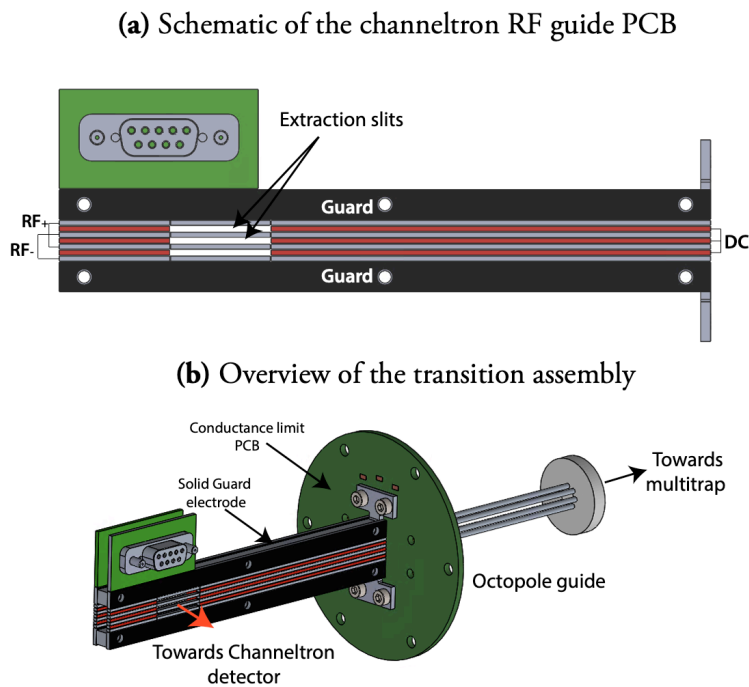


**Figure 7.6:** (a) Schematic of the planar RF guide PCB showing the different electrode designs. RF electrodes depicted in gray, DC bias electrodes depicted in red, and guard electrodes depicted in black. (b) An overview of the transition assembly including the planar RF guide and an octupole guide. The assembly is mounted on either side of a circular PCB that plays the role of a conductance limit.

## Planar cryogenic multi-trap assembly

One of the unique features of this instrument is the cryogenic multi-trap device. The implementation of this device aims to enable multiplexed spectral acquisition of multiple isomeric species simultaneously. Among the crucial aspects to take into consideration while

implementing a new technology for analytical purposes, is the duration of a measurement. While an IR spectrum contains specific features that allow for unambiguous identification of different isomers, adding a spectral acquisition step leads to an increased total measurement time. Over the last years, major improvements in term of sensitivity and signal stability of our instruments as well as the use of a new commercial light source, has allowed us to reduce spectral acquisition time from ~40 min, down to 1-3 minutes per spectrum. For a complex biological sample with ten analytes of interest, for example, the acquisition time would be in the order of tens of minutes.

The multiplexed approach was developed to reduce the acquisition time. By using a segmented trap, it is possible to trap mobility-separated isomers in different compartments. Isomers with different mobilities are loaded sequentially into the multi-trap and then cooled and tagged by collisions with the cold buffer gas that is pulsed in the trap region prior to the ions arrival. The process of sequentially loading analytes requires on the order of milliseconds and does not impact the measurement time.

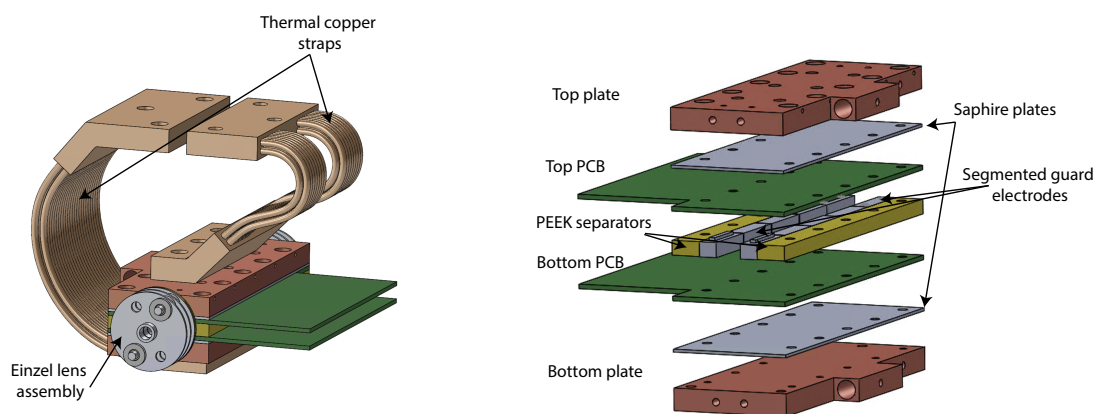


**Figure 7.7:** 3D model of the cryogenic multi-trap assembly including Einzel-lens assemblies at the entrance and exit of the trap and thermal straps connecting the trap to the cold head of the cryostat. The left panel of the figure shows an exploded view of the trap including the top and bottom copper plates, sapphire plates, segmented guard electrodes and PEEK separators.

The trap assembly including the entrance and exit Einzel lenses and copper thermal straps are shown in the left panel of Figure 7.7. An exploded view of the multi-trap assembly is shown in the right panel of Figure 7.7. The planar cryogenic multi-trap is composed of a pair of PCBs (Rodgers 4k series) separated by solid guard electrodes, which define the distance between the boards (5 mm) and help restrict the gas flow inside the trap. The gas is pulsed through a 2 mm opening in one of the solid electrodes and is pumped through the entrance and exit of the trap assembly.

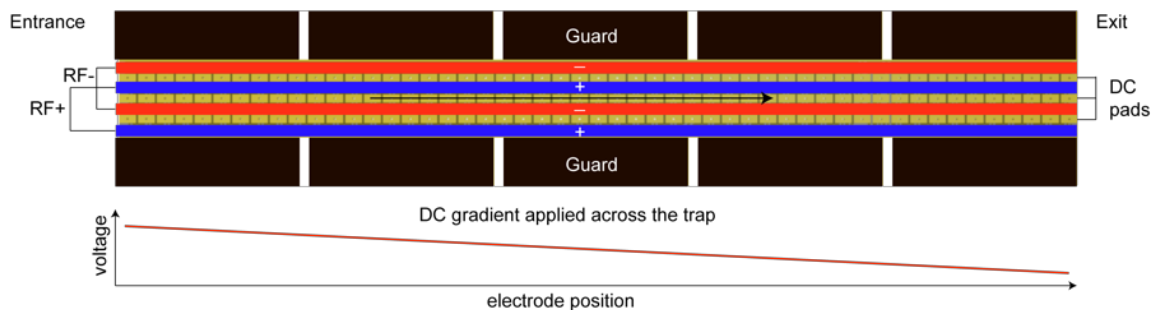


**Figure 7.8:** Representation of the trap PCB. The RF electrodes are depicted and red and blue for denoting the different RF phases applied to them. The DC pads are depicted in gold, and the segmented guard electrodes in black. A gradient is applied across the trap to unload the trapped ions.

The basic principle of the multi-trap electrode design is similar to that of the planar trap described in Chapter 3, with the difference being a more elongated shape and additional DC electrodes to divide the trap volume into separate segments. Figure 7.8 shows the electrode design of the trap PCBs, which includes 4 RF electrodes (blue and red) that extend through the entire length of the trap. It also includes 51 separately controlled columns of 3 DC pads each (gold) that ensure the transport and trapping of ions. This device can thus be used as a single ion trap or as a segmented trap with up to 10 compartments with 5 columns of DC pads each. Five guard electrodes on either side of the trap (black segments) are used to ensure ion confinement in the direction perpendicular to the long axis of the trap. The use of segmented guard electrodes allows to adapt the guard voltage to the potential gradient applied to the DC pads at different positions of the trap. The PCBs are

'sandwiched' by two copper plates placed on the top and bottom to ensure homogenous cooling. Each copper plate is connected to the cold head of a He closed-cycle, dual-stage refrigerator (RDK 408 Sumitomo, Japan) through thermal straps made of braided OFHC grade copper. Sapphire plates are placed between each PCB and its corresponding copper plate to ensure a good thermal contact while insulating the electric connections from the grounded copper plates. Cartridge heaters are placed in specific compartments of the copper plates and enable to control the temperature of the trap using a temperature controller (Lake Shore Cryotronics, Inc.). A pair of Einzel lens assemblies are placed on both the entrance and exit of the trap assembly and are used to focus the ion beam. The entire assembly is supported by an aluminum structure, attached to one of the side flanges of the cube chamber, which is mounted on rails for the ease of assembly and alignment.

The choice of the electrode geometry and spacing and the guard design was based on SIMION simulations of several configurations. The size of the electrodes was optimized to fit the 5 mm separation between the pair of PCBs needed to accommodate the laser beam and to maximize the trapping volume.

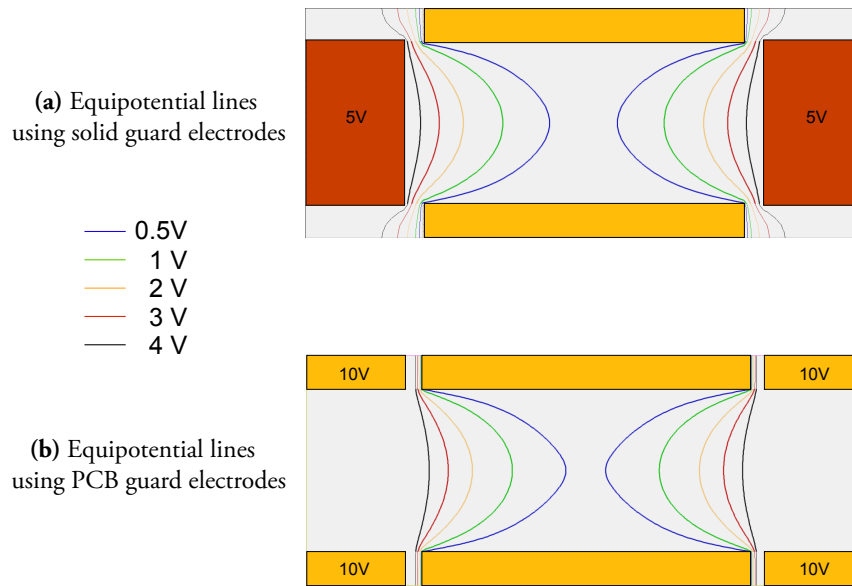


**Figure 7.9:** SIMION simulation results showing the penetration of the equipotential lines resulting from (a) the application of 5V to solid guard electrodes (b) the application of 10V to PCB guard electrodes.

Figure 7.9 shows a comparison between the equipotential lines resulting from applying 5 V to the solid electrodes (Figure 7.9(a)) as opposed to applying 10 V to PCB guard electrodes with open space in between them (Figure 7.9(b)). The different colors represent the equipotential at different positions of the trap. The simulations suggest that the minimum voltage that needs to be applied to confine the ions while using PCB guard electrodes is 10 V and that it can be reduced to 5 V by using solid guard electrodes. Therefore, the use of solid guards not only enables to restrict the gas flow within the trap, but also allows for confining the ions using a lower voltage compared to the use of open guard electrodes.

In addition, the simulations show that in the case of applying a relatively high guard voltage, ions are pushed towards the PCB electrodes (i.e., towards the top and bottom), which is a result of the electric guard potential penetrating deeper into the trap center. Figure 7.10 shows the position of the field-free region ('ion pipe') in which ions are situated when applying 5 V to solid guards (blue circle in Figure 7.10(a)) and when applying 10 V to open PCB guard electrodes (purple circle in Figure 7.10(b)) at one moment in time, using

an RF voltage of 100V. A displacement of ions from the axis of the trap can be problematic for the tagging process, as the ion temperature will increase with proximity to the RF electrodes due to RF heating. The fact that ions are not in a perfectly central position within the trapping volume may also result in a less efficient photodissociation following IR irradiation due to decreased overlap between laser beam and ion cloud. The effect of the guard voltage on the tagging efficiency will be discussed in the following sections.

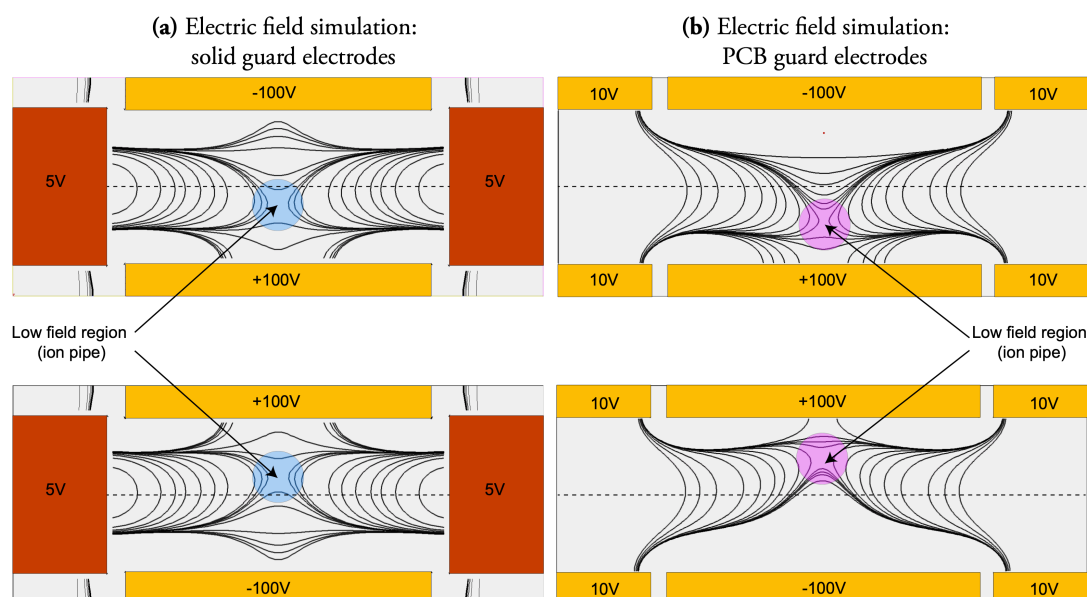


**Figure 7.10:** SIMION simulation showing the electric field resulting from (a) the application of 5 V to solid guard electrodes. The field-free region is depicted by blue circles and the top and bottom panels show the result at the points in time with maximum and minimum RF amplitude, respectively. (b) The application of 10 V to open PCB guard electrodes. The field-free region is depicted in purple.

An overview of the multi-trap operation is shown in Figure 7.11. A gas pulse is introduced through a hole in one of the guard segments prior to the arrival of the mobility separated analytes (step 1 in Figure 7.11). The gas molecules are cooled upon contact with the cold

trap surfaces. Ions are then trapped in different compartments by sequentially applying a blocking DC voltage to a row of electrodes defining the size of the sub-traps. The separately trapped ions are collisionally cooled and tagged by the messenger gas molecules prior to being irradiated by the IR laser beam (steps 2 and 3 in Figure 7.11). It is important to note that the tagged ions are trapped for tens of milliseconds to allow for the IR interrogation step and for pumping the gas left in the trap region prior to unloading, thus preventing the dissociation of the weakly bound tags due to collisions with residual gas molecules. The ions are then unloaded sequentially towards the TOF mass analyzer and the ratio of tagged to untagged ions is measured as a function of the IR laser wavenumber to generate an infrared spectrum (step 4 in Figure 7.11).

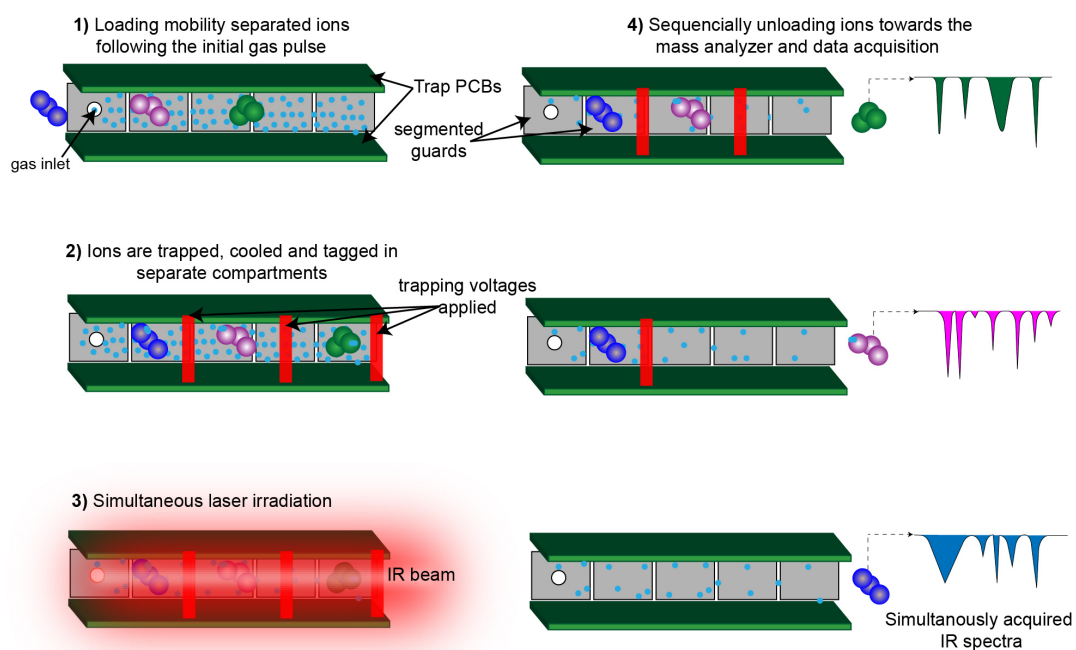


**Figure 7.11:** Overview of the multi-trap operation in multiplexed messenger tagging cryogenic IR spectroscopy experiments.

## 7.4. Electronics, time-sequence generation, and data acquisition

To operate the instrument, a multitude of DC voltages, RF voltages and triggers are required. The DC and RF voltages are generated using 5 commercial power supplies (MIPS modular system, GAA custom electronics) including 10 RF generators. The MIPS systems provide the voltage needed for the ESI, as well as all the DC and RF voltages needed for the different components of the apparatus, including the ion guides, the SLIM IMS module, as well as the multi-trap assembly. The MIPS systems are also used to generate the TW potentials needed to operate the SLIM IMS sections (accumulation, separation, CID, etc.). A custom multi-switch device is used to control the switching of different TW and DC voltages needed for ion accumulation and release, cyclic IMS, and the use of the SLIM traps for different purposes. The voltages needed to operate the TOF mass analyzer are generated using the commercial power supply. The different time sequences and delays are generated using a delay generator (Berkley Nucleonics, California US).

Arrival-time distributions and mass spectra are acquired using a data acquisition (DAQ) system provided with the TOF device (TOFWERK). The DAQ system includes an analogue-to-digital converter and generates data that is collected in HDF5 type files, structured to contain different data dimensions. The arrival-time information as well as the mass spectra and the ion current at each of the segments (data points) composing the ATD can be extracted from the generated files. The laser system is controlled using a custom LabView program, which allows the definition of scan parameters such as the output power, the scan speed, and the wavenumber range.

Another LabView program is used to initiate the IR spectra acquisition and allows remote control of the TOFWERK software to start and finish a specific measurement in coordination with the laser scanning program. In the process, the wavenumber information as a function of scanning time is extracted and added to the HDF5 file. Further

developments of the data acquisition method are in process and aim to automate the IR data extraction step, thus allowing for rapid processing of the acquired data.

This instrument can be operated in three data acquisition modes:

**Mass spectrometry.** When operating as a classic mass spectrometer, a continuous ion beam is transmitted through the instrument with no mobility separation. In this case, a defined number of extractions are averaged. Each acquired mass spectrum is an average of a number of extractions defined by a data dimension referred to as *waveforms* in the TOF acquisition software. The number of waveforms, combined with the frequency of TOF extractions, define the repetition rate at which the generated data file is updated. For example, using a 10kHz TOF extraction frequency (100  $\mu$ s between two successive TOF extractions) and 1000 waveforms, data is written into the HDF5 file at a frequency of 10 Hz (i.e., every 100 ms).

**Ion mobility.** When operating in ion mobility mode, an ion pulse is introduced into the SLIM separation region periodically. The period is defined by the number of waveforms and a second data dimension referred to as segments. One segment includes an average of the mass spectra defined by the waveform parameter. The waveforms define the sampling rate of a given ATD and is kept as low as possible (1-3 averaged waveforms) for an accurate definition of the mobility peaks. For example, in case of working with a 2-waveform average at a sampling rate of 10 kHz, the ATD time resolution will be  $2 \times 100\mu\text{s} = 200\mu\text{s}$ . A typical setting would be to use 1 waveform and 2000 segments which results in an experiment repetition rate of 5 Hz, thus a period of 200ms in which mobility separation can be performed. The information within each segment can be averaged in what is referred to as blocks before being written in the HDF5 file.

**IR spectroscopy.** IR spectroscopy is performed similarly to the operation in ion mobility separation mode. Mobility-separated ions are trapped in separate sections of the trap for tens of milliseconds to accommodate for the tagging and IR irradiation processes and to

leave enough time to pump the residual gas in the trap region prior to extraction. Typical parameters used in IR spectroscopy mode are 1 waveform, 2000 segments, and 1 block. The use of a single block average allows to speed-up the laser scanning process thus shorten the data acquisition time. This, of course, depends on the signal stability among other considerations. A typical time sequence used to operate in IR spectroscopy mode is shown in Figure 7.12. Ions are introduced in pulses 1-3 ms wide, and  $\Delta t_1$  denotes the separation time on the SLIM module that can be adapted, depending upon the molecule and the number of separation cycles. The trapping time during which the ions are tagged and interrogated spectroscopically is denoted by  $\Delta t_2$  and is in the range of tens of milliseconds. Lastly,  $\Delta t_3$  denotes the flight time of the released ions before they reach the TOF extraction region and can be optimized for maximum sensitivity by fine tuning the release trigger. The gas pulse needs to be introduced prior to the analyte's arrival for tagging and optimal trapping efficiency.

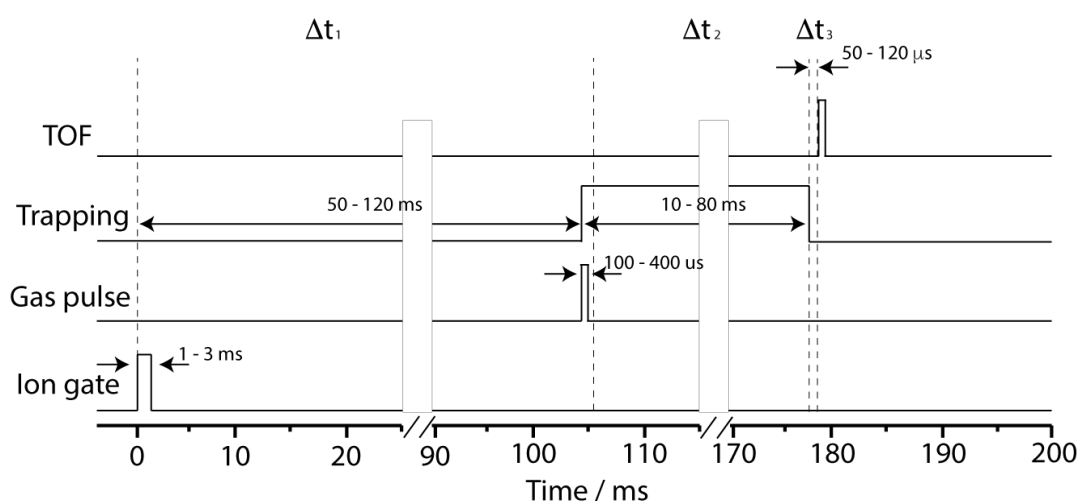


**Figure 7.12:** Typical time sequence used in SLIM IMS messenger tagging IR spectroscopy experiment using the newly developed instrument.

## 7.5. Characterization results

In this section we present the characterization results of the different sections of the newly designed instrument. The focus was on characterizing ion transmission, which is crucial to

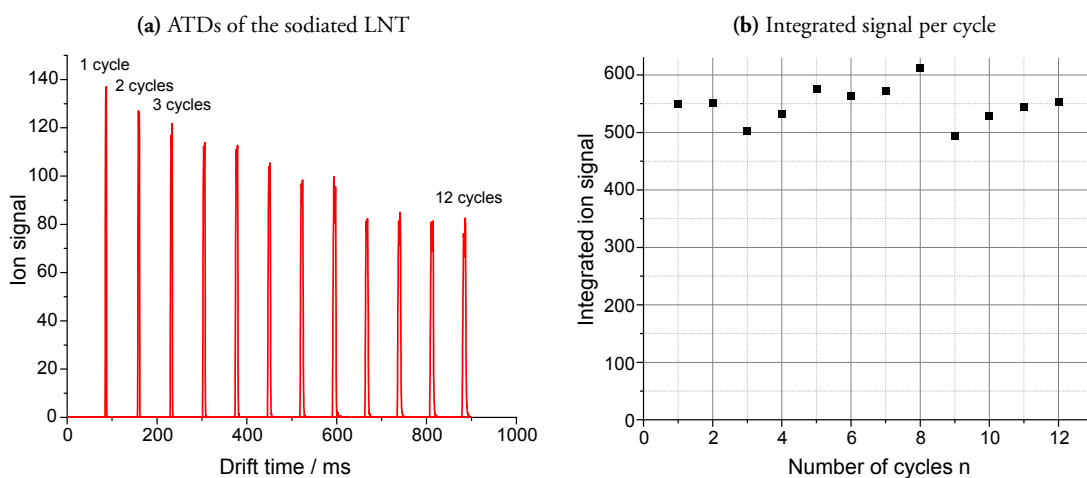
the sensitivity of the instrument, IMS resolution, which is determinant in isomer separation, as well as the different aspects involved in IR spectral acquisition process. The latter includes trapping analytes in different segments of the multi-trap, determining the tagging efficiency, and overlap of the ion cloud with the IR laser.

**Sample preparation.** The different molecules used for characterization were purchased from Sigma Aldrich, UK, and Carbosynth, UK. The solutions were prepared by diluting the powder sample in a 50/50 water/methanol mixture to a concentration of  $\sim 5 - 30\mu\text{M}$ . In some cases, a 3% volume of formic acid was added to the solution to favor the production of protonated ions by ESI. Sodium is naturally present in solution due to the containers and ESI emitters used, which is why sodiated species are always produced during the ionization process.

## 7.5.1 SLIM IMS module

### Ion transmission

Ion transmission is among the most critical attributes that need to be considered when building an analytical instrument. In addition to high ion utilization, lossless mobility separation is key to accurately identify the components of a given sample. The ion transmission per cycle was characterized using the human milk tetrasaccharide lacto-N-tetraose (LNT) in its singly sodiated form. The SLIM module was run at a 2.1 mbar  $\text{N}_2$  pressure at room temperature, an RF frequency of 570 kHz, and an RF amplitude of 120  $V_{\text{pp}}$ . The travelling-wave height was set to 25 V and the speed such that the ions were rolling over with a low probability.



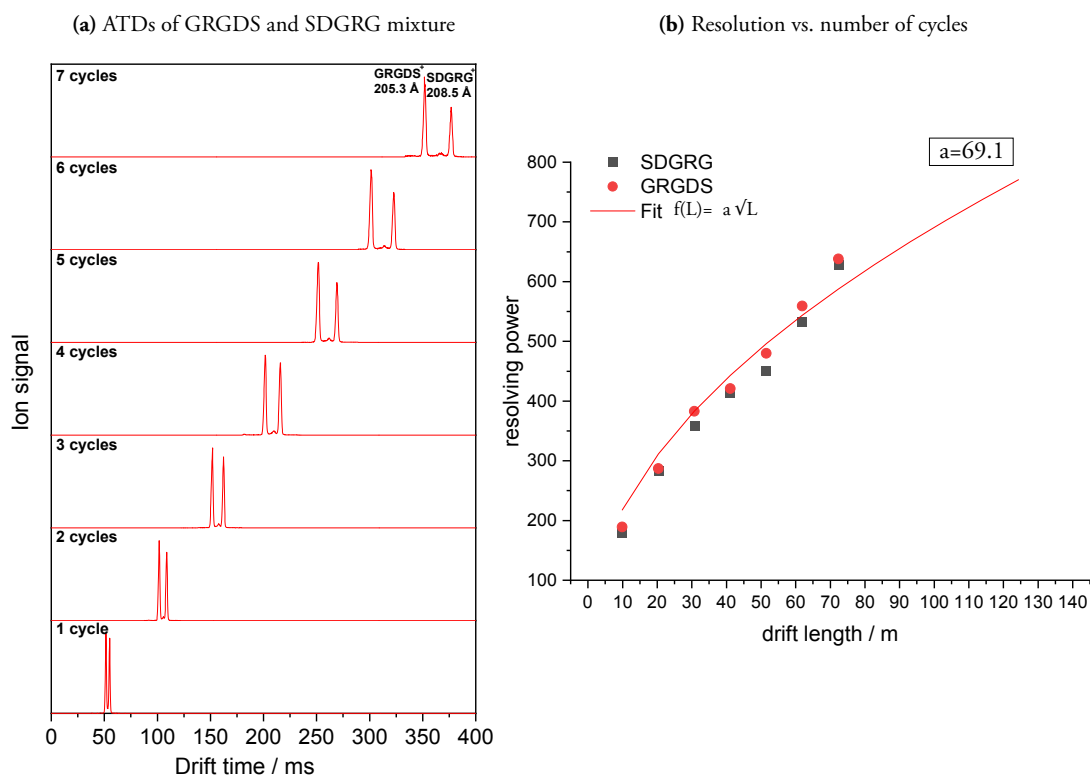
**Figure 7.13:** (a) ATDs of the singly sodiated LNT ions after different number of SLIM cycles. (b) The integral of the LNT ATD signal per cycle as a function of the number a cycles  $n$ , showing lossless transmission after 12 SLIM cycles.

Figure 7.13(a) shows the ATDs of the singly sodiated LNT ions after different numbers of round trips ( $n$ ) within the SLIM module (up to 12 cycles corresponding to a 120 m drift path!). As the number of cycles increases, we observe that the mobility peaks become wider, since ions are occasionally rolling over the travelling wave. To quantify the total ion signal after each cycle, the mobility peaks were integrated. Figure 7.13(b) shows the integrated area of the mobility peaks as a function of the number of cycles. Despite fluctuations that can be attributed to unavoidable spray instabilities, we observe no significant signal drop after the 12 cycles, which confirms the lossless property of SLIM IMS module.

## SLIM IMS resolution

Aiming to produce isomer-specific IR fingerprints suitable for accurate analysis of the composition of a given sample, maximal IMS resolution is required. The lossless ion transmission achievable using SLIM allows for a large number of separation cycles and thus an extended path length that leads to an increased IMS resolution. The IMS resolution of the newly developed instrument was characterized using the pair of reverse-sequence

peptides GRGDS and SDGRG, which differ in their collisional cross section by  $\sim 1.5\%$  in their singly protonated form (note that the resolution of our SLIM prototype was characterized using  $2+$  ions, which differ in their CCS by  $2.8\%$ ).<sup>2</sup> A solution containing both peptides was prepared following the previously described protocol, then electrosprayed. The SLIM module was run at 2 mbar nitrogen pressure, RF frequency of 570 kHz, RF amplitude of  $100 V_{pp}$ , and separation-TW conditions. Since the SLIM module is based on TW technology, CCS values cannot be directly extracted from the measured drift times. Instead, we use previously published CCS values of GRGDS<sup>+</sup> and SDGRG<sup>+</sup> in N<sub>2</sub> ( $205.3 \text{ \AA}^2$  and  $208.5 \text{ \AA}^2$ , respectively)<sup>3</sup> to determine the resolution. The ATDs of the peptide mixture after undergoing different separation cycles in the SLIM module are shown in Figure 7.14(a). As the number of cycles increases, we observe that the mobility peaks get further separated. The resolution of the SLIM IMS separation was quantified using the method described in Section 3.6, and yields a single-cycle resolving power of  $\sim 180$ .



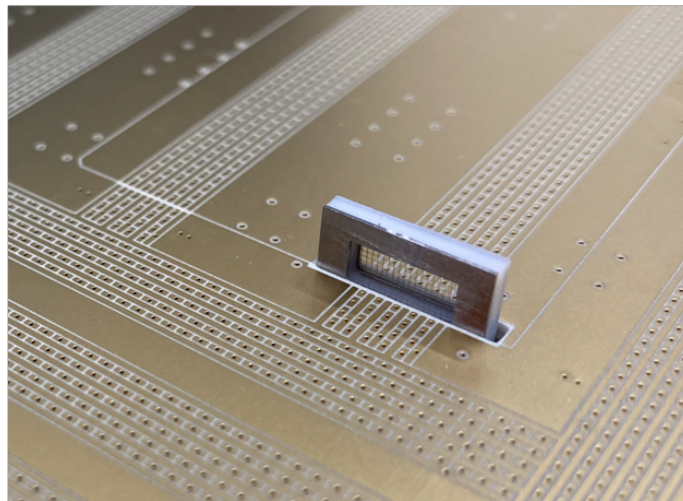
**Figure 7.14** (a) ATDs from the mixture of the isomeric peptides GRGDS and SDGRG (singly protonated form) displayed for different number of separation cycles  $n$ . (b) IMS resolution of the SLIM device as a function of the drift length. The fit function is shown in red where the fitting parameter  $a=69.1$ .

Figure 7.14(b) shows the evolution of the IMS resolution as a function of the drift length. The fit function (red line) is of the form  $f(L) = 69.1\sqrt{L}$  and confirms the  $\sqrt{L}$  dependence of  $R$  to the drift length. The instrument reaches a resolution of  $\sim 650$  for the considered pair of peptides after 7 cycles which corresponds to a 70 m drift path length. The number of cycles can further be increased but comes at the cost of the repetition rate of the experiment, as drift times would be further extended.

## Grid assembly for CID

The SLIM module includes several traps that can be used for various applications. The electrodes composing the two traps on the top section of the boards (black rectangle, red

region in Figure 7.5) have separate connections in a way such to enable performing collision induced dissociation (CID). The use of SLIM to perform CID was first reported by Webb *et al.* and was based on the early gradient SLIM design at a lower pressure of around  $10^{-1}$  mbar (see Figure 2.6(a)). A SLIM CID module was installed in a differentially pumped region downstream of the IMS region and allowed for performing CID by switching the bias voltage applied to one of the boards.<sup>4</sup> As the CID module was placed after the SLIM IMS module, it was not possible to perform IMS<sup>n</sup> type experiments. It is only recently that Bansal *et. al* modified our previously described prototype to include a CID trap within the SLIM IMS region, enabling IMS<sup>n</sup> type experiments.<sup>1</sup> The implementation details and description of the experimental workflow will be part of a different work. In this section we focus on the use of a grid assembly, which ensures a well-defined homogeneous electric field accelerating the parent ions in the region between the grids, thus enhancing the efficiency of SLIM CID.



**Figure 7.15:** Picture of the grid assembly

One of the two CID traps includes a slit in the PCB material that allows to introduce a grid assembly at its entrance as shown in Figure 7.15. The grid assembly is composed of two stainless-steel frames 0.3 mm thick containing the two grids. A Teflon spacer with a thickness of 0.8 mm defining the distance between the grids is 'sandwiched' between the

frames using epoxy glue. A different voltage is applied to each grid allowing for the steep voltage drop required for CID. The SLIM electrodes following the second grid are connected to a separate bias voltage which can be adapted to the voltage of the second grid.

Collision-induced dissociation experiments were performed using the grid assembly, and the fragmentation yield was characterized using the singly sodiated LNT molecules. The solution was prepared following the previously described protocol then electrosprayed, and the SLIM module was run at 2 mbar N<sub>2</sub> pressure, an RF frequency of 570 kHz, and RF amplitude of 120 V<sub>pp</sub>. Figure 7.16(a) shows the normalized mass spectra obtained using various voltage drops between the grids. In the bottom panel the mass spectrum obtained at 0 V gradient is shown and display a single peak at *m/z* 730 corresponding to the singly sodiated LNT ions. As the gradient is increased, we observe new peaks corresponding to fragments appearing in the mass spectra. At 85 V gradient we observe a signal at *m/z* 550 corresponding the B<sub>3</sub>/Z<sub>3</sub> fragments of LNT, then, at 95 V a second peak appears at *m/z* 568 corresponding to the C<sub>3</sub>/Y<sub>3</sub> fragment. At higher voltages (105 V – 125 V) we observe fragments at *m/z* 406, 388 and 365, corresponding to the C<sub>2</sub>, B<sub>2</sub>, and Y<sub>2</sub> fragments, respectively. The presence of these fragments indicate that the fragmentation occurs mainly at the glycosidic linkage.

(a) Mass spectra of the singly sodiated LNT and its fragment

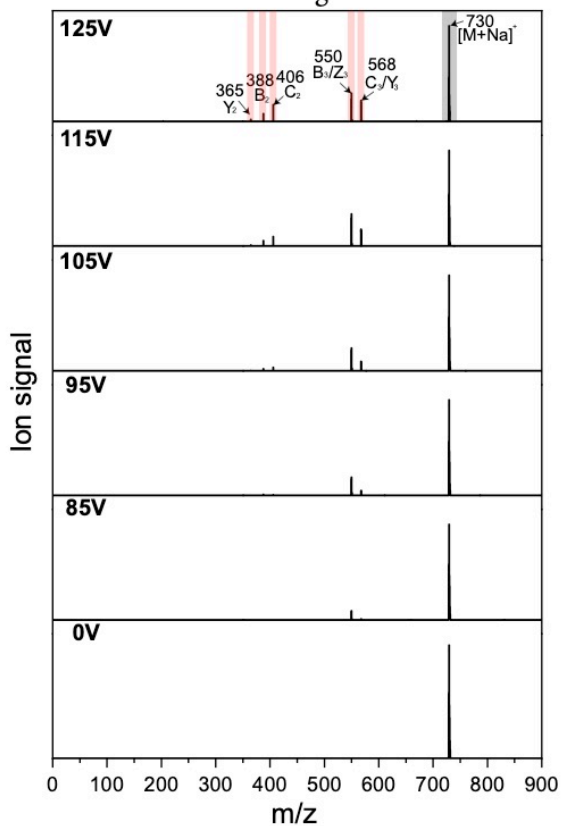
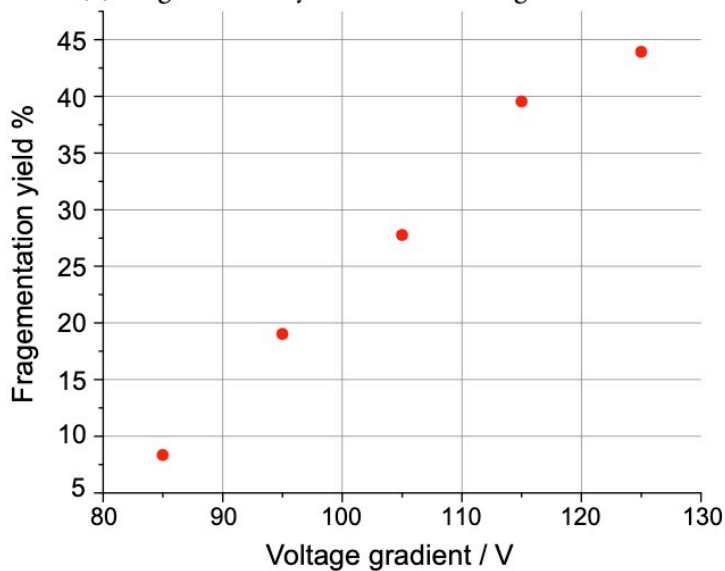


Figure 7.16: (a) Mass spectra of the sodiated LNT ions recorded at different voltage gradients between the CID grids. The peak corresponding to the precursor ion is shown in grey and the peaks corresponding to the different fragments are shown in red (b) The fragmentation yield as a function of the voltage gradient between the CID grids.

(b) Fragmentation yield vs Grids voltage difference



The fragmentation yield was calculated by dividing the sum of the integrated peaks of the fragment ions by the sum of the fragments and the parent, and is shown in Figure 7.16 (b) as a function of the gradient voltage. We observe an increase in the fragmentation yield as a function of the voltage applied between the grids, reaching ~44% at a 125 V difference between the grids (> 1500 V/cm electric field!).

It is important to note that the yield calculated in this experiment represents a lower limit of the actual yield of the fragmentation process. In fact, the experiment was performed at RF settings that are optimal for the transmission of the parent molecules, thus hindering that of the fragment ions due to RF dependence of the SLIM device for optimal transmission of different  $m/z$  values. Furthermore, the relatively high pressure (2 mbar) in the CID region adds to the difficulty of the fragmentation process.

## 7.5.2 Cryogenic planar multi-trap

### Segmented trapping

The design of the cryogenic trap, which can be segmented into multiple sections, is central to our multiplexing approach. The main characteristic of the new trap design is the separate control over every DC pad, resulting in modulable number of sub-traps. The aim is to trap different isomeric species at different locations, then release them sequentially after spectroscopic interrogation. To characterize the trapping process in different sections, we used a solution of Bradykinin and monitored the total ion signal using a channeltron detector initially placed at a distance of 10 cm behind the trap assembly, representing the position of the TOF extraction region. The size and position of the trap sections are defined by controlling separately the first and last electrodes of each sub-trap configuration. A gas pulse is introduced prior to the ions arrival and enable trapping by carrying away translation energy of the injected ions *via* collisions. The trapping and release process for characterizing the trap was done as follows. (1) A high voltage (100 V) is applied to the exit electrode of the sub-trap prior to the ion's arrival. (2) Once the ions arrive inside the desired section, a

high voltage is applied to the entrance electrode of that sub-trap, preventing ions from escaping. (3) Trapped ions are then released by lowering the voltage applied to the exit electrode and are subsequently detected. The trap was held at room temperature with an RF frequency of 1.65 MHz, an RF amplitude of 450V, and an average pressure of  $\sim 10^{-6}$  mbar of a gas mixture composed of 90% He and 10% N<sub>2</sub> in the chamber housing the trap.

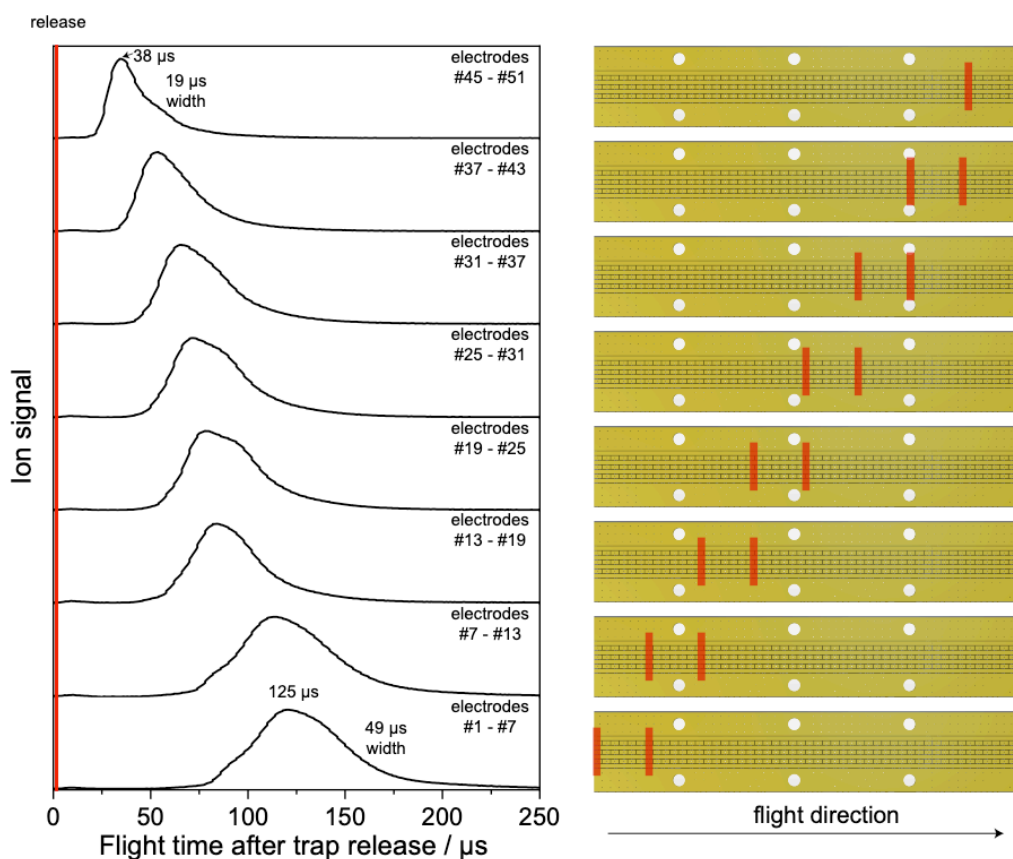


**Figure 7.17:** ATDs of the BK ions when released from different sections of the multi-trap (shown in the left panel), showing the flight time differences when using different traps at a constant trap DC gradient.

Figure 7.17 shows the arrival time of the analytes after trapping and releasing from eight different sections of the trap. The exact positions of the sub-traps are depicted by the two red rectangles placed at the entrance and exit DC pads of the trap PCB (right panel of the

figure). A gradient of 3 V was applied across the trap, which pushes the ions toward the exit of the module. We observe that when trapping in the last section of the trap (i.e., closest to the trap exit), ions take 38  $\mu\text{s}$  to reach the detector, with a FWHM of 19  $\mu\text{s}$  for the entire ion distribution. Sub-traps located at the entrance of the module produced an ion packet that was wider and arrives later (49  $\mu\text{s}$  width and 125  $\mu\text{s}$  arrival time), which is expected, since the gradient applied across the trap was relatively low. As the tagging and irradiation processes typically require tens of milliseconds, the differences in flight time are neglectable and do not pose a problem. The precise time of the TOF extraction pulse, however, needs to be considered to sample a maximum number of ions from each of the sub-traps.

## Characterization of messenger-tagging IR spectroscopy

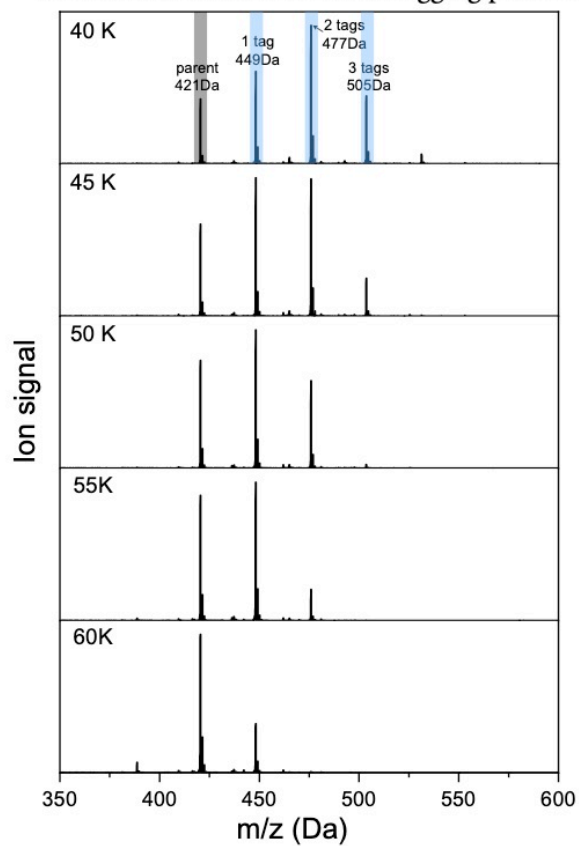
When performing messenger-tagging, cryogenic, IR spectroscopy, the quality of the spectra is highly dependent upon the stability of the signal, the tagging efficiency, and the IR absorption.

### Messenger tagging

The mechanism driving the messenger-tagging process was described in detail in Chapter 2. A gas pulse composed of a mixture of He and N<sub>2</sub> is introduced into the trap prior to the arrival of the ions. The gas is cooled upon collisions with the cold surfaces of the trap, and allows the formation of clusters with the injected ions *via* a three-body collision process. Ions are cooled by the first collisions, then subsequently tagged by the cold gas molecules. Clusters are then irradiated by IR photons and gently unloaded from the trap towards the detector. The temperature of the trap is a crucial parameter that needs to be controlled accurately to optimize the cooling and tagging process. While the effective temperature of the ions directly depends upon the temperature of the gas molecules they collide with, it also can be affected by RF heating. As a result, the position of the ions relative to trap PCBs can strongly affect the tagging process. To characterize this process, we used a previously studied disaccharide GalNac- $\alpha$ (1-3)Gal in its sodiated form. The disaccharide was O-

methylated at the C<sub>1</sub> carbon and locked in the  $\alpha$  configuration. The solution was prepared following the previously described protocol then electrosprayed. The multi-trap was operated at an RF frequency of 1.65 MHz and an RF amplitude of 450 V, while the temperature, pressure, and guard voltages were varied to characterize their effect on the tagging efficiency. We first focus on the effect of the temperature. Figure 7.18(a) shows normalized mass spectra obtained after trapping the disaccharide molecules for 50 ms at different temperatures of the trap at a constant average pressure of  $\sim 10^{-6}$  mbar of a gas mixture composed of 90% He and 10% N<sub>2</sub>, and using a guard voltage of 7 V. At 60 K we observe the bare ion at  $m/z$  421 as well as the singly tagged molecule at  $m/z$  449. At lower temperature new peaks appear in the mass spectrum corresponding to the doubly and triply tagged ions at  $m/z$  477 and 505 respectively, following what looks like a thermal distribution. The tagging yield as a function of the temperature is displayed in Figure 7.18(b).

(a) Mass spectra of the singly sodiated disaccharides and the clusters formed in the tagging process



(b) Tagging yield vs Temperature

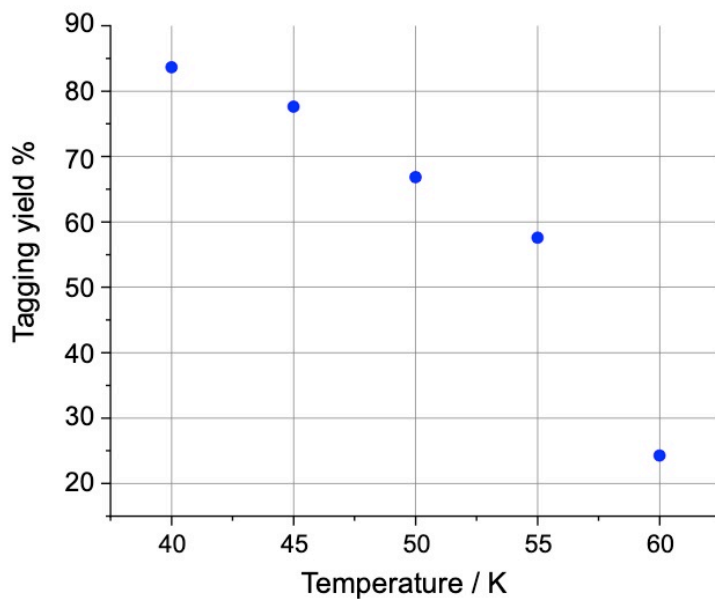


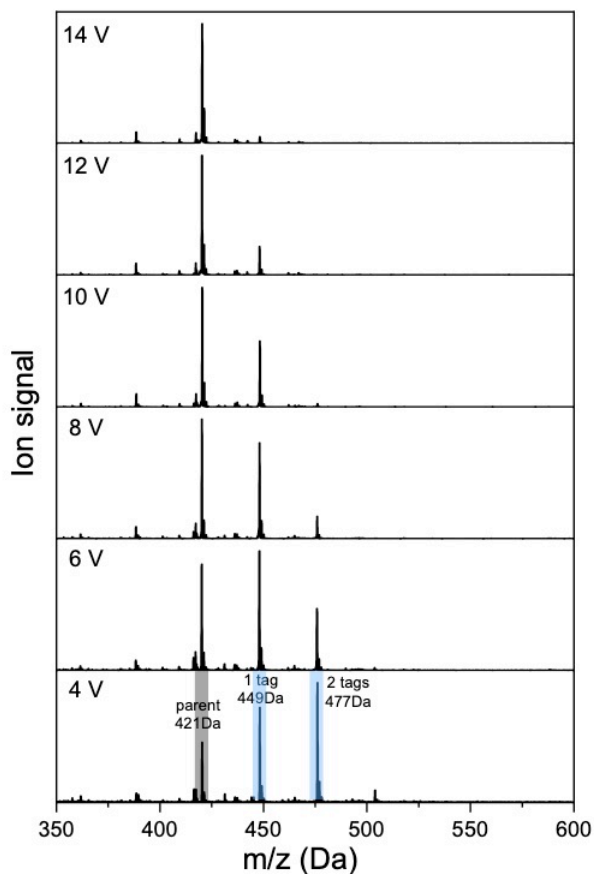
**Figure 7.18:** (a) Mass spectra of the sodiated GalNac- $\alpha$ (1-3)Gal ions recorded using different temperatures. The peak corresponding to the parent molecules is shown in grey and the peaks corresponding to the different clusters are shown in blue. (b) The tagging yield as a function of the temperature.

We observe that the tagging yield increases from 25% at  $T = 60$  K to 83% at 40 K. As expected, lower temperatures result in a more efficient tagging process and favor the formation of clusters including multiple tags. This observation can be explained by the lower internal energy of the ions resulting from collisions with colder gas molecules, which ultimately results in an increased probability of forming higher-order clusters with lower binding energies for each additional  $N_2$  tag.

A second crucial parameter for the observation of tagged species is the guard voltage. As shown in the previous section, simulations indicate that at high guard voltage, the resulting electric potential penetrates into the trapping region and can lead to ions being pushed towards the PCBs of the trap, thus potentially increasing the ion temperature as a result of RF heating. In this experiment, we explore the effect of varying the guard voltage on the tagging efficiency.

Figure 7.19(a) shows the normalized mass spectra obtained after trapping the sodiated disaccharide ions for 10 ms at different guard voltages, while the trap temperature and pressure were held constant at 55 K and  $\sim 10^{-6}$  mbar respectively.

(a) Mass spectra of the singly sodiated disaccharides and the clusters formed in the tagging process



(b) Tagging yield vs guard voltage

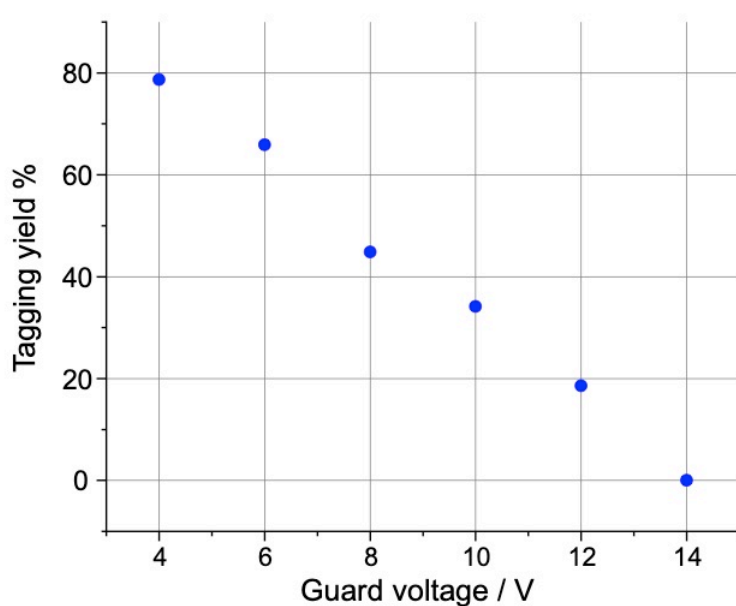


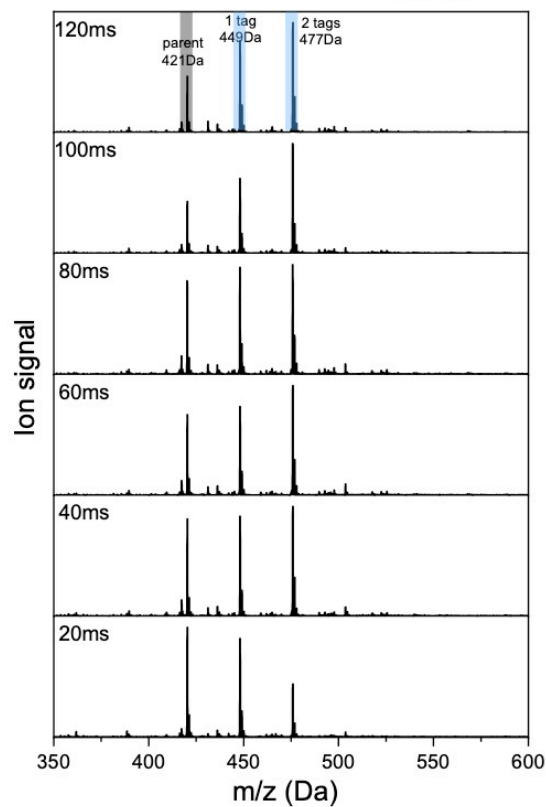
Figure 7.19: (a) Mass spectra of the sodiated GalNac- $\alpha$ (1-3)Gal ions recorded using different guard voltage values. The peak corresponding to the parent molecules is shown in grey and the peaks corresponding to the different clusters are shown in blue. (b) The tagging yield as a function of the guard voltage.

At a guard voltage of 4 we observe signals at  $m/z$  421 corresponding to the bare ion, as well as peaks at  $m/z$  449, 477, and 505, corresponding to clusters composed by the parent ion plus 1, 2, and 3 tags, respectively. As the guard voltage is increased, the intensity and number of tags decrease in a manner similar to that observed when increasing the temperature of the trap. The tagging yield as a function of the guard voltage is shown in Figure 7.19(b) and decreases from ~80% at 4 V to almost no tagging at 14 V. This suggests that as the guard voltage increases, ions are pushed closer to the RF electrodes on the PCBs (see Figure 7.10), which leads to RF-heating.

It has been shown that the nature of messenger tag can have an influence on the obtained IR spectra by affecting the structure of an ion.<sup>3</sup> In a similar way, the number of tags can influence the hydrogen-bonding pattern of the ion and thus its recorded fingerprint.<sup>5-6</sup> As a result, observing a single tag is considered to be the best condition to generate reproducible IR spectra in a robust manner. For this reason, the ability to control the tag distribution by varying the guard voltage can prove useful to ensure the robustness of the spectral acquisition.

Another parameter that can influence on the observed tag distribution is the trapping time, which we investigate here. During these experiments, the trap temperature was held at 55 K, the pressure at  $\sim 10^{-6}$  mbar and the guard voltage at 7 V. Figure 7.20(a) shows the normalized mass spectra obtained upon releasing the analytes after different trapping times.

(a) Mass spectra of the singly sodiated disaccharides and the clusters formed in the tagging process



(b) Tagging yield vs trapping time

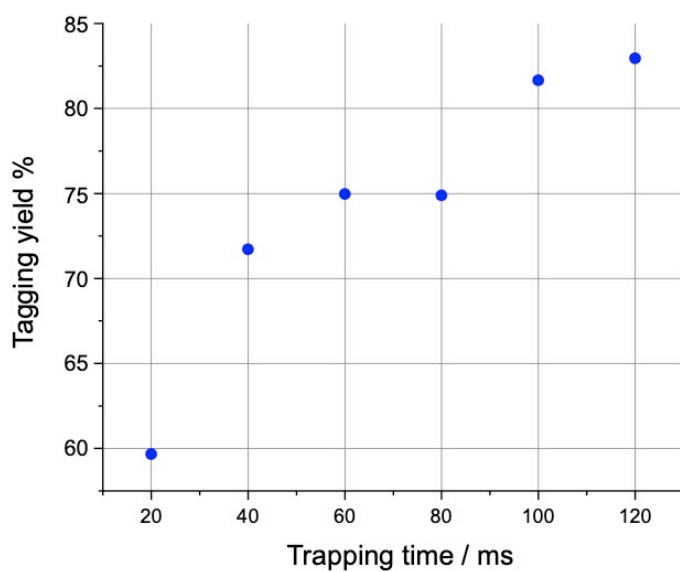


Figure 7.20: (a) Mass spectra of the sodiated GalNac- $\alpha$ (1-3)Gal ions recorded after different trapping times. The peak corresponding to the parent molecules is shown in grey and the peaks corresponding to the different clusters are shown in blue. (b) The tagging yield as a function of the trapping time.

While all mass spectra include signals corresponding to the bare ion at  $m/z$  421, as well as to the singly and doubly tagged molecules at  $m/z$  449 and 477, respectively, we observe a change in relative intensities when the trapping time is varied. The tagging yield as a function of the trapping time, displayed in Figure 7.20(b), clearly indicates that larger number of tags can be observed when ions are trapped over longer periods of times. A difference of 100 ms in trapping time results in a ~23% increase in tagging yield. The observed difference in the tagging distribution originates from differences in the trap instantaneous pressure at the time when the ions are released. By trapping over longer time periods, ions are extracted at a lower pressure and thus have a lower probability of colliding with residual gas molecules. Collisions with gas molecules during extraction pose a problem as they can lead to fragmentation of the weakly bound clusters, altering the number of tagged species that are observed in the mass spectrum.

## Vibrational spectroscopy

One of the major reasons that gas phase IR spectroscopy has so far not been implemented on commercial instruments is the complexity of the required laser systems. However, recent advances in laser design has resulted in the development of compact, robust, and highly efficient mid-infrared laser systems that are tunable over a wide range.<sup>7</sup> We make use of a commercially available continuous-wave hybrid laser (CLT series, IPG Photonics, Oxford, UK) which uses a Cr:ZnSe/S crystal pumped by a thulium fiber laser. It has a wavelength tuning range of 2.6 to 3.1  $\mu\text{m}$  with a power output of 1-4W across this interval.

After trapping the analyte ions and controlling the tagging process, the weakly bound clusters are irradiated by an IR laser beam. Upon absorption of a resonant photon, the photodissociation of the clusters is monitored as a function of the wavelength in order to generate an IR fingerprint. We used the same sodiated disaccharide molecule as in the previous section to characterize the IR spectroscopy process. Figure 7.21(a) shows the difference in mass spectra of the trapped disaccharide molecules when resonant photon absorption occurs (bottom panel) vs. no photon absorption (top panel).

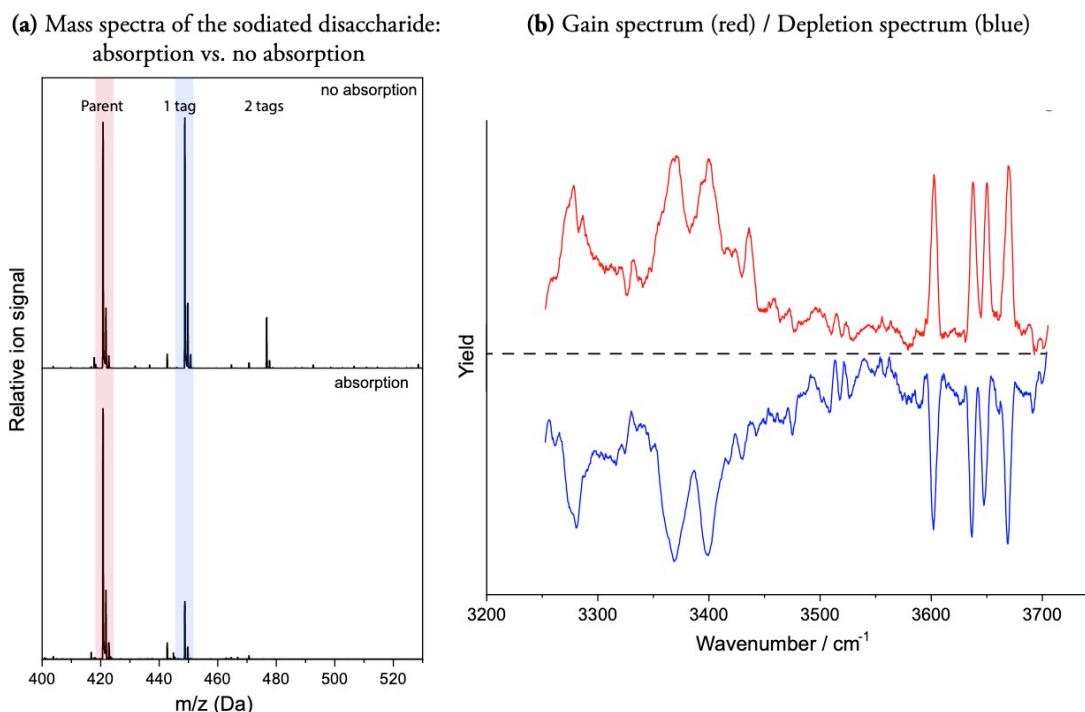


**Figure 7.21:** (a) Mass spectra of the sodiated GalNac- $\alpha$ (1-3)Gal ions when a resonant photon is absorbed (bottom panel) and when no photon is absorbed (top panel). The peak corresponding to the bare ions is shown in red and that corresponding to the singly tagged ions in blue. (b) Messenger tagging IR spectrum of the sodiated GalNac- $\alpha$ (1-3)Gal. The gain spectrum obtained by monitoring the bare-ion signal as a function of the wavenumber (red). The depletion spectrum obtained by monitoring the tagged-ion signal as a function of the wavenumber (blue).

In case no absorption occurs, we observe two equally intense signals at  $m/z$  421 and 449 corresponding to the bare molecule and to the singly tagged molecule, respectively. The absorption of a photon is accompanied by a decrease in intensity of the signal corresponding to the singly tagged ions as shown in the bottom panel. By monitoring the intensity of the signal corresponding to the bare molecules as a function of the wavelength of the incident photons we obtain a gain spectrum. The variation in the intensity of the singly tagged species as a function of the wavelength yields the depletion spectrum, which displays dips whenever a photon is absorbed and a tag is boiled off. Both spectra are shown in Figure 7.21(b) and are depicted in red and blue, respectively.

To ensure that the obtained IR spectrum accurately reflects the IR absorption cross-sections, we perform the spectroscopy experiments at constant laser power across the frequency range. This is important, as it allows to use not only band positions as unique identifiers of a given molecule, but also their relative intensities. To use the information from the relative intensities for identification, band saturation needs to be avoided.

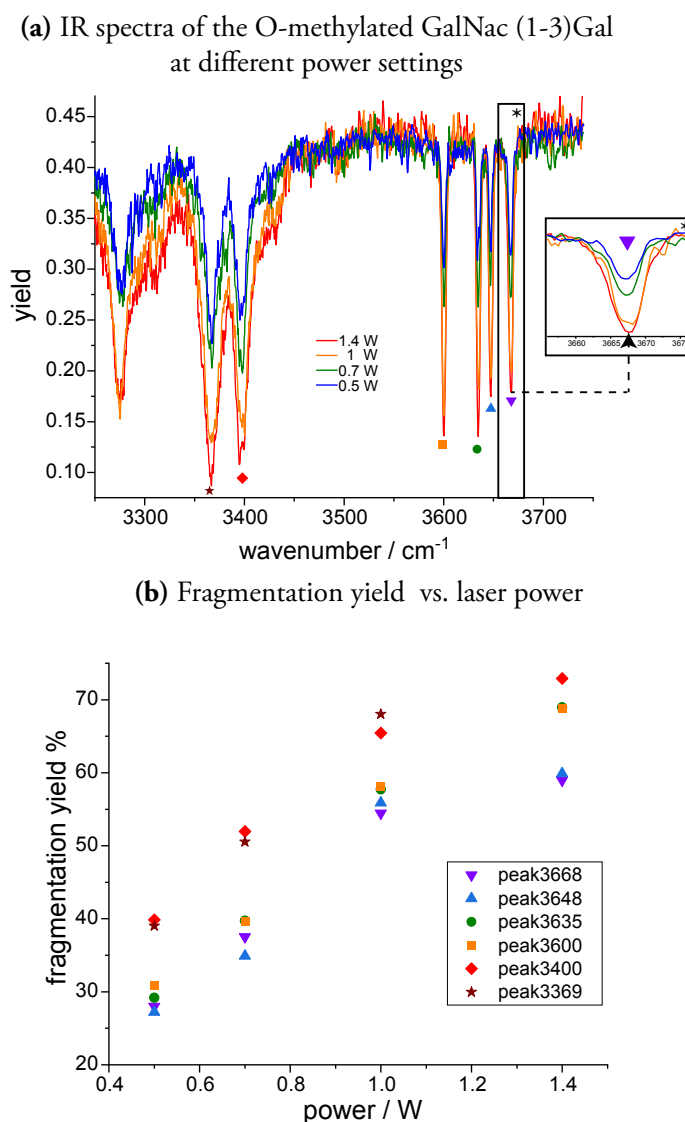


**Figure 7.22:** (a) IR spectra of the sodiated GalNac- $\alpha$ (1-3)Gal ions measured at different laser power settings: 0.5 W (blue), 0.7 W (green), 1 W (orange), and 1.4 W (red). A magnified view of the

absorption band at  $3668\text{ cm}^{-1}$  is shown in the inset. **(b)** The fragmentation yield as function of the laser power for the most prominent absorption bands.

IR spectra of the sodiated disaccharide measured at different laser power settings (0.5 W – 1.4 W) are shown in Figure 7.22(a). It should be noted that we make use of a beam expander to increase the diameter of the beam to approx. 5 mm, thereby ensuring uniform irradiation of the ion cloud. We observe higher depletion with increasing laser power up to 1 W, while the relative intensities of the absorption bands remain similar, indicating no considerable saturation. A closer look at the fragmentation yield at select wavenumbers (depicted in Figure 7.22(b)) indicates that at higher power settings (1 W – 1.4 W), the fragmentation yield no longer increases linearly, which indicates that saturation starts to occur.

## Towards reducing the measurement time

The tremendous number of samples required to be analyzed in fields such as medical diagnostics and pharmaceutical quality control results in a desperate need for rapid, yet accurate analytical tools. It is no surprise that the measurement speed is among the vital criteria when evaluating a given technique as an analytical tool. One of the reasons behind the development of this instrument was to offer a way to generate highly resolved IR spectra on a time scale similar to, or faster than, currently used analytical techniques. The most time-consuming step of our approach is spectral acquisition, as we need to scan the laser wavenumber in order to generate an IR spectrum and use it as fingerprint to identify a given molecule. While acquiring an IR spectrum, the main limitation to the acquisition speed is signal instability, as a number of measurements need to be averaged to obtain an accurate spectrum. The use of SLIM on-board accumulation to cancel out spray instabilities as well as the careful design of the rest of the instrument has led to a higher overall signal stability compared to our prototype instrument.

Figure 7.23 shows the spectra obtained using different laser scanning speed parameters resulting in different spectral acquisition times. All spectra were recorded at  $T = 50$  K, an RF frequency of 1.65 MHz, RF amplitude of  $400 V_{pp}$ , a gradient across the trap of 5 V, and a guard voltage of 4V.

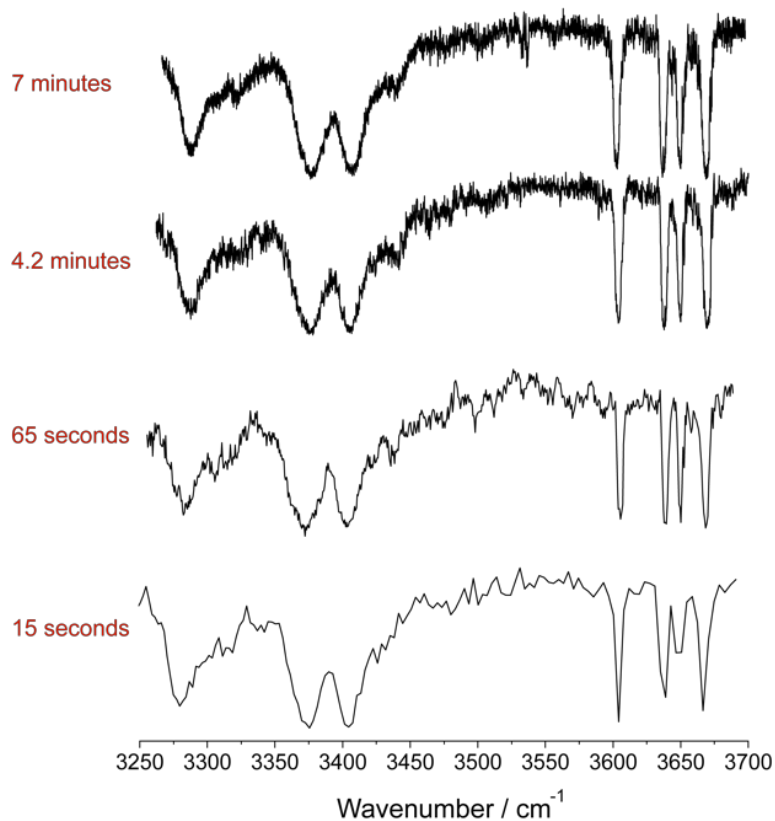


**Figure 7.23:** IR spectra of the sodiated GalNac- $\alpha$ (1-3)Gal ions measured at different laser scanning speeds.

The spectra acquired with different scan speeds resulted in acquisition times of 7 minutes down to only 15 seconds. Comparing the resolution of the sharpest absorption features between  $3600 \text{ cm}^{-1}$  and  $3700 \text{ cm}^{-1}$ , we observe that an acquisition time as short as 65 seconds does not result in a significant loss of resolution nor of overall quality of the data. All the

features (band positions and relative intensities) that are characteristic to the 7 min spectrum are reproduced identically while scanning seven times faster. Remarkably, a scanning time of only 15 seconds results in a spectrum that can still serve as a spectral fingerprint since all major absorptions are reproduced. However, the shortest acquisition comes at the expense of spectral resolution, as the absorption bands become under-sampled. Nevertheless, the 15 s spectrum is still well-structured and includes distinctive features that can be used for identification purposes. Moreover, the acquisition time can further be reduced by scanning a shorter wavenumber range which contains characteristic features that can serve as a fingerprint and used for identification. In the case of the disaccharide molecule, scanning from  $3550\text{ cm}^{-1}$  to  $3700\text{ cm}^{-1}$  would be sufficient and would only require a third of the acquisition time, thus as fast as 5 seconds for the entire scan.

Another angle that was explored while aiming to reduce the average measurement time is the development of a multiplexing approach. The multi-trap design allows for simultaneously recording spectra of different species, thus offering a way to further speed up the measurement time. To test this capability, we used a solution of the tetrasaccharide LNT prepared following the previously described protocol and generated singly sodiated ions.

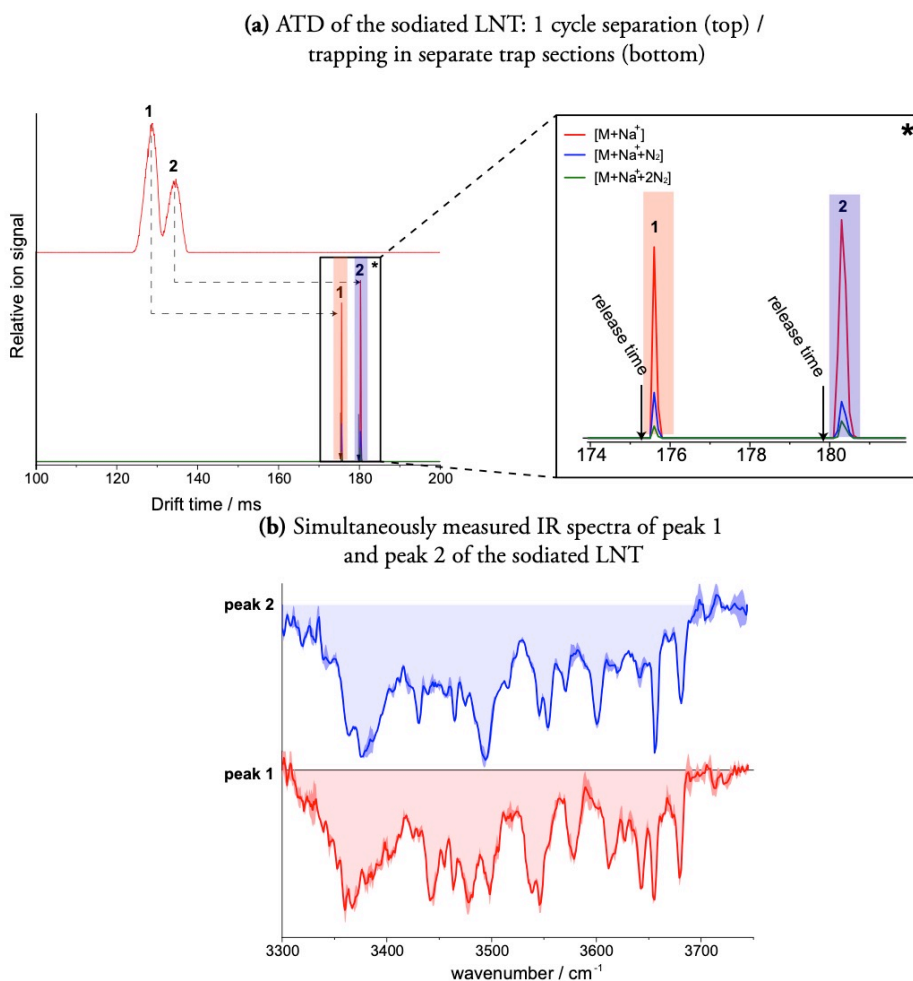


**Figure 7.24:** (a) ATD of the sodiated LNT ions after a single cycle of SLIM separation (top panel). The ATD of the trapped LNT ions is shown in the bottom panel. A magnified view (\*) of the ATD of the trapped ions shows the presence of the singly and doubly tagged LNT molecules. (b) IR spectra of both LNT mobility peaks (peak 1 in red, peak 2 in blue) measured simultaneously using a 1-minute scan.

Figure 7.24(a) shows the arrival time distribution obtained after 1 separation cycle in the SLIM module of sodiated LNT (top panel). Each mobility peak was then trapped in a separate sub-trap for  $\sim 40$  ms to allow for the tagging and IR irradiation processes. The arrival time distribution of the trapped ions upon release at different times from the different sections of the trap is depicted in the bottom panel of Figure 7.24(a). Moreover, a magnified section (\*) of the ATD shows the presence of the singly tagged ions (blue) as well as the doubly tagged ions (green) in addition the bare ions (red). We observe a comparable signal

intensity and tagging yield while using both traps. The IR spectra that were recorded simultaneously are displayed in Figure 7.24(b) in red for peak 1 and blue for peak 2. Each spectrum represents an average of two measurements to increase confidence and the standard error is represented by the shaded area of the respective color around the solid line representing the spectrum. The scan-time for these experiments was set to 1-minute at  $T = 50$  K, an RF frequency of 1.65 MHz, RF amplitude of 400 V, a gradient across the trap of 2 V, and a guard voltage of 4 V. The obtained fingerprints show distinctive features for each LNT isomer that are highly resolved and well suited for identification purposes. This multiplexed approach allows to simultaneously measure the IR spectra of multiple isomeric species thus significantly reducing the scan-time per spectrum. We are currently exploring the use of more traps which will result in an increased overall throughput of our method.

## References

1. Bansal, P.; Yatsyna, V.; AbiKhodr, A. H.; Warnke, S.; Ben Faleh, A.; Yalovenko, N.; Wysocki, V. H.; Rizzo, T. R., Using SLIM-Based IMS-IMS Together with Cryogenic Infrared Spectroscopy for Glycan Analysis. *Anal Chem* **2020**, *92* (13), 9079-9085.
2. Kemper, P. R.; Dupuis, N. F.; Bowers, M. T., A new, higher resolution, ion mobility mass spectrometer. *International journal of mass spectrometry* **2009**, *287* (1-3), 46-57.
3. Kevin Giles, J. L. W., Steven Pringle, David Langridge, Peter Nixon, John Garside, Peter Carney, Characterizing a T-wave enabled multi-pass cyclic ion mobility separator. *Waters corporation*, **2015**.
4. Webb, I. K.; Garimella, S. V.; Norheim, R. V.; Baker, E. S.; Ibrahim, Y. M.; Smith, R. D., A Structures for Lossless Ion Manipulations (SLIM) Module for Collision Induced Dissociation. *J Am Soc Mass Spectrom* **2016**, *27* (7), 1285-8.
5. Spieler, S.; Duong, C. H.; Kaiser, A.; Duensing, F.; Geistlinger, K.; Fischer, M.; Yang, N.; Kumar, S. S.; Johnson, M. A.; Wester, R., Vibrational Predissociation Spectroscopy of Cold Protonated Tryptophan with Different Messenger Tags. *J Phys Chem A* **2018**, *122* (40), 8037-8046.
6. Masson, A.; Williams, E. R.; Rizzo, T. R., Molecular hydrogen messengers can lead to structural infidelity: A cautionary tale of protonated glycine. *J Chem Phys* **2015**, *143* (10), 104313.
7. Vasilyev, S.; Moskalev, I.; Mirov, M.; Smolski, V.; Mirov, S.; Gapontsev, V., Ultrafast middle-IR lasers and amplifiers based on polycrystalline Cr:ZnS and Cr:ZnSe. *Optical Materials Express* **2017**, *7* (7).

## 8. Summary and future perspectives

The combination of ion mobility spectrometry with mass spectrometry has proven to be a powerful tool in glycan analysis. Adding a spectroscopic dimension to the analysis allows to generate isomer-specific IR fingerprints that can be used to unambiguously identify glycan isomers present in given mixture. The need for the development of such tools originates from the challenges that classical analytical techniques encounter when dealing with highly complex glycan structures.

In this work, we first constructed a prototype instrument by adding an ultrahigh-resolution SLIM IMS section to a previously developed instrument that combines IMS with messenger tagging cryogenic IR spectroscopy. The isomer selective capabilities of the new IMS section allowed us to record isomer-specific IR fingerprints of glycans. In the case of disaccharides, we have demonstrated that high-resolution IMS can produce results of similar quality to those obtained using complex IR double-resonance spectroscopic schemes in terms of their ability to record isomer-specific spectra.<sup>1</sup>

Using the prototype instrument, we successfully used a database approach to identify different isomers present in mixtures of disaccharide molecules as well as a mixture of the human milk oligosaccharide molecules LNT and LnNT.<sup>2</sup>

A third application of the technique highlighted its isomer selectivity by detecting the two anomers of a given disaccharide molecule. We were able to unambiguously identify the  $\alpha$  and  $\beta$  reducing-end anomers of the disaccharide GalNAc  $\alpha$ (1-3) Gal by first identifying the absorption band corresponding to the C<sub>1</sub> anomeric OH of each isomer using <sup>18</sup>O labeling. We then used  $\alpha$  and  $\beta$  O-methylated disaccharides to identify which mobility peak corresponded to which anomer. In a related experiment, we used our approach to extract mutarotation rate coefficients for  $\alpha$  and  $\beta$  glucose anomers interconverting in solution.<sup>3</sup>

Furthermore, a second-generation instrument combining SLIM-based IMS with cryogenic vibrational spectroscopy in a high throughput configuration was presented. The instrument was designed and constructed to allow for maximum sensitivity and signal stability, as well as for a high-throughput analysis, aiming to fulfill the requirements for commercially viable analytical techniques. The apparatus includes a high-resolution cyclic SLIM device with a single-pass resolution of  $\sim 180$  that can be operated to perform IMS<sup>n</sup> experiments *via* the incorporation of on-board CID traps. The CID process was further optimized by adding a grid assembly that allows for an accurate definition of the electric field used to accelerate the parent ions, resulting in well-defined CID conditions. The main novelty of the instrument was the design and implementation of a new multi-trap device that allows for multiplexing the IR fingerprinting process. The motivation behind the design as well as the characterization of the IMS capabilities and IR fingerprinting process were presented and discussed. Notably, the instrument is capable of acquiring an IR fingerprint of a disaccharide within 15 seconds. In addition, we report the simultaneous acquisition of the IR spectra of two mobility separated LNT isomers obtained using a one-minute scan. This study is the first where multiplexed IR spectral acquisition was performed, which emphasizes the unique capabilities of this home-built instrument.

The successful application of the hereby presented combination of analytical techniques to identify glycan isomers holds promise when it comes to addressing the current challenges in glycomics. Moreover, the latest developments aiming to increase the sensitivity as well as the throughput *via* our multiplexing approach opens the door to the implementation of experimental protocols that produce highly accurate and reproducible results with a low sample consumption and with a total duration that is comparable or faster than the currently employed state-of-the art technologies. The ability to add a spectroscopic dimension without increasing the measurement time represents a significant advance in glycan analysis.

All these developments have the objective of fulfilling the needs of the analytical community to produce a tool for highly accurate and rapid analyses applicable to a wide range of molecules. In this context, we plan to expand the scope of applications beyond glycans, addressing classes of molecules such as peptides, lipids, and metabolites wherever isomer identification remains challenging.

The use of ultrahigh resolution IMS as a prefilter for IR spectroscopic interrogation, producing isomer-specific IR fingerprints has already proven to be a powerful tool to study the gas phase structure of molecular ions. The application of the combination of these highly orthogonal techniques for analytical purposes will undoubtedly have a considerable impact on a large range of applications in biomolecular analysis that we hope will greatly advance research in the life sciences.

## References

1. Warnke, S.; Ben Faleh, A.; Pellegrinelli, R. P.; Yalovenko, N.; Rizzo, T. R., Combining ultra-high resolution ion mobility spectrometry with cryogenic IR spectroscopy for the study of biomolecular ions. *Faraday Discuss* **2019**, *217* (0), 114-125.
2. Ben Faleh, A.; Warnke, S.; Rizzo, T. R., Combining Ultrahigh-Resolution Ion-Mobility Spectrometry with Cryogenic Infrared Spectroscopy for the Analysis of Glycan Mixtures. *Anal Chem* **2019**, *91* (7), 4876-4882.
3. Warnke S., B. F. A., Scutelnic V, Rizzo T. R., Separation and Identification of Glycan Anomers Using Ultrahigh-Resolution Ion-Mobility Spectrometry and Cryogenic Ion Spectroscopy. *J. Am. Soc. Mass Spectrom.* **2019**, *30* (11), 2204–2211.

## Annex A

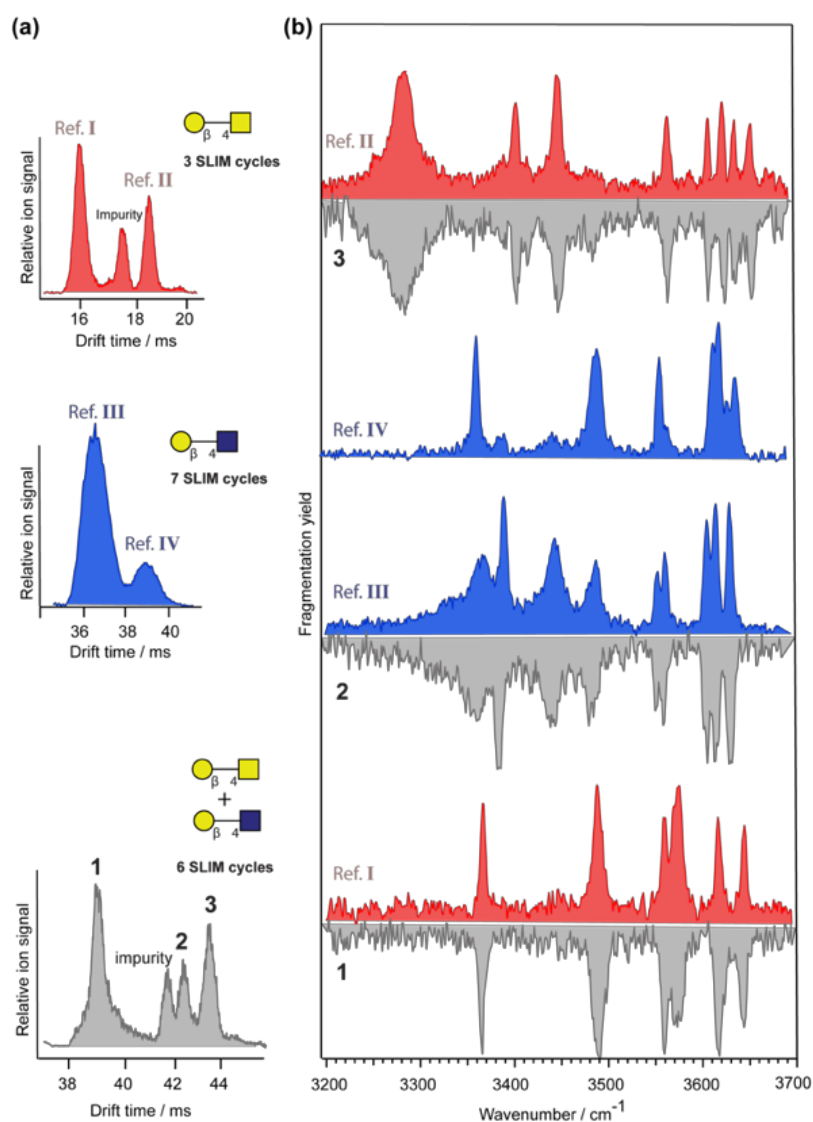


**Figure A.1:** Arrival time distribution of the mixture of the two sodiated disaccharides (grey) and of the references electrospayed individually (blue and red). IR spectra of the different nitrogen tagged, mobility-selected species from the mixture (gray) and obtained from individually investigated substances as references (red and blue).

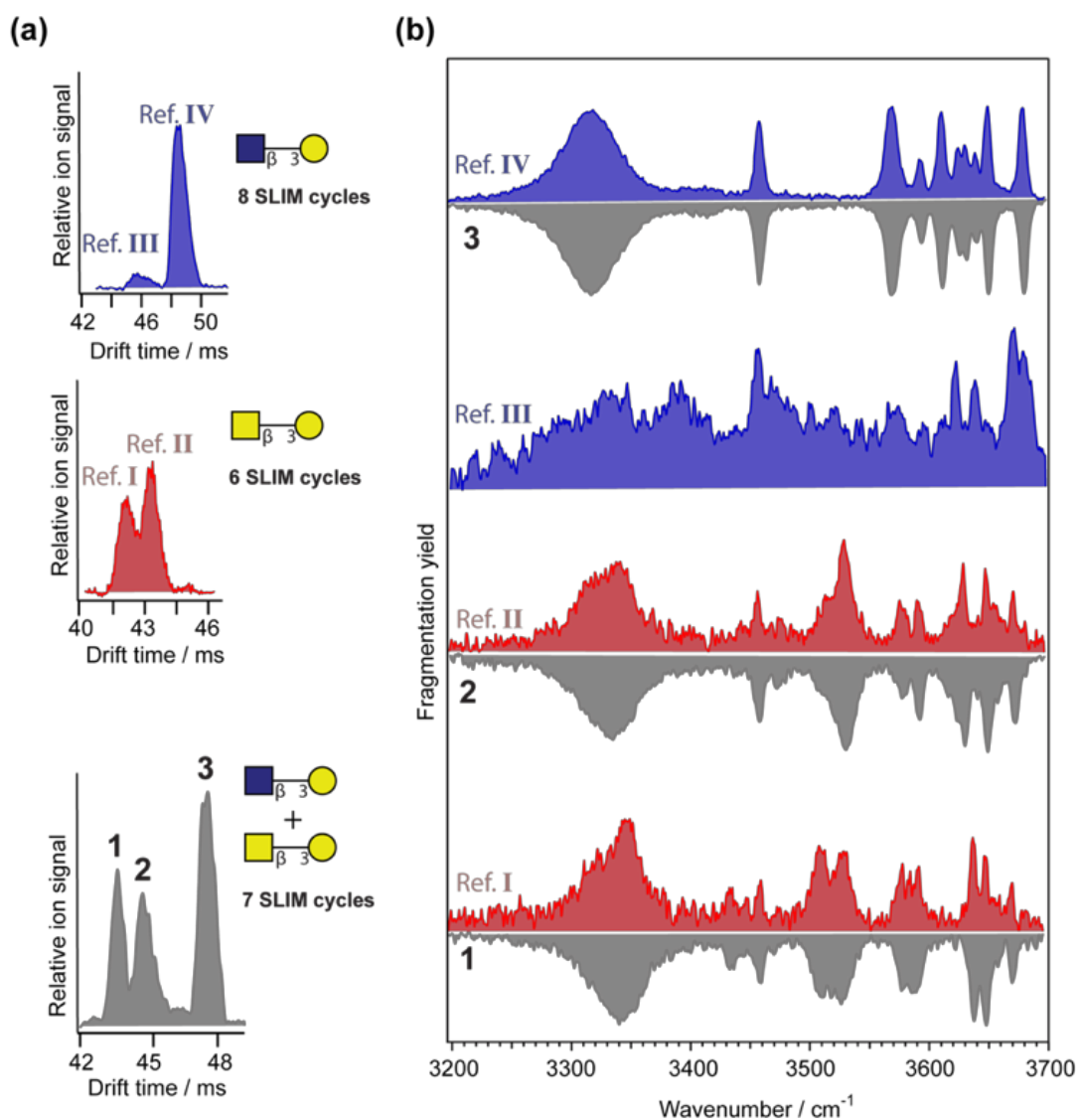


**Figure A.2:** Arrival time distribution of the mixture of the two sodiated disaccharides (grey) and of the references electrosprayed individually (blue and red). IR spectra of the different nitrogen tagged, mobility-selected species from the mixture (gray) and obtained from individually investigated substances as references (red and blue).

## Annex B

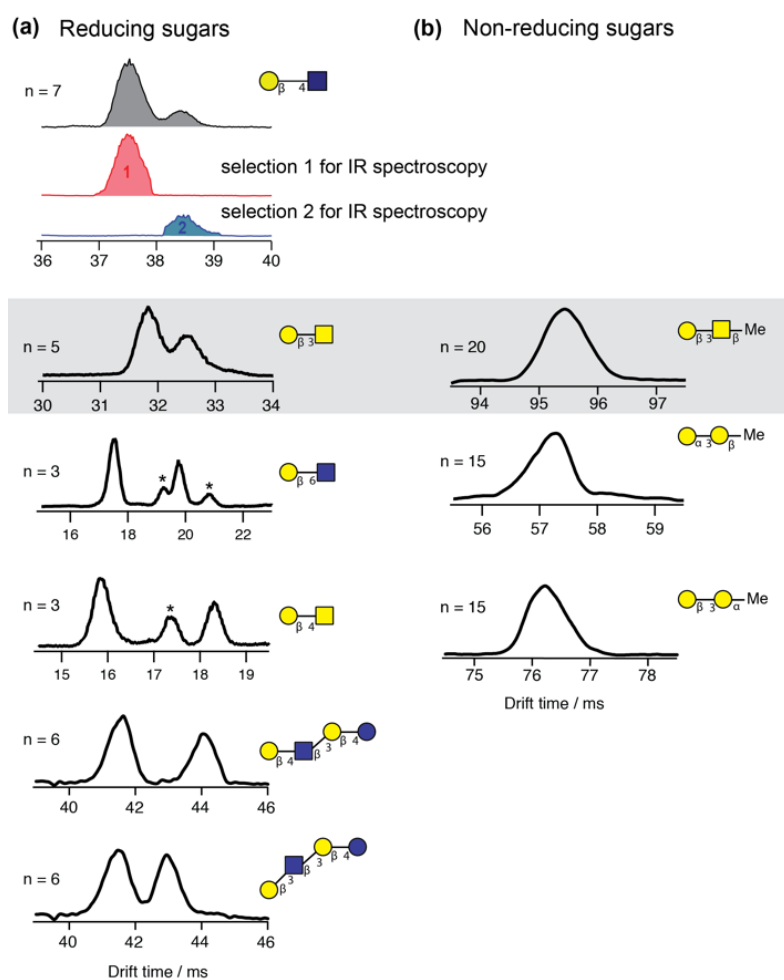


**Figure B.1:** (a) ATDs of glycans with a free reducing-end OH group that are able to form  $\alpha$  and  $\beta$  anomers at different number  $n$  of IMS cycles on the SLIM board. The type of sugar is annotated in Oxford nomenclature. The top three panels show exemplarily how two different drift peaks are selected into two portions that can then be investigated separately. (b) ATDs of glycans with a methylated reducing-end. As a consequence, the C1 carbon on the reducing-end of these glycans

are locked in their  $\alpha$  and  $\beta$  anomeric con-figuration. An asterisk marks signals that are due to ions of slightly different  $m/z$ , which could not sufficiently filtered with the quadrupole MS used.

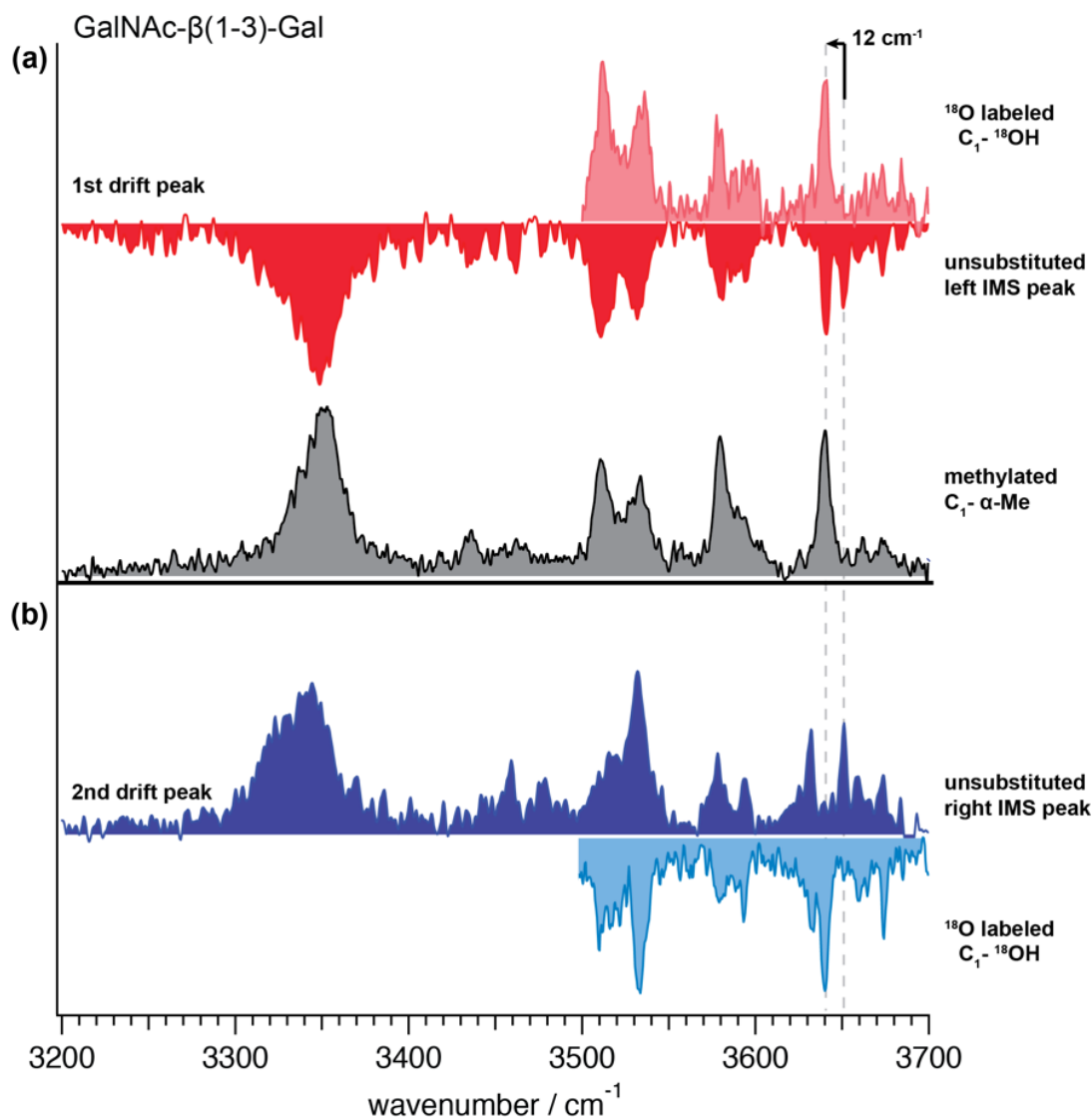


**Figure B.2:** Infrared spectra of the mobility-selected left ((a), dark red) and right ((b), dark blue) drift peak of the disaccharide GalNAc- $\beta$ (1-3)-Gal and the equivalent species with  $^{18}\text{O}$ -substituted C1-OH group (light colors), which exhibit a 12  $\text{cm}^{-1}$  redshift in one absorption band. The spectrum of the methylated species GalNAc- $\beta$ (1-3)-Gal- $\alpha$ -Me (grey) matches the spectrum of the left drift peak in position and intensities of absorption bands, with the exception of the absent C1-OH oscillator for the methylated species. The left drift peak is thereby identified as the  $\alpha$  anomeric form of GalNAc- $\beta$ (1-3)-Gal and the right peak (by exclusion) as the  $\beta$  anomeric form.

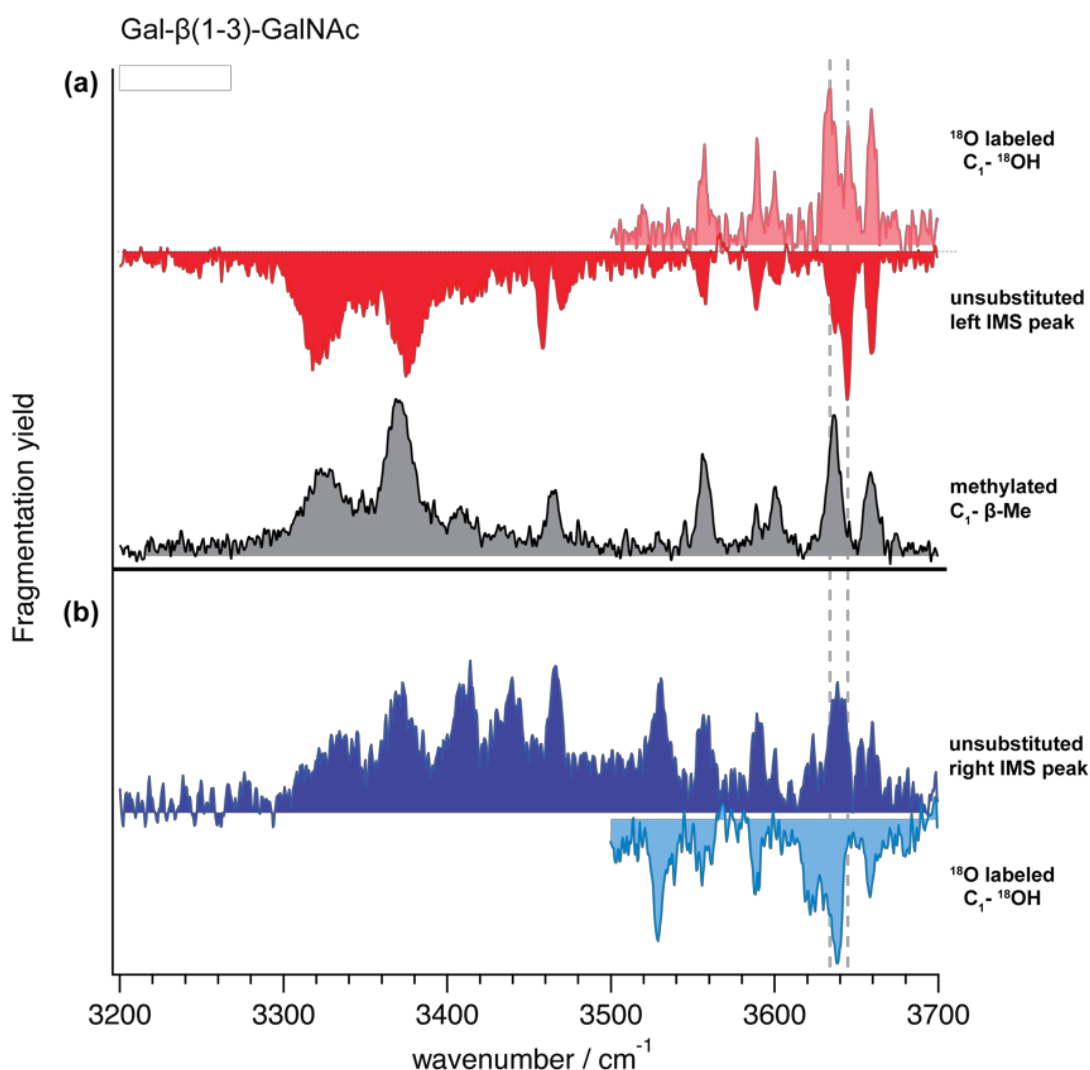


**Figure B.3:** Infrared spectra of the mobility-selected left ((a), dark red) and right ((b), dark blue) drift peak of the disaccharide Gal- $\beta$ (1-3)-GalNAc and the equivalent species with  $^{18}\text{O}$ -substituted  $\text{C}_1\text{-OH}$  group (light colors), which exhibit a  $12\text{ cm}^{-1}$  redshift in one absorption band. The spectrum of the methylated species Gal- $\beta$ (1-3)-GalNAc- $\beta$ -Me (grey) matches the spectrum of the left drift peak in position and intensities of absorption bands, with the exception of the absent  $\text{C}_1\text{-OH}$  oscillator for the methylated species. The left drift peak is thereby identified as the  $\beta$ -anomeric form of Gal- $\beta$ (1-3)-GalNAc and the right peak (by exclusion) as the  $\alpha$  anomer.

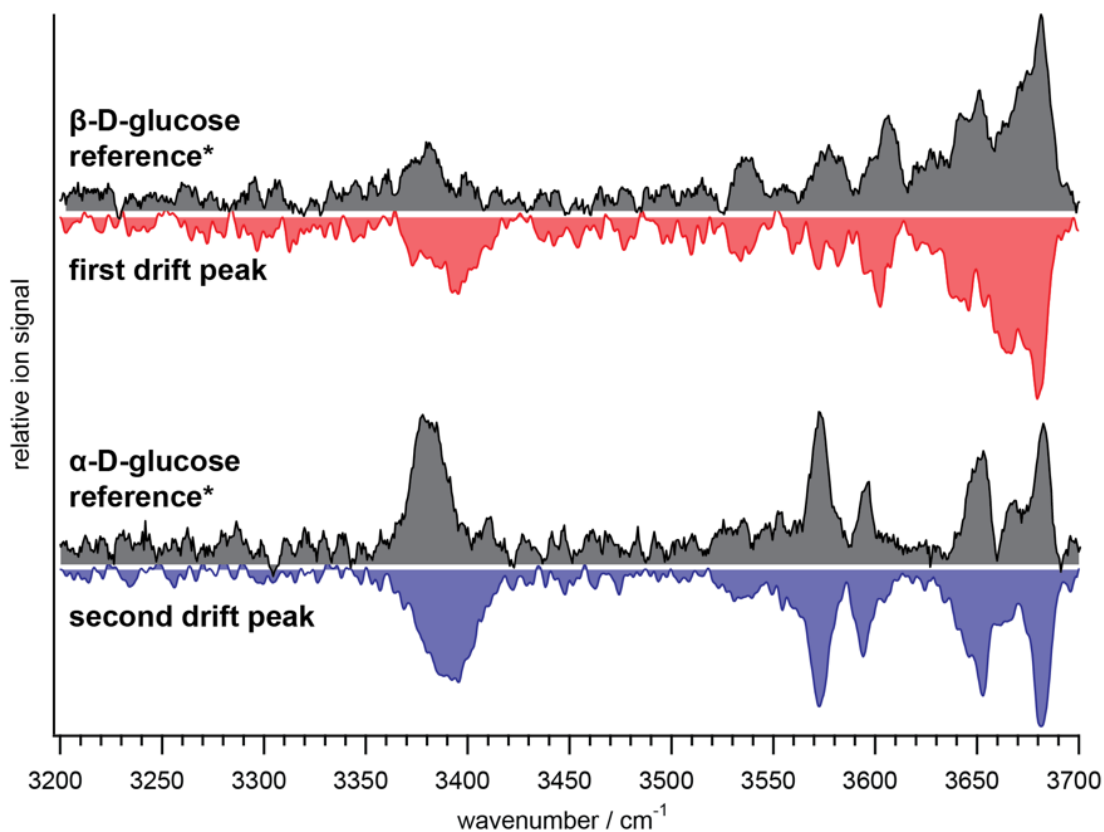


**Figure B.4:** Infrared spectra of the mobility-separated first (red) and second (blue) drift peak of electrospayed  $\alpha$ -D-glucose and previously published reference spectra of the  $\alpha$  and  $\beta$  anomers of glucose from a cryogenic, messenger-tagging, double-resonance spectroscopic experiment. The good agreement with the reference spectra leads to the assignment of the  $\alpha$  and  $\beta$  anomers to the first and second IMS drift peak, respectively.

## Glucose mutarotation

The conversion reaction  $\alpha$ -D-glucose  $\rightleftharpoons_{k_\beta}^{k_\alpha}$   $\beta$ -D-glucose can be treated as a first order reaction and the rate equation follows as

$$-\frac{dc_\alpha(t)}{dt} = \frac{dc_\beta(t)}{dt} = k_\alpha c_\alpha(t) - k_\beta c_\beta(t).$$

Using the substitution for the observable rate  $k = k_\alpha + k_\beta$  and the total concentration  $c_0$ , this can be written as

$$\frac{dc_\alpha(t)}{dt} + kc_\alpha(t) = k_\beta c_0.$$

Under consideration of the boundary conditions for  $c_\alpha$  and  $c_\beta$

$$\begin{aligned} c_\alpha(t_0) &= c_0 \\ c_\beta(t_0) &= 0 \\ c_i(t \rightarrow \infty) &= c_i^{eq} \end{aligned}$$

the rate differential equation can be solved for  $c_\alpha(t)$  and  $c_\beta(t)$ , respectively, with

$$\begin{aligned} c_\alpha(t) &= c_\alpha^{eq} + (c_0 - c_\alpha^{eq})e^{-kt} \\ c_\beta(t) &= c_\beta^{eq} - c_\beta^{eq}e^{-kt}. \end{aligned}$$

The parameters  $c_{\alpha}^{eq}$ ,  $c_{\beta}^{eq}$ , and  $k$  can be obtained from fitting the experimental data describing the abundance of the  $\alpha$  and  $\beta$  anomeric forms with these functions (Fig. 6.4b in the main manuscript). To obtain the specific rate constants we find the relationships

$$k_{\beta} = \frac{c_{\alpha}^{eq}}{c_0} k \quad \text{and} \quad k_{\alpha} = k - k_{\beta} = \left(1 - \frac{c_{\alpha}^{eq}}{c_0}\right) k.$$

# Acknowledgements

Lausanne, le 30 décembre 2021,

It is all about the journey! Isn't it? When the journey comes to an end, you take a step back and try to understand what made it possible. How could you have possibly accomplished what, not a long time ago, seemed like a goal far away from your reach? I guess my answer to that is 'I am not sure...' It took some hard work, no question about that, but that is far from being the only thing. Truth is, without the people around me, nothing of this would have been possible.

When can anybody say that they succeeded in doing something? Well, I am not sure either... What I know though, is that being happy doing what you do is the closest feeling to success. Also, happiness is an everyday business, meaning that if you are happy doing whatever you are doing, you most probably are in the right place, at the right time, and with the right people. It also means that you are a very lucky person!!!

During the last 11 years, I had the unconditional financial and moral support of both my parents, every day, all day. But most importantly, the confidence they put in me allowed me to always move forward, and for that, I will forever be grateful. I know parents are supposed to do that but still, mine took their job pretty seriously. I am lucky to have them with me and I hope they will stay with me for a long time. Best parents ever!! It is my thesis and I can say whatever I want!!!

I also had the unconditional support of my family in Switzerland. My cousins Walid, Wadih, Zied, and Asma were my pillars in here. Always there for me when in need, for financial help, manpower, and a good laugh. I also found a family in my friends, Mehdi,

Wissem, Seif (Ejjon), Slama & Dhekra, Fahd, Jida, les Jijis, Yasmine, Maryem, Halleb, Nadia, Sameur. Yes, I am naming everybody, and whenever I remember a name I come back and add it to the list!! Anybody who had the chance to live abroad knows the importance of having a family of friends who are there for you every time you need, and cheer you up when life gives you lemons (copyright Sarah's poster, to whom we will come back with further details in the remaining of this section). My friends back in Tunisia are yet another family to me, Hassene, Haythem (lghorch), and Jabloun, thank you for being there for me and my parents when it mattered most. You made up for my absence in the best of ways and you were always there when I needed you most. I am grateful to you guys and I am sure you know that none of this would have been the same without your presence in my life. And In case you didn't know now you know!!

I started my PhD roughly four years ago. And it just happens to be the time I met my preferred human on this planet 'Sarah'. I am not sure if I learned more during the last four years from my work in the lab or from being around her. I will probably get no diploma from her though, so... Anyway, thanks to her full support, especially in the rough times, that I could always go forward. She has the ability to get an honest laugh from people even in the darkest moments when everything is going wrong, and that is definitely a real rare skill. She is my companion, my best friend, my all. Thank you for being there for me all the time, it is a blessing to share my life with you every day!! I am happy when I am around you which means my life is a success (See paragraph one for more detail about the theory). I am also especially grateful to Sarah's family, Ricardo, Suzanne, and Thomas as well as her aunt and uncles who truly are my second family here in Lausanne. Thank you for considering me as one of yours. Yes, I have too many families and yes, I am a blessed person!!!

I am also grateful to Dr. Stephan Rauschenbach who introduced me to scientific research. His personality and his approach to science played a huge part in my choice to go for the PhD.

None of this would have been possible if not for my Professor Thomas Rizzo. He is my mentor and I learned a lot from Prof. Rizzo as a scientist. Thanks to him I developed skills such as critical thinking and presenting scientific ideas and content in a clear and precise way (and I am still learning). It was a blessing to work with him for the last four years and I hope that our journey as a team will go on for as long as possible. I also learned a lot from Thomas Rizzo the man. His kindness and his unconditional support helped me develop as a person and as a scientist. He believed in me during even the toughest of times and for that, I will be forever grateful.

On the first day of the job, I met Dr. Stephan Warnke. To be honest, I think I owe him almost everything I know in our field. He is a brilliant scientist no doubt, but he also is a great colleague. He never gets tired of explaining the same thing over and over again (not indefinitely, but a pretty big number of times). He taught me everything I know about instrument design, experiment design, lab organization, and above all, the importance of details. For that knowledge, I am grateful and will be forever indebted. He is a colleague a mentor and a friend, and I hope that we can go forward as a team for as long as possible.

I also wanted to thank my colleagues, Chiara, Val, Irina, Vasyl, Ali, Priyanka, Eduardo, Lei, Veronika, Ana, Bo-Jung. I am also grateful to Dr. Andreas Osterwalder for the scientific and non-scientific discussions around a coffee, and the support. A special thank you to my buddy Robert, I wish you all the best man, and to Angeles Alarcon who did everything to make my life easier from an administrative point of view but not only. She always knew what to say to cheer me up when I was going through dark times. You are wonderful!!!

I am especially grateful to André Fattet, Yves Morier, Guillaume Fancey from the ISIC mechanical workshop, Benjamin LeGeyt and Grégoire Pasche from the electronic workshop. None of this would have been possible without your contribution.

The Phd chapter comes to an end but the journey has just begun, and since it is all about the journey... Being grateful comes with the realization that none of what was accomplished

would have been possible if not for an extensive list of wonderful people. Thank you for allowing me to be happy and thus lead a successful life.